Phase Behavior and Phase Separation Kinetics in Polymer Solutions under High Pressure

Wei Zhang

Dissertation submitted to the Faculty of

Virginia Polytechnic Institute and State University

in Partial Fulfillment of the Requirements for the Degree of

Doctor of Philosophy

in

Chemical Engineering

Dr. Erdogan Kiran (Chair)

Dr. Garth L. Wilkes

Dr. S. Ted Oyama

Dr. John C. Hassler

Dr. Larry T. Taylor

April 5, 2005

Blacksburg, VA

Keywords: Phase Behavior, Phase Separation Kinetics, Polymer Solution, Supercritical Fluids, High Pressure, Light Scattering, Crystallization, and Green Chemistry

Phase Behavior and Phase Separation Kinetics in Polymer Solutions under High Pressure

Wei Zhang

(Abstract)

The phase behavior and phase separation kinetics in polymer solutions in binary mixtures of supercritical carbon dioxide (CO_2) and organic solvents were studied for two systems. Solutions of polyethylene (PE) in CO_2 + n-pentane were selected as one model system to study both the solid-fluid (S-F) and liquid-liquid (L-L) phase transitions as well as the interplay of these two types of phase separations on the final morphological and thermal properties of PE crystals. Solutions of polysulfone (PSF) in CO_2 + tetrahydrofuran (THF) were selected as another model system because of the technological importance of this membrane forming polymer and because of the broad interest in developing new solvent/non-solvent systems for forming microporous materials. These phase boundaries were determined using a high-pressure view-cell and optical techniques over a temperature range of 90-165 ^oC and pressures up to 55 MPa for PE/n-pentane/CO_2 system, and over a temperature range of 25 to 155 ^oC and pressures up to 70 MPa for PSF/THF/CO_2 system.

For PE solutions, it has been found that the addition of CO_2 to the PE/n-pentane system shifts the L-L phase boundary to significantly higher pressures, but moves the S-F phase boundary only slightly to higher temperatures. The S-F phase boundary which represents the crystallization/melting process in the polymer solution was about 10 ^oC lower than the crystallization/melting temperatures of the neat polyethylene samples determined by differential scanning calorimetry (DSC). It was further found that the S-F phase boundary in n-pentane displays a unique sensitivity to the pressure-temperature conditions and moves to lower temperatures in the pressure range from 38 to 42 MPa. This effect even though not as augmented remains also for the S-F boundary in the solutions in CO_2 + n-pentane mixtures.

The miscibility of PSF in THF + CO_2 was investigated at CO_2 levels up to 14 wt %. This system shows lower critical solution temperature (LCST)-type phase behavior at low CO_2 content, which is shifted to upper critical solution temperature (UCST)-type at higher CO_2 levels along with an increase in the miscibility pressures. In contrast to the PE system, this system was found to display multiple miscibility windows. A 'U'-shaped phase boundary in 92 % THF + 8 % CO_2 mixture was observed to transfer to a "W"-shaped phase boundary at 10 wt % CO_2, which was further separated into a double 'U'-shaped phase boundary at 13 wt % CO_2. The specific volume of the polysulfone solutions were found to display a variation parallel to this changing pattern in the phase boundaries, with reduced miscibility being accompanied with an increase in the specific volume.

The phase separation kinetics in these two polymer solutions were investigated using time- and angle-resolved light scattering techniques. With the PE solutions, the focus was on the kinetics of S-F phase separation (crystallization) and miscibility and

(melting) in n-pentane. Experiments were conducted with relatively dilute solutions at concentrations up to 2.3 wt %. The results show that the crystallization which was induced by cooling at constant pressure is dominated by a nucleation and growth process. In the majority of the experiments the particle growth process was observed to last for about 1 minute with a slight dependence on the crystallization pressure.

The phase separation kinetics in PSF solutions were conducted only in a solvent mixture containing 90 wt % THF and 10 wt % CO_2. Polymer concentrations were varied up to 3.3 wt %. This system was also observed to undergo phase separation by only nucleation and growth mechanism under these conditions upon reducing the pressure at constant temperature. Several experiments were conducted using a multiple rapid pressure drop technique to identify the depth of the metastable region.

PE crystals that were produced by crossing the S-F boundary by different paths were collected and characterized by field emission scanning electron microscopy (FESEM) and DSC. Crystallization was carried out either by cooling at constant pressure, or by cooling without pressure adjustment, or by first crossing the L-L boundary via pressure reduction at a constant temperature followed by cooling. For crystal recovery, the system was depressurized to ambient conditions irrespective of the path. It was found that all of the crystals formed from these solutions show multiple melting peaks in their first DSC heating scans, which however collapse into one crystallization peak in the cooling scans and one melting peak in the second heating scans. The temperatures corresponding to the multiple melting peaks were lower than the single melting temperature of the original PE sample and the melting temperature observed in the second heating scans for all samples. The multiple melting peaks were attributed to the presence of different lamellar thickness that are formed in the crystallization, final depressurization and sample collection stages. Depending upon the crystallization path some differences were noted. The crystals formed by first going through L-L phase separation displayed predominately double melting peaks in the first DSC scan. It was observed that the overall crystallinity is increased by more than 10 % to about 75 % compared to the crystallinity of the original PE sample, which is about 63 %.

FESEM characterization showed that the prevailing morphology is composed of plate-like lamellae that show different level of agglomeration depending on the crystallization conditions. The overall structures of the particles were ellipsoid for crystals formed from dilute solutions. For crystals formed from the 1% PE solution, crystal sizes ranged from 4 μm × 10 μm for crystals formed at 14 MPa to 30 μm × 45 μm at 45 MPa. The crystals formed from 5 wt % solutions in n-pentane at pressures in the range of 38-54 MPa showed different morphologies with features of stacked lamellae structures which were however not preferred morphologies in crystals formed from n-pentane + CO_2 solutions. The crystals that were formed from first crossing the L-L phase boundary followed by cooling showed two distinct particle size ranges that were attributed to crystals formed from the polymer-rich and polymer-lean phases that evolve when the L-L phase boundary is crossed.

Acknowledgements

It's hard to overstate my gratitude to my Ph.D. supervisor, Professor Erdogan Kiran. With his inspirational guidance, his enthusiasm, his encouragement, and his support in every aspect of my studies at Virginia Tech, he helped me to carry out my doctoral work at Virginia Tech. He is not only a teacher, but also a lifetime friend and advisor to me.

My special thanks go also to the members of my advisory committee, Professors John C. Hassler, S. Ted Oyama, Larry T. Taylor, and Garth L. Wilkes for their guidance and helpful discussions.

I am grateful to the Mr. Wendell Brown, Michael Vaught and Riley Chan for their excellent work on building and maintaining the experimental equipments. The secretaries of the Chemical Engineering Department, Chris Moore, Diane Cannaday, Lee Bishop, and Jane Price are thanked for their willingness to help at all the times. I thank Mr. Stephen McCartney for the SEM work.

I thank my fellow students and the visiting scholars in Professor Kiran's group, Ke Liu, Cigdem Dindar, Zeynep Bayraktar, Kun Liu, Gerd Upper, Jian Fang, and Prof. Sangdo Yeo for their help and support. I appreciate the encouragements, the friendship and the help from Herb and Evelyn Hobbs during my study at Virginia Tech.

Finally, I want to express my appreciation to my wife, Hailing Yang, and my parents, Huaxin Zhang and Yuxiang Cao, for their love, endless support, and never failing faith in me.

Table of Contents

List of Tables

Page

List of Figures

Page

Chapter 1
Introduction

Understanding the phase behavior and the phase separation dynamics of polymers in fluid and fluid mixtures is important for many processes encountered in polymer synthesis, purification, processing, and modifications. For example, the solubility of monomer in the oligomer or polymer phase during polymerization could affect the reaction rate. The solubility of a polymer in the reaction medium can affect the miscibility and may lead to phase separation. In polymer processing and modifications such as those encountered in forming membranes, particles, fibers and other micro-structured materials, the knowledge of the phase behavior and phase separation dynamics is essential to control the process and the final structures.

Phase separation can be induced by changing the control parameters such as temperature, pressure, composition, or applied field. When a homogenous mixture is brought into the heterogeneous state, the phase separation can proceed via either spinodal decomposition or nucleation and growth. The phase separation pathway depends on the quench depth into the two-phase region (Cahn, 1959, 1961; Hashimoto, 1988; Kiran, 2000). Spinodal decomposition occurs if the system is quenched into the thermodynamically unstable region inside the spinodal envelope, while nucleation and growth occurs if the system is quenched into the metastable region bounded by the binodal and spinodal boundaries. These two processes can result in quite different morphologies in polymer mixtures. Bi-continuous structure or percolation structure is usually considered as the characteristic representation of the initial stage in spinodal

decomposition, while a structure that shows phase separated isolated domains in another continuous phase is the characteristic feature for the nucleation and growth process. During the intermediate or late stage of phase separation by spinodal decomposition, the bi-continuous structure can break up to form isolated phases in a continuous phase driven by surface energy, known as percolation-to-cluster transition. The co-continuous structure formation is not linked to spinodal decomposition. It can also be formed from the growing and interpenetration of phases even if the process may have started with a nucleation and growth mechanism (Binder, 1990; Binder and Fratzl, 2001).

Due to the environmental concerns regarding hazardous chemicals, carbon dioxide (CO_2) in liquid, near-critical or super-critical states, has been considered as a replacement for some conventional organic solvents. However, it is not a good solvent for most polymers. Some studies have been carried out to improve the solubility of polymers in CO_2. One method is to use CO_2-philic polymers such as fluoropolymers, fluorinated polymers, and siloxane containing polymers as a stabilizer of polymer-CO_2 systems (Beckman, 2004; Yazdi et al., 1996; Desimore, Guan and Elsbernd, 1992; Desimone and Tumas, 2003; Guan and Desimone, 1994; Liu and Kiran, 1999; Luna-Barcenas et al., 1998; McHugh, 2003; Kazarian, 2000). Another approach is to incorporate a good solvent for the polymer of interest with CO_2 to form a binary mixture and use this binary mixture as a solvent. In this case, even though the conventional organic solvent is not eliminated, there are some advantages over using pure solvent or CO_2 by itself. First, the amount of organic solvent can be reduced greatly. Second, the addition of CO_2 can help in the recovery of organic solvent. Finally, in some cases, the addition of CO_2 into a polymer solution brings about phase separation for structure

formations and separations. There have been a series of studies reported on the phase behavior of polymers in mixtures of organic solvents and carbon dioxide (Kiran and Zhuang, 1994b; Xiong and Kiran, 1994, 1995, 2000; Bungert, Sadowski and Arlt, 1997; Zhuang and Kiran, 1998; Lee, Lee and Hwang, 2000; Kuk et al., 2001; Joung et al., 2002). In these ternary systems with polymer + solvent + CO_2, the miscibility of a polymer in solution is reduced with increase in the CO_2 content, and the type of phase behavior may be altered at a certain CO_2 level. For example, in a 10 wt % polyethylene (PE) (Mw = 16,400) in *n*-pentane system, the lower critical solution temperature (LCST) type of phase behavior is altered to the upper critical solution temperature (UCST) type of phase behavior when the CO_2 content is above 50 % by mass (Zhuang, 1995).

The main goal of this study is to further our understanding of the phase behavior and phase separation dynamics in polymer solutions in binary mixtures of an organic solvent and CO_2 under high pressures. The polymer solutions chosen for this study are polysulfone (PSF) in tetrahydrofuran (THF) and CO_2 mixtures and polyethylene in *n*-pentane and CO_2 mixtures. Polysulfone is a very important commercial polymer that is widely used for membrane formation. THF, although a good solvent for polysulfone, is not an environmentally benign chemical. CO_2 is introduced to this system to reduce the amount of the THF and to bring about phase separation, which offers a new approach for fabrication of polysulfone membranes. The other system, polyethylene in *n*-pentane and CO_2, is chosen as a model system for extending the effort to studies on the solid-fluid phase behaviors and the crystallization and melting of polymers in solutions under high pressure. Even though the liquid-liquid phase separation in PE + *n*-pentane + CO_2 systems have been extensively studied, there is very little information on the solid-fluid

phase boundary and dynamics of phase separation and miscibility during crystallization and melting.

This thesis is organized in the following way. Chapter 2 is devoted to a review of the theoretical background, the experimental approaches, and some literature findings that are relevant to this work. The background on the thermodynamics and the phase separation kinetics are discussed first. The light scattering techniques used for the study of the phase separation mechanics, such as pulse induced critical scattering (PICS), pressure pulse induced scattering (PPICS), multiple-rapid-pressure-drop (MRPD), and the extrapolation method are included. Some literature work on high pressure studies are then reviewed.

The experimental systems used in the present study, a high-pressure view-cell and a time- and angle-resolved light scattering system, and the operational procedures are described in Chapters 3 and 4, respectively. The experimental procedures include determining the miscibility and volumetric properties of polymer solutions and performing of light scattering experiments during the pressure- and/or temperature-induced phase separations.

The miscibility and the volumetric properties of polyethylene in *n*-pentane and *n*-pentane + CO_2 mixtures are presented in Chapter 5. The effect of CO_2 level on the solid-fluid (S-F) and liquid-liquid (L-L) phase boundaries are discussed. Based on the phase boundary information, the crystallization and melting kinetics and the interplay of S-F and L-L phase separations of PE in *n*-pentane solutions are described in Chapter 6. The evolution of the PE crystals in *n*-pentane and the melting of these crystals are also included in this chapter. The effect of pressure on light scattering profiles and the average

particle sizes that were evaluated from the light scattering profiles are also discussed. Chapter 7 focuses on the morphological and thermal properties of the PE crystals formed in *n*-pentane and *n*-pentane + CO_2. Some unique features are observed for PE crystals formed in *n*-pentane under high pressure. The DSC results of these PE particles reveal that different crystal sizes are formed during the sample collection process. The effects of pressure, polymer concentration, and the composition of CO_2 on the morphological and thermal properties are also presented in detail. A crystallization mechanism is proposed in order to explain the morphological and thermal observations.

Chapter 8 presents the miscibility and volumetric properties of PSF in THF + CO_2 system. These studies are focused on the liquid-liquid phase boundary. A unique phase behavior, multiple miscibility windows, is observed in this system. The effect of CO_2 on the phase behavior and the shift of the multiple miscibility windows is discussed. The results on specific volume of the polysulfone solutions display a parallel variation to that of the phase boundary, which means that the specific volume is larger when the polymer solution has a poor miscibility and is smaller when the polymer solution has a good miscibility. The pressure-induced phase separations in polysulfone solutions in THF + CO_2 are investigated using light scattering, and the results are presented in Chapter 9. The light scattering profiles at several conditions indicate that the metastable gap is very large, while the spinodal envelope is calculated using the extrapolation method.

The following publications have already appeared based on the present thesis research:

> Wei Zhang, Cigdem Dindar, Zeynep Bayraktar and Erdogan Kiran. Phase Behavior, Density, and Crystallization of Polyethylene in *n*-Pentane and in *n*-

Pentane/CO_2 at High Pressures**.** *Journal of Applied Polymer Science* (2003), 89(8), 2201-2209.

Wei Zhang and Erdogan Kiran. (p,V,T) Behavior and Miscibility of Polysulfone + THF + Carbon Dioxide at High Pressures. *Journal of Chemical Thermodynamics* (2003), 35(4), 605-624.

Wei Zhang and Erdogan Kiran. Phase Behavior and Density of Polysulfone in Binary Fluid Mixtures of Tetrahydrofuran and Carbon Dioxide under High Pressure: Miscibility Windows**.** *Journal of Applied Polymer Science* (2002), 86(9), 2357-2362.

Wei Zhang and Erdogan Kiran, "Miscibility of Polymer in Binary Fluid Mixture at High Pressures: Polysulfone + THF + CO_2" in *Proceedings of the 4th International Symposium on High Pressure Technology and Chemical Engineering – High Pressure in Venice*, Venice, Italy, September 22-25, 2002, edited by A. Bertucco, Vol. 1, pp. 791-96.

Gerd Upper, Daniel Beckel, Wei Zhang and Erdogan Kiran. "High Pressure Crystallization in Supercritical or Dense Fluids" in *Proceedings of the 6th International Symposium on Supercritical Fluids*, Versailles, France, April 28-30, 2003, Vol. 3 – Materials Processing, pp. 1509-1514.

The following manuscripts are being prepared for publications based on portions of the present thesis research:

Wei Zhang and Erdogan Kiran. High-Pressure Crystallization and Melting Kinetics of Polyethylene in n-Pentane, To be submitted to *Polymer*.

Gerd Upper, Wei Zhang and Erdogan Kiran. High-Pressure Crystallization of Polyethylene in n-Pentane and n-Pentane + Carbon Dioxide Fluid Mixtures. To be submitted to *Journal of Supercritical Fluids*.

Chapter 2

Theoretical Background and Literature Review

2.1 Phase Behavior of Polymer Solutions

For a mixture of two components involving a polymer and a solvent, the Gibbs free energy of mixing ΔG^M must be negative to form a homogenous mixture. Figure 2.1 shows a schematic diagram of ΔG^M as a function of polymer concentration at different temperatures or pressures in the upper part (Utracki, 1994). A temperature (pressure)-polymer concentration (x) phase diagram is shown in the lower part of Figure 2.1. At T1, ΔG^M shows only one minimum over the polymer concentration range. Therefore, the system is completely miscible over the whole range of polymer concentration as shown in the phase diagram. At T2 and T3, even though ΔG^M is lower than zero for the whole range of polymer concentration, the system is only partially miscible. Since ΔG^M shows two local minima, in order to have the free energy ΔG^M of the system at the overall minimum, the system will separate into two phases with the concentrations of the two phases determined by the tangent points on the ΔG^M curve where

$$\left.\frac{\partial\left(\Delta G^M\right)}{\partial x}\right|_1 = \left.\frac{\partial\left(\Delta G^M\right)}{\partial x}\right|_2 \tag{2.1}$$

These two points are called binodal points, and the curve connecting all these points at different temperatures (pressures) is the binodal curve. The inflection points of $\Delta G^M - x$ curve corresponding to $\partial^2\left(\Delta G^M\right)/\partial x^2 = 0$ are the spinodal points, and the curve that connecting these points is the spinodal curve. The spinodal and binodal curves meet at

the critical point where $\partial^2\left(\Delta G^M\right)/\partial x^2 = \partial^3\left(\Delta G^M\right)/\partial x^3 = 0$. In the phase diagram, the region above the binodal curve is the stable region where a homogenous solution can be formed. The region inside the spinodal curve is the unstable region corresponding to $\partial^2\left(\Delta G^M\right)/\partial x^2 < 0$, where the system spontaneously phase-separates into two co-continuous phases. Between the binodal and spinodal curves, the system may be one phase but not stable, which is called the metastable region, where $\partial^2\left(\Delta G^M\right)/\partial x^2 > 0$. At T4, the free energy of mixing is larger than zero, and therefore the system is completely immiscible over the whole range of the polymer concentrations. This is not shown in the phase diagram.

The phase behavior shown in the lower part of Figure 2.1 is the typical behavior of systems showing an upper critical solution temperature (UCST), where the system enters the one phase region upon increasing temperature from C to A. If increasing temperature brings the system from miscible to immiscible region, it is referred to a lower critical solution temperature (LCST) type of phase behavior. Figure 2.2 shows different combinations of these two types of behaviors. In addition to only UCST (B) and LCST (C), a system can display both types of phase behaviors. This is illustrated by diagram D and E, which shows an island of immiscibility. The UCST and LCST branches in Diagram D can merge to form an hourglass shape phase diagram. This type of transition has been observed experimentally in polystyrene solutions in acetone (Luszczyk, Rebelo and van Hook, 1995) where two branches at higher pressures move to each other and merge at lower pressures. The liquid-liquid phase behavior can be much more complex than the phase diagrams shown in Figure 2.2. Fortunately, Scott and van

Konynenberg (1970) have summarized all known binary liquid-liquid phase diagrams into five classes, from which all the phase diagrams discussed above can be obtained.

The phase behavior can be more complex with the introduction of a third component. The third component can improve or reduce the miscibility of the binary system. In some instances, the two non-solvents for a solute can act together to dissolve the solute like a good solvent. This effect is called cosolvency. Schneider and coworkers (Pöhler and Schneider, 1995; Schneider and Scheidgen, 2000; Scheidgen and Schneider, 2000; Gauter et al. 2000) have conducted several systematic studies and reported on the cosolvency effects, miscibility windows and islands on ternary systems with carbon dioxide + 1-alkanol + alkane. Wolf et al. (Wolf and Malinari, 1973; Wolf and Blaum, 1976; Blaum and Wolf, 1976) have studied the cosolvency of one polymer (such as polystyrene) in two poor solvents (such as acetone and diethyl ether) where the mixture of two poor solvents can make a good solvent for the polymer.

Another important phase transition is the solid-fluid phase separation. This type of phase behavior is important for polymer solutions because the polymer can exist in the crystalline state if the polymer chains have a regular structure (such as linear polyethylene, polypropylene, polycarbonate, nylon). In the presence of solvent, the crystallization and melting temperatures can be highly reduced to lower temperatures. In a solution of a semi-crystalline polymer, the solid-liquid phase behavior is involved when the melts or solutions are undercooled below the crystallization temperature. For a binary system, the solid-liquid phase separation temperature T can be described by the following equation.

$$T = \frac{\Delta H^0_{mi}/R + gT(1-x_i)^2}{\Delta H^0_{mi}/RT^0_{mi} - \ln x_i} \tag{2.2}$$

Here T^0_{mi} is the melting temperature of pure components, g is the interaction function, and x_i is the composition of component i. A schematic T-x phase diagram of a semi-crystalline polymer in solution, which can be calculated from Eq. 2.2 together with a liquid-liquid phase boundary, is shown in Figure 2.3 (Koningsveld, Stockmayer and Nies, 2001). Diagram **a** shows a submerged liquid-liquid phase boundary under the solid-fluid phase boundary. As the melting temperature of the polymer (T_{m2}) decreases, the liquid-liquid critical point meets the solid-fluid line (**b**), shown as an open circle. As T_{m2} moves further down to lower temperatures, the L-L phase boundary is exposed with a UCST type of phase diagram (**c**) or with both the UCST and LCST boundaries (**d** and **e**).

2.2 Kinetics of Phase Separation

It is of great importance to understand the dynamic aspects of the phase separation as well as the thermodynamic aspects. Hence, in this section, the basic theories on the phase separation kinetics will be briefly reviewed. Starting from the stable region, the polymer solution can be quenched to the metastable region or unstable region. Depending on the location where the system is brought to, the system will undergo phase separation via two different mechanisms: nucleation and growth (see section 2.2.1), or spinodal decomposition (see section 2.2.2).

2.2.1 Nucleation and Growth Mechanism

When a polymer solution is brought from the stable region into the metastable region as shown by the arrow in Figure 2.1, the system can either exist as a single phase that is thermodynamically unstable or undergo phase separation. This is because even the free energy of the system is not at the global minimum, which corresponds to the common tangent line to the free energy curve, but it is at a local minimum. Therefore, the system is stable to small concentration, temperature, or pressure fluctuations. However, if the fluctuation is large enough, the system will phase separate into two coexisting phases, a polymer-rich and a solvent-rich phase. These concentration fluctuations can be considered as "polymer-rich" or "solvent-rich" clusters, from which the phase separation starts. These clusters have a concentration close to the concentration of the new phase. For a system with an overall concentration located on the left side of the critical concentration in the phase diagram, the newly-formed polymer-rich phase is surrounded with a polymer-lean region, which is different from the bulk phase. This is typical for a liquid-liquid phase separation process. Similar behavior can also happen if the system is brought into the solid-fluid phase-separated region. The difference is that the solid phase may be crystals of polymer chains free of solvent molecules. This process is favored by a decrease in the free energy. However, between these clusters and their surroundings of polymer-lean region and between the polymer-lean region and the bulk solution, the interfacial free energy rises and contributes to the total free energy change. For formation of a spherical cluster with radius of R, the free energy change (ΔF) is given by

$$\Delta F = -\frac{4\pi}{3} R^3 \Delta G + 4\pi R^2 \sigma \tag{2.3}$$

where ΔG is the change in the Gibbs free energy related to the degree of supersaturation and σ is the interfacial energy between the polymer-rich clusters and their surroundings. This is the classical nucleation theory, which uses the bulk properties of the new phase for the clusters and the solution properties for their surrounding regions, and assumes a sharp interface in between (Gunton et al., 1983; Gunton, 1999; Wagner, Kampmann and Voorhees, 2001). It is illustrated in Figure 2.4 where the newly-formed cluster with diameter $2R$ reaches its coexisting concentration c_α with a sharp interface (Hashimoto, Itakura and Shimidzu, 1986; Utracki, 1994; Binder and Fratzl, 2001).

The first term in Eq (2.3) is proportional to the volume of the new phase while the second term is proportional to the surface area. The free energy change is sketched in Figure 2.5 as function of R for a spherical cluster (Wagner et al., 2001). Here, ΔF shows a maximum (ΔF^*) at the critical radius R^* of the new phase. The clusters that are smaller than R^* redissolve back into the solution while those clusters larger than R^* grow spontaneously. The critical value of ΔF^* and R^* can be derived from equation 2.3 as:

$$\Delta F^* = \frac{16\pi\sigma^3}{3\Delta G^2} \tag{2.4}$$

$$R^* = \frac{2\sigma}{\Delta G} \tag{2.5}$$

Assuming a steady state and assuming that the growth rate is slower than the rate of critical cluster generation, the nucleation rate J can be found to be:

$$J = J_0 \exp(-W^*/kT) \tag{2.6}$$

where the preexponential factor J_0 is related to the mobility of the molecules, surface area of the critical cluster and the total number of clusters (Gunton et al., 1983; Gunton, 1999; Granasy, 1997). The classical nucleation theory was originally developed for the condensation of supercooled vapors, and it has been quite successful in predicting the nucleation rate in such systems.

However, the classical nucleation theory can only qualitatively describe the nucleation in supersaturated fluids. This is because it is quite questionable to use bulk properties to describe the clusters because the critical cluster may contain a very limited number of molecules. Also because of the small size of the cluster, the surface structure may not be well defined yet. The difficulty of the experimental observations during the nucleation stage makes it impossible to measure these values directly (Anderson and Lekkerkerker, 2002). Non-classical theories were developed in two directions. One approach uses a free energy function that depends on the spatial distribution of the order parameter instead of bulk properties for the cluster. This is the density functional theory (DFT) (Cahn, 1959; Cahn and Hilliard, 1958, 1959). The second approach is to use a diffuse interface instead of a sharp interface, but still use the bulk properties at least for the center of the cluster. The interfacial free energy is then represented by a function depending on the distance from center of the cluster and the characteristic interface thickness. This is the diffuse interface theory (DIT) (Granasy, 1997).

Despite its limitations, the classical nucleation theory has been applied to super-cooled liquids and particle formation in supercritical fluids (Zhuang, 1995; Debenedetti, 1990). And there are many studies on the crystallization of polymer from melts because the nucleation is related to the mechanical and optical properties (Stein and Rhodes,

1960; Tahara, Fukao and Miyamoto, 2002). Nakata and Kawate (1992) applied this theory to the phase separation in the polymer solution system using light scattering techniques. For a system of spherical particles having a size distribution which has $N(R)$ number particles between the radius range R to R + dR, the angular dependence of scattering intensity is given by

$$I(q) = A\int_0^\infty N(R)(R^3/q^3)J_{3/2}^2(qR)dR \tag{2.7}$$

where A is related to the optical constant of the system, q is the scattering vector in the medium defined as $q = (4\pi/\lambda)\sin(\theta)$ where λ is the wavelength of the incident radiation in the medium, 2θ is the scattering angle. $J_{3/2}(qR)$ is the Bessel function of order 3/2. At small angles, this equation can be approximated for practical purpose as (Nakata and Kawate, 1992; Zhuang, 1995)

$$I(q) = I_0 \exp(-0.221\, R_m^2 q^2) \tag{2.8}$$

where R_m is the mean radius of the particles and I_0 is the scattered light intensity at zero angle. Another method to measure the length scale of a heterogeneous system is using the correlation length that was developed by Debye and Bueche (1949). The scattered light intensity $I(q)$ is correlated to the correlation length ξ (which is a measure of the average phase size) by the following equation:

$$I(q) = \frac{A}{\left(1+\xi^2 q^2\right)^2} \tag{2.9}$$

where A is a constant (Debye, Anderson and Brumberger, 1957). Therefore a Debye-Bueche plot of $I(q)^{-1/2}$ vs q^2 should show a linear dependence

$$\left(I(q)\right)^{-1/2} = A^{-1/2} + A^{-1/2}\xi^2 q^2 \tag{2.10}$$

The ξ^2 can be determined from the ratio of the slope and the intercept. The Debye-Bueche plots have been used to calculate the characteristic length scale during crystallization in polymer films (Koberstein and Stein, 1980; Pogodina et al., 1999; Kawai and Strobl, 2004).

2.2.2 Spinodal Decomposition

When a system is brought from the stable region to the unstable region, phase separation may proceed by a spinodal decomposition mechanism. This is because the energy barrier to form a new phase disappears, and the phase separation process takes place spontaneously. This is displayed as spontaneously growing long-wavelength fluctuations in the system. It is illustrated in Figure 2.6. In comparison to the nucleation and growth mechanism, there is no sharp interface formed from t_0 to t_2, which happened during the late stage of phase separation (t_3). During the earlier stage of the spinodal decomposition, the wavelength does not change, but the amplitude of the fluctuation waves increases with time. This stage is described by the linear Cahn-Hilliard theory (Binder and Fratzl, 2001; Gunton et al., 1983; Gunton, 1999), which is briefly described below.

The Cahn-Hilliard theory describes the concentration fluctuation in a multi-component system as:

$$\frac{\partial c(x,t)}{\partial t} = M\nabla^2 \times \left\{ \left(\frac{\partial f[c(x,t)]}{\partial c} \right)_T + r^2 k_B T \nabla^2 c(x,t) \right\} \tag{2.11}$$

where $c(x, t)$ is the concentration field, M is the mobility, f is the free energy density which is a function of the concentration, k_B is the Boltzmann constant, and r is the range of effective interaction. Since the mobility and free energy may strongly depend on the concentration, this equation is highly nonlinear. However, for the very early stage during spinodal decomposition, the amplitude of the concentration fluctuations relative to the overall concentration c_0 is small. Therefore, it can be assumed that the concentration dependencies can be neglected and Eq. (2.11) can be linearized as:

$$\frac{\partial c(x,t)}{\partial t} = M_0 \left[\left(\frac{\partial^2 f}{\partial c^2} \right)_{T,c_0} \nabla^2 c + r^2 k_B T \nabla^4 c \right] \tag{2.12}$$

with $M_0 = M(c_0)$. Introducing Fourier transformations to Eq. (2.12) yields

$$\delta c_k(t) = \delta c(0) \exp[R(k)t] \tag{2.13}$$

Here, k is the wave vector defined as $k = (4\pi/\lambda)\sin(\theta/2)$ which is also denoted as q with λ being the wavelength in the medium and θ being the scattering angle. $R(k)$ is the time-independent rate factor defined as:

$$R(k) = -M_0 k^2 \left[\left(\partial^2 f / \partial c^2 \right)_{T,c_0} + r^2 k_B T k^2 \right] \tag{2.14}$$

If only the long-wavelength fluctuations are considered, the second term in Eq (2.12) can be neglected because the long wavelength fluctuations are out of the effective interaction range r. An apparent diffusion coefficient can be defined as:

$$D_{app} = M_0 \left(\frac{\partial^2 f}{\partial c^2} \right)_{c_0} \tag{2.15}$$

The equal-time structure factor $S(k, t)$ is given by the thermal average of the Fourier transformed concentration fluctuation as:

$$S(k,t) = \langle \delta c_{-k}(t) \bullet \delta c_k(t) \rangle_T \tag{2.16}$$

Inserting Eq. (2.13) into Eq. (2.16) given

$$S(k,t) = S_0(k,0)\exp[2R(k)t] \tag{2.17}$$

$S(k,0)$ is the structure factor at time zero before quenching. Since the scattered light intensity is proportional to the structure factor, it can be shown that

$$I_S \propto \exp[2R(k)t] \tag{2.18}$$

If the system is quenched into the unstable region, $\left(\partial^2 f / \partial c^2\right)_{c_0} < 0$ and therefore the apparent diffusion coefficient is also negative because the atom mobility is always positive. This is called "uphill" diffusion. Since $R(k)$ is positive for $0 < k < k_c$, with k_c is defined as:

$$k_c = \left[-\left(\partial^2 f / \partial c^2\right)_{T,c_0} / \left(r^2 k_B T\right)\right]^{1/2} \tag{2.19}$$

Therefore, the structure factor and the scattered light intensity should grow exponentially inside this region. Also, the structure factor stays constant for $k = k_c$ ($R(k_c) = 0$) but decays for $k > k_c$ ($R(k_c) < 0$). But if the system is quenched into the metastable region, $\left(\partial^2 f / \partial c^2\right)_{c_0} > 0$ and D_{app} is positive and it is "downhill" diffusion. The variations of rate factor and the structure factor with wave vector are shown in Figure 2.7. From this figure, both $R(k)$ and $S(k, t)$ show a maximum at $k_m = k_c / \sqrt{2}$. And the structure factor has a maximum growth rate at $R_m = R(k_m)$ while the k_m stays constant.

However, this linearized Cahn-Hilliard theory only works for the very early stage of spinodal decomposition. This is because the linearization process neglects short-range interactions and interrelationships between the concentration field and other relaxing variables (Binder and Fratzl, 2001). An experimental verification of the theory is difficult because the quench rate is always finite and short time scale of the early stage spinodal decomposition that obeys the linear theory for systems involving small molecules. Nevertheless, studies on the phase separation in polymer mixtures have shown the validity of linear theory for the very early stage of phase separation (Binder and Fratzl, 2001). The high viscosity and the visco-elasticity effects of the flexible polymer chains slow down the phase separation process and therefore enable the experimental observations of the early stage of spinodal decomposition. The characteristics of the early stage spinodal decomposition, exponentially growing structure factor with fixed maximum wave vector, were observed (Maguey, van Nuland and Navard, 2001).

During the intermediate stage, the nonlinear effects play even larger roles. Langer-Bar-on-Miller theory, which considers high order correlation functions of Eq. (2.11), describes the behavior of the structure factor and peak wave vectors (Maguey et al., 2001; Binder and Fratzl, 2001). It predicts that the scattering peak moves to smaller wave vectors instead of staying at a stagnant value as predicted by the linear theory. This evolution of scattering peak corresponds to a growth in domain size. Meanwhile, the amplitude of the concentration fluctuations grows till it reaches the equilibrium concentration and the phase separation enters the late stage.

For the late stage of spinodal decomposition, self-similar growth in morphology is observed (Maguey et al., 2001; Binder and Fratzl, 2001). In scattering experiments, this

coarsening process is characterized by an increase in the peak intensity, I_m and a decrease in the peak wave vector k_m. This stage is usually approximated by scaling functions and the power law (Maguey et al., 2001; Binder and Fratzl, 2001; Puri and Binder, 2001; Takeno et al., 2000). The power law approximations are in the forms of:

$$k_m \sim t^{-\alpha} \tag{2.20}$$

and

$$I_m \sim t^{\beta} \tag{2.21}$$

For solid binary mixtures, α = 1/3 due to droplet evaporation-condensation mechanism (Puri and Binder, 2001). For fluid systems where the coarsening process proceeds via droplet diffusion and coagulation mechanism, the scaling exponent $\alpha = 1/d$ where d is the dimension of the system. However, α yields a value of 1 in the time region where hydrodynamic interactions are dominant and the phase-separated structures are kept percolated (interconnected) (Takeno et al., 2000). Also it was found that $\beta \approx 3\alpha$ for the systems that grow with self-similarity. During the late stage, the bicontinuous structure that results from the spinodal decomposition may break up to form droplet structures, which is called percolation-to-cluster transition (PCT). So that even when the phase separation starts with a spinodal decomposition mechanism, the structure at a certain stage could display isolated domains. Therefore the method that uses morphological features to distinguish the phase separation mechanisms is only valid for the earlier stage of the phase separation (Binder and Fratzl, 2001).

2.3 Experimental Techniques for the Phase Behavior and Phase Separation Kinetics in Polymer Solutions

2.3.1 Determination of Phase Boundaries

Two types of methods are usually used on determination of phase boundaries: analytic method or synthetic method. The first method loads the vessel with the components to be studied, and brings the system to a phase separated state and in equilibrium. A pair of binodal points can be determined by measuring the concentration of each phase. It involves either sampling and offline measurement or online measurements. However, sampling might affect the equilibrium state if the sample amount is large compared to the total amount. Online measurement with spectroscopy can avoid the problem caused by sampling, but it requires calibration before the experiments. After a pair of equilibrium data are taken, the external conditions are changed and the above procedures are repeated to map out a phase diagram. This method is very efficient for large-scale vessels where the sampling amount can be neglected. The synthetic method is straightforward, load a vessel with the components with known composition. The phase separation is observed by changing the external conditions. A phase diagram can be mapped out with many loadings at different concentrations. The latter is usually used for small amounts of samples. However, the determination of spinodal points is not so straightforward by either procedure.

Two approaches are usually used to determine the critical point and the spinodal points. One is the extrapolation method based on Debye's scattering theory. Scattered light intensity is recorded as a function of the temperature or pressure as the system is

brought to the vicinity of the critical point or spinodal line. Then the reciprocal of the scattered light intensity is plotted as a function the temperature or pressure, and the spinodal temperature or pressure is determined by extrapolation to zero. Then the temperature or pressure at the intercept is determined as the critical point or the spinodal point.

As a system approaches its critical point or the spinodal point, the long-range interactions rise and cause critical opalescence. According to Debye theory, the scattered light intensity can be given by the following equation (Debye, 1959; Debye and Woermann, 1960; 1962).

$$\frac{I_\theta}{I_o} = C_\theta \cdot \frac{T}{T - T_c} \tag{2.22}$$

where T_c is the critical temperature and T is the temperature at which the scattering light is measured, C_θ is the instrument constant, I_θ, I_o are the scattered and incident light intensity respectively. Equation 2.22 suggests that as the temperature approaches the critical temperature, the scattered light intensity goes to infinity. Scholte (1972) pointed out that this equation is applicable to all the spinodal points T_s

$$\frac{I_\theta}{I_0} = C'_\theta \frac{T}{T - T_S} \tag{2.23}$$

with T_s being the spinodal temperature. Kiepen and Borchard (1988a, b) made a further modification to Equation 2.23 for the systems using pressure as the independent parameter. By replacing the spinodal temperature T_s with spinodal pressure P_s, Equation 2.23 can be rewritten as:

$$I_{\theta}^{-1} = C''_{\theta} \cdot \frac{P - P_s}{P} \tag{2.24}$$

C'_{θ} is also a constant. From Equation 2.23 and 2.24, the spinodal temperature or pressure can be determined from a plot of the inverse of the scattered light intensity as a function of temperature or pressure, when the inverse of the scattered light intensity goes to zero. Using this extrapolation method, the system is kept in the one phase region, but is brought to the vicinity of the critical point and binodal point.

The other method for the determination of the critical and the spinodal points is the quench-induced phase separation method. It utilizes the time evolution of the scattered light intensity after the system is quenched into the two-phase region. In the determination of the spinodal pressures, a series of fast pressure quenches are applied to the system to bring it from the homogenous region into the two-phase region. The scattered light intensity evolution with time is then plotted as a function of the end pressure (or the quench depth). From such a plot, an envelope similar to the spinodal curve can be derived, which is believed to have a close relationship with the real spinodal envelope (Zhuang, 1995). This method is called multiple rapid pressure drop (MRPD) technique. Figure 2.8 shows such a plot for a polyethylene solution in n-pentane at 150 ^{o}C (Zhuang, 1995), where the spinodal pressure was determined from the rate of the scattered light intensity change versus end pressure of pressure quenches.

2.3.2 Kinetics of Pressure or Temperature induced Phase Separation

There are two types of techniques used to study the phase separation kinetics, real-space or reciprocal-space techniques (Cabral et al., 2001). The first type of techniques include optical microscopy, transmission and scanning electron microscopy

(TEM and SEM) and atom force microscopy (AFM). Scattering technique belongs to the second type, reciprocal-space technique.

The real-space techniques can be used in on-line experiments, but they are mostly utilized offline. Therefore, the sample preparation is critical for this measurement. The "frozen-in" method is widely used for sample preparation. Typically, a homogeneous sample is first quenched into the two-phase region, and then at a certain stage, the phase separated system is further quenched to a temperature lower than the glass transition temperature for non-crystalline polymers or melting temperature for crystalline polymers. In this process, the quench rate is required to be fast enough to stop the phase separation and freeze the phase separating structure. Nevertheless, the quench process would take a few seconds. Therefore this method is only applicable for systems with a long relaxation time, such as polymer blends. In such systems the phase separation usually takes several hours or even several days. But for solutions of small molecules and polymer solutions, it is quite questionable because the phase separation process may finish before the end of the quench process. A comparison of the real-space and reciprocal-space techniques was recently carried out on a temperature-induced phase separating solution of poly(methyl methacrylate) in cyclohexane using SEM and SALS techniques (Graham, Pervan and McHugh, 1997). It has been demonstrated that with increasing domain size, the maximum intensity in the scattering pattern moves to smaller angles.

It has already been mentioned that the spinodal point can be experimentally determined by the extrapolation of the scattered light intensity. But the light scattering technique can also be used to follow the phase separation kinetics online (Xiong, 1998). In contrast to the extrapolation method, quench methods are usually used to bring about

the phase separation and the kinetics of the phase separation can be followed by microscopic or scattering techniques. Most of the quench methods utilized in the literature are temperature or composition quenches under ambient pressures. However, it is very difficult to study the earlier stage of the phase separation kinetics using the conventional temperature or composition quenches for fluid systems. This is due to the short time scale of the phase separation itself and the finite quench speed that can be applied on the system. Then pressure quench was first introduced to bring about a fast temperature quench (Wong and Knobler, 1979). Even though this did not solve the finite quench problem, it provides a new thought of using a pressure quench as a way to bring about phase separation. The advantages of a pressure quench over the temperature quench are not only limited to the speed. The pressure quench can be posted onto the system easily in both directions and they are uniform within the sample volume (Steinhart et al., 1999). This method has been used by several other research groups to study the pressure-induced or temperature-induced phase separation in mixtures of small molecules (Metz and Schneider, 1990a, b; Wells, de Loos, and Kleintjens, 1995), for polymer solutions (Kiepen and Borchard, 1988a, 1988b; Wells et al., 1993; Kojima et al., 1995; 1999), and for mixture of oligomeric polymers (Steinhoff et al., 1997). Balsara and coworkers used small angle neutron scattering instead of light scattering to study the kinetics of the pressure jump induced phase separation in polymer blends (Hammouda, Balsara, and Lefebvre, 1997; Lefebvre et al., 1999; 2000). The pressure quench induced phase separation has been extensively studied in our lab on several polymer solutions, such as polyethylene/n-alkane (Kiran, Xiong and Zhuang, 1994; Liu and Kiran, 2001), polystyrene/methylcyclohexane (Xiong, 1998; Xiong and Kiran, 2000),

polydimethylsiloxane/carbon dioxide (Liu and Kiran, 1999), and poly(4-Methyl-1-Pentene) in *n*-pentane and *n*-pentane/CO_2 systems (Fang and Kiran, 2005). Other recent applications involve pressure-jump techniques including x-ray scattering study on the pressure-induced un/refolding reaction of water-soluble protein (Woenckhaus et al., 2000), lipid-water dispersions (Pressl et al., 1997) and phase transitions in liquid crystalline phospholipid (Steinhart et al., 1999).

To induce phase separation by pressure quench, three types of techniques were used in the literature. The first technique involves breaking a deformable diaphragm, a rupture disk or a bursting glass tube, or opening a valve in the system to the atmosphere, upon which an extremely fast pressure quench can be achieved (Wenzel et al., 1980; Quednau and Schneider, 1989; Metz and Schneider, 1990a, b; Sieber and Woermann, 1991). The disadvantage of this method is that the experiments cannot be repeated without replacing the glass tube, rupture disk, the fluid on the pressure side of the diaphragm, or recharging the system. The second approach uses a piston or bellows, a mercury plug that is moved by a pressure generator, a internal valve operated by hand or a volume expansion rod operated by air-activated diaphragm can be used to achieve pressure quench (Kiepen and Borchard, 1988b; Szydlowski et al., 1991; 1992; Wells et al., 1993; Kiran and Zhuang, 1994; Xiong and Kiran, 1998; Xiong, 1998). The quench depth and rate vary and depend on the way of operation. For the systems that use pressure generators can only produce large, but slower quenches. The systems that use air-activated valves can bring about large and fast quenches (Xiong and Kiran, 1998; Xiong, 1998). A third approach is to use a dual cell design to bring up small or large pressure changes at very fast quench rate (Kiran and Zhuang, 1994; Zhuang and Kiran, 1996).

This design uses two high-pressure cells with different volumes where the small cell is used as the scattering cell and large cell used as the dissolution cell. The large cell is first set at a designed lower pressure than that of the small cell. Before the experiments, two cells are connected so that the pressure in the small cell is released into the large cell.

Using the dual-cell design, multiple rapid pressure drops (MRPD) can be made on a specific solution with different quench depths entering metastable or unstable regions of the solution. This technique was successfully applied on several polymer + solvent systems such as polyethylene + n-pentane, polyethylene + n-pentane + carbon dioxide (Zhuang, 1995). Later, this technique was adapted to the multiple angle light scattering system equipped with internal valve and air-activated expansion rod and utilized to study the kinetics of phase separation in the polystyrene + methycyclohexane (Xiong, 1998; Xiong and Kiran, 2000), polyethylene + n-pentane (Liu and Kiran, 2001) and PDMS + CO_2 systems (Liu and Kiran, 1999).

2.4 Literature Review

2.4.1 Phase Behavior of Polymer Solutions

The extrapolation method was used by several research groups to experimentally determine the spinodal curve of polymer solution systems under high pressures (Kiepen and Borchard, 1988a, b; Szydlowski et al., 1992; Wells et al., 1993; Luszczyk et al., 1995). The pressure-pulse-induced critical scattering was combined with the extrapolation method and used for determination of the spinodal curve of oligomeric polystyrene solutions in n-pentane (Kiepen and Borchard, 1988a, b). It also showed the equivalence of temperature-induced and pressure-induced critical scattering. The binodal

points and spinodal points of polystyrene/acetone and polystyrene/deuteroacetone solutions are experimentally measured using a high pressure light scattering system, using the scattered light at very low angles (2-4^o). It has been shown that with lowing pressure, increasing deuteroacetone ratio, or increasing the polymer molecular weight, the miscibility can be decreased from UCST and LCST types of phase behaviors to hourglass type of phase behavior (Luszczyk et al., 1995). The binodal and spinodal surfaces for polystyrene/methylcyclohexane solution under high pressures were determined by using a high-pressure optical cell, utilizing the scattered light at 30^o and 90^o (Wells et al., 1993).

2.4.2 Phase Separation Kinetics in Polymer Solutions

The pressure jump induced phase separation in polymer solutions such as polypropylene in trichlorofluoromethane (Kojima et al., 1995; 1999), polystyrene in methylcyclohexane (Xiong, 1998; Xiong and Kiran, 2000), polyethylene in n-pentane (Liu and Kiran, 2001), polydimethylsiloxane in carbon dioxide (Liu and Kiran, 1999), and poly(4-Methyl-1-Pentene) in *n*-pentane and *n*-pentane/CO_2 systems (Fang and Kiran, 2005) were carried out to test the Cahn linearized theory during the earlier stage of the spinodal decomposition. The time evolution of the scattered light intensity as a function of scattering angle is obtained for the phase separating systems. For polymer solutions at their critical concentration, spinodal decompositions were observed as featured with a maximum in the scattered light intensity over scattering angles. The exponential increase in the scattered light intensity predicted by Cahn's theory during the earlier stage of phase separation was observed in all these polymer solution systems at all the scattering angles. But for off-critical polymer solutions, the shallow pressure quenches that take the system

into the metastable regions in phase diagram induce phase separation via nucleation and growth mechanism. This is characterized by scattering light profiles with monotonously decay from low to high scattering angles. The scattered light intensity was observed to increase with time at all the scattering angles. However, for the deeper off-critical quenches, similar scattering profiles as those of critical concentrations were observed. This is because the system is quickly brought to the two-phase region instead of metastable region and therefore spinodal decomposition takes place. Combining with MRPD methodology, the spinodal boundaries were determined from the dependence of the scattering pattern on the pressure quench depth. It has been shown that at a concentration far from the critical concentration, the metastable gap between the binodal and spinodal curves is very large. For example, for a solution of PDMS (0.38 wt %, which is far from the critical concentration, 5.5 wt %) in carbon dioxide at 323 K spinodal decomposition was not observed even at a quench depth of 7 MPa (Liu and Kiran, 1999).

The phase separation of a polycarbonate-carbon dioxide system was studied by Hatanaka and Saito using a high-pressure light scattering system (Hatanaka and Saito, 2004). The CO_2 is first allowed to dissolve into the polycarbonate films and then raised to a certain temperature where the liquid-liquid phase separation takes place. Depending on the annealing temperature and pressure, nucleation and growth or spinodal decomposition processes were observed.

2.5 Interplay of Liquid-Liquid Phase Separation and Crystallization

An example of the interplay of liquid-liquid and solid-fluid phase separations is illustrated in Figure 2.9a. This figure is a schematic of the phase diagrams of isotactic polypropylene solutions in methyl salicylate that were recently reported in the literature (Matsuyama et al., 2000). This system displays a UCST type L-L phase boundary above the S-L phase boundary (crystallization line). This figure shows a branch of the L-L boundary. The L-L and L-S phase boundaries cross at a special triple point, which is referred to as monotectic point. This crossing for this system occurs at a polymer concentration of 55 % by volume at 100 ^{o}C.

Another example of the interplay of L-L phase boundary with S-L phase boundary is illustrated in Figure 2.9b. This represents the results of the simulations for a polymer solution with submerged L-L phase boundary (as the case of **a** and **b** in Figure 2.3) under the L-S phase boundary by Hu and Frenkel (2004). The simulations were done for three situations: L-L metastable critical point right on the S-L phase boundary (1), below the S-L phase boundary (2), and far below the S-L phase boundary (3). The interplay between the L-L demixing and L-S phase separation is believed to play a very important role on the phase separation kinetics. The morphologies of polymer crystalline can also be very sensitive to the competition of these two types of phase separation. Also, the intermediate morphology during L-L phase separation can be frozen by crystallization, which is very important for membrane fabrication (Matsuyama et al., 2000).

The kinetics of polymer crystallization has been viewed as a classical nucleation and growth process. Several recent simulation and experimental studies show that this

can be true for a system far from the liquid-liquid phase boundaries (Wolde and Frenkel, 1997; Hu, 2000; Hu and Frenkel, 2004; Bonnett et al., 2003; Olmsted et al., 1998; Sear, 2001; Shang et al., 2003; Talanquer and Oxtoby, 1998). However, a different mechanism is suggested by these studies when the melting temperature is very close to a liquid-liquid demixing point.

Wolde and Frenkel (1997) showed that near the metastable fluid-fluid critical point, the pathway for crystal nucleation is changed and the nucleation is highly enhanced for globular protein solution with short-range interactions. This is because, prior to the crystal nucleation, the large density fluctuations around the critical point first lead to the formation of a liquid-like droplet. The crystal nucleation then takes place inside the liquid-like droplet as shown in Figure 2.10 with comparison with the classical nucleation and growth mechanism. This liquid-like droplet can be a well-defined liquid phase or just the density fluctuation near the critical point. Via this kinetic process, the free energy barrier for nucleation is largely reduced compared to the classical nucleation.

The extended work on the polymer solution system with a submerged liquid-liquid phase boundary reveals that the morphology of polymer crystallites is strongly affected by this L-L demixing. For a system with L-L critical point very close to the melting point (case 1 in Figure 2.9b), small crystals in big amounts formed. This is attributed to the density fluctuations near the critical point where the crystallization is confined to the regions with high density. In contrast, larger but fewer crystals formed in a system with larger difference between the L-L critical point and the melting point (case 3 in Figure 2.9b) because the density inhomogeneity was not fully developed before the crystallization starts (Hu and Frenkel, 2004).

A contour outside of the poly(ethylene oxide) (PEO) crystal was observed for crystals formed from *N,N*-dimethylacetamide (DMAc) solutions (Sasaki et al., 2002). The authors attributed this contour to be the trace of a liquid-liquid phase separation before the onset of crystallization. The crystallization takes place only in the PEO-rich phases, but not in the polymer-lean phase. However, the experimental study by Bonnett et al. (2003) on the crystallization of a deep-quenched methyl(E)-2-[2-(6-trifluoromethylpyridine-2-yloxymethyl)-phenyl]-3-methoxyacrylate solution in water-methanol mixture, where a submerged L-L phase boundary is below the S-F phase boundary, shows that the crystallization takes place in both liquid phases since they are in equilibrium with the same solute chemical potential and same supersaturation. Quite different morphologies were observed for the crystals formed from different phase separation paths: cross the S-F phase boundary only using a shallow quench or cross both the submerged L-L phase boundary and S-F phase boundary using a deep quench.

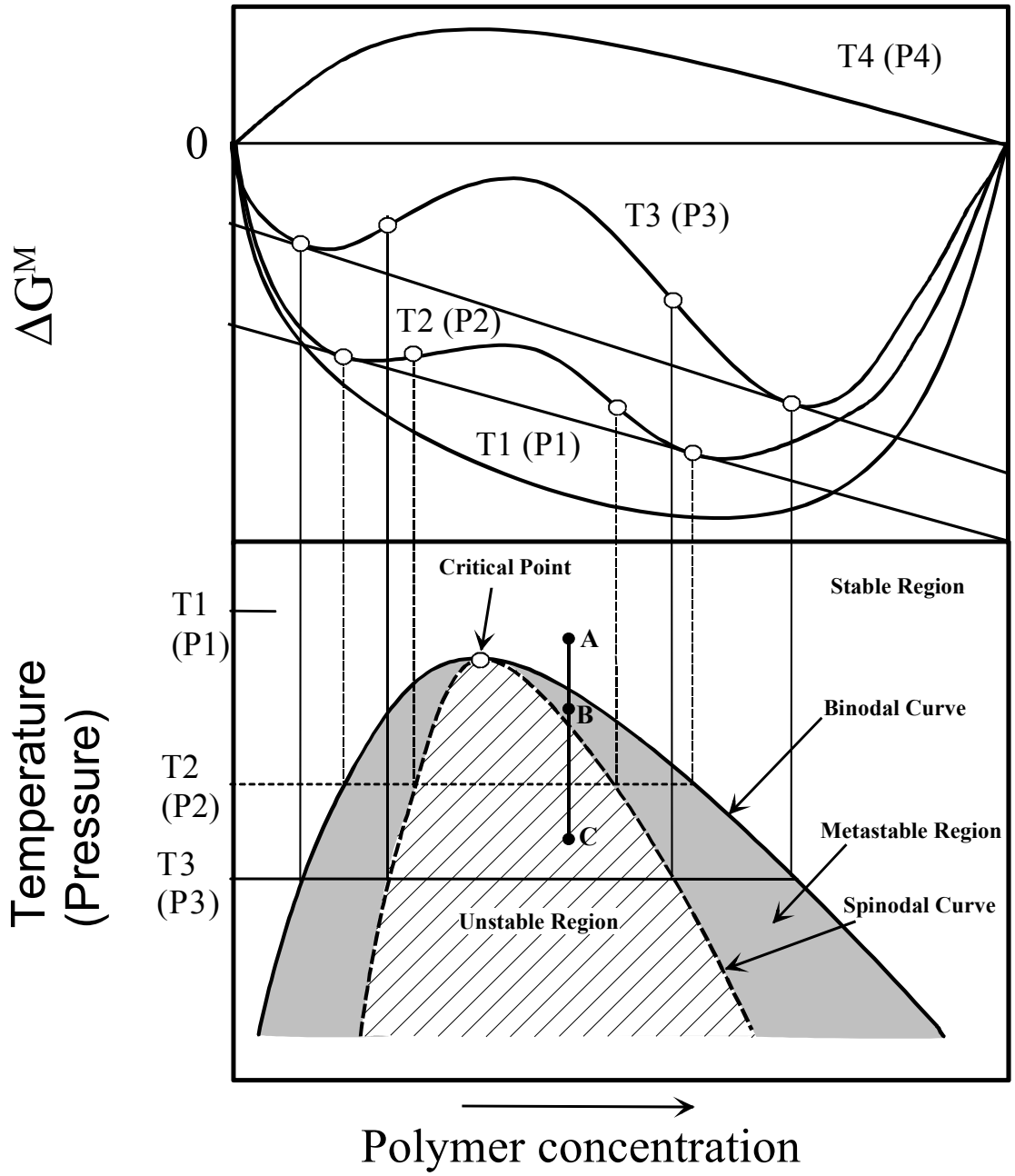

Figure 2.1. Schematic diagram of Gibbs free energy of mixing as a function of polymer concentration (Adapted from Utracki, 1994).

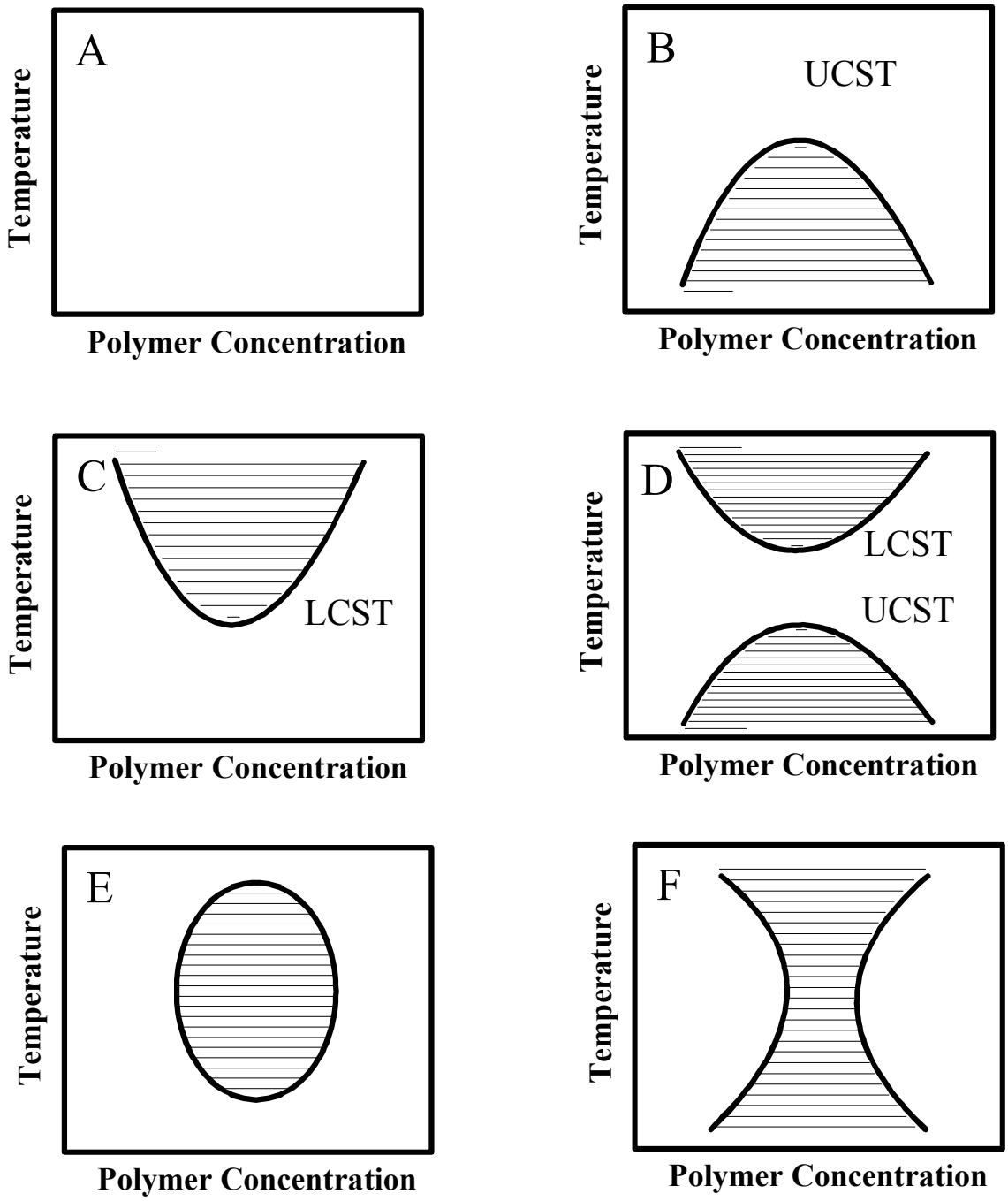

Figure 2.2. Schematic of phase behavior in polymer solutions. Shaded areas represent the two-phase regions and the un-shaded areas represent one-phase regions (Adapted from Olabisi, 1979).

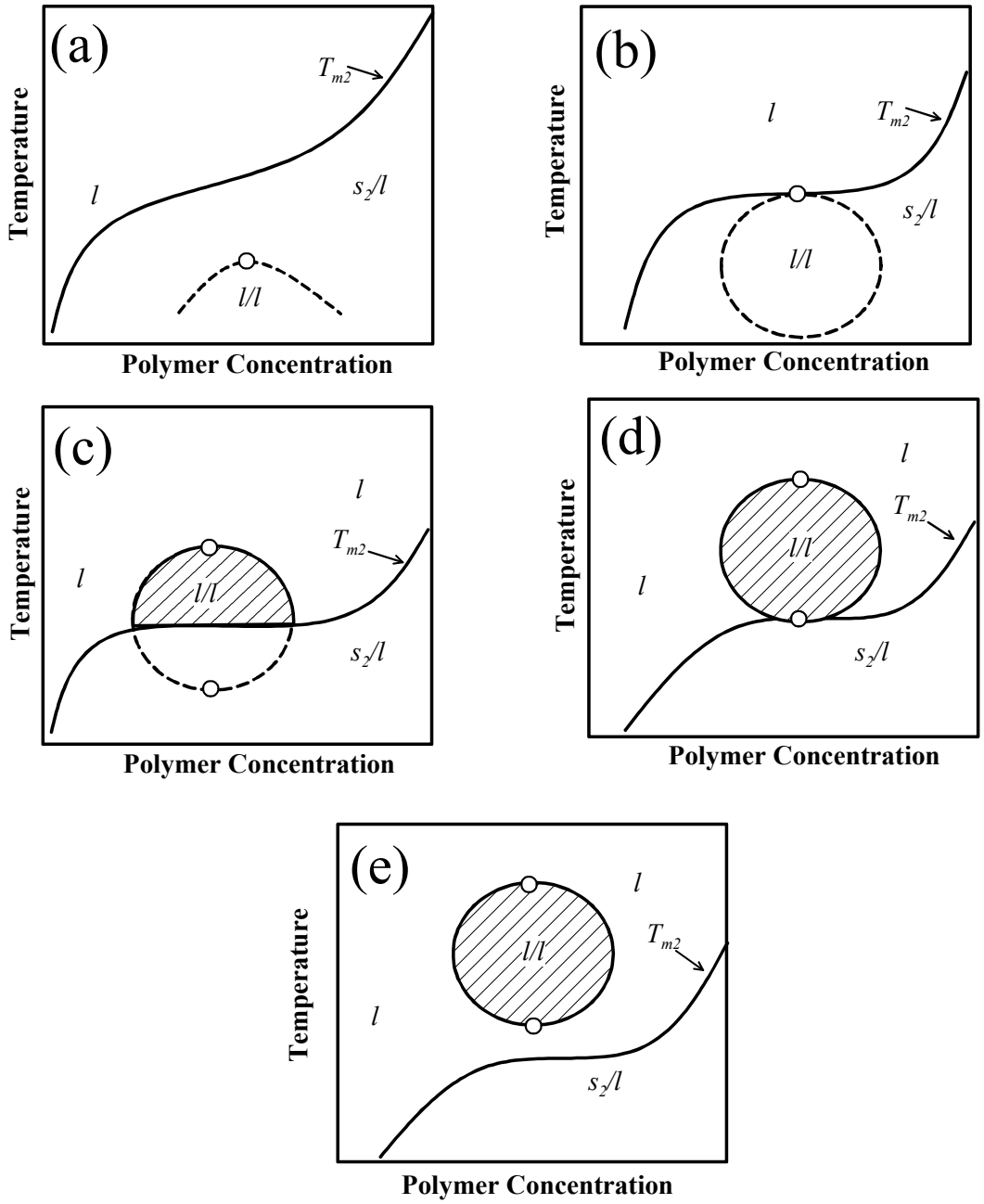

Figure 2.3. Schematic phase diagrams showing the interference of liquid-liquid with solid-liquid phase equilibria adapted from (Adapted from Koningsveld et al., 2001). T_{m2} is the melting temperature of a semi-crystalline polymer and s_2 means the crystalline phase.

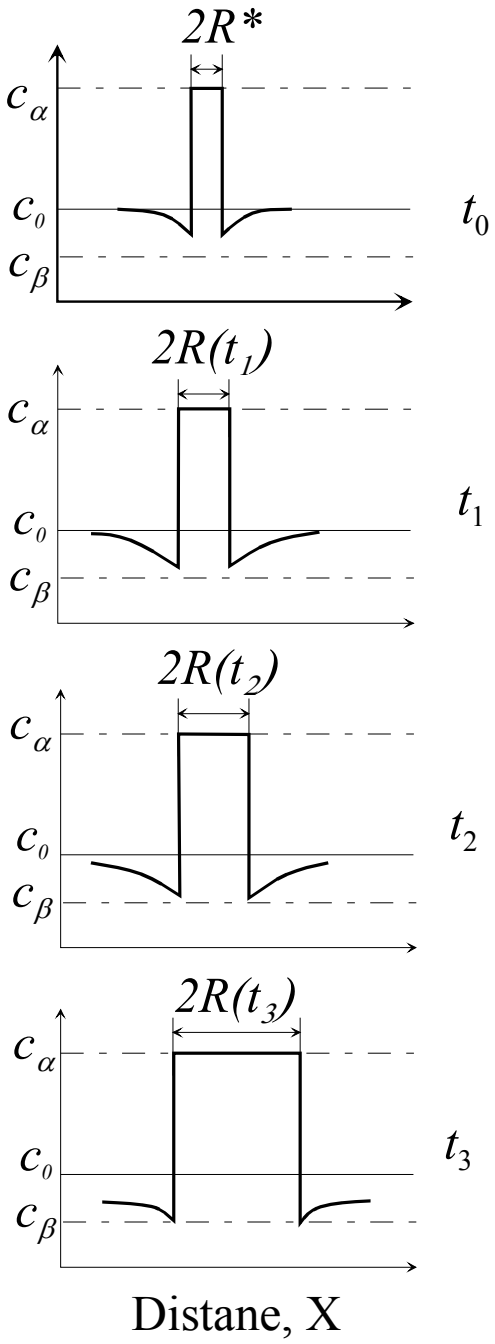

Figure 2.4. Schematic concentration profile after the system is quenched into metastable region, from which the phase separation proceeds via nucleation and growth mechanism. The concentration c(x) is plotted against the spatial coordinate x at time t_0, t_1, t_2, and t_3. The diameter of a critical droplet is shown as $2R^*$. c_0 is the concentration of the whole solution before phase separation, while c_α and c_β are the coexisting concentrations. (Adapted from Hashimoto et al., 1986; Utracki, 1994; Binder and Fratzl, 2001).

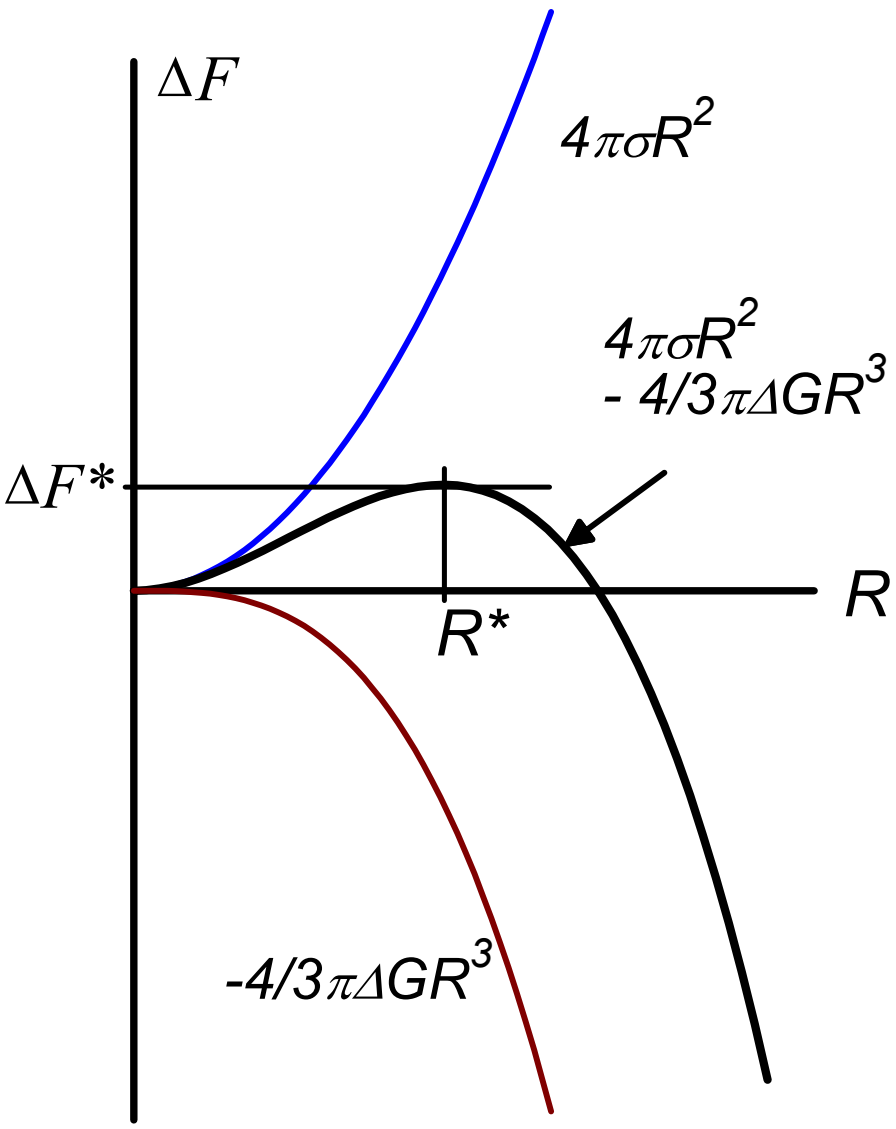

Figure 2.5. The free energy change *(ΔF)* for formation of a cluster as a function of the cluster size (R) consists of the volumetric contribution $-\frac{4\pi}{3}R^3\Delta G$ and surface contribution $4\pi R^2\sigma$. The critical value of W is $\Delta F^* = \frac{16\pi\sigma^3}{3\Delta G^2}$ at critical cluster size $R^* = \frac{2\sigma}{\Delta G}$. (Adapted from Wagner et al., 2002).

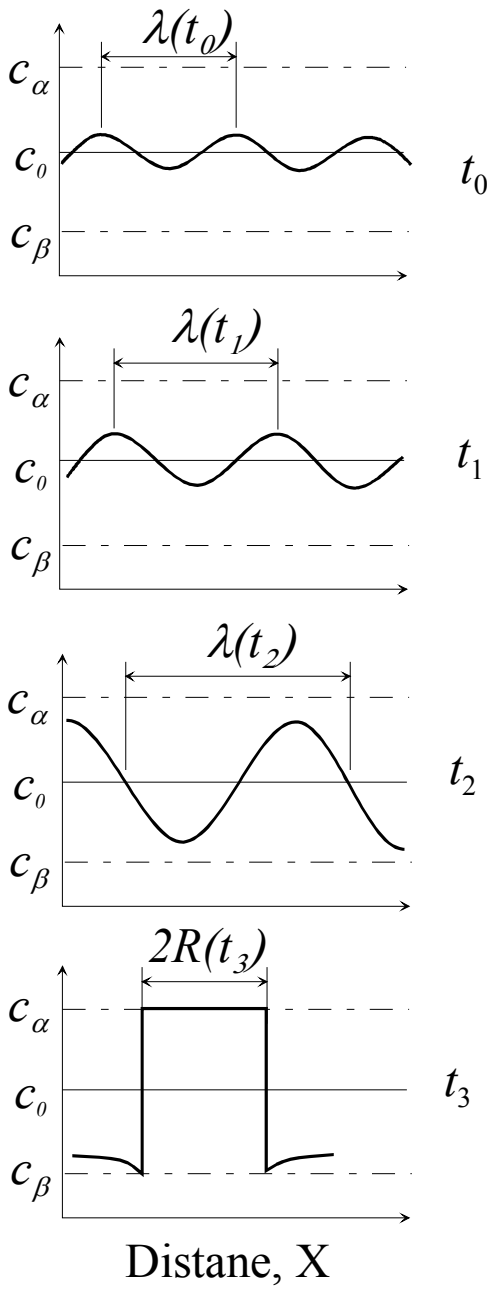

Figure 2.6. Schematic concentration profile after the system is quenched into unstable region, from which the phase separation proceeds via spinodal decompostion mechanism. The concentration c(x) is plotted against the spatial coordinate x at time t_0, t_1, t_2, and t_3. c_0 is the concentration of the whole solution before phase separation, while c_α and c_β are the coexisting concentrations. (Adapted from Hashimoto et al., 1986; Utracki, 1994; Binder and Fratzl, 2001).

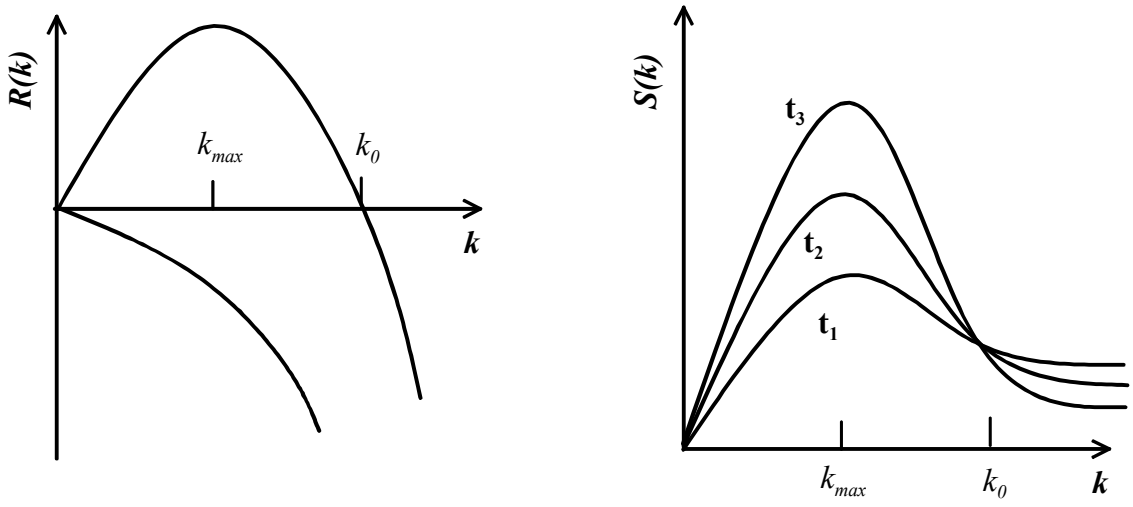

Figure 2.7. Qualitative behavior of growth rate $R(k)$ (a) and structure factor $S(k, t)$ (b) as a function of wavenumber k (or q) (Adapted from Binder and Fratzl, 2001; Granasy, 1997).

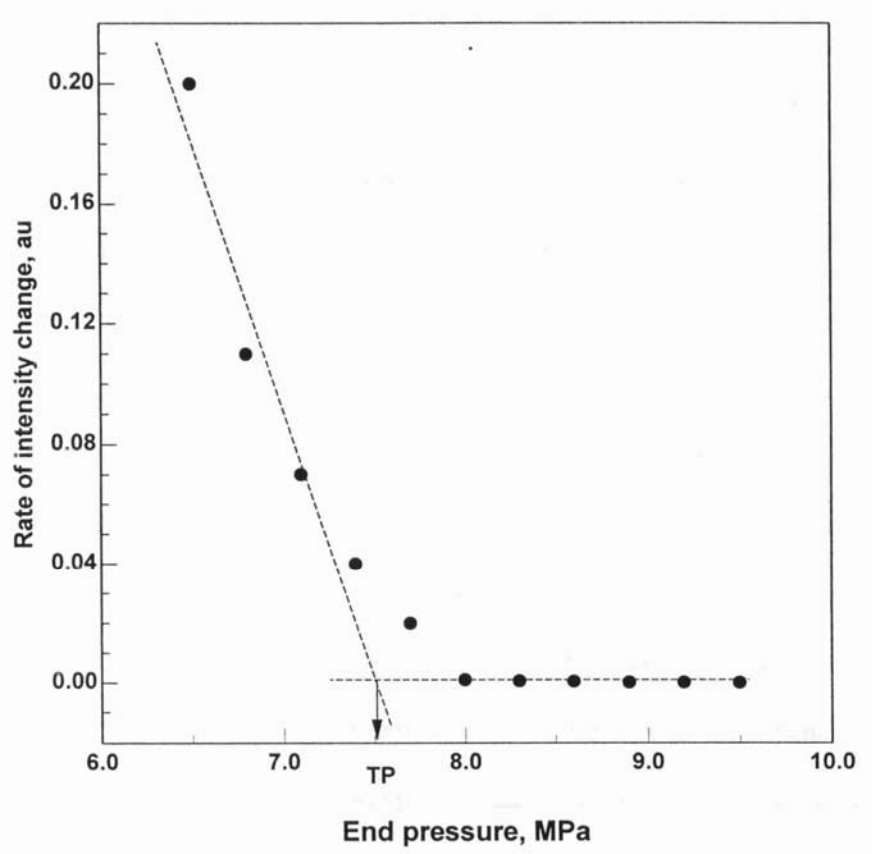

Figure 2.8. Rate of change in the scattered light intensity versus the end pressure of pressure quenches in a polyethylene solution in n-pentane at 150 ^{o}C (Zhuang, 1995).

(a)

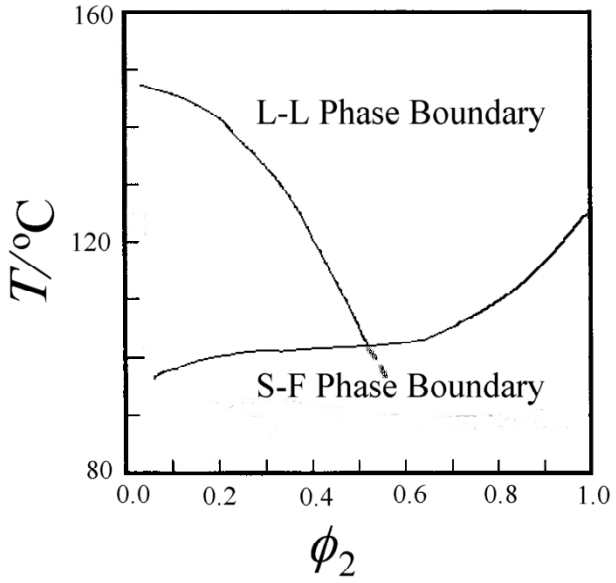

(b)

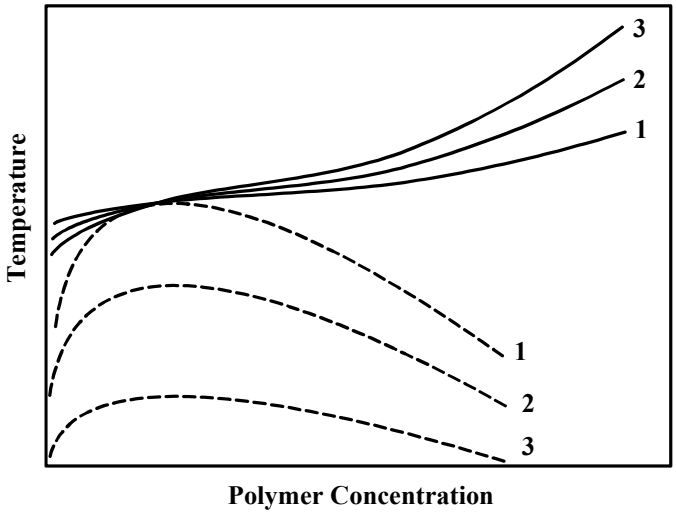

Figure 2.9. Schematic phase of polymer solution with L-L and L-S phase boundaries. **a**. phase diagram of iPP/MS (Adapted from Matsuyama et al., 2000); **b**. UCST phase boundary submerged under L-S phase boundary (Adapted from Hu and Frenkel, 2004).

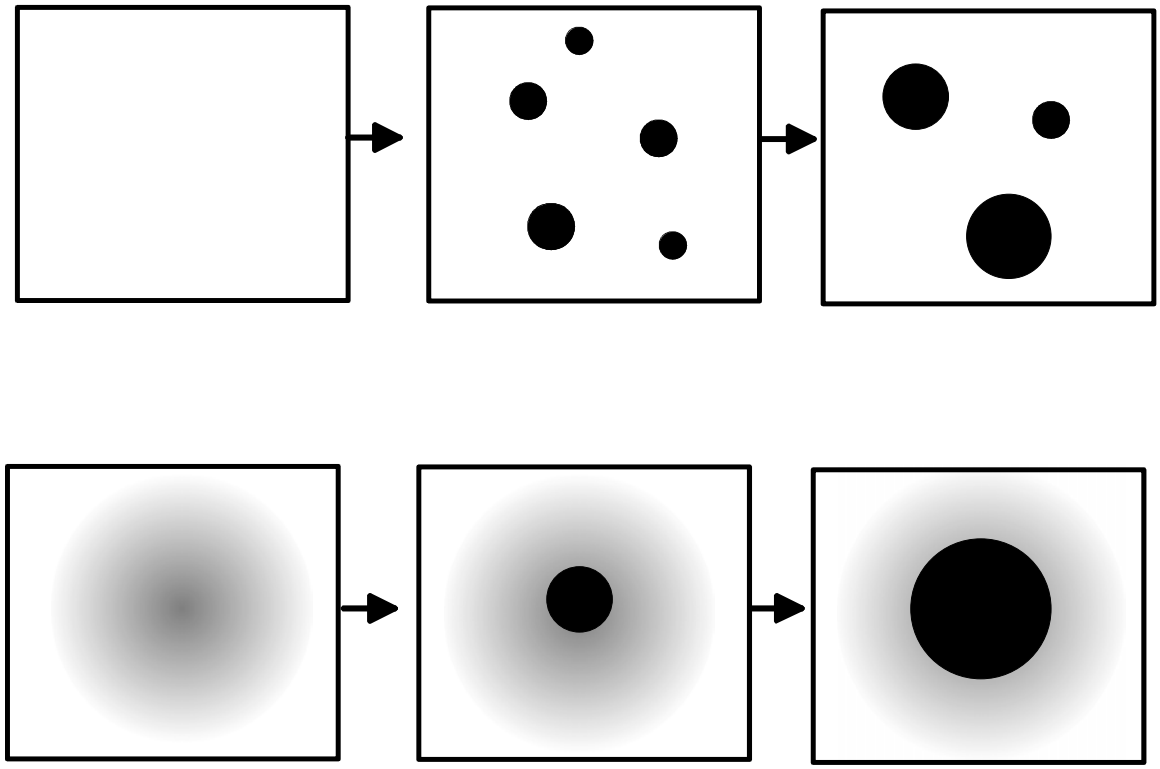

Figure 2.10. Crystallization via nucleation and growth upon crossing only the S-F phase boundary (top) and crossing both the submerged L-L phase boundary and the S-F phase boundary, in which a fluid-like droplets are formed first followed by nucleation and growth inside the droplets (below) (Adapted from Wolde and Frenkel, 1997; Anderson and Lekkerkerker, 2002).

Chapter 3

Experimental System Part I: High Pressure View-Cell

3.1 Experimental Apparatus

Figure 3.1 shows the schematic diagram of the high-pressure view-cell system that was used for determination of the phase behavior and volumetric properties of polymer solutions at high pressures. It consists of a high-pressure view-cell which can be operated at temperatures up to 200 ^{o}C and pressures up to 70 MPa, a solvent delivery system, a pressure line, a pressure generator, a temperature control system, and a data acquisition system. The solvent line and pressure line share a single high-pressure liquid pump (Model: LDC/Milton Roy). The pressure generator was purchased from High Pressure Equipment Company (model number: 37-6-30).

The detail of the high temperature, high-pressure view-cell is schematically shown in Figure 3.2. This view-cell consists of (1) a view-cell equipped with two sapphire windows for visual observation or optical detection; (2) variable volume attachment that changes the internal volume in the range of 16 to 24 mL, which is determined by the position of the piston by a LVDT (linear variable differential transformer) at any temperature and pressure; (3) four cartridge heaters inserted into the cell body and controlled by an Omega controller; (4) pressure and temperature sensors (Dynisco, Model: TPT 432A-10M) with pressure accuracy of ±0.03 MPa and temperature accuracy of ±0.5 K; (5) optical devices including a light source and a photoelectric detector; (6) a stirring bar operated by a magnetic stirrer for

homogenization; and (7) a computerized data acquisition system which records the temperature, pressure and transmitted light intensity (I_{tr}) and permits determination of the demixing conditions. The data acquisition system utilizes a data acquisition board (model number: CIO-DAS16/JR) to collect digital data from the sensors. The data is recorded and displayed in real time using a Labview program. The pressure limit is controlled by a safety device, a rupture disk installed directly on the main body. The sapphire windows are 0.5 inch thick and 1 inch in diameter and are sealed with gold foil. The variable volume attachment is secured on the cell body using a Teflon O-ring for sealing. The piston is made of brass carrying an O-ring to separate the fluids in the pressure line and the cell.

3.2 Operational Procedure for Determination of Demixing Conditions

To start an experiment, the cell is first opened by removing the variable volume attachment. An accurately weighted polymer sample is loaded into the cell. The variable volume attachment is then secured with a new Teflon O-ring. The whole system is then purged with a small amount of solvent or CO_2, if CO_2 is one component of the system to be studied. To remove the purging solvent, the cell temperature is raised slightly above the boiling point of the solvent. Solvents are then loaded by pumping them through the solvent line from a solvent container. The amount of the solvent charged is determined from the weight loss of the solvent container. For the experiments involving CO_2, a similar procedure is followed to charge the cell from a high-pressure stainless steel transfer vessel.

After the polymer and the solvent mixtures are loaded, the system is brought to the region of complete miscibility by adjusting the temperature and pressure. Pressure adjustments at a given temperature are achieved by the movement of the piston in the variable-volume part of the cell. The magnetic stirrer facilitates the dissolution process. Once complete miscibility is achieved, starting from the one-phase region, different paths were followed to determine the phase boundaries. Figure 3.3 shows the schematic representation of the different paths that were followed in determining the phase boundaries. These include a constant temperature (Path A), a constant pressure (Path B) or a variable pressure and temperature (Path C) path.

When temperature is maintained constant and the pressure is reduced by decreasing the pressure on the backside of the movable piston with the aid of a pressure generator (Figure 3.1 and 3.2), the transmitted light intensity decreases rapidly upon phase separation. During the experiment, with the aid of a computerized system, the temperature, pressure and the transmitted light intensity are recorded as a function time. The data is then manipulated to generate a plot showing the change in transmitted light intensity with pressure. The departure point from the base transmitted light intensity for the homogeneous solution is identified as the incipient demixing pressure (P_i). In the present study, the pressure corresponding to the transmitted light intensity going to zero is also identified as P_f. Traditional cloud point determinations based on visual observations lie in between these two pressures. This is shown in Figure 3.3 for Path A. If instead pressure is held constant, and temperature is changed, once again the two-phase regions can be entered, and this is also recorded as a decrease in the transmitted light intensity as shown in Figure 3.3 for Path B. The incipient temperature (T_i) and

temperature corresponding to the transmitted light intensity going to zero (T_f) are then determined for this path, as illustrated in Figure 3.3. The phase separation conditions may also be approached without holding the temperature or pressure constant. As shown in Figure 3.3, Path C shows another phase separation pathway where the pressure is reduced due to the decrease in the temperature without making any adjustments in the piston position to compensate for the reduction in pressure. An LVDT coil is used to monitor the position of the movable piston to determine the internal volume in the view-cell at any given T and P, from which the density of the polymer solutions can be calculated using the initial mass loading.

Only path A was followed for the PSF + THF + CO_2 system, and all three paths were used in the system of PE +n-pentane + CO_2. Figures 3.4 a, b and c demonstrate the actual computer outputs for these paths for a 5 wt % solution of polyethylene in n-pentane. In Figure 3.4a, along the constant temperature path at 423 K, the demixing pressures are identified as P_i = 13.0 MPa and P_f = 12.3 MPa. In Figure 3.4b, along the constant pressure path at 53.3 MPa, the demixing temperatures are identified as T_i = 376.8 K and T_f = 374.0 K. In Figure 3.4c, the demixing temperatures and pressures are identified as T_i = 379.1 K, P_i = 46.8 MPa and T_f = 374.5 K, P_f = 44.9 MPa.

3.3 Operational Procedure for Volumetric Properties Measurements

The density of the PSF solutions was also measured during the phase boundary determination process. The LVDT coil (as shown in Figure 3.1 and 3.2) was used to monitor the position of the movable piston in the variable-volume part (VVP). To determine the position of the piston, this LVDT coil was moved with a piston locator

screw (PLS) to find the position of the ferromagnetic metal piece attached the piston, which moves with the piston and induces a current in the LVDT coil. When the piston is at the top, which is achieved by charging some CO_2 in the view-cell to generate a pressure (~50 bar) inside while maintaining ambient pressure in the pressure line behind the piston, the position readout unit (PRU) is set to zero which corresponds to the maximum internal volume of the system. When the solution is pressurized by moving the piston to a new position, the actual distance traveled by the piston is determined with the PRU reading with an accuracy of ±0.013 mm. Using the inner cross-sectional area of VVP (1.95 cm^2) and the maximum internal volume (23.46 cm^3), the volume and then the density of the cell content is calculated at any temperature and pressure from the following equation:

$$D = L/ [23.46 – (1.95B)] \quad (3.1)$$

where D is the density, g/cm^3; L is the total loading in gram and B is the piston position in cm. With this system, volume changes are determined with an accuracy of ±0.0025 cm^3, and the densities are determined with an accuracy of ±1.2 %.

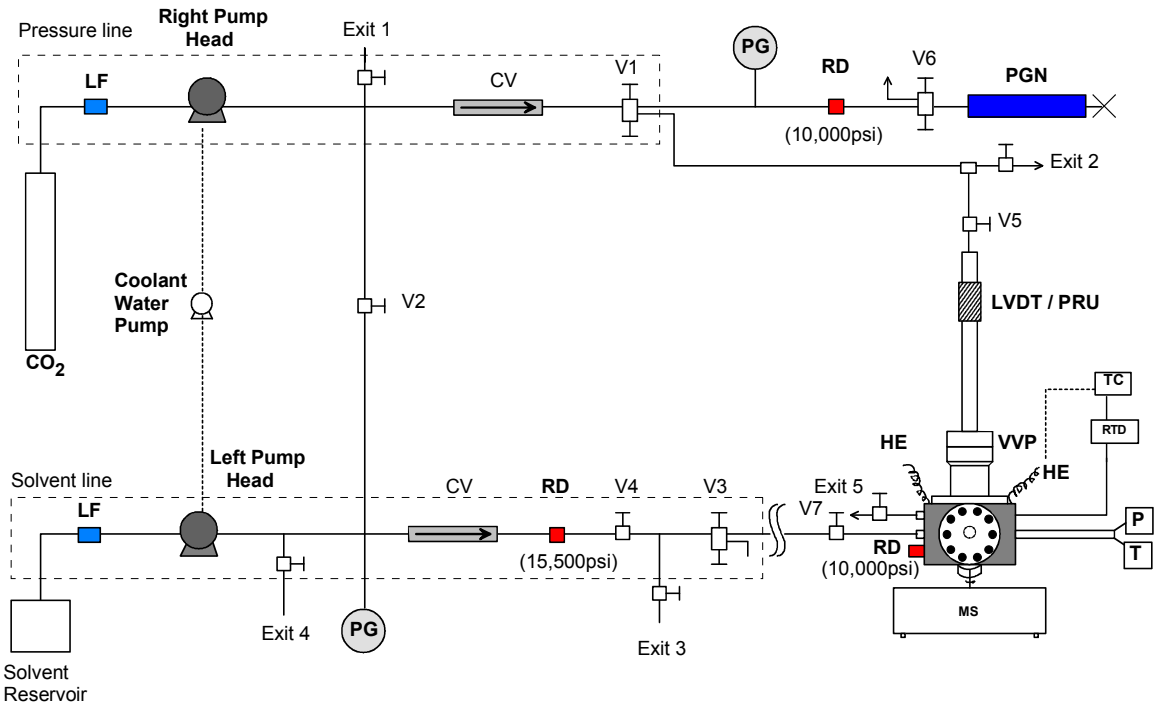

Figure 3.1. Schematic diagram of the experimental system for determination of miscibility conditions and densities. LF = line filter; RD = rapture disc; PG = pressure gauge; CV = check valve; PGN = pressure generator; V = valve; HE = cartridge heaters; MS = magnetic stirrer; LVDT = linear variable differential transformer; PRU = position readout unit; VVP = variable volume part; P = pressure; T = temperature; TC = temperature controller

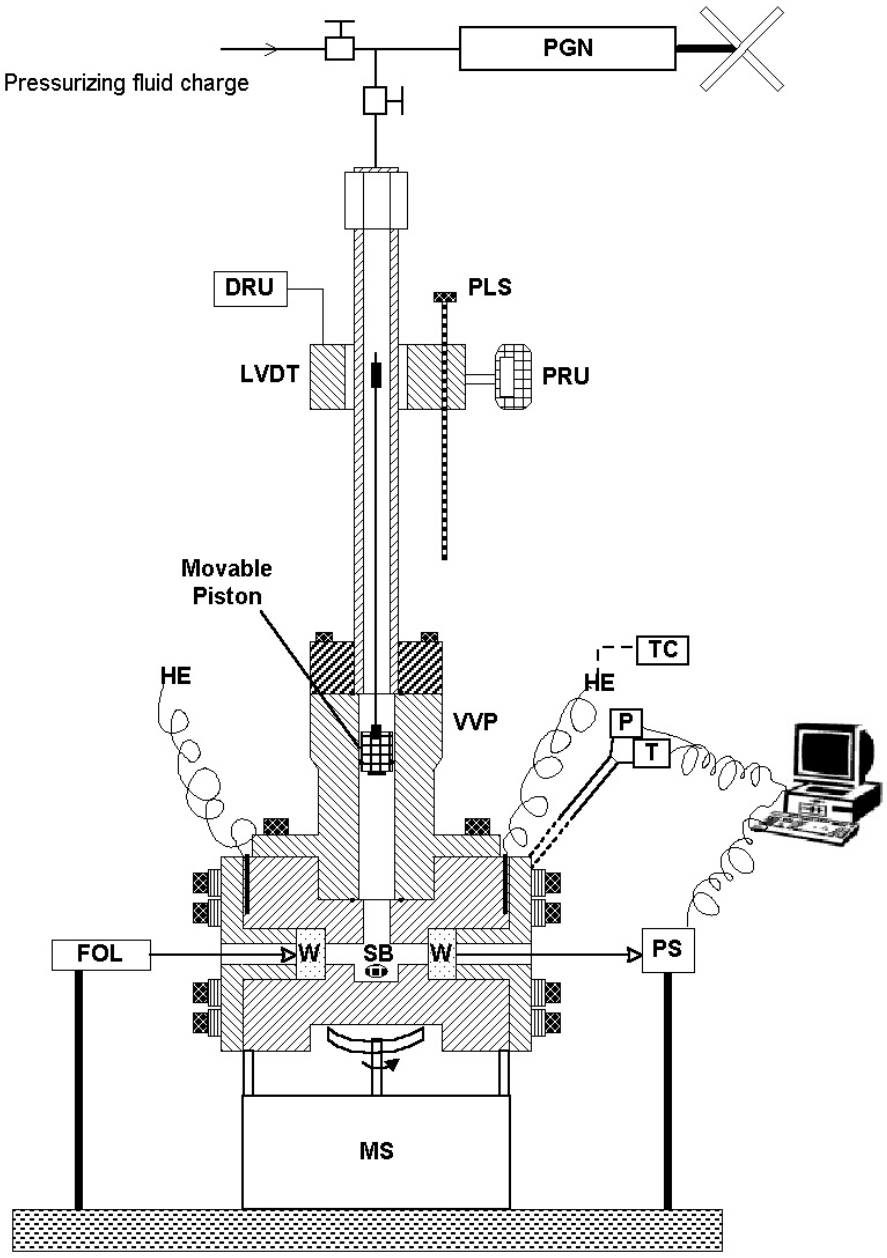

Figure 3.2. Schematic diagram of the high temperature, high pressure view-cell. PGN Pressure Generator; DRU digital voltage readout unit; PRU position readout unit; PLS position locator screw; LVDT linear-variable differential transformer; TC temperature controller; HE cartridge heating elements; VVP variable volume part housing the movable piston; P pressure; T temperature; FOL fiber optical illuminator; W sapphire window; SB stirring bar; PS photodiode sensor; MS magnetic stirrer.

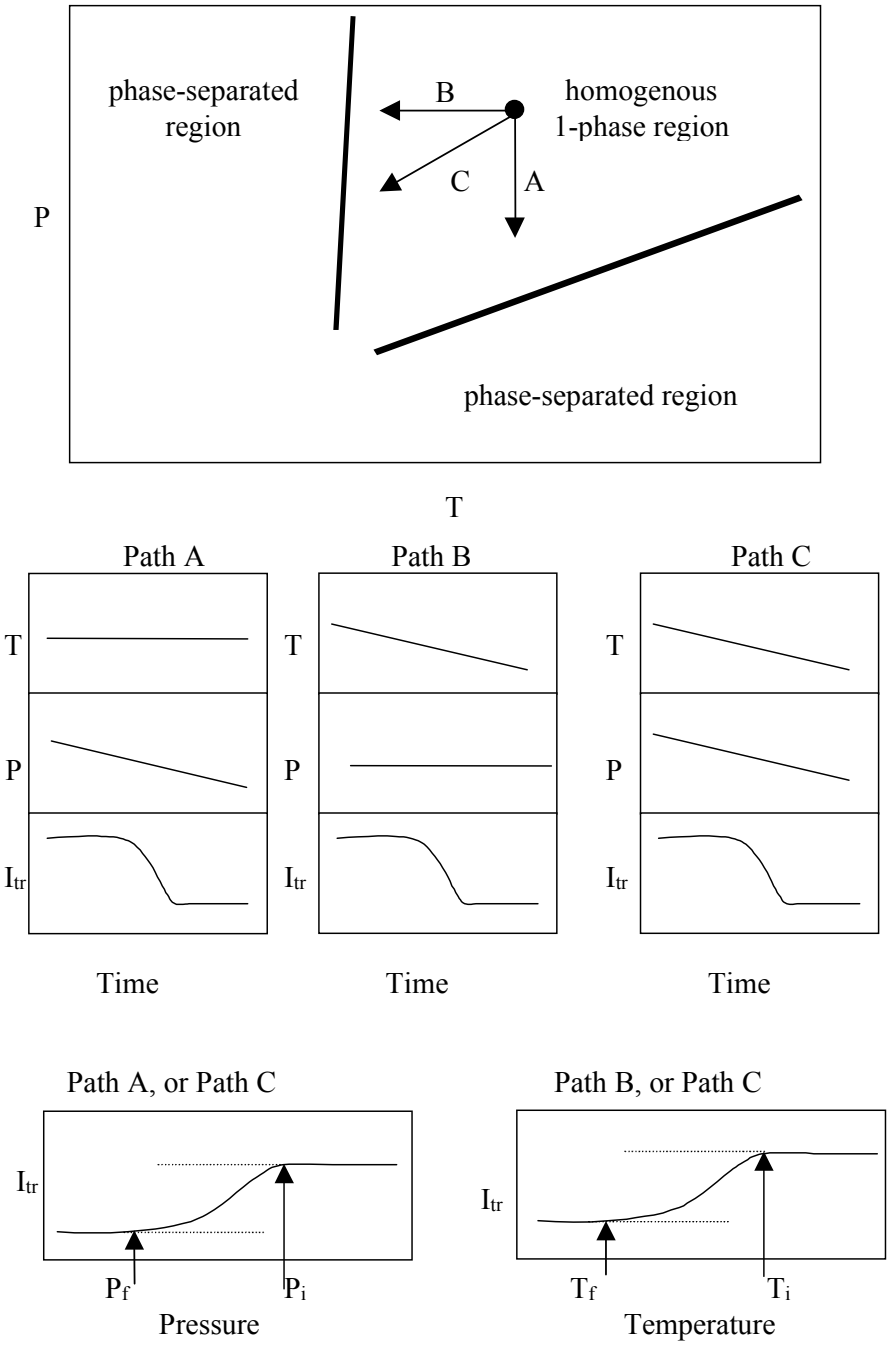

Figure 3.3. Illustration of the different paths followed to determine phase boundaries and the corresponding changes in temperature (T), pressure (P), and transmitted light intensity (I_{tr}) with time. The lower part of this figure demonstrates the incipient demixing pressure (P_i) or temperature (T_i) and the condition corresponding to transmitted light intensity going to zero (P_f or T_f) Path A: constant temperature; Path B: constant pressure; Path C: variable pressure and temperature.

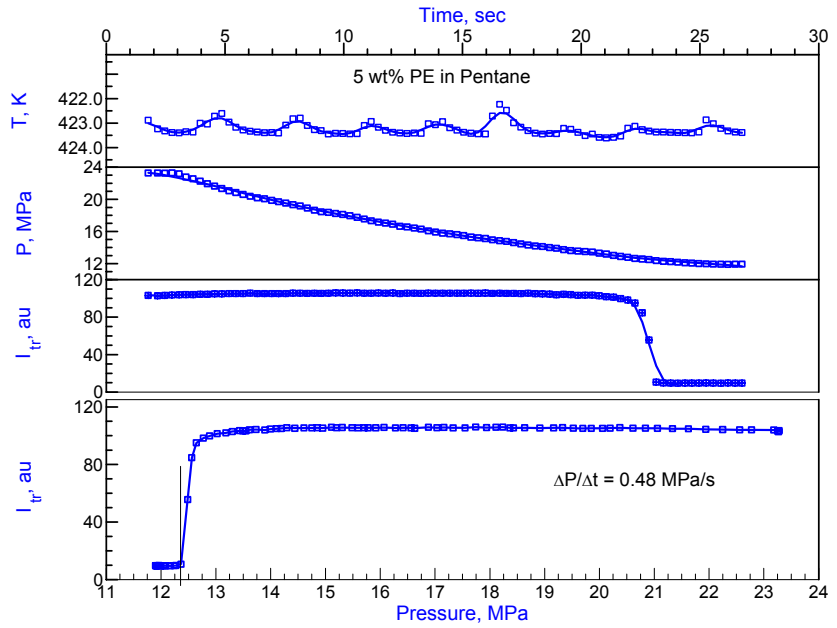
Time, sec
5 wt% PE in Pentane
T, K
P, MPa
I tr, au
ΔP/Δt = 0.48 MPa/s
Pressure, MPa

a

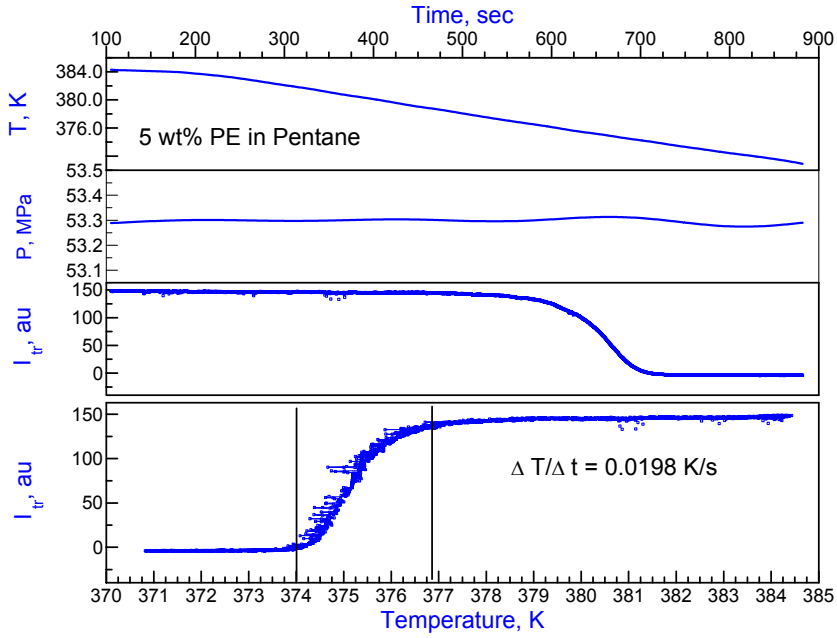
Time, sec
5 wt% PE in Pentane
T, K
P, MPa
I tr, au
Δ T/Δ t = 0.0198 K/s
Temperature, K

b

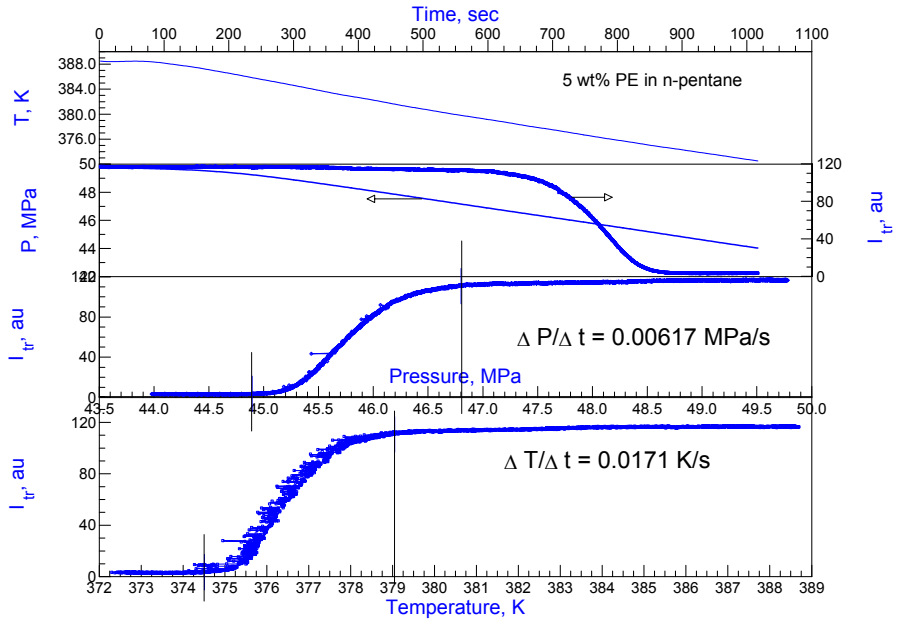

c

Figure 3.4. Variation of temperature (*T*), pressure (*P*), and transmitted light intensity (I_{tr}) with time during the different paths followed in the phase boundary determination. The incipient demixing conditions and the demixing conditions at I_{tr} = 0 are determined from the variation of the transmitted light intensity with pressure or temperature (lower curves in the figures). a. constant temperature path in 5 wt % solution of polyethylene in n-pentane at 423 K; b. constant pressure path in 5 wt % solution of polyethylene in n-pentane at 53.3 MPa; and c. variable temperature and pressure path in 5 wt % solution of polyethylene in n-pentane start from 388 K and 50.0 MPa.

Chapter 4

Experimental System Part II: Time- and Angle-Resolved Light Scattering System

4.1 Experimental Apparatus

Figure 4.1 shows a schematic layout of the special time- and angle-resolved light scattering system used to study the kinetics of the pressure- and temperature-induced phase separations.. It consists of a high-pressure variable-volume scattering cell, a recirculation loop, optical components, and the temperature and pressure controlling units. The system can operate at 70 MPa and up to 200 ^{o}C.

The scattering cell is made of two flat sapphire windows separated by a stainless steel spacer of a thickness of 250 microns. This sandwiched scattering cell is then placed in the metal enclosure and clamped with other metal pieces using 6 bolts. Two O-rings are used to seal the metal enclosure and the clamp pieces, while gold foils are placed in between the sapphire windows and the clamp pieces. Two metal blocks are attached to this cell on the top and bottom. These blocks are used to incorporate two inlet/outlet ports, a movable piston housing, an expansion valve, a movable rod driven by an air actuated diaphragm, and the temperature and pressure sensors. The movable piston on the top is operated by a pressure generator through pressurizing fluids to bring about small to moderate pressure changes. The movable rod at the bottom is used to generate the large and fast pressure changes. The expansion valve is used to bring about very small but rapid pressure changes.

Besides the scattering cell, a polymer loading and dissolution chamber (MR), a recirculation pump (RP), two isolation valves (V4, V14), and a line filter are included in the recirculation loop. A high-pressure gear pump is used to recirculate the contents in the system. There were two built-in isolation valves made to reduce the internal volume. However, it is impossible to replace them when they are worn out. Two external valves were used to replace these internal ones with small changes to the internal volume. All these components are enclosed in a heating oven for temperature control.

A He-Ne laser (30 mW, λ = 632.8) is used as the light source. The laser light passes an iris diaphragm (ID) and a Glan-Thompson polarizer (GTP) and then is guided to the center of the scattering cell. The scattered light is collected by two convex lenses and recorded by a linear image sensor (LIS). The LIS has 256 pixels giving an angular coverage of 1.9^{o} to 12.7^{o} in air for the present setup. An Avalanche photodiode detector (APD) is used to record the transmitted light, which is necessary for background corrections.

4.2 Experimental Procedure

4.2.1 Loading and Homogenization Procedure

The procedures for polymer and solvent charge and homogenization are different from the View-Cell system. First, a certain amount of polymer sample is loaded in the mixing chamber (MR) instead of the main cell. To drive out the air trapped in the system, a small amount of solvent is charged into the system. Then the temperature is raised to at least 10 ^{o}C above the boiling temperature of the solvent, Then the solvent is evaporated and discharged to remove any entrapped air from the system. This is repeated at least 3

times. During this stage, the amount of the solvent absorbed by the polymer and the amount of polymer dissolved in the solvent are assumed to be negligible. However, when CO_2 is used as a solvent or a component of the solvent mixture, CO_2 is the only component used to flush the system. Then the desired amount of solvent for a target polymer concentration is charged into the system from a transfer vessel previously loaded with the solvent. The amount of solvent charged is determined from the change in the mass of the transfer vessel.

After the polymer and solvent are loaded, the system is pressurized with the pressure generator through the movable piston (MP) as shown in Figure 4.1. The system′s temperature is then raised to a given temperature, which is predetermined from the miscibility measurements using high-pressure view-cell. The high-pressure gear pump (RP) is then used to recirculate and homogenize the contents in the system. The completion of dissolution is usually verified by visual observations through the window. A clear window at higher pressures and a cloud point appearing during depressurization that is very close to the cloud point determined from view-cell measurement indicate a complete dissolution of polymers. However, the solution may appear clear because the polymer has not been dissolved at all. This usually happens when the recirculation loop is clogged by the swollen or molten polymer so that the gear pump is not able to push the solution through. Unlike a completely homogenized solution, a clogged system displays a clear window before and after depressurization. In this case, the pressure generator and the isolation valves, V4 and V14 are used to apply a large pressure difference on the clogged part of the loop.

4.2.2 Demixing Pressure, Crystallization and Melting Temperature Determination Procedure

Even though the demixing conditions have already been determined previously using the view-cell, the demixing pressures and temperatures are usually repeated before the pressure quench experiments. This is because an accurate value of the demixing condition is needed for the pressure quench experiments. However, the compositions in two measurements can be made very close to each other, but cannot be exactly the same. It should be noted that the optical length in these two optical cells are quite different (250 μm in scattering cell versus 4 cm in view-cell). Therefore, some differences in the demixing conditions are expected.

Procedures similar to those followed in view-cell measurements are used to determine the demixing pressures. In these measurements, the pressure reduction is carried out very slowly as opposed to quench experiments. During this process, the temperature (T), pressure (P), scattered light intensities at different angles ($I_{s,\theta}$) and the transmitted light intensity (I_{tr}) are recorded. The scattered light intensities at different angles are also averaged over all angles and recorded as $I_{s,avg}$. From the variation of $1/I_{s,avg}$ with P, the onset of the demixing pressure is determined. Figure 4.2 shows an actual computer output of this pressure reduction process in 1.99 wt % PSF in THF + CO_2 (90:10 by mass) solution at 362 K. Here the change in both the transmitted light intensity and the inverse scattered light intensity are used for determination of the demixing pressure, which is 19.5 MPa.

Similarly, the crystallization and melting temperatures can be determined from the variation of $1/I_{s,avg}$ with T during a slow cooling or heating process. Figure 4.3a is an

actual computer output of a constant pressure cooling process of a 1.0 wt % PE solution in n-pentane at 23 MPa. Figure 4.3b shows the constant pressure melting process at the same pressure. In addition to the constant pressure cooling process, an isothermal and isobaric crystallization process can be studied using this light scattering system. The temperature is lowered to the crystallization temperature ($T_{c,Iso}$) at constant pressure and then is held for 20 minutes before further cooling. Figure 4.3c shows the variation of the transmitted and averaged scattered light intensities, temperature and pressure during an isothermal isobaric crystallization experiment for a 0.5 wt % PE solution in n-pentane. Here, the system was held isothermally at a selected crystallization temperature (T_c = 367.5 K) for about 20 minutes at 52 MPa. It is shown in the lower curves of this figure that the variation of $T_{c,Iso}$ during crystallization is less than 0.2 K around 367.5K.

4.2.3 Procedure of Rapid Pressure Quench Experiments

After the demixing pressure is determined for a particular polymer solution at a given temperature from the slow pressure reduction experiments, the phase-separated solution is then homogenized by recirculating at about 3 MPa above the demixing pressure. This is because the flow in the system may induce phase separation, which is to be prevented during recirculation. After the system is stabilized, the pressure is then carefully brought to about 0.1 MPa above the demixing pressure. This process is usually accompanied with a small temperature variation so that the system is equilibrated for at least 10 minutes to get ready for the pressure quench experiment. Now, a rapid pressure quench with desired depth is applied to the system by three methods. The first method is to retract the pressurizing fluids from the backside of the movable piston quickly. As mentioned before, it may not be fast enough for some systems. However, this method can

generate small to moderate pressure quenches with reasonable speed. The second method is to turn out the expansion valve to a certain degree. A very small pressure quench can be produced by this method. But larger pressure quenches are not achievable because this needle valve has a very limited changeable volume and the quench speed is determined by the turning speed of the operator. Very large pressure quenches are usually imposed on the system by the third method: retracting the expansion rod at the bottom of the cell. Since the rod is operated by an air-actuated assembly, it can be very fast. The displacement of the expansion rod is used to control the quench depth.

During the pressure quench process, the transmitted light, the scattered light intensities at all angles, the temperature and the pressure changes are all recorded as a function of time. These changes are demonstrated in Figure 4.4 for a 2.87 wt % PSF solution in THF + CO_2 (90:10 by mass). The system was quenched from 17.90 MPa to 15.50 MPa at a rate of pressure change of about 4.8 MPa/s. It is observed that the temperature in the cell drops by 0.4 ^{o}C. This temperature decrease comes from the cooling effect of the fast quench, which is nearly an adiabatic expansion. The temperature bounces back to the original value with time because of the heat transfer from surroundings, which also results in an increase in the pressure. Figure 4.5 shows the time evolution of the scattered light intensity as a function of scattering angles after this quench. It is shown that the scattered light intensity increase at all angles with time.

4.3 Correction of the Scattered Light Intensity

Even though the optical path is very short (250 μm), the turbidity of the phase separating polymer solution can reduce the transmitted light greatly. Multiple scattering effects could also influence the results. Therefore, some corrections have to be done on

the raw data. The following equation is used to correct the scattered light intensity to take account of the background scattering and turbidity (Liu and Kiran, 2001; Xiong, 1998; Szydlowski et al., 1992).

$$I_{s,\theta,corr}(t) = \left\{\frac{I_{s,\theta}(t)}{I_{tr}(t)}\right\} - \left\{\frac{I_{s,\theta}(t=0)}{I_{tr}(t=0)}\right\} \quad (4.1)$$

where $I_{s,\theta}$ (t) is the scattered light intensity at angle θ and I_{tr} (t) is the transmitted light intensity measured at time t. The scattered light intensity is normalized by the transmitted light intensity (first term) in order to compensate for the turbidity. The second term on the right side of Equation 4.1 is considered as scattering background at time zero. In pressure quench and crystallization experiments where temperature or pressure is lowered from homogeneous solutions, the scattered light intensity is corrected using the data at time zero for the background scattering. However, this is not suitable for the melting experiments of PE crystals because the data collection starts with the system initially being at a phase separated state. Therefore, in the present study, during melting experiments, the background correction term is evaluated at the end of the experiment when the PE crystals are melted and mixed with the solvent, instead of its value at zero time where the system is heterogeneous.

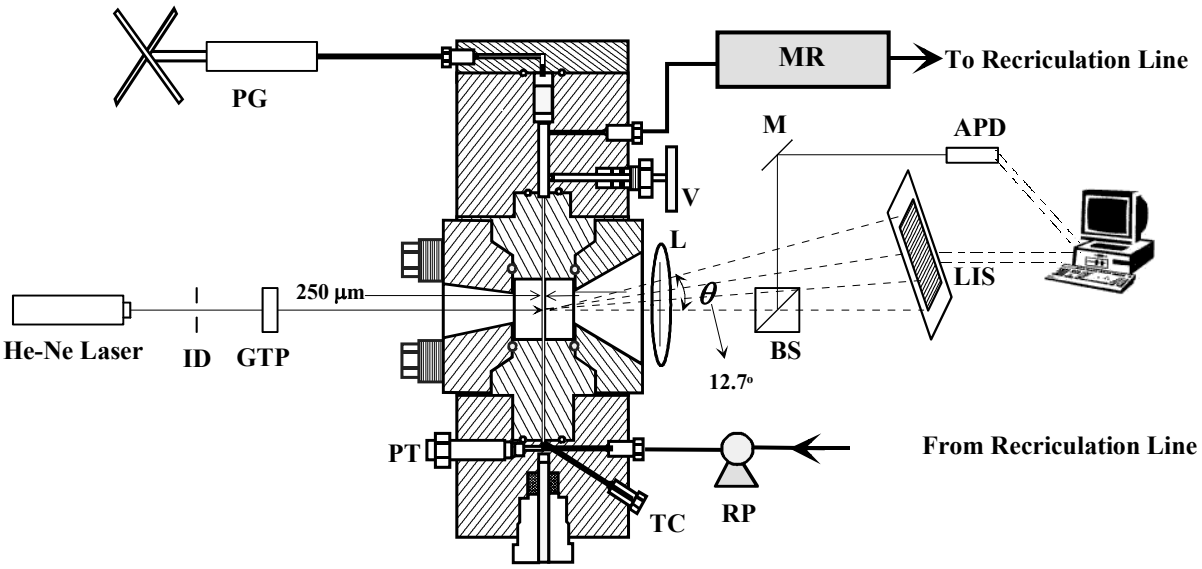

Figure 4.1. Experimental system for time- and angle-resolved light scattering studies at high pressures. [APD = Avalanche Photodiode Detector; BS = Beam Splitter; GTP = Glan-Thompson Polarizer; ID = Iris Diaphragm; L = Convex Lens; LIS = Linear Image Sensor; MP = Movable Piston; MR = Micro-reactor; PG = Pressure Generator; PT = Pressure Transducer; RP = Recirculation Pump; TC = Thermocouple Sensor]

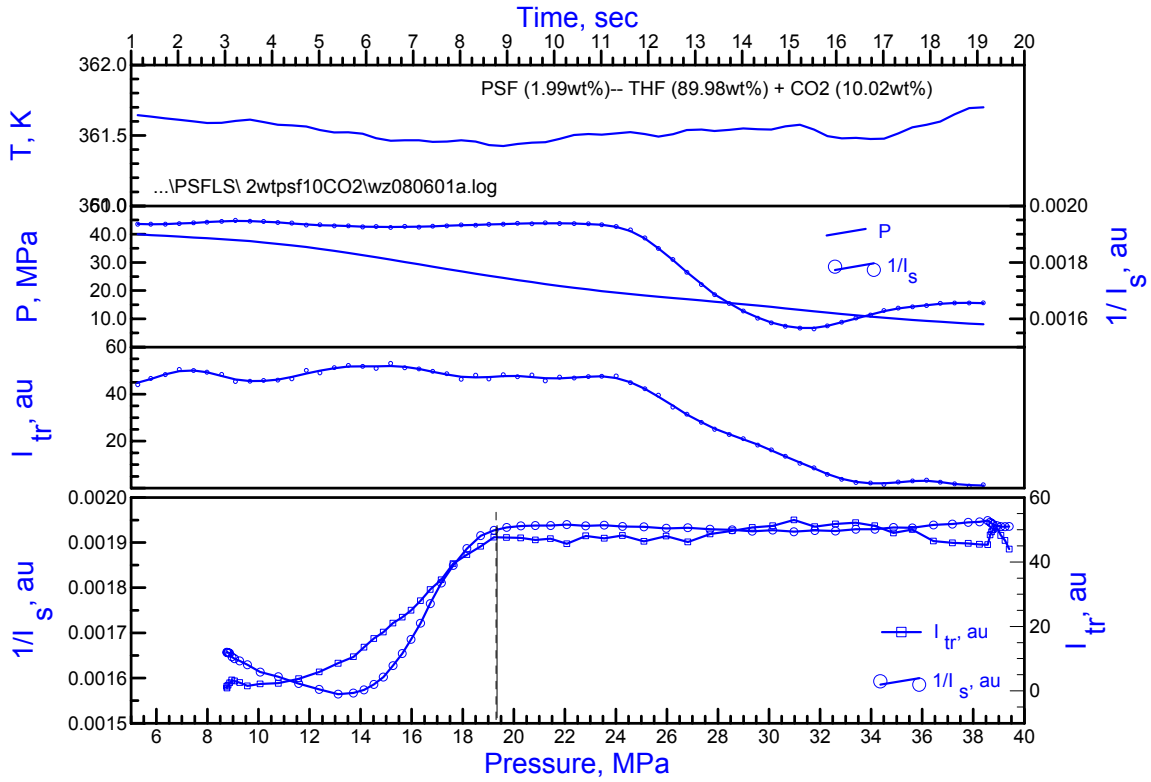

Figure 4.2. Variation of temperature (T), Pressure (P), transmitted light intensity (I_{tr}), and inverse of the scattered light intensity (I_s) with time during a slow pressure reduction process in a 1.99 wt % solution of Polysulfone in mixture of THF and CO_2 (90:10 by mass). The demixing pressure is determined from the variation of the scattered- and transmitted-light intensity with pressure (lower curves in the figure).

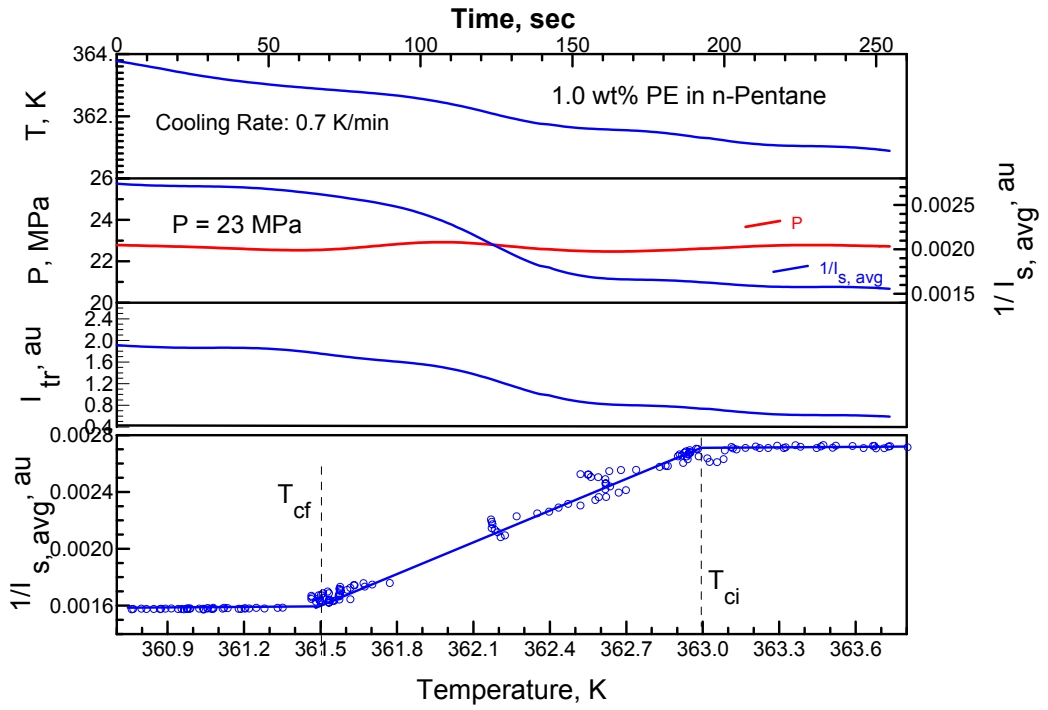
Time, sec
1.0 wt% PE in n-Pentane
Cooling Rate: 0.7 K/min
T, K
P = 23 MPa
P, MPa
P
1/I s, avg
1/ I s, avg, au
I tr, au
1/I s, avg, au
T cf
T ci
Temperature, K

a

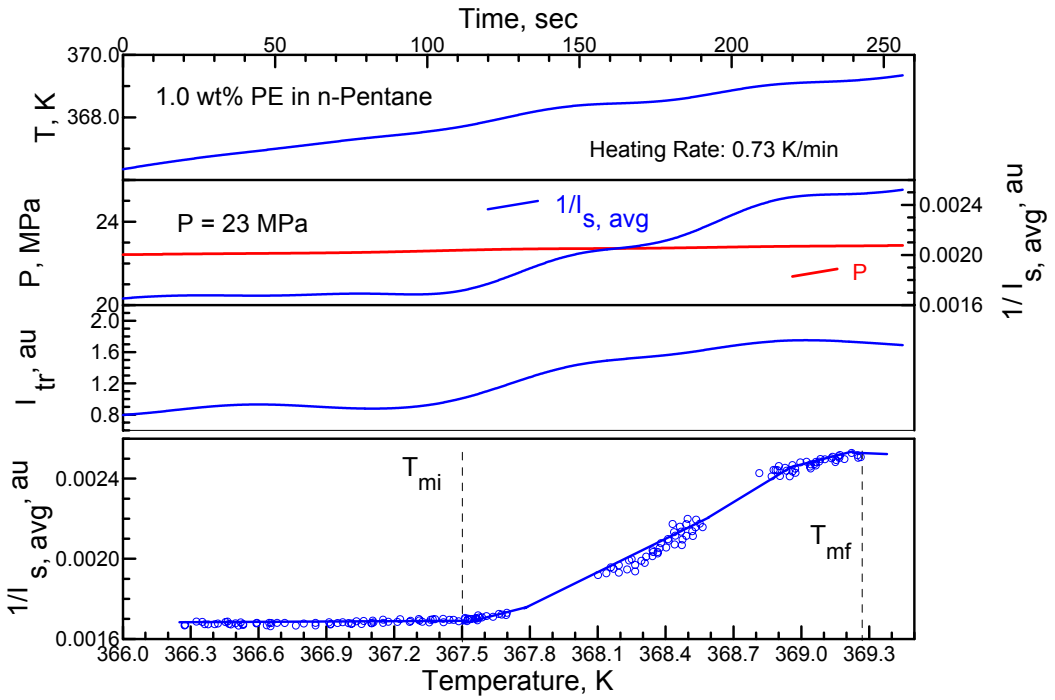
Time, sec
1.0 wt% PE in n-Pentane
Heating Rate: 0.73 K/min
T, K
P = 23 MPa
P, MPa
1/I s, avg
P
1/ I s, avg, au
I tr, au
1/I s, avg, au
T mi
T mf
Temperature, K

b

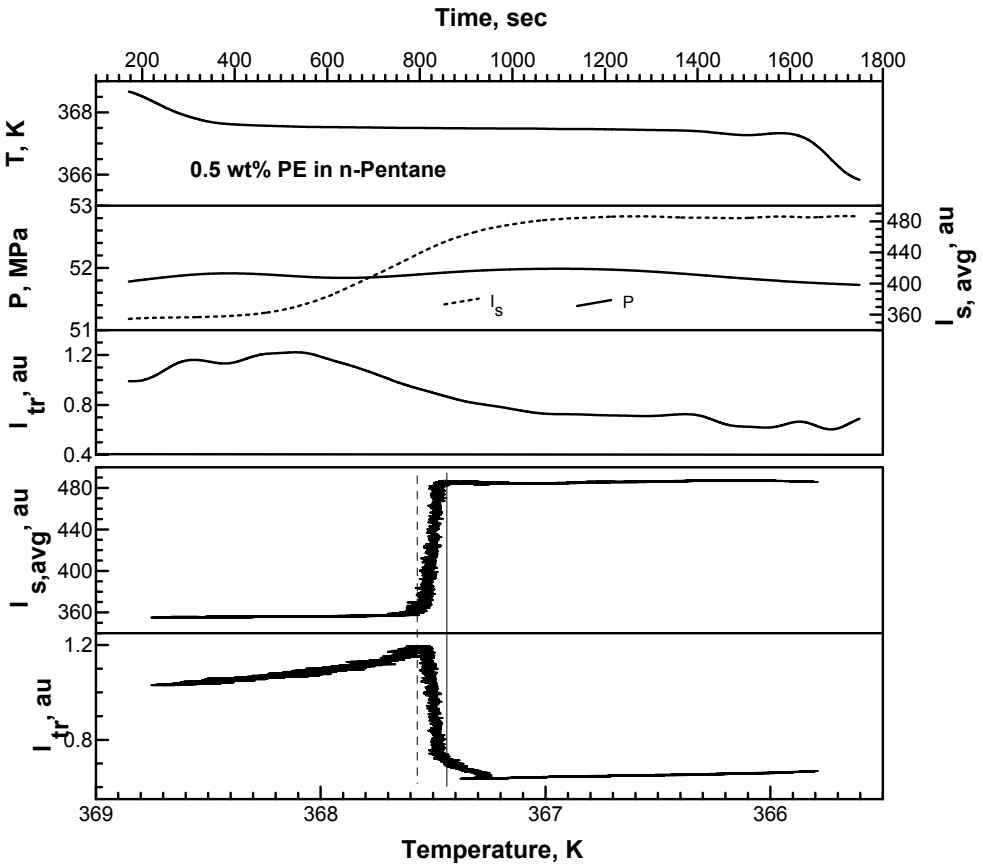

c

Figure 4.3. Variation of temperature (T), Pressure (P), transmitted light intensity (I_{tr}), and scattered light intensity (I_s) with time during a constant pressure cooling process in the 1.0 wt % solution of PE in n-pentane (**a**); a constant pressure heating process in the 1.0 wt % solution of PE in n-pentane (**b**), and a constant pressure cooling in the 0.5 wt % solution of PE in n-pentane where temperature is kept at T_c for 20 minutes before further cooling (**c**). The initial crystallization and melting temperatures (T_{ci} and T_{mi}), the annealing temperature T_c, and final crystallization and melting temperatures (T_{cf} and T_{mf}) are determined from the variation of the scattered- and transmitted-light intensity with temperature (lower curves in the figures).

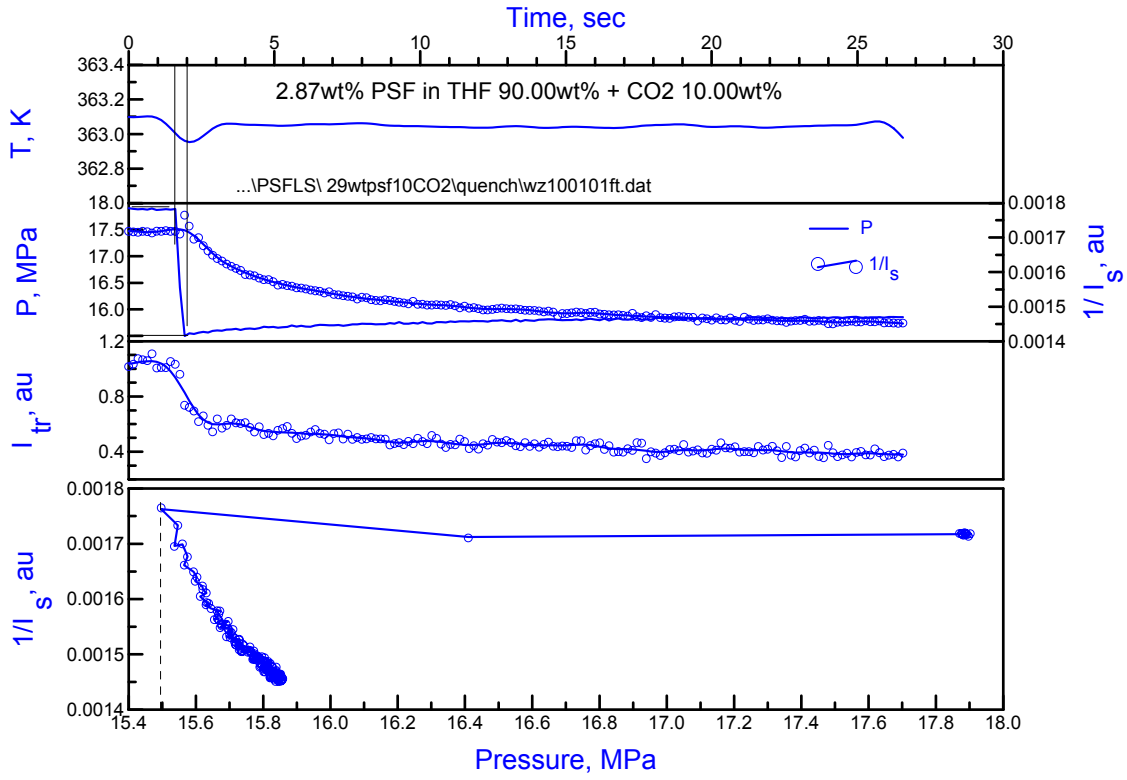

Figure 4.4. Variation of temperature (T), Pressure (P), transmitted light intensity (I_{tr}), and inverse averaged scattered light intensity ($1/I_s$) with time during a fast pressure reduction in 2.87 wt % solution of PSF in THF + CO_2 (90:10 by mass). The times corresponding to the beginning and end of the imposed quench (t_i and t_f) are indicated.

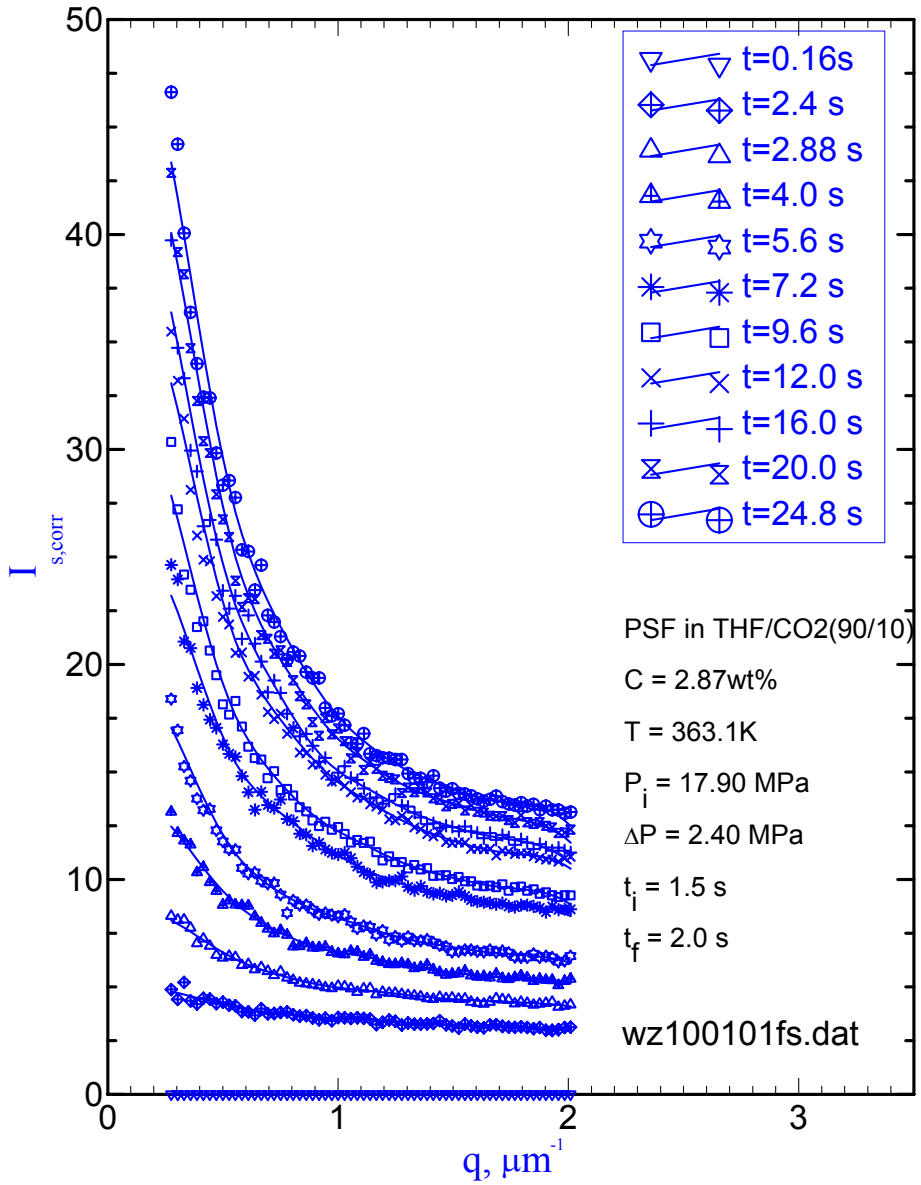

Figure 4.5. Time evolution of the scattered light intensity with time as a function of wave number q after a pressure quench of 2.40 MPa in 2.87 wt % solution of PSF in THF + CO_2 (90:10 by mass) at 361 K.

Chapter 5

Miscibility and Volumetric Properties of Polyethylene in n-Pentane and n-Pentane + CO_2 Mixtures*

In this chapter, the results on the miscibility of polyethylene in solutions of n-pentane and n-pentane + carbon dioxide mixtures are presented. All the phase separation paths shown in Figure 3.3 were used for the determination of solid-fluid (S-F) or liquid-liquid (L-L) phase boundaries. The optical cells described in Chapter 3 and 4 were both used. The high pressure view cell was first used to determine the miscibility and the volumetric properties, and the high-pressure scattering cell was used to study the crystallization and melting kinetics by the light scattering technique. The results on the phase boundary are described in this chapter, while the results on the phase crystallization and kinetics of solid-fluid phase separation are included in next chapter. At each concentration, the demixing pressures were first measured using a constant temperature path (Path A) at the different temperatures up to 438 K. Then, the constant pressure cooling path (Path B) was used to determine the S-F phase boundary at different pressures up to 70 MPa. Path C was also used to determine the S-F phase boundary at a few starting conditions for comparison with those of Path B. Besides, the volumetric properties of 5 wt % PE in n-pentane and n-pentane + carbon dioxide mixtures were also measured. They are included in this chapter. The numerical data of both phase boundary and density of this system are included in Appendix A.

---

*Portions of this chapter have been published in: "Zhang, W., Dindar, C., Bayraktar, B., Kiran, E. Phase Behavior, Density, and Crystallization of Polyethylene in n-Pentane and in n-Pentane/CO_2 at High Pressures**.** *Journal of Applied Polymer Science* (2003), 89(8), 2201-2209."

5.1 Materials

The polyethylene sample used in this study was characterized previously with M_w = 121,000, PDI = 4.3. Tetrahydrofuran (purity > 99.5 %) was obtained from EM Science. n-Pentane, with a stated minimum purity of 99+%, was purchased from Sigma-Aldrich. Carbon dioxide was obtained from Air Products and Chemicals with a purity > 99.99%. The polymers and solvents were used without further purification.

5.2 The Phase Behavior of Polyethylene in n-Pentane and in n-Pentane + CO_2

5.2.1 Phase Behavior of Polyethylene + n-Pentane by High-Pressure View-Cell

Figure 5.1 shows the demixing pressures and temperatures for a 5 wt % polyethylene solution in n-pentane. These were determined from experiments such as those demonstrated in Figures 3.3a-c. Determinations of the demixing conditions by lowering the pressure at constant temperature were carried out at 12 different temperatures in the range from 378 to 438 K. Figure 3.4a demonstrates the case at 423 K. The pressure reduction rate in those determinations were about 0.5 MPa/sec. Figure 5.1 shows the incipient phase separation (open circles) and the demixing conditions corresponding to transmitted light being completely blocked (filled circles). The difference between these reading is in the order of 1 MPa. The boundary obtained is the L-L phase boundary with a positive slope, with the demixing pressures increasing from about 6 to 15 MPa over the experimental temperature range, which is typical of systems that show LCST-type behavior. Here, at a fixed pressure, increasing the temperature

(above 378 K) will take the system into the two-phase region. The region above the L-L phase boundary corresponds to the homogenous one-phase region.

The phase boundary at temperatures below 378 K was determined by lowering the temperature starting at the selected pressures in the homogenous one-phase region as demonstrated in Figure 3.4b at 53.3 MPa. In Figure 3.4b, the system was cooled from 384 to 370 K at a rate of 0.02 K/sec. These experiments were repeated at 16 different pressures in the range from 55 to 8 MPa. As shown in Figure 5.1, the phase boundary shows greater sensitivity to the mode of observation in these experiments because the incipient phase separation and the transmitted light becoming zero condition differs by about 3 K. This phase boundary is the solid-fluid boundary and displays some unique features. As shown in Figure 5.1, the demixing temperatures that depend upon the pressure range show both increasing and decreasing variations with pressure. This is particularly noticeable in the pressure range from 35-45 MPa. DSC studies on the melting temperature of polymer samples crystallized at different pressure confirm these variations as shown in Figure 5.2 (Upper, 2002, Upper et al. 2003). It has been noted that the shape of the S-F phase boundaries in polyethylene glycol (PEG) + nitrogen and PEG + CO_2 systems (Weidner et al. 1997a, b; Weidner and Wiesmet, 1999) have similar sensitivity to T/P conditions. The solid-fluid boundaries that have been reported for poly(ethylene-co-hexene-1) and poly(ethylene-co-octene-1) in propane in the literature are also very steep (Watkins et al., 1991; Condo et al., 1992) as in the present study. However, the unique features of sensitivity to the pressure range have not been reported for these polymers, which may be due to the limited number of data points that have been generated.

Figure 5.3 shows the difference between the solid-fluid phase boundary and the temperature of fusion for an infinitely long linear $–CH_2$ chain. The pressure dependence of the temperature of fusion for an infinitely long linear $–CH_2$ chain is expressed by the following equation given in the literature (Hohne and Blankenhorn, 1994).

$$T_{fus} = 414.8 + 0.2503\ P – 1.348\times10^{-4}\ P^2 \qquad (5.1)$$

Temperature of fusion (T_{fus}) and pressure (P) are in Kelvin and MPa respectively. As demonstrated, there is a significant difference, which is about 45 K. Differences in the temperature of fusion and the temperature of crystallization are expected unless the heating and cooling rates employed are extremely slow. There may be additional factors contributing to this large difference compared to an infinitely long chain which may arise from the presence of the solvent, or from the different molecular weight and molecular weight distribution of the PE sample. The DSC studies on the polymer investigated in the present study gives a melting peak at about 405 K at 10 K/min heating rate conditions (Bayraktar and Kiran, 2001). In the present study, the most significant contribution to the lowering of the crystallization temperature must come from the presence of pentane. In a previous study on the miscibility and crystallization of PE in n-pentane, depending upon the heating and cooling rates, a difference of nearly 20 K was observed (Kiran and Liu, 2002).

Figure 5.4 compares the solid-fluid boundary in terms of the demixing temperatures obtained along a constant pressure path (Path B in Figure 3.3) versus the demixing temperature obtained along a variable-pressure and temperature path (Path C in Figure 3.3). In path C, both pressure and temperature are reduced as demonstrated in Figure 3.4c. The system has been cooled from 389 to 372 K, while the pressure is

reduced from 50 MPa to 44 MPa with the rates indicated in the figure. Both paths approach the phase boundary from the homogenous one-phase region. During these experiments, the temperature and pressure have been reduced slowly, with 0.017 K/s and 0.006 MPa/s respectively. The data in Figure 5.4 show that with such slow cooling and depressurizing rates, both paths lead to the same demixing conditions, leading to similar values for either the incipient phase separation or $I_{tr} = 0$ conditions.

5.2.2 Crystallization and Melting Temperatures of Polyethylene + n-Pentane Studied by High-Pressure Scattering Cell

The crystallization and melting of PE in n-pentane were studied using the high-pressure scattering cell at lower concentrations. The results on the phase boundary are presented in this section, while the results on the phase crystallization and kinetics are described in the next chapter.

Figure 5.5 shows the crystallization and melting temperatures of PE in n-pentane solutions at 3 other concentrations 0.5, 1.0 and 2.3 wt %. These phase transition temperatures were determined from the light scattering data as shown in Figure 4.3. These phase transition temperatures were determined via the constant pressure path at the selected pressure levels, specifically, 10, 14, 18, 21, 24, 28, 31, 35, 38, 42, 45, 48, and 52 MPa.

The results show that crystallization and melting temperatures increase with pressure. At the heating or cooling rates that were employed in this study, the observed melting temperatures were higher than the crystallization temperatures. Even though linear lines have been used to compare the trends in Figure 5.5, the close analysis of the

data reveals that crystallization and melting temperatures display a pressure dependence, where the T_m and T_c decrease notably at a pressure range from about 20 to 40 MPa. This is very similar to that of 5 wt % solutions. The incipient crystallization and melting temperatures are plotted as a function of polymer concentration at 4 pressures, 20, 30, 40, and 50 MPa in Figure 5.6. The melting and crystallization temperatures appear to pass through a minimum at 1 wt % except for crystallization at 20 MPa.

It is noted that, with increasing pressure, the crystallization temperature, T_{ci} increased from about 363 to 368 K, and the melting temperature T_{mi} increased from 368 to 373 K. Even though the trend is same, the temperature range of T_{ci} for the 5 wt % solution is from 374 to 378 K. There is about 5-6 K difference. This difference may be attributed to the difference in the concentration. It may also be a result of the significant difference in the optical path lengths (250 μm vs. 4 cm) and the observed turbidity. Another factor may be the surface effects. In the confined geometry of the scattering cell, the crystallization and melting are taking place in a narrow gap between the sapphire windows, where surface effects may play a role, and the results can be expected to be different. In crystallization and melting in bulk solutions, as would be case in the view cell experiments, the surface effects from the vessel may not play as much a role.

5.2.3 Phase Behavior of Polyethylene + *n*-Pentane + CO_2 by High-Pressure View-Cell

The influence of CO_2 on the L-L and S-F boundary has also been investigated by adding carbon dioxide to the system that already had 5 wt % PE. After CO_2 addition, the solution composition was 4.4 wt % PE in a mixture of n-pentane (86 wt %) and CO_2 (14

wt %). Figure 5.7a shows the phase boundaries in this ternary system. The demixing pressures corresponding to L-L boundary are shifted to higher pressures compared to the demixing pressures for 5 wt % PE in pure n-pentane, as can be seen from the comparison with Figure 5.1. The demixing pressures are now in the 31 to 36 MPa range, compared to 6-15MPa in Figure 5.1. Figure 5.7a shows that there is again about 1 MPa difference between the incipient demixing pressures and the demixing pressures at $I_{tr} = 0$. This is a measure of variation that may be inherent in traditional cloud point measurements based on visual observations.

The demixing temperatures that correspond to the S-F boundary were determined in the pressure range of 35 to 57 MPa by following the constant pressure paths. As in the case of pure pentane, approximately 3 K difference is observed between the incipient phase separation temperatures and the demixing temperatures at $I_{tr} = 0$. Figure 5.7b is an enlargement of the T-scale to show the variation of this boundary with temperature at different pressures. This enlarged figure shows that the S-F demixing temperature initially decreases with pressure and then increases, followed by another region of decreasing temperatures at even higher pressures. A behavior somewhat similar to this has also been reported in the literature for PEG + nitrogen or CO_2 systems (Weidner et al. 1997a, b; Weidner and Wiesmet, 1999). For PEG + CO_2 system, these variations were attributed to a competition between the effect of hydrostatic pressure and the solubility of CO_2 in PEG. Pressure normally is expected to cause an increase in the S-F boundary, but the amount of solvent dissolved in the polymer, which may increase with pressure, would tend to lower the S-F boundary. This type of competition may in part be playing a role in the present system as well. It is also likely that the volumetric behavior of polyethylene

itself with pressure and its crystallization as a function of pressure play a role. The nature of the crystals that are formed at these conditions will be explored in the near future to provide new insights on these morphologies.

A comparison of Figure 5.7a and Figure 5.1 shows that the S-F boundary in the presence of CO_2 in this ternary system is observed at higher temperatures by about 3 K. This means that the phase separation is encountered sooner when the system is cooled from the one-phase region.

Figure 5.8 shows the behavior when more CO_2 is added to the system. The phase boundaries shown correspond to a solution with 4.1 wt % PE in n-pentane (81 wt %) + CO_2 (19 wt %). As depicted in Figure 5.8, the demixing pressures for L-L boundaries are shifted to even higher pressures. The L-L phase boundary is now between 38 and 41 MPa in the temperature range studied, which is from 392 to 438 K. The difference between the incipient demixing pressures and the demixing pressures at $I_{tr} = 0$ is about 0.8 MPa. The demixing temperatures corresponding to the S-F boundary were determined in the pressure range from 42 to 57 MPa, following constant pressure paths. The slope of the S-F boundary and its variation with the temperature and pressure are similar to the higher-pressure range of what is observed with lower CO_2 content. Here also, it is noted that the more CO_2 addition shifts the demixing temperatures to higher temperatures, by about 1 K. It should be noted that these systems do not correspond to the same polymer concentration. The 3-4 K difference between the incipient demixing temperatures and the demixing temperatures at $I_{tr} = 0$ is also observed here, as seen in Figure 5.8 a and b.

Figure 5.9 is a summary figure that compares the demixing pressures and demixing temperatures of 5 wt % polyethylene solutions in n-pentane with different

amount of CO_2 added to the system. For clarity, only the incipient demixing data are compared. This figure demonstrates the significant increases in the demixing pressures corresponding to L-L phase boundary, and the observable increase in the demixing temperatures corresponding to the S-F boundary, with the addition of CO_2 to the system.

Figure 5.10 is a similar comparison of the demixing pressures and demixing temperatures corresponding to $I_{tr} = 0$.

5.3 Volumetric Properties of Polyethylene in n-Pentane and n-Pentane + CO_2 Mixtures by High-Pressure View-Cell

The density data were generated along the constant temperature or constant pressure paths from the one-phase region into the two-phase region during all phase boundary determination experiments. The density data represent the overall mixture density irrespective of the phase state of the system. Along the constant pressure paths, the density measurements were conducted in 2 K intervals. Along the constant temperature paths, the determinations were done in 3.45 MPa (500 Psi) intervals. Figure 5.11 presents the variation of the mixture density with temperature for 5.0 wt % PE in n-pentane along the constant pressure paths from 370 K up to 390 K at pressures from 7.85 to 49.47 MPa. In this figure, the solid-fluid phase separation conditions that are observed on each path are also noted.

Figure 5.12 shows the variation of density with temperature for the ternary system with 4.4 wt % PE in n-pentane (86 wt %) + CO_2 (14 wt %), along selected constant pressure paths. Again, the solid-fluid phase separation points are shown. Similarly, the variation of density along constant temperature path as a function of pressure was also

determined. Figure 5.13 shows these results at nine different temperatures from 398 to 438 K. The density data points at which the L-L demixing took place are connected with a solid line for the incipient demixing pressure and a dotted line for the final demixing pressure. Figure 5.14 and 5.15 show similar density vs. temperature and density vs. pressure plots for the ternary mixture with 4.1 wt % PE in 81 wt % n-pentane + 19 wt % CO_2 fluid mixture.

These plots of density versus temperature or pressure along with the determination of the phase separation conditions (density) are helpful in visual and quick assessment of the degree of volume expansion that may be required to bring about phase separation. Also, the phase change in principle is expected to lead to density change in the systems that could be taken as an additional evidence for crossing a phase boundary. However, in these solutions as shown in figures 5.11-15, the compressibility curves are relatively smooth without significant shift in the volumetric property, as the system undergoes phase separation. This indicates that the phases in equilibrium must have either similar densities, or if they differ, the difference appears to be compensated. Another factor may be the fact that the polyethylene concentration is low for the mixture density effects associated with phase separation to be observed.

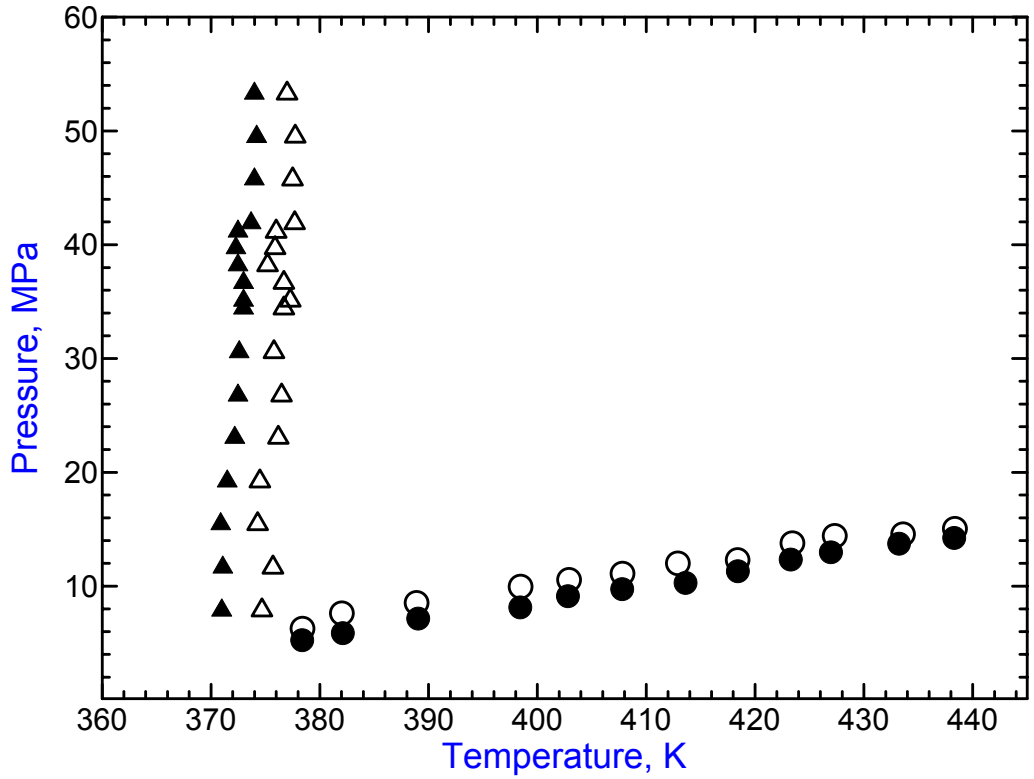

Figure 5.1. Variation of demixing pressures or temperatures for 5 wt % polyethylene (M_w = 121,000; PDI = 4.3) solution in n-pentane. ○, ●: demixing temperatures via Path A of Figure 3.3. Δ, ▲: demixing pressures via Path B of Figure 3.3. Open symbols are the incipient demixing pressures or temperatures and the filled symbols are the demixing pressures or temperatures at I_{tr} going to zero. S-F refers to solid-fluid and L-L to liquid-liquid boundary.

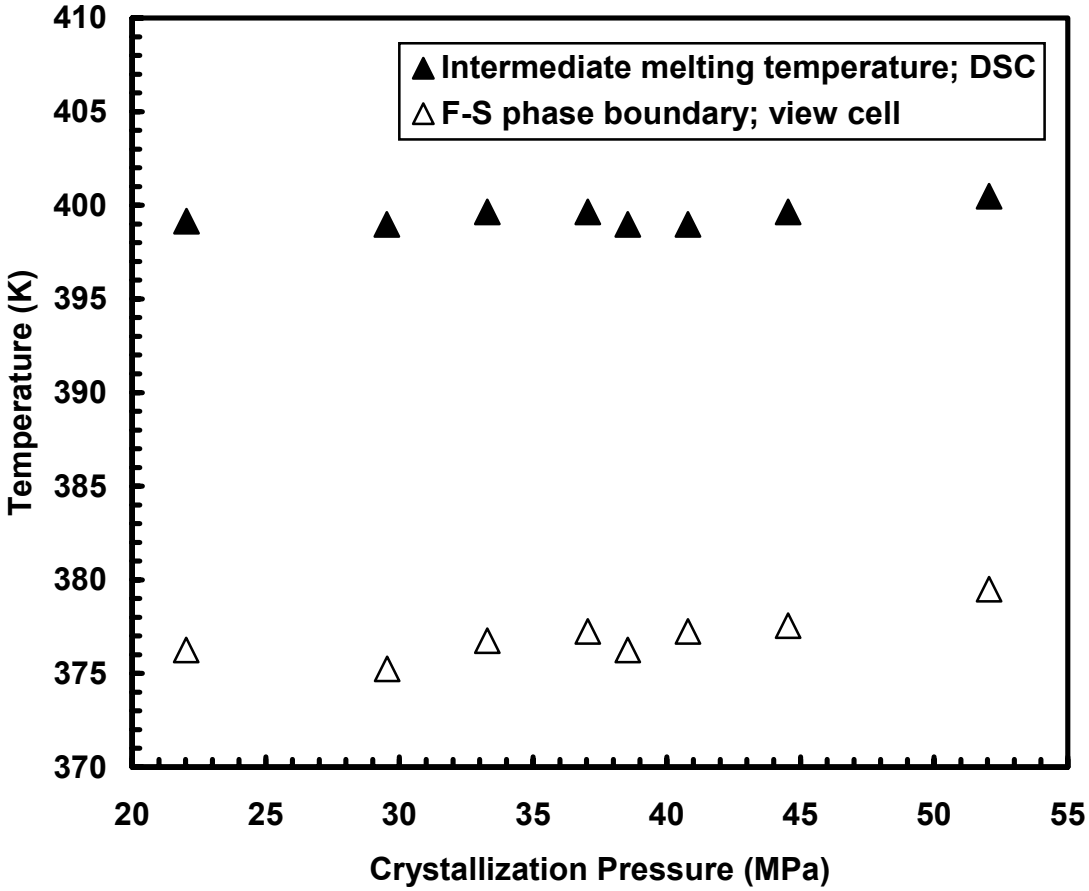

Figure 5.2. DSC results on the melting temperature of the PE crystals formed in 5 wt % solution of n-pentane (Upper, 2002; Upper et al. 2003).

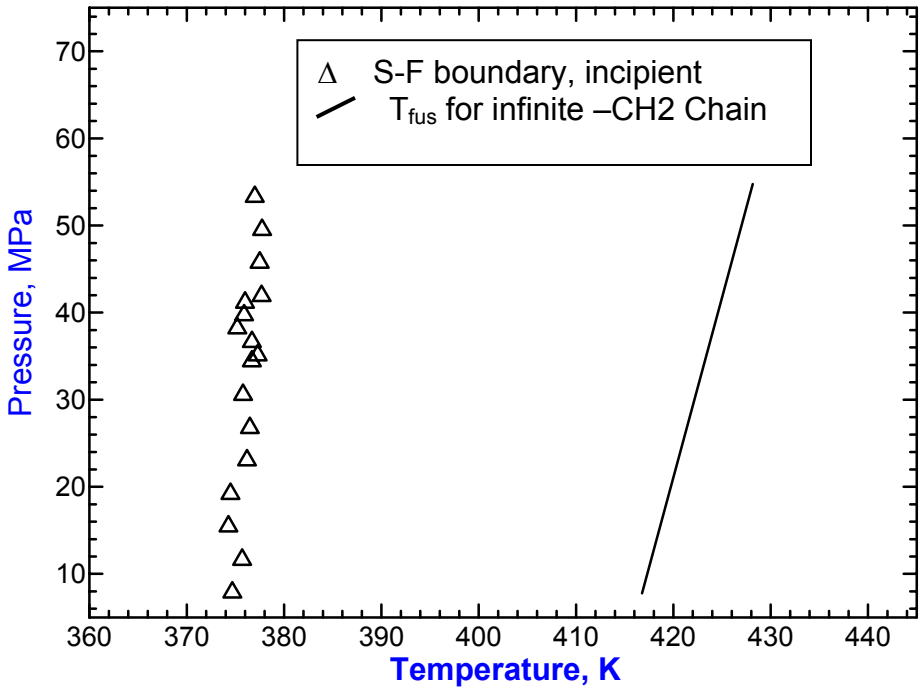

Figure 5.3. Comparison of demixing pressures for 5 wt % polyethylene (M_w = 121,000; PDI = 4.3) solution in n-pentane. Δ: incipient demixing temperatures via Path A of Figure 3.3. Solid line is from the equation for fusion temperature of infinite long $–CH_2$ chain (Hohne and Blankenhorn, 1994). S-F refers to solid-fluid boundary.

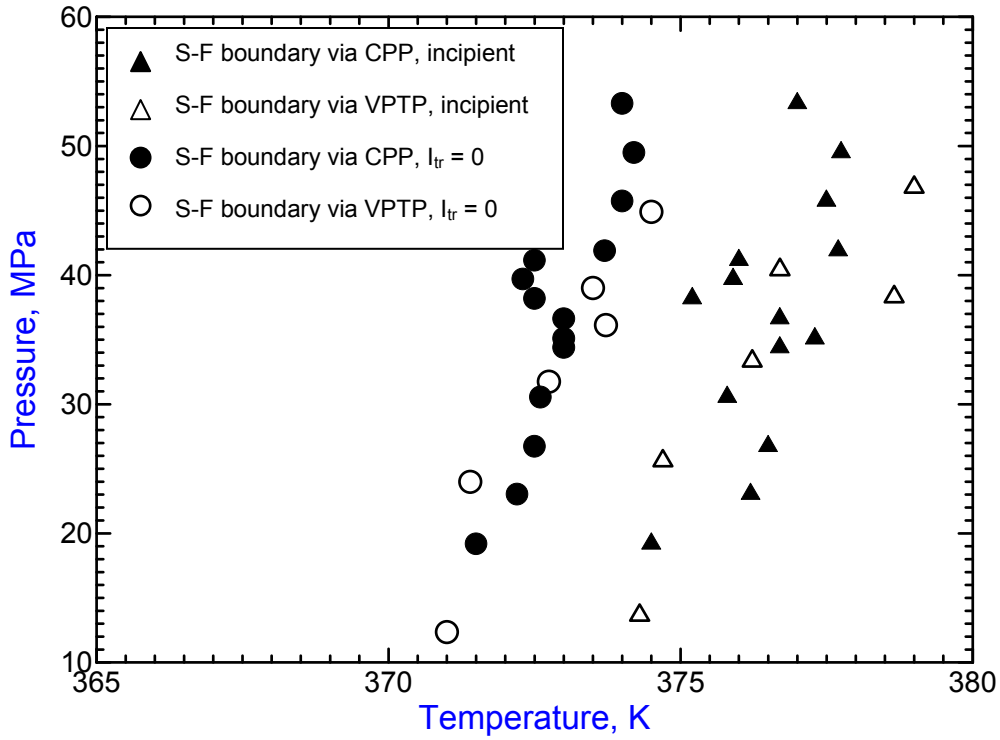

Figure 5.4. Comparison of demixing temperatures obtained from different paths, filled symbols: constant pressure path (CPP, Path B in Figure 3.3) and open symbols: variable pressure and temperature path (VPTP, Path C in Figure 3.3) for 5 wt % PE solution in n-pentane.

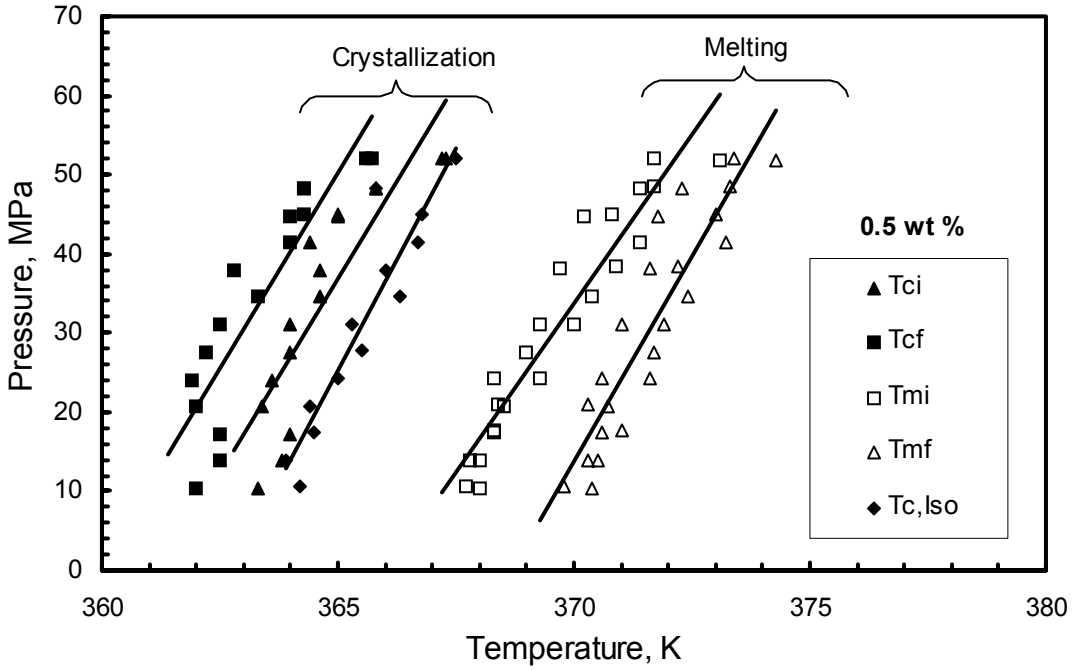
Crystallization
Melting
0.5 wt %
Tci
Tcf
Tmi
Tmf
Tc,Iso
Pressure, MPa
Temperature, K
0
10
20
30
40
50
60
70
360
365
370
375
380

a

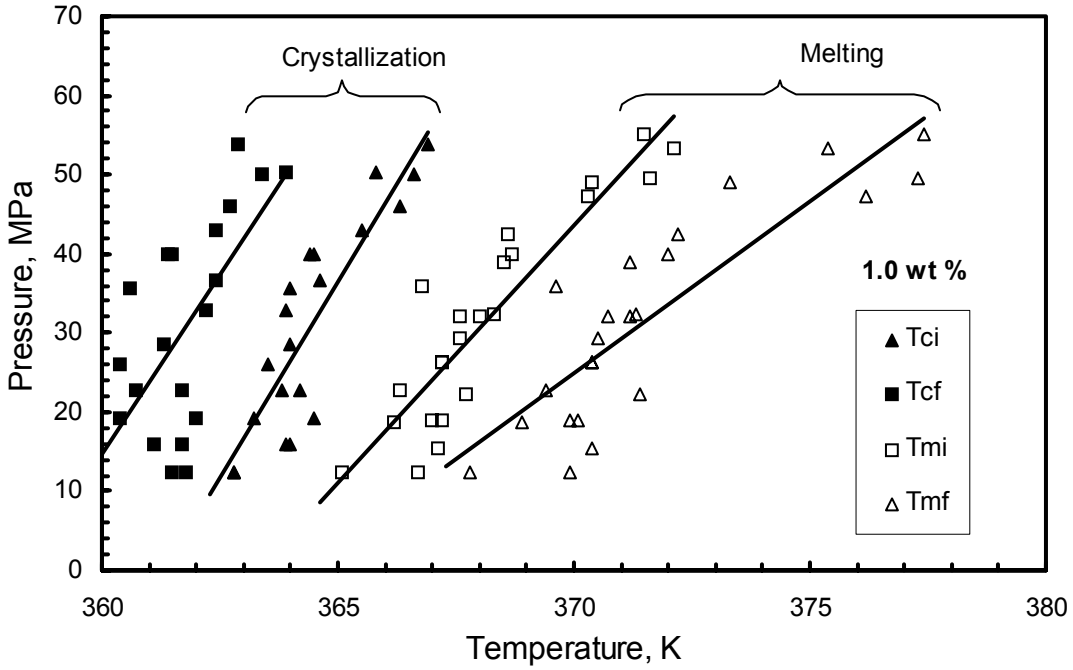
Crystallization
Melting
1.0 wt %
Tci
Tcf
Tmi
Tmf
Pressure, MPa
Temperature, K
0
10
20
30
40
50
60
70
360
365
370
375
380

b

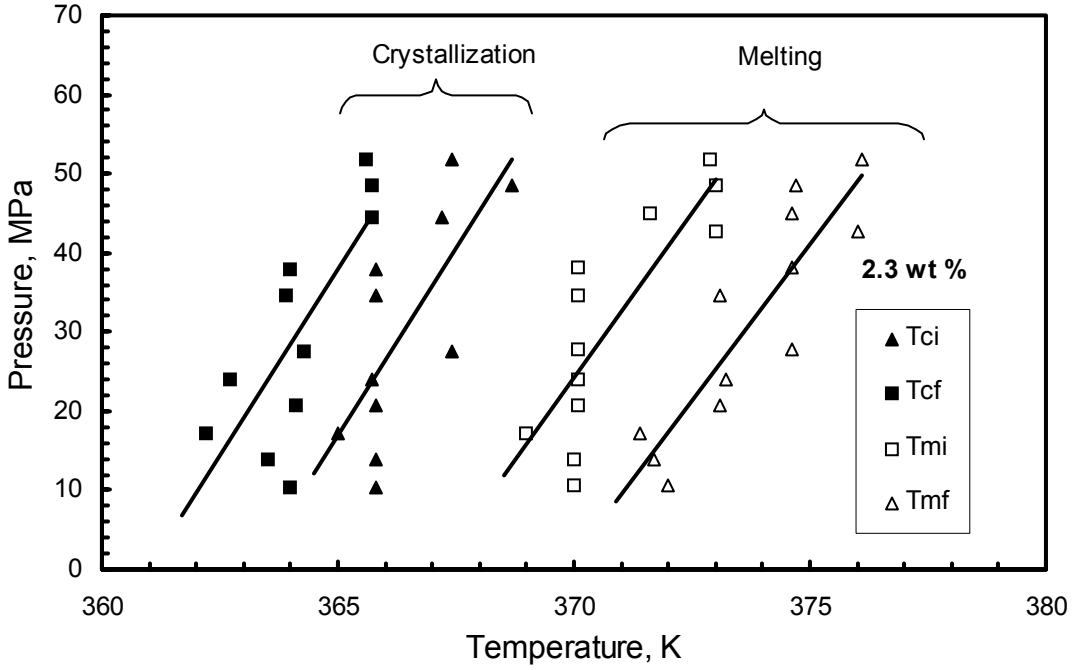

c

Figure 5.5. Variation of the crystallization temperatures (▲: T_{ci}, ■: T_{cf}, ◆: T_{ci}-isothermal) and melting temperatures (□: T_{mi}, Δ: T_{mf}) with crystallization pressure in PE solutions of n-pentane with 0.5 (**a**), 1.0 (**b**) and 2.3 (**c**) wt % PE.

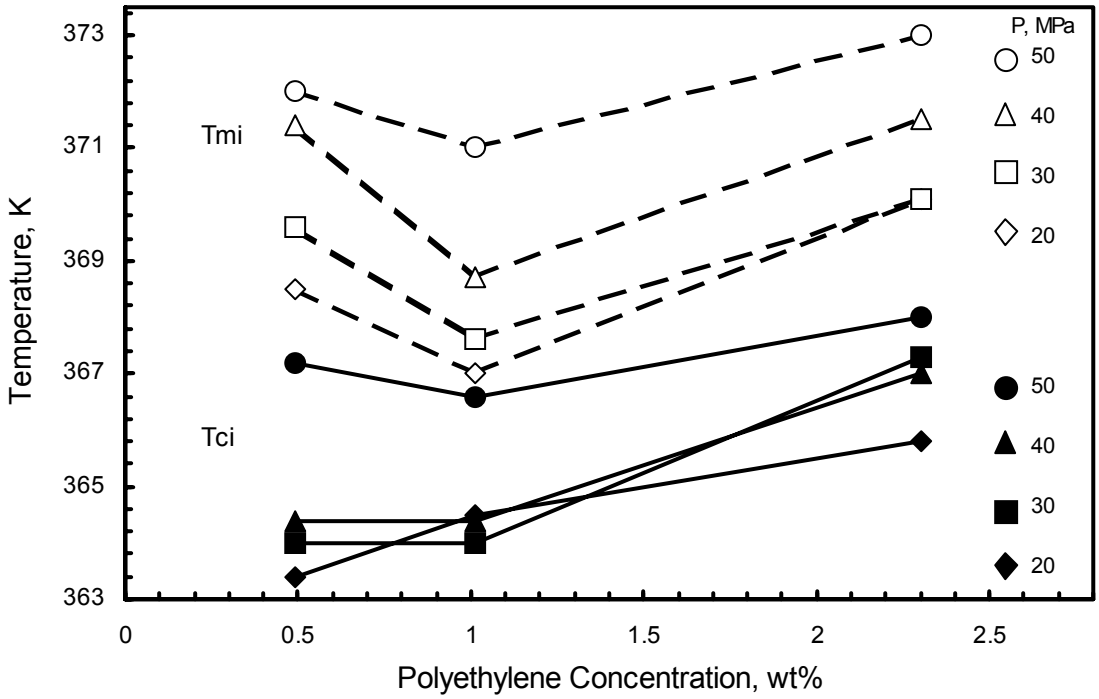

Figure 5.6. Variation of the incipient crystallization, T_{ci} (filled points) and melting, T_{mi} (open points) temperatures with polymer concentration at different pressures. The data are generated from constant pressure cuts of Figures 5.5. a-c.

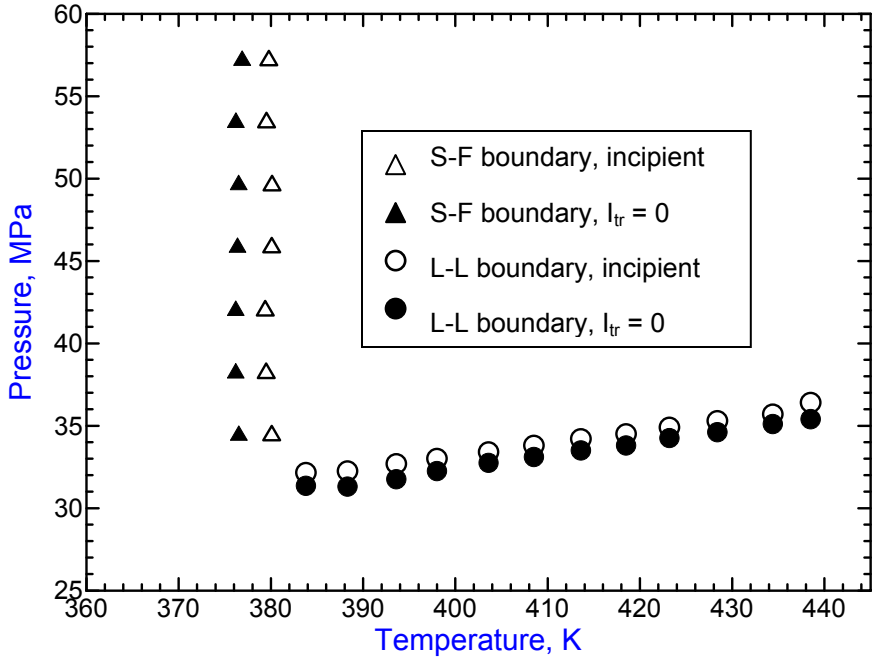

a

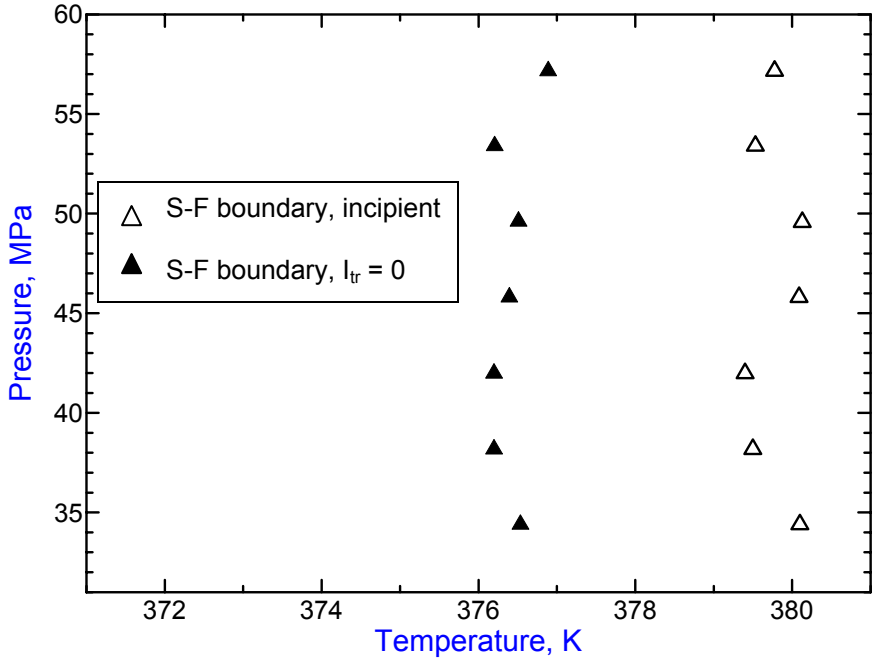

b

Figure 5.7. a: Variation of demixing pressures or temperatures for 4.4 wt % PE (M_w = 121,000; PDI = 4.3) solution in n-pentane (86 wt %) and CO_2 (14 wt %). The triangles are demixing temperatures via Path A of Figure 3.3. The circles are demixing pressures via Path B of Figure 3.3. Open symbols are the incipient demixing pressures or temperatures and the filled symbols are the demixing pressures or temperatures at I_{tr} going to zero. **b**: enlarged demixing temperature curve.

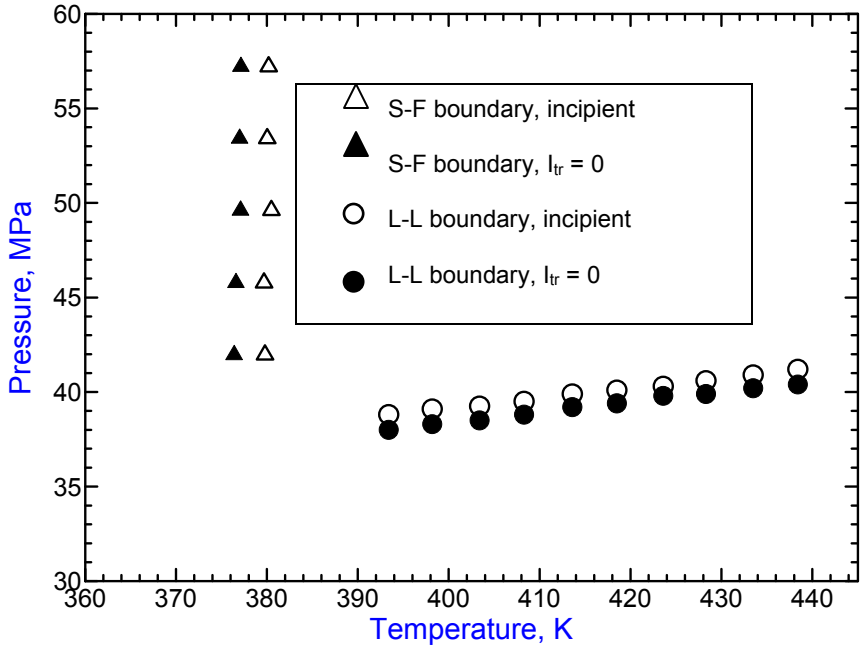

a

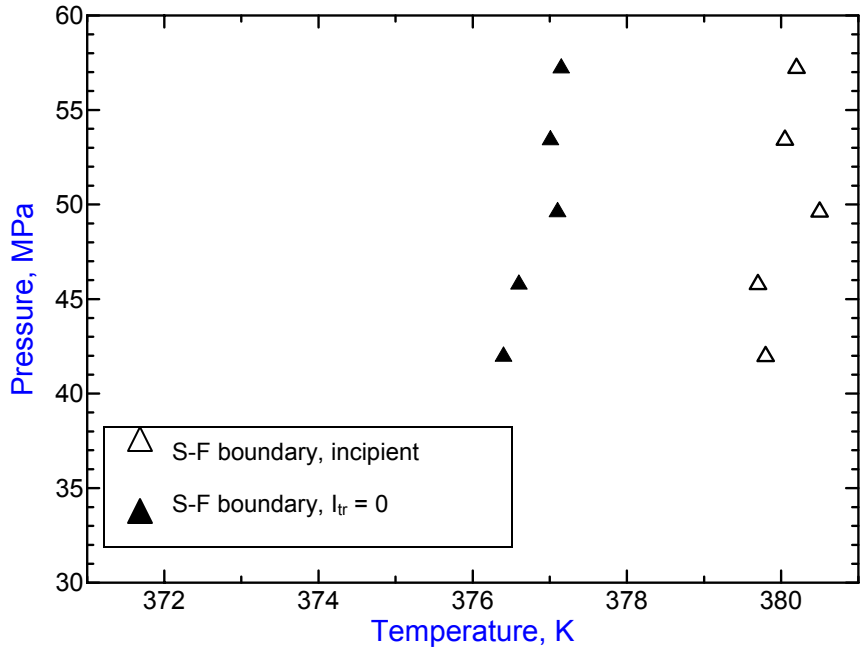

b

Figure 5.8. a. Variation of demixing pressures or temperatures for 4.1 wt % PE (M_w = 121,000; PDI = 4.3) solution in n-pentane (81 wt %) + CO_2 (19 wt %). The triangles are demixing temperatures via Path A of Figure 3.3. The circles are demixing pressures via Path B of Figure 3.3. Open symbols are the incipient demixing pressures or temperatures and the filled symbols are the demixing pressures or temperatures at I_{tr} going to zero. **b**. enlarged demixing temperature curve.

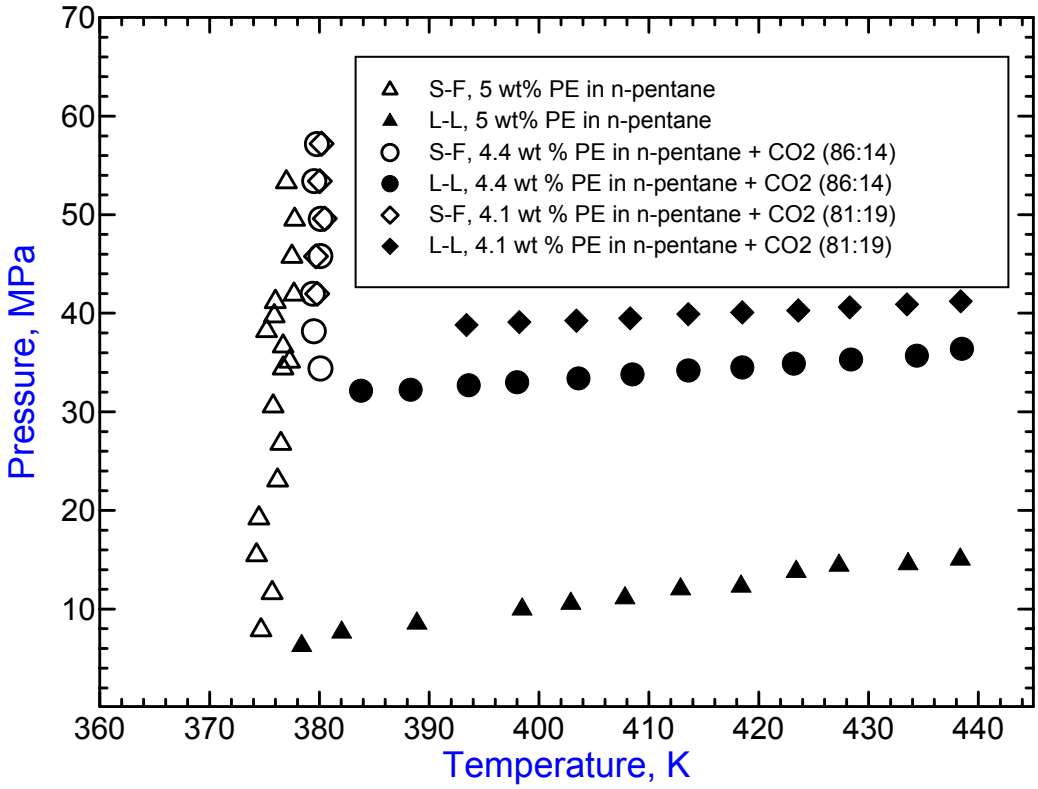

Figure 5.9. Comparison of incipient demixing pressures and demixing temperatures for 5 wt % PE in n-pentane, 4.4 wt % PE solution in n-pentane (86 wt %) and CO_2 (14 wt %), and 4.1 wt % PE solution in n-pentane (81 wt %) + CO_2 (19 wt %). Filled symbols are the liquid-liquid phase boundary, and the open symbols are for solid-fluid phase boundary.

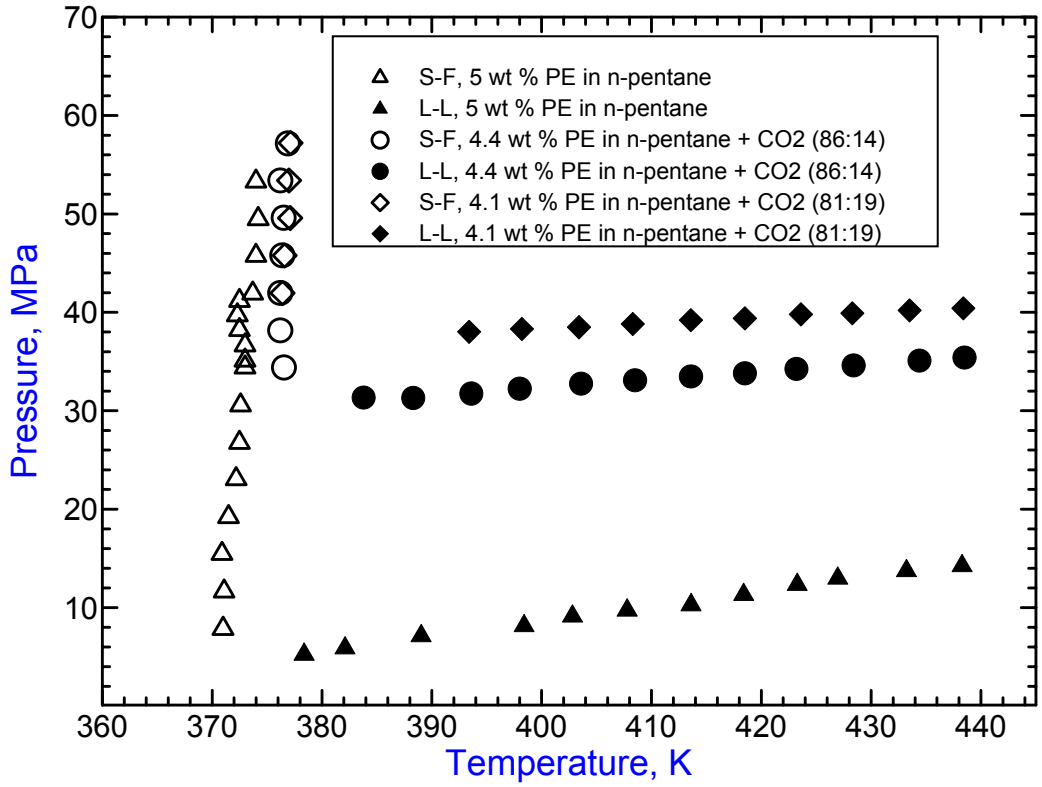

Figure 5.10. Comparison of demixing pressures and demixing temperatures corresponding to $I_{tr} = 0$ for 5 wt % PE in n-pentane, 4.4 wt % PE solution in n-pentane (86 wt %) and CO_2 (14 wt %), and 4.1 wt % PE solution in n-pentane (81 wt %) + CO_2 (19 wt %). Filled symbols are the liquid-liquid phase boundary, and the open symbols are for solid-fluid phase boundary.

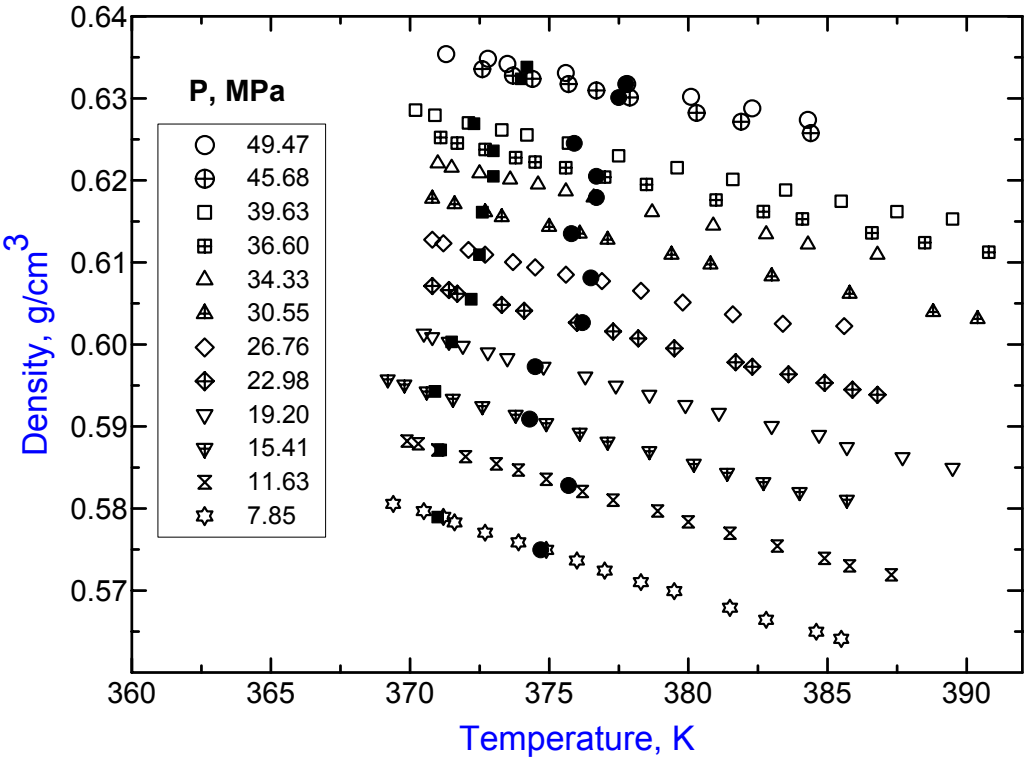

Figure 5.11. Temperature dependence of density for 5.0 wt % PE in n-pentane at pressures 49.47, 45.68, 39.63, 36.60, 34.33, 30.55, 26.76, 22.98, 19.20, 15.41, 11.63, and 7.85 MPa. Filled circles and squares are the incipient S-F phase boundary and S-F phase boundary at $I_{tr} = 0$, respectively.

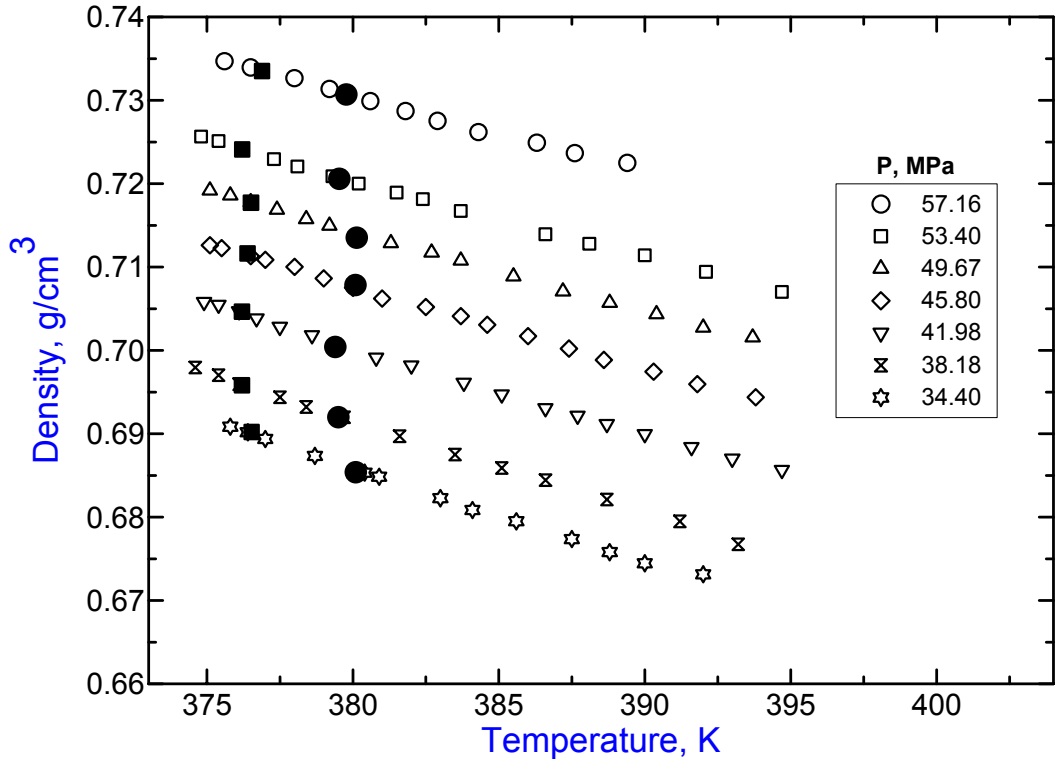

Figure 5.12. Temperature dependence of density for 4.4 wt % PE in n-pentane (86 wt %) + CO_2 (14 wt %) at pressures 57.16, 53.40, 49.67, 45.80, 41.98, 38.18, and 34.40 MPa Filled circles and squares are the incipient S-F phase boundary and S-F phase boundary at $I_{tr} = 0$, respectively.

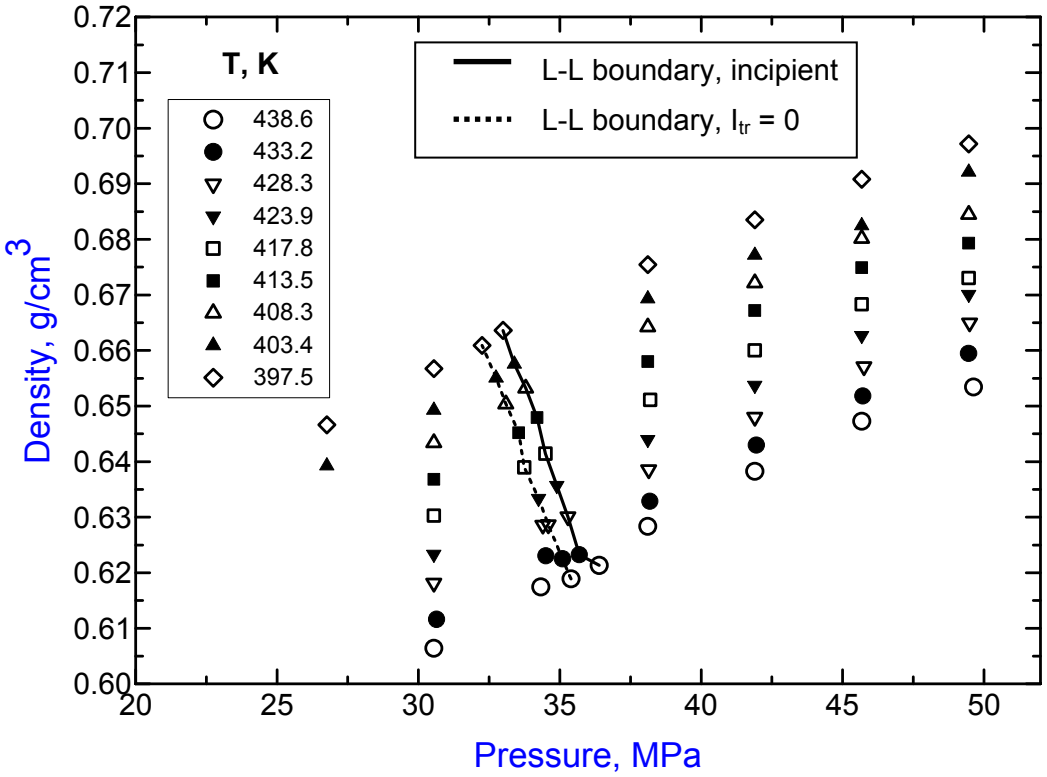

Figure 5.13. Pressure dependence of density for 4.4 wt % PE in n-pentane (86 wt %) + CO_2 (14 wt %) at temperatures 438.6, 433.2, 428.3, 423.9, 417.8, 413.5, 408.3, 403.4, and 397.5 K.

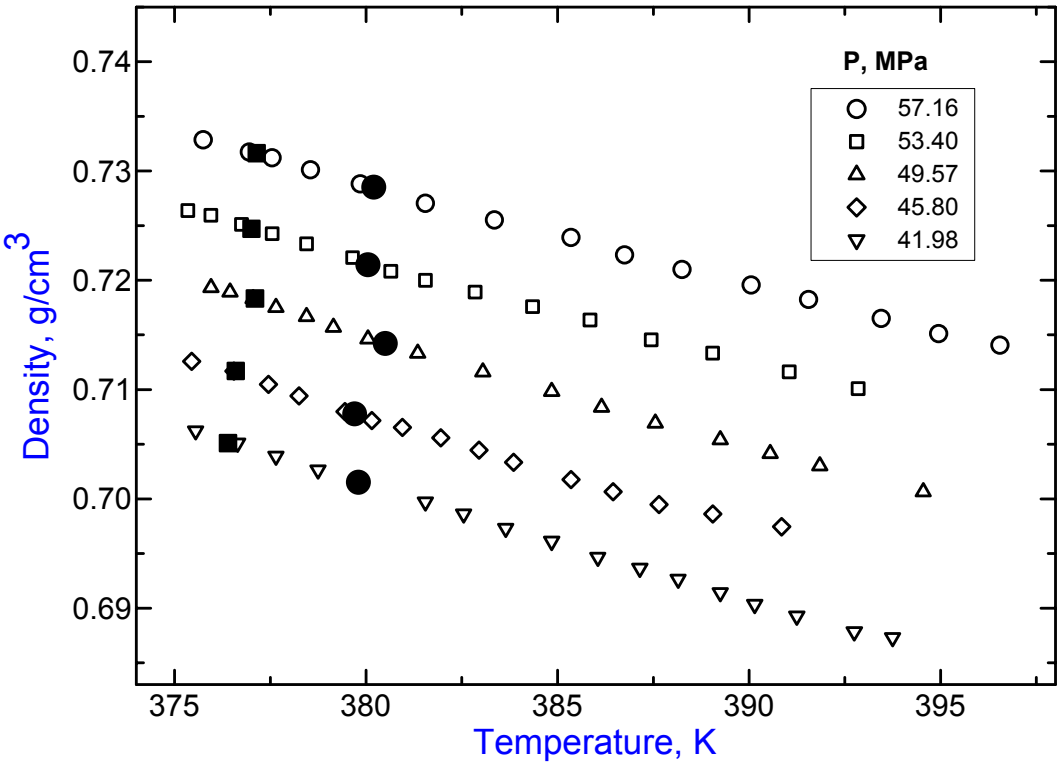

Figure 5.14. Temperature dependence of density for 4.1 wt % PE in n-pentane (81 wt %) + CO_2 (19 wt %) at pressures 57.16, 53.40, 49.57, 45.80, and 41.98 MPa. Filled circles and squares are the incipient S-F phase boundary and S-F phase boundary at I_{tr} = 0, respectively.

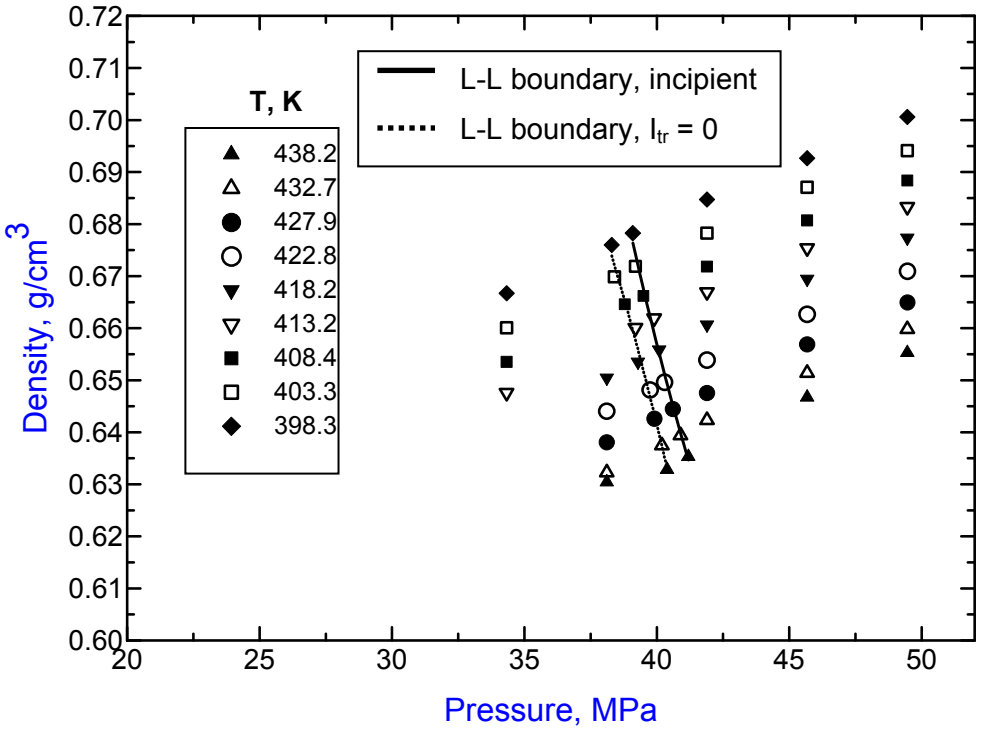

Figure 5.15. Pressure dependence of density for 4.4 wt % PE in n-pentane (81 wt %) + CO_2 (19 wt %) at temperatures 438.2, 432.7, 427.9, 422.8, 418.2, 413.2, 408.4, 403.3, 398.3 K.

Chapter 6

Crystallization and Melting Kinetics of Polyethylene in n-Pentane

This chapter describes the results on the crystallization and melting kinetics and the interplay of S-F and L-L phase separation of polyethylene solutions in n-pentane using time- and angle-resolved light scattering techniques. At three different polymer concentrations, 0.5, 1.0 and 2.3 wt %, the scattered light intensity profiles of both the crystallization and melting process are discussed for the constant pressure processes (the constant pressure heating and cooling). The light scattering experiments at higher polymer concentrations were not carried out because of experimental limitations on making a homogeneous solution. Since the phase separation mechanism of PE crystallization in n-pentane is observed to be only the nucleation and growth mechanism, the evolution of the crystal size during the cooling process and the dissolution during heating process of particles was studied at different pressures from 10 to 55 MPa. Experiments were also accomplished via the two other phase separation pathways for comparison with the constant pressure cooling path. In order to understand the differences of these phase separation routes, the PE samples collected after these three routes were further studied using microscopy and calorimetry. The results regarding the morphological and thermal properties are presented in the next chapter, together with results of other experiments.

6.1 Time Evolution of the Scattered Light Intensity

As discussed in the previous chapter, the constant pressure crystallization and melting experiments of PE in n-pentane were carried out at polymer concentrations of 0.5, 1.0 and 2.3 wt % at pressures ranging from 10 to 54 MPa. These data are listed in Table 6.1 and 6.2 for the crystallization and melting experiments, respectively. The numerical data of the crystallization and melting temperatures are also listed in this table.

Figure 6.1 shows the time evolution of the corrected scattered light intensity $I_{s,\,corr}(q,t)$ versus wave number q during cooling of 1.0 wt% PE in n-pentane at 23 MPa, corresponding to the system described in Figure 4.3a. The T_{ci} and T_{cf} are determined from Figure 4.3a to be 363.0 K and 361.5 K, respectively. The corrected scattered light intensity starts from zero at all angles at zero time (t = 0 s) and increases with time for about 224 seconds.

Figures 6.2 – 6.8 show the time evolution of scattered light intensity profiles for the constant pressure cooling process at 7 other selected pressures, as listed in Table 6.1 (the bold entries). It is noted that there are no maxima in the scattered light intensity over the scattering angles from 1.9^o to 12.7^o. Figures 6.9 and 6.10 represent the scattering profiles during the constant pressure cooling process for solutions with 0.5 wt % and 2.3 wt % PE in n-pentane at 23 MPa.

Figures 6.11-6.18 show the time evolution of the scattered light intensity profiles of the constant pressure melting process at 8 selected pressures as listed in Table 6.2 (the bold entries). The variations of the temperature, pressure, transmitted light intensities, and the inverse of the averaged scattered light intensities are shown as an example in

Figure 4.3b. The incipient and the final melting temperatures are determined from the plots like Figure 4.3b and this data is given in the figures corresponding to the pressures. At the start of an experiment, the system is a higher scatter of light, and with time and progress towards melting, the scattered light intensities decrease, which is the reverse of the changes during crystallization process shown in Figure 6.1. As mentioned in Chapter 4, the melting process is followed until the scattered light intensity drops back to the value close to that before crystallization. This value is taken as the background scattering and used for background correction. Figure 6.19 and 6.20 are the scattered light profiles for the 0.5 and 2.3 wt % solutions at 23 MPa during the melting processes. These plots show a similar dependence of the scattered light intensities on the scattering angle as those of the crystallization process. This kind of monotonously decaying scattering profile is a characteristic feature of systems undergoing phase separation by a nucleation and growth process (Stein and Rhodes, 1960; Nakata and Kawate, 1992; Xiong, 1998).

Table 6.1. Crystallization Temperatures of 0.5, 1.0 and 2.3 wt % PE in n-pentane under different pressures. The light scattering profiles corresponding to the data shown in bold entries are also shown in figures with the figure number given.

PE, wt%	P, MPa	T_{ci}, K	T_{cf}, K	Fig #	PE, wt%	P, MPa	T_{ci}, K	T_{cf}, K	Fig #	PE, wt%	P, MPa	T_{ci}, K	T_{cf}, K	Fig #
0.5	10.3	363.3	362.0		1.0	**12.4**	**362.8**	**361.5**	6.2	2.3	10.4	365.8	364.0	
	13.8	363.8	362.5			**16.0**	**363.9**	**361.7**	6.3		13.9	365.8	363.5	
	17.3	364.0	362.5			19.2	364.5	362.0			17.3	365.0	362.2	
	20.7	363.4	362.0			**22.8**	**363.8**	**360.7**	6.1		20.7	365.8	364.1	
	24.0	**363.6**	**361.9**	6.9		26.0	363.5	360.4			**24.0**	**365.7**	**362.7**	6.10
	27.5	364.0	362.2			**28.5**	**364.0**	**361.3**	6.4		27.6	367.4	364.3	
	31.2	364.0	362.5			32.8	363.9	362.2			32.0	367.2	363.7	
	34.5	364.6	363.3			**35.6**	**364.0**	**360.6**	6.5		34.6	365.8	363.9	
	37.9	364.6	362.8			36.6	364.6	362.4			38.0	365.8	364.0	
	41.4	364.4	364.0			40.0	364.4	361.4			44.4	367.2	365.7	
	44.8	365.0	364.0			**43.0**	**365.5**	**362.4**	6.6		48.4	368.7	365.7	
	44.9	365.0	364.3			46.0	366.3	362.7			51.8	367.4	365.6	
	48.2	365.8	364.3			**50.0**	**366.6**	**363.4**	6.7					
	52.0	367.3	365.7			**53.8**	**366.9**	**362.9**	6.8					

Table 6.2. Melting Temperatures of 0.5, 1.0 and 2.3 wt % PE in n-pentane under different pressures. The light scattering profiles corresponding to the data shown in bold entries are also shown in figures with the figure number given.

PE, wt%	P, MPa	T_{ci}, K	T_{cf}, K	Fig #	PE, wt%	P, MPa	T_{ci}, K	T_{cf}, K	Fig #	PE, wt%	P, MPa	T_{ci}, K	T_{cf}, K	Fig #
0.5	10.6	367.7	369.8		1.0	**12.4**	**366.7**	**369.9**	6.12	2.3	10.5	370.0	372	
	14.0	368.0	370.3			**15.4**	**367.1**	**370.4**	6.13		14.0	370.0	371.7	
	17.6	368.3	371.0			19.0	367.2	370.1			17.3	369.0	371.4	
	20.8	368.5	370.7			22.3	367.7	371.4			20.8	370.1	373.1	
	20.9	368.4	370.3			**24.0**	**366.3**	**369.4**	6.11		**24.0**	**370.1**	**373.2**	6.20
	24.2	**369.3**	**371.6**	6.19		26.4	367.2	370.4			27.7	370.1	374.6	
	27.6	369	371.7			**29.3**	**367.6**	**370.5**	6.14		34.6	370.1	373.1	
	31.2	370.0	371.9			32.2	368.0	371.2			38.1	370.1	374.6	
	34.6	370.4	372.4			**36.0**	**366.8**	**369.6**	6.15		42.6	373.0	376	
	38.3	370.9	372.2			38.8	368.5	371.2			45.1	371.6	374.6	
	41.5	371.4	373.2			40.0	368.7	372			48.4	373.0	374.7	
	44.8	370.2	371.8			**42.5**	**368.6**	**372.2**	6.16		51.8	372.9	376.1	
	44.9	370.8	373.0			47.2	370.3	376.2						
	48.3	371.4	372.3			**49.6**	**371.6**	**377.3**	6.17					
	48.4	371.7	373.3			53.2	372.1	375.4						
	51.9	373.1	374.3			**55.0**	**371.5**	**377.4**	6.18					

6.2 Time Evolution of the Size of PE Crystals

It is very interesting to find out the correlation lengths or the sizes of the crystals during both the crystallization and the melting processes. As pointed out in Chapter 2, the mean radius of particles can be determined from the angular distribution of scattered light intensities via two approaches. One is using the Debye–Bueche function (Equation 2.10) and the other is using the Guinier function (Equation 2.8). Both of these methods will be used and compared here. Even though this may be of limited applicability for the present system, such an analysis is still instructive in terms of dynamics of the phase growth. The Guinier function (Equation 2.8) can be written in its logarithmic form as:

$$\ln\left(I_{s,corr}(q)\right) = \ln\left(I_0\right) - 0.221R_m^2q^2 \tag{6.1}$$

From the slope of a plot of $\ln\left[I_{s,corr}(q)\right]$ versus q^2, which should be linear, the mean particle radius R_m can be evaluated. Even though this equation has its limitations for its applicability for systems where multiple scattering may be present, such an analysis is still instructive in terms of dynamics of the phase growth.

Figure 6.21 shows such a plot of $\ln\left(I_{s,corr}(q)\right)$ versus q^2 for the scattering data that have been shown in Figure 6.1. These plots shown in Figure 6.21 do not display a linear variation over the full q range, which suggests a distribution in the size of the particles. If the particles can be considered as bimodal, the mean radius for larger particles can be calculated by fitting the data at smaller q as R_{mL}. The mean radius of smaller particles can be determined by fitting the data at larger q as R_{mS}. This is demonstrated with the scattered light intensity data corresponding to t = 16 s in Figure 6.21. A mean radius R_m

may also be evaluated by a best-fit line through all data points, and this is illustrated for the data set corresponding to t = 48 s in the same figure.

The evolution of the mean particle size over time corresponding to Figure 6.21 is presented in Figure 6.22. The mean particle radius R_m initially increases with time from around 0.6 μm to 1.3 μm for 120 s and then levels off, which appears to be the stable size. The R_{mL} and R_{mS} that were determined by assuming a bimodal distribution are also shown in this figure. The R_{mS} shows almost no variations during the process, while the larger size R_{mL} increases for about 100 s and levels off at around 2.7 μm. It is this growth that has been captured in the scattered light intensity profiles shown in Figure 4.3a. However, as stated in the literature (Nakata and Kawate, 1992; Zhuang, 1995), Equation 2.8 is only valid for low scattering angles. Therefore, the larger particle size, R_{mL} is more reliable than the other two averages using all the data of all scattering angles R_{m} and larger scattering angles R_{mS}.

Using a similar procedure, the evolutions of the mean radii R_m, R_{mS} and R_{mL} for the melting of PE crystals are plotted against time in Figure 6.23, which is basically the reverse of the crystallization process. The mean radii that are initially stable at R_{mS} = 0.6, R_m = 1.2 and R_{mL} = 2.5 μm show a decrease with the onset of melting, which in these heating experiments correspond to t = 120 s.

Figure 6.24 shows typical results for Debye–Bueche plots of the scattering intensity data that has been shown in Figure 6.1. The data has a poor linearity for the data over the whole scattering angles range. However, a linear fit of the scattering intensity at small angles show a better linearity. Similar to the Guinier plots, the correlation length is calculated using only the data at small angles, large angles and all scattering angles.

These linear fits are illustrated using the scattering data for t = 80 s. The correlation lengths calculated from these plots are shown in Figure 6.25. The evolution of the correlation length over time is almost identical to that of Figure 6.22 in spite of the absolute values. The value of correlation length calculated from Debye–Bueche plots is only about 1/3 of the radius calculated from the Guinier plots. As shown by the microscopy data in the next section, the results calculated from Guinier plots are much closer to the particle size observed by microscopy even there are still some differences. Therefore, only the radius data calculated by using Guinier plots will be used in the future discussion.

Figure 6.26 shows the mean particle radius R_{mL} as a function of the crystallization pressure for all three polymer concentrations. As shown, in all these solutions, even though the pressure effects are not large, the crystallization at higher pressures was observed to result in larger particle sizes. Particle sizes that form from 0.5 and 2.3 % solutions are in the 1-3 micron range. Somewhat larger particles were formed in the 1.0 wt % solutions, while the trends for 0.5 and 2.3 wt % are very similar.

6.3 The Interplay of S-F and L-L Phase Separation Studied by Light Scattering

Using either the temperature or the pressure as the controlling parameter, both the solid-fluid and liquid-liquid phase boundaries have been identified at several concentrations in the pressure range from 10 to 70 MPa and the temperature range from 360 to 440K. However, the details of the phase boundaries in the P-T range where the S-F and L-L phase boundaries may cross are not clearly identified in the P-T phase

diagrams shown in Chapter 5. This region is, however, quite interesting because both liquid-liquid and fluid-solid phase separations may take place and as such may provide the opportunity to study how one type of phase separation may influence the other type of phase separation. Even though limited, studies have been published about bringing the homogenous solution into a submerged L-L metastable region inside the S-F phase separated region of a system (Bonnett et al., 2003).

In the present study, the polymer solution has been brought to the final state where the samples are collected for further studies, via three different pathways that are similar to those discussed in Chapter 3. The first route is to bring the system into the S-F phase separated region, followed by a depressurization process. The second route is to perform a pressure quench into the L-L phase separated region, and then cool down to the final temperature. The third route is to bring the system through the P/T region where the L-L and S-F phase boundaries merge (shaded region in Figure 6.27) and to the final state for sample collection. These three routes are depicted in Figures 6.27-6.30 in the schematic T-X diagrams.

Figure 6.28 shows Route 1 on a T-X diagram, where the pressure is kept constant. The polyethylene in n-pentane system displays a LCST type of phase boundary at higher temperatures and a S-F phase boundary at lower temperatures. The arrow shows that the homogenous solution (open circle) is brought into the S-F phase separated region (filled circle) during the constant pressure cooling process (Route 1) from T1 to T2.

Figure 6.29 is a schematic diagram of Route 2 on T-X phase diagrams. The homogenous solution (open circle) is brought to the L-L phase separated region with a pressure quench from P1 to P2, which is shown as a change in the L-L phase boundary in

this figure. The system is separated into two co-existing phases (a polymer-rich phase and a polymer-lean phase) shown as two filled circles located on the L-L phase boundary. These two phases undergo a similar process as that of Route 1 to cross the S-F phase boundary during further cooling process as shown the arrows in the lower diagram.

Figure 6.30 illustrates the third phase separation route on the T-X phase diagrams. As the pressure and temperature drops, the homogenous solution (open circle) moves toward the S-F phase boundary. Meanwhile, the L-L phase boundary is also getting closer to the S-F phase boundary. If the L-L boundary moves faster, it will cross the open circle first before it reaches the S-F boundary, which makes this route similar to Route 2. On the other side, if the open circle is moving faster than that of the L-L boundary to S-F boundary, this becomes Route 1. Here, the system should be brought into the shaded area of Figure 6.27 at P = Ps and T = Ts so that the competition between crystallization and L-L phase separation takes place and may have an effect on the morphology and the properties of the polymer samples.

The scattered light intensity, transmitted light intensity, pressure, and temperature are recorded for these processes. Figures 6.31, 6.32 and 6.33 show the average scattered light intensity, pressure and temperature changes during these three different routes on a P-T phase diagram. The data points are previously measured S-F and L-L phase separation conditions. For Route 1, Figure 6.31 shows that the scattered light intensity increases rapidly when the temperature approaches the incipient S-F phase boundary, which is about 363 K. After reaching a plateau value, the scattered light intensity does not change for the rest of the process except a small variation at beginning of the depressurization process around 350 K. This figure also shows that the pressure was well

maintained at 10 MPa when the system is crossing the S-F phase boundary. In comparison, for Route 2 (Figure 6.32), the scattered light intensity shows an increase when a pressure quench of 12 MPa is applied on the system. But the scattered light intensity drops after this initial increase until the system crosses the projected S-F phase boundary, which is again around 363 K. A further increase was observed at around 345 K. These two increases are likely to be the S-F phase transition in the two co-existing phases. As shown in Figure 6.33, the scattered light intensity change for Route 3 is very similar to that of Route 1, which displays only one increase during the pressure and temperature reduction process. The pressure and temperature change during the phase separation process was controlled so as to pass through the intersection of L-L and S-F phase boundaries, which is different from those of Route 1 and Route 2. The interplay of S-F and L-L phase separation will be further discussed in next chapter, including information on the collected PE samples after these phase separation routes.

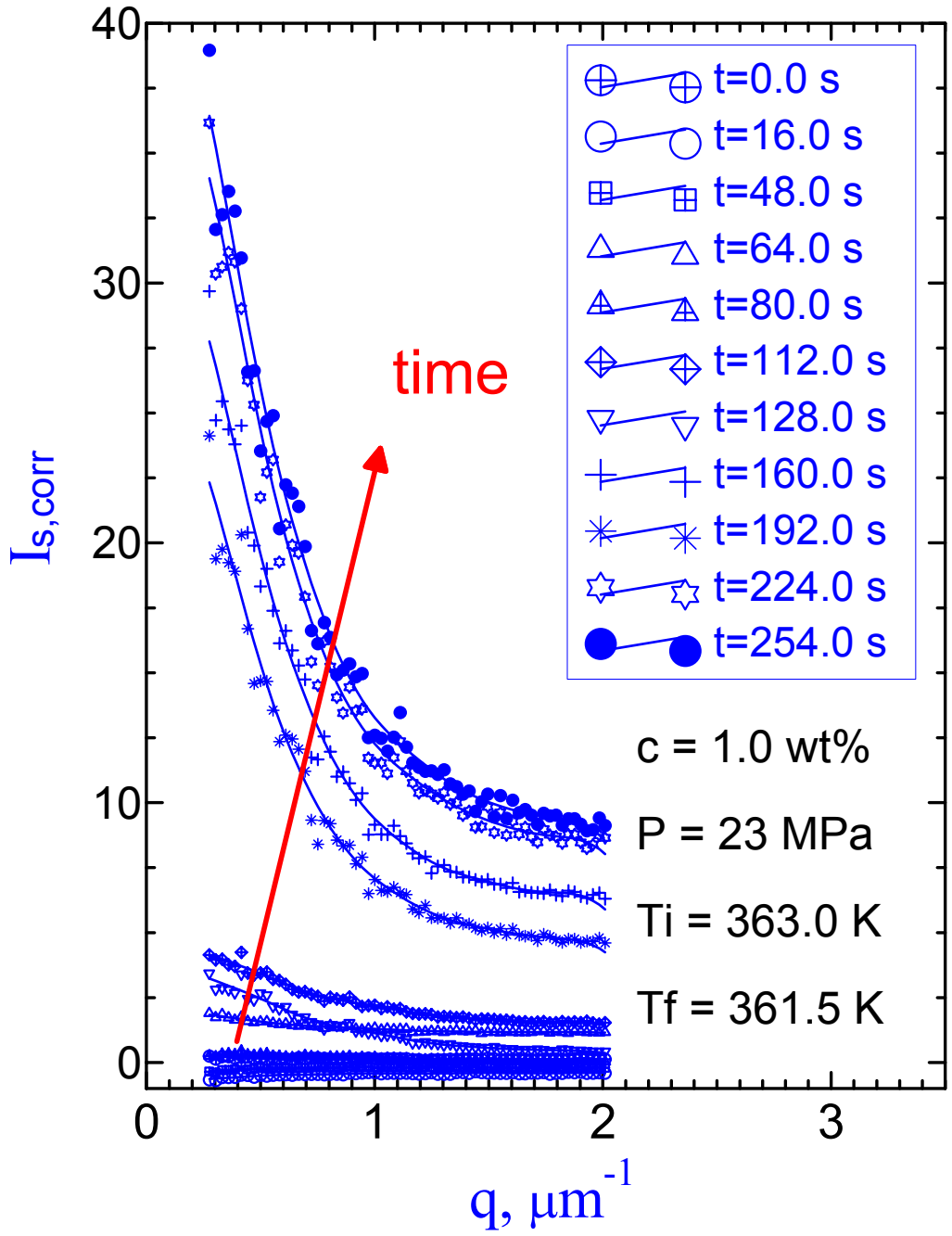

Figure 6.1. Variation of the corrected scattered light intensity $I_{s,\,corr}(q,t)$ versus wave number q at selected times during constant pressure cooling of 1.0 wt % PE in n-pentane at 23 MPa.

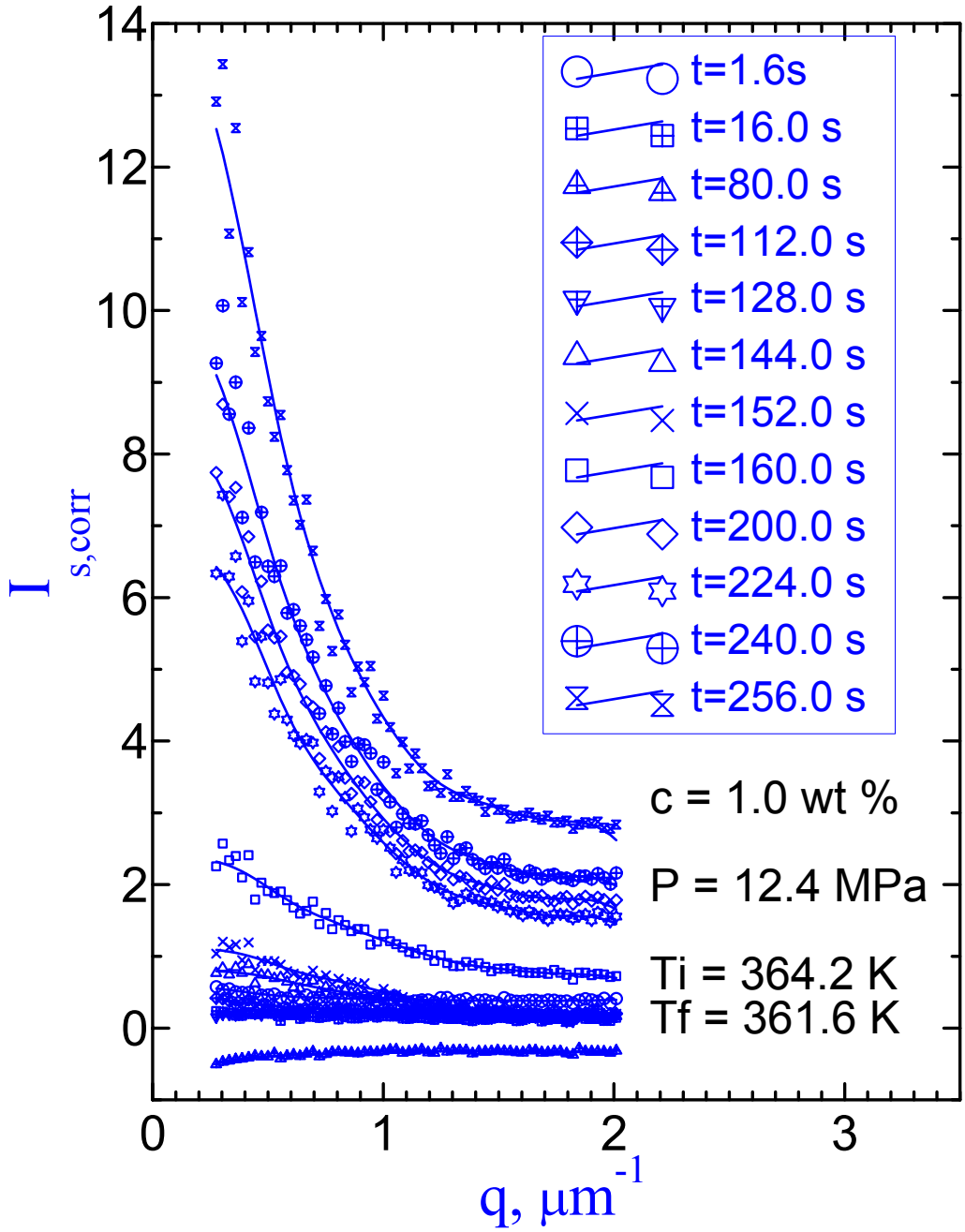

Figure 6.2. Variation of the corrected scattered light intensity $I_{s,\,corr}(q,t)$ versus wave number q at selected times during constant pressure cooling of 1.0 wt % PE in n-pentane at 12 MPa.

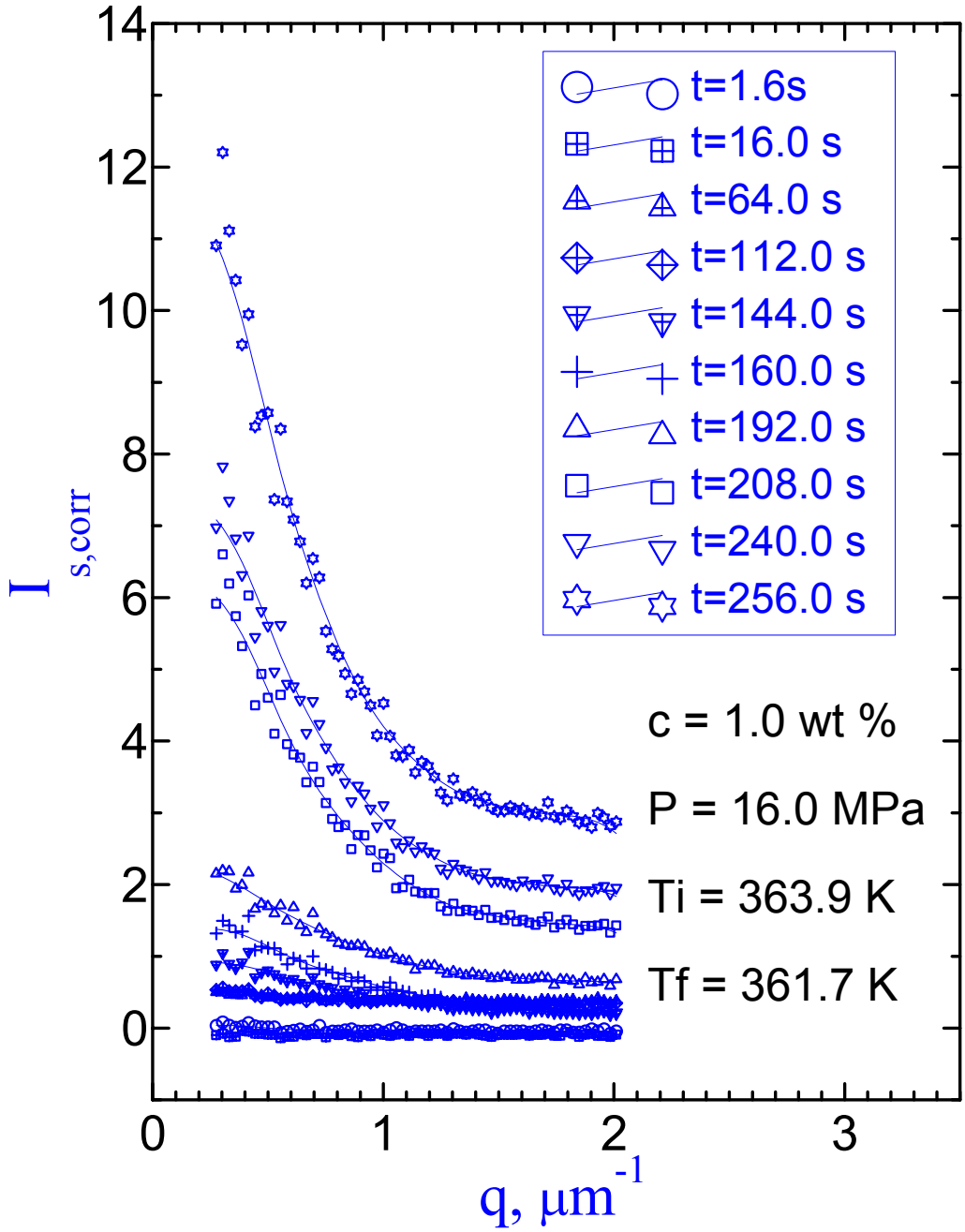

Figure 6.3. Variation of the corrected scattered light intensity $I_{s,\,corr}(q,t)$ versus wave number q at selected times during constant pressure cooling of 1.0 wt % PE in n-pentane at 16 MPa.

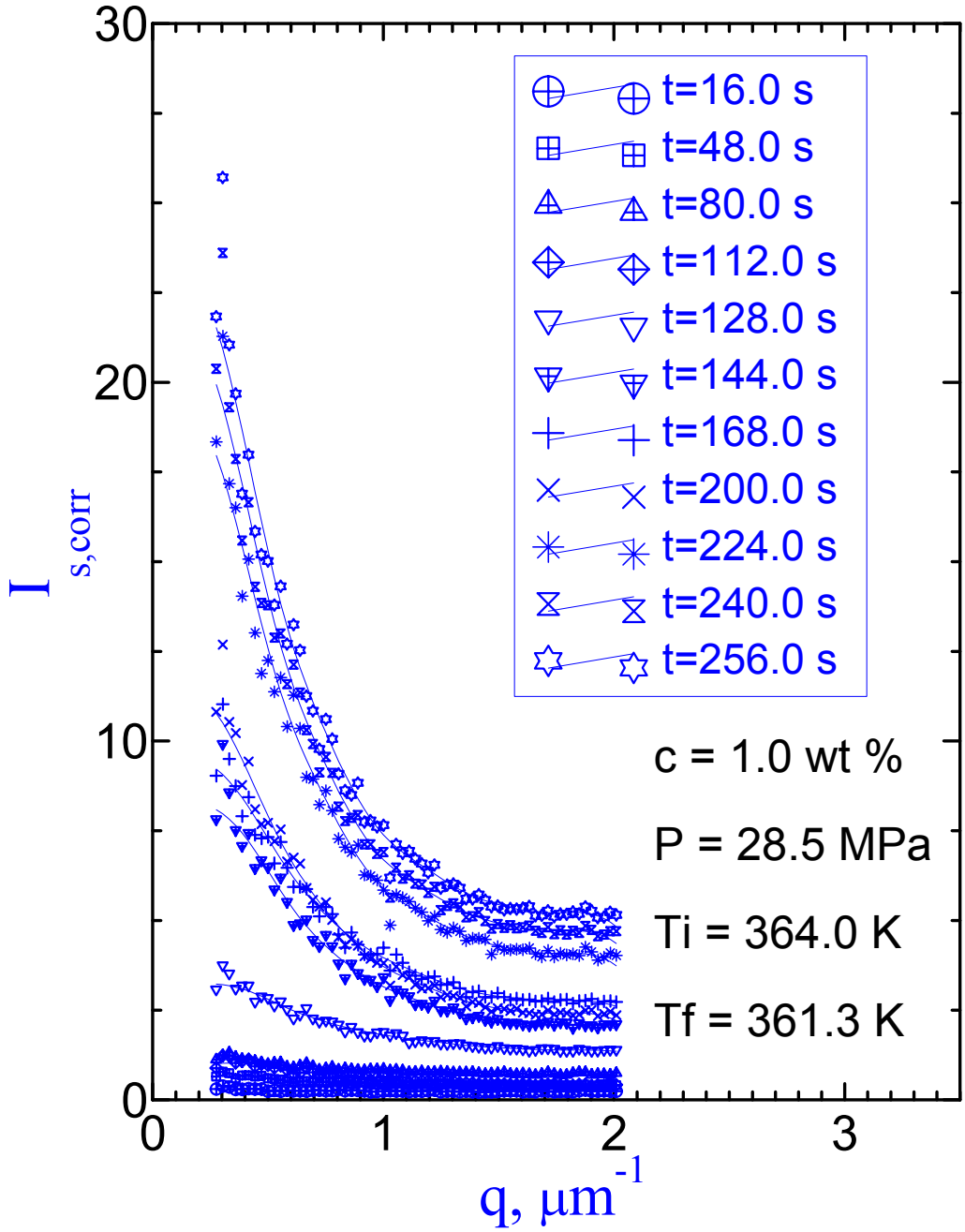

Figure 6.4. Variation of the corrected scattered light intensity $I_{s,\,corr}(q,t)$ versus wave number q at selected times during constant pressure cooling of 1.0 wt % PE in n-pentane at 28.5 MPa.

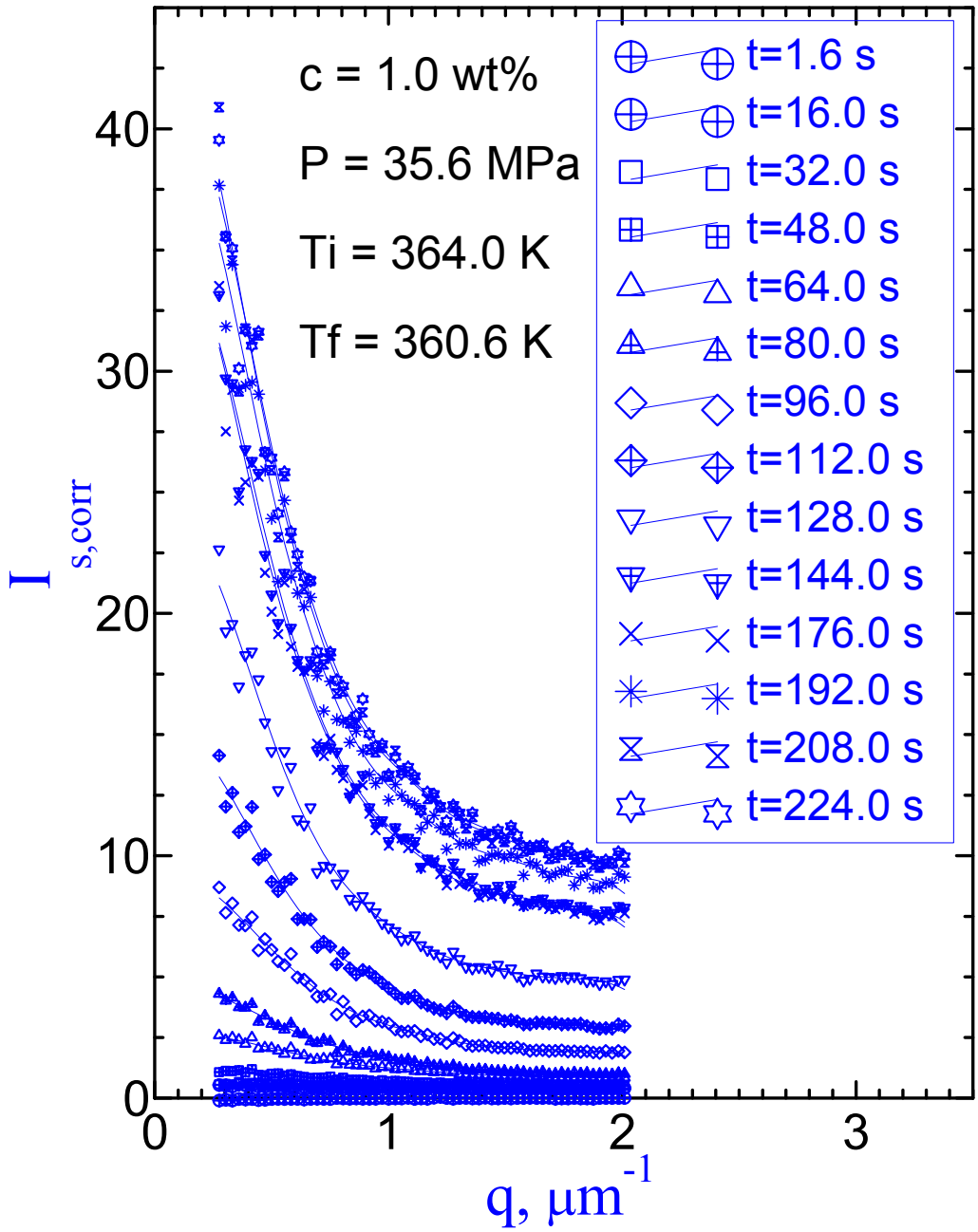

Figure 6.5. Variation of the corrected scattered light intensity $I_{s,\,corr}(q,t)$ versus wave number q at selected times during constant pressure cooling of 1.0 wt % PE in n-pentane at 36 MPa.

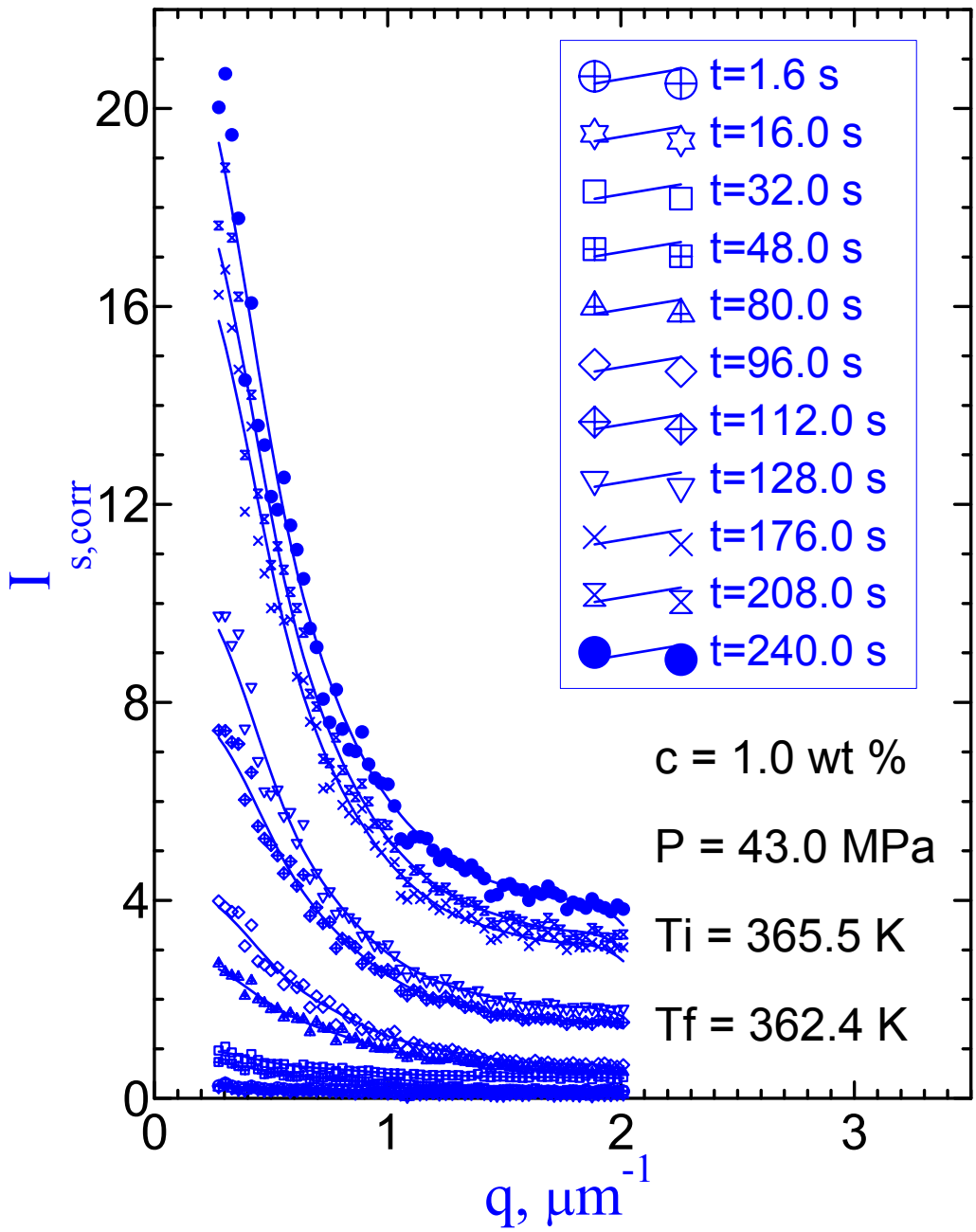

Figure 6.6. Variation of the corrected scattered light intensity $I_{s,\,corr}(q,t)$ versus wave number q at selected times during constant pressure cooling of 1.0 wt % PE in n-pentane at 43 MPa.

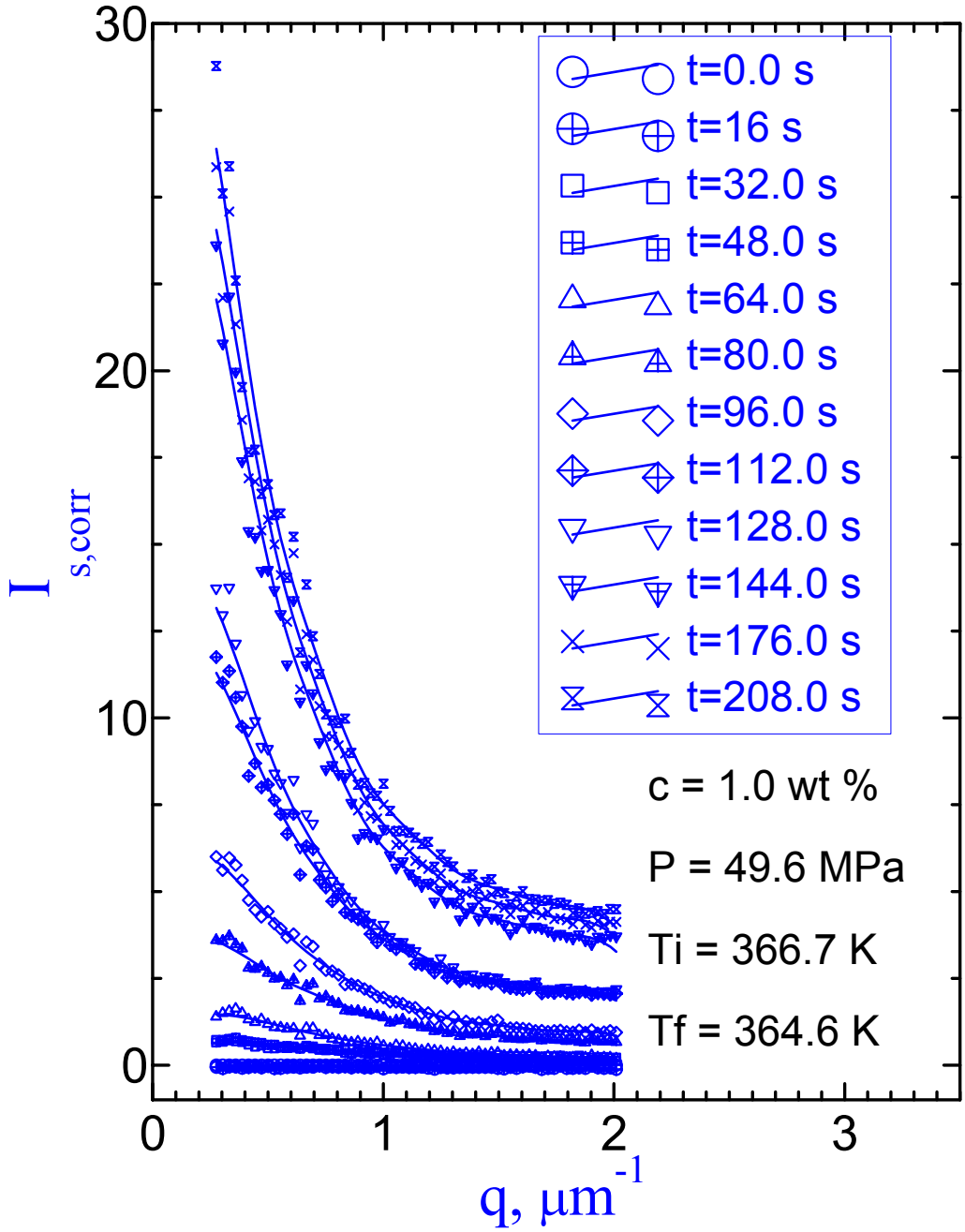

Figure 6.7. Variation of the corrected scattered light intensity $I_{s,\,corr}(q,t)$ versus wave number q at selected times during constant pressure cooling of 1.0 wt % PE in n-pentane at 50 MPa.

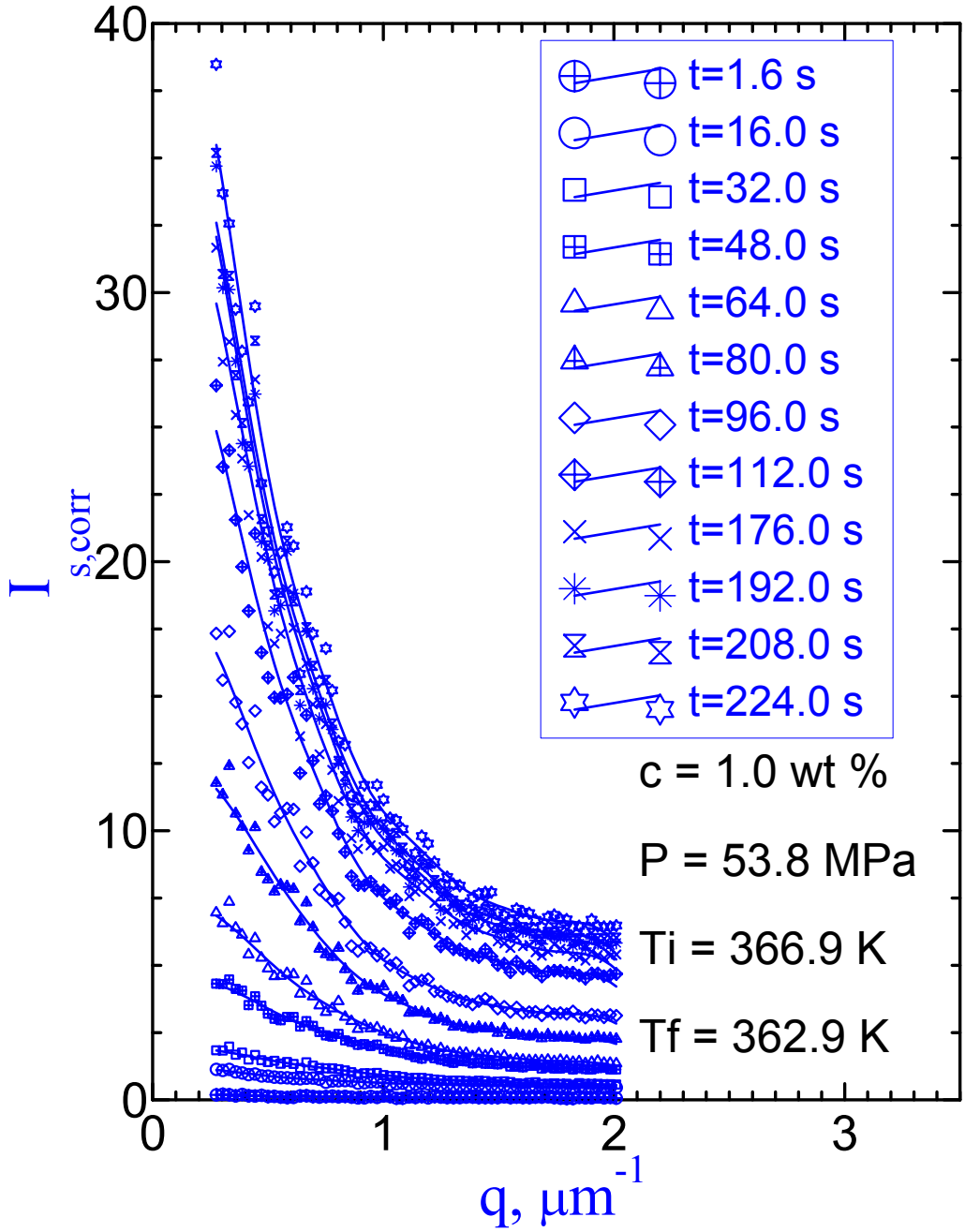

Figure 6.8. Variation of the corrected scattered light intensity $I_{s,\,corr}(q,t)$ versus wave number q at selected times during constant pressure cooling of 1.0 wt % PE in n-pentane at 54 MPa.

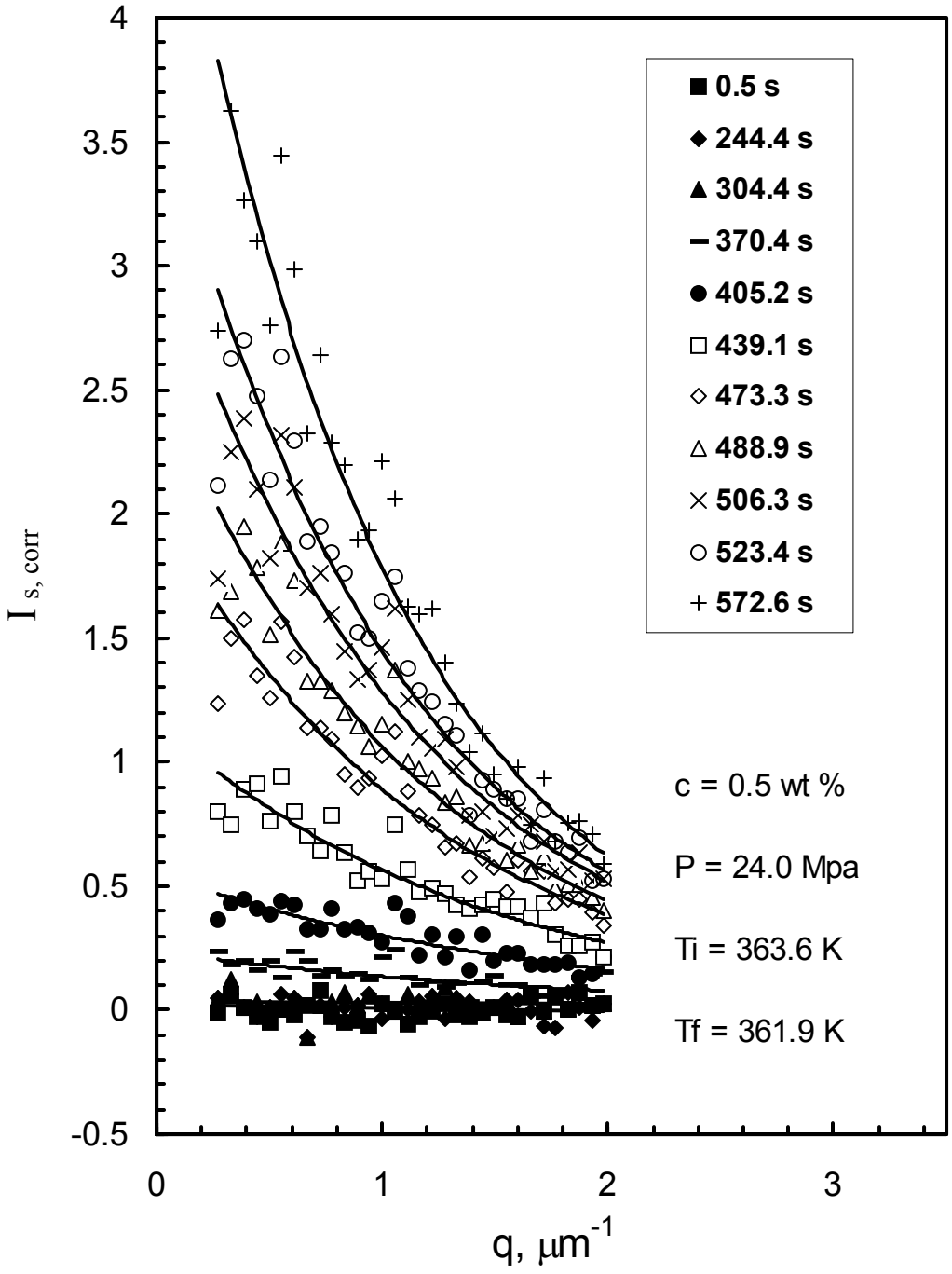

Figure 6.9. Variation of the corrected scattered light intensity $I_{s,\,corr}(q,t)$ versus wave number q at selected times during constant pressure cooling of 0.5 wt % PE in n-pentane at 24 MPa.

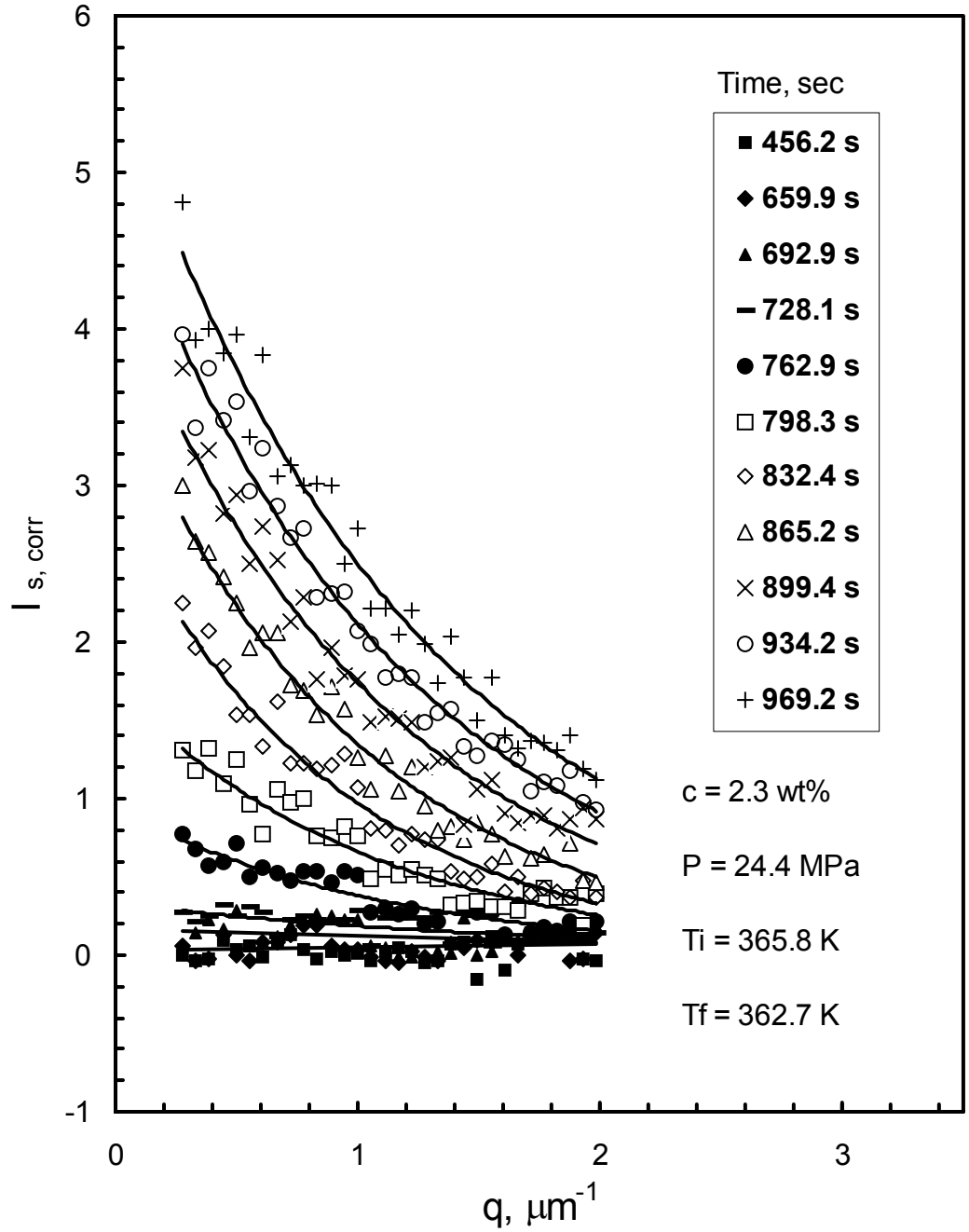

Figure 6.10. Variation of the corrected scattered light intensity $I_{s,\,corr}(q,t)$ versus wave number q at selected times during constant pressure cooling of 2.3 wt % PE in n-pentane at 24 MPa.

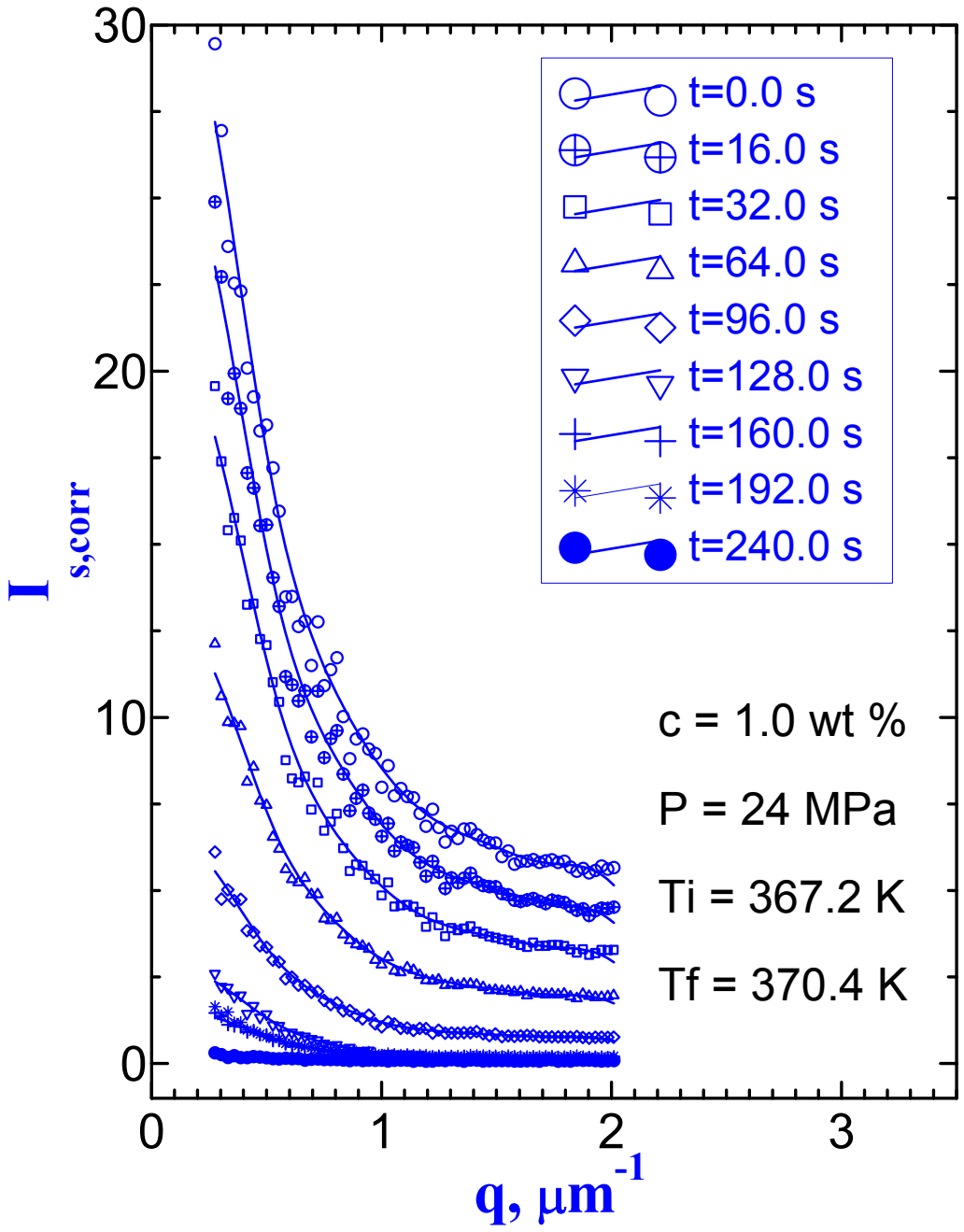

Figure 6.11. Variation of the corrected scattered light intensity $I_{s,\,corr}(q,t)$ versus wave number q at selected times during constant pressure heating of 1.0 wt % PE in n-pentane at 24 MPa.

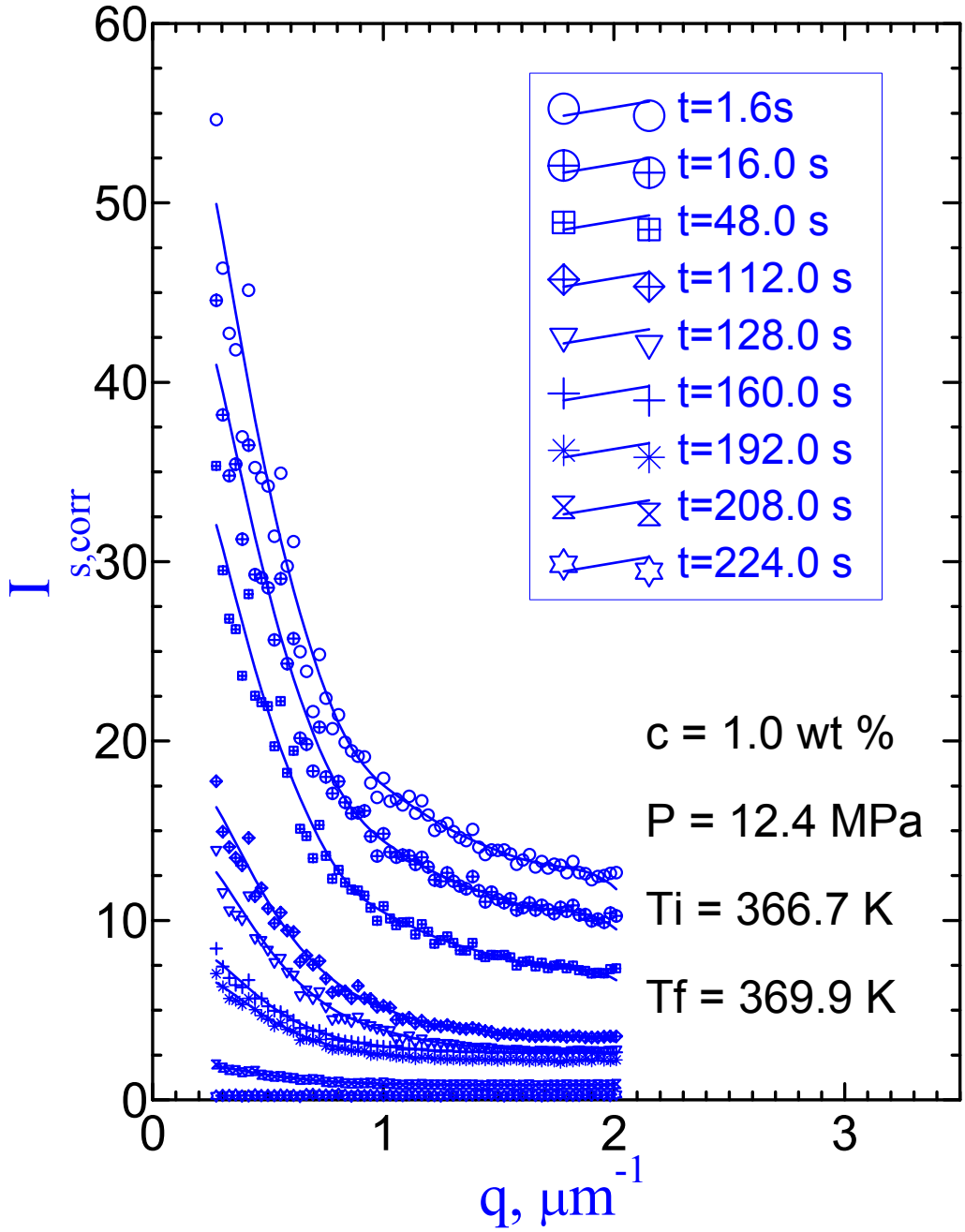

Figure 6.12. Variation of the corrected scattered light intensity $I_{s,\,corr}(q,t)$ versus wave number q at selected times during constant pressure heating of 1.0 wt % PE in n-pentane at 12 MPa.

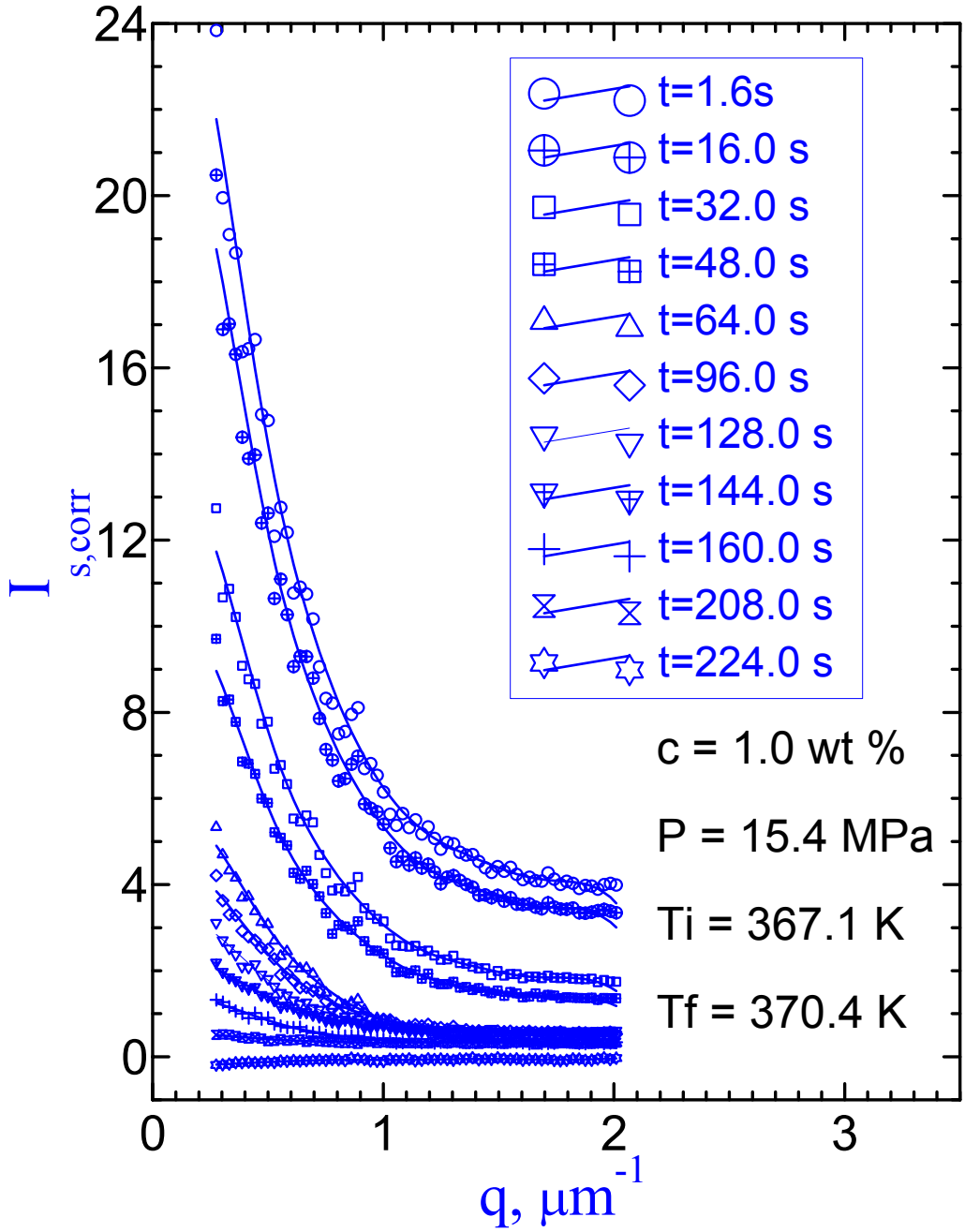

Figure 6.13. Variation of the corrected scattered light intensity $I_{s,\,corr}(q,t)$ versus wave number q at selected times during constant pressure heating of 1.0 wt % PE in n-pentane at 15 MPa.

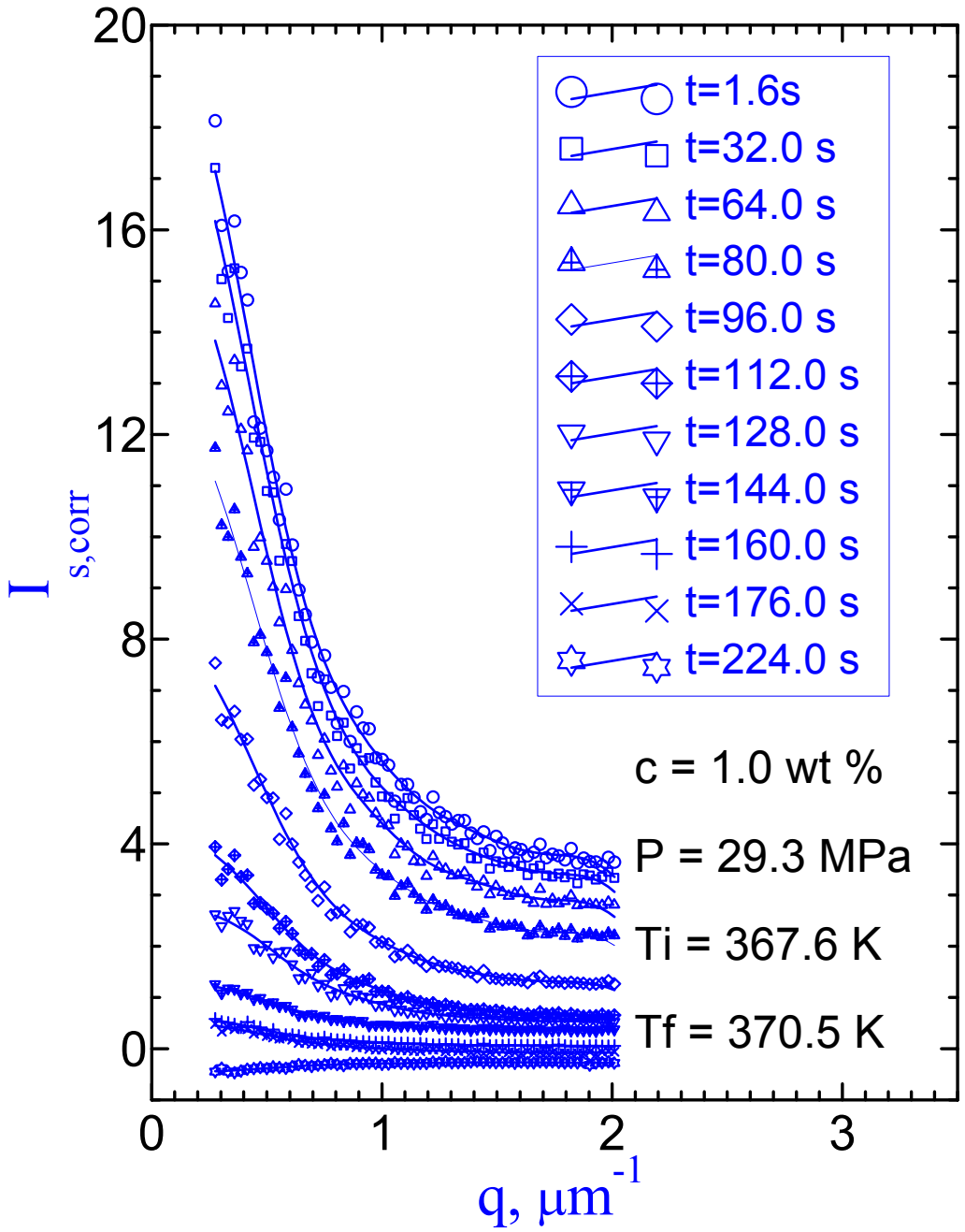

Figure 6.14. Variation of the corrected scattered light intensity $I_{s,\,corr}(q,t)$ versus wave number q at selected times during constant pressure heating of 1.0 wt % PE in n-pentane at 29 MPa.

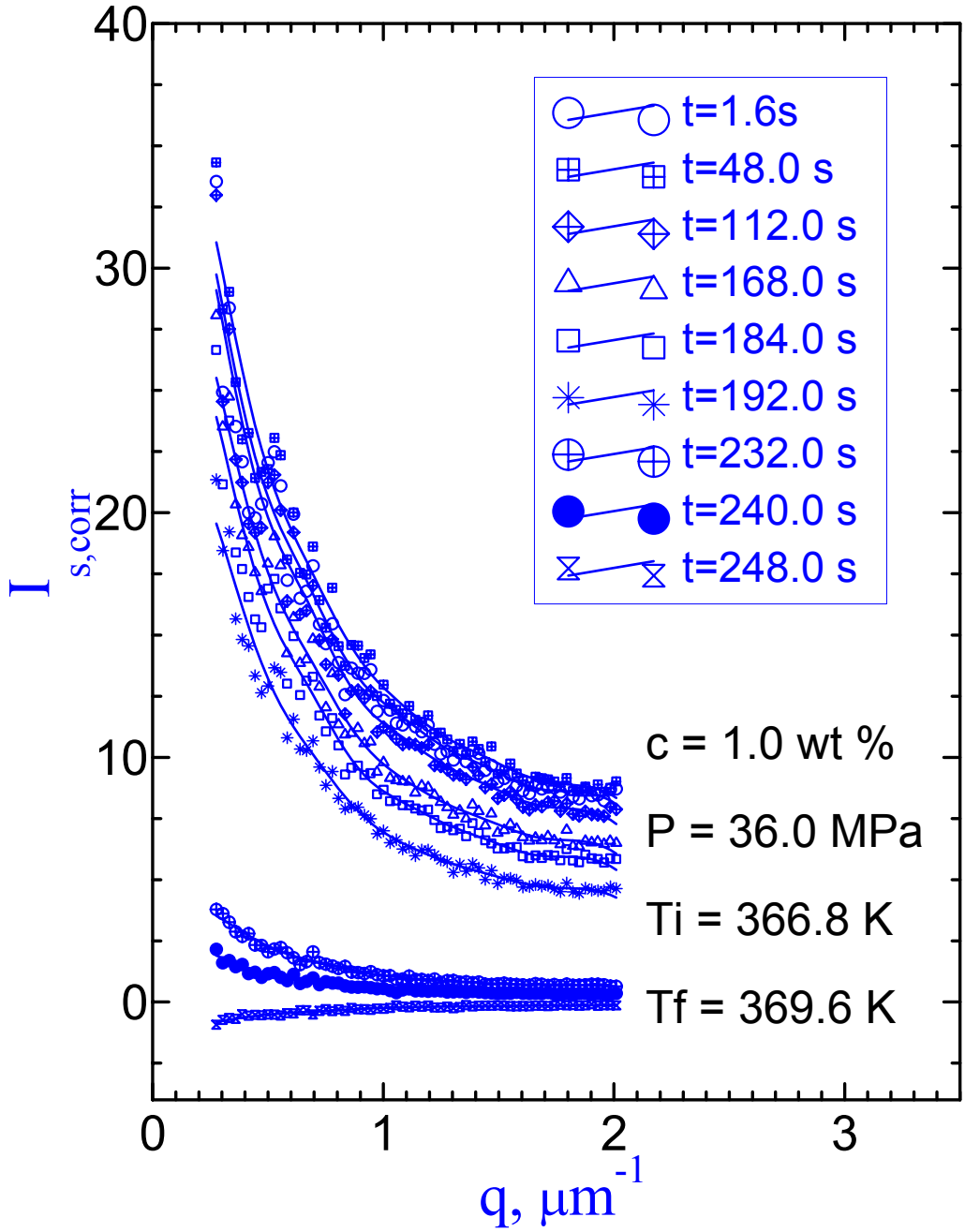

Figure 6.15. Variation of the corrected scattered light intensity $I_{s,\,corr}(q,t)$ versus wave number q at selected times during constant pressure heating of 1.0 wt % PE in n-pentane at 36 MPa.

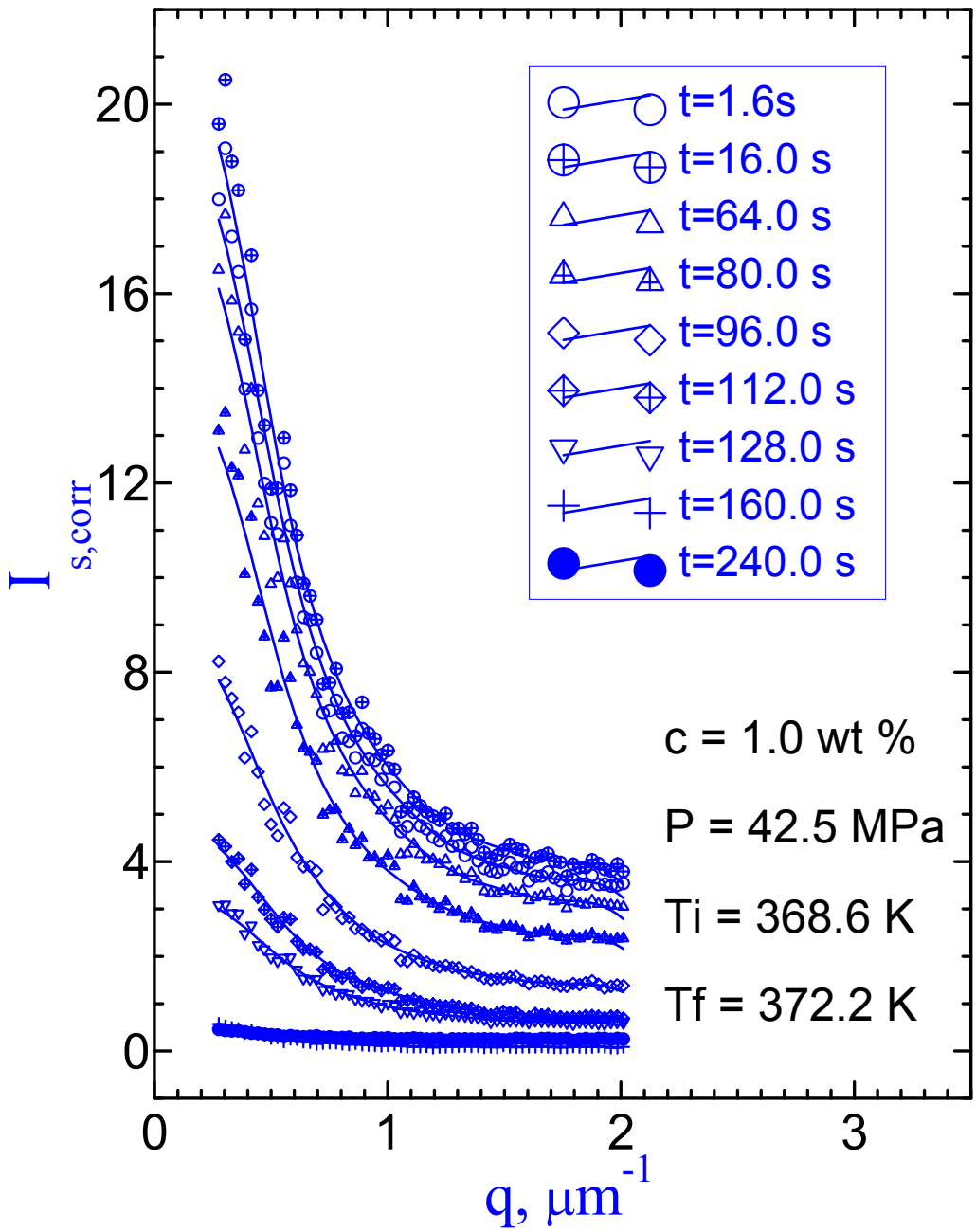

Figure 6.16. Variation of the corrected scattered light intensity $I_{s,\,corr}(q,t)$ versus wave number q at selected times during constant pressure heating of 1.0 wt % PE in n-pentane at 42.5 MPa.

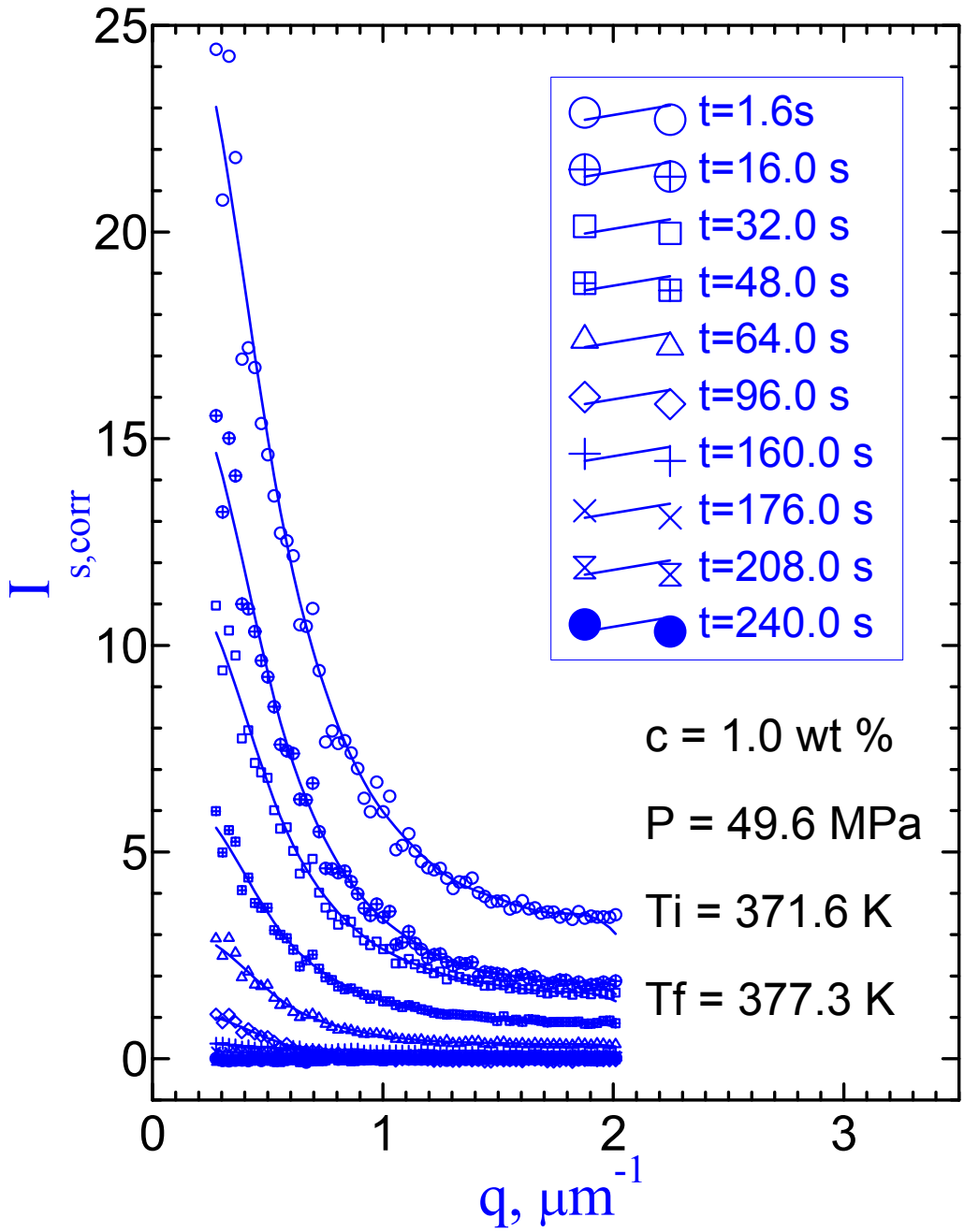

Figure 6.17. Variation of the corrected scattered light intensity $I_{s,\,corr}(q,t)$ versus wave number q at selected times during constant pressure heating of 1.0 wt % PE in n-pentane at 49.6 MPa.

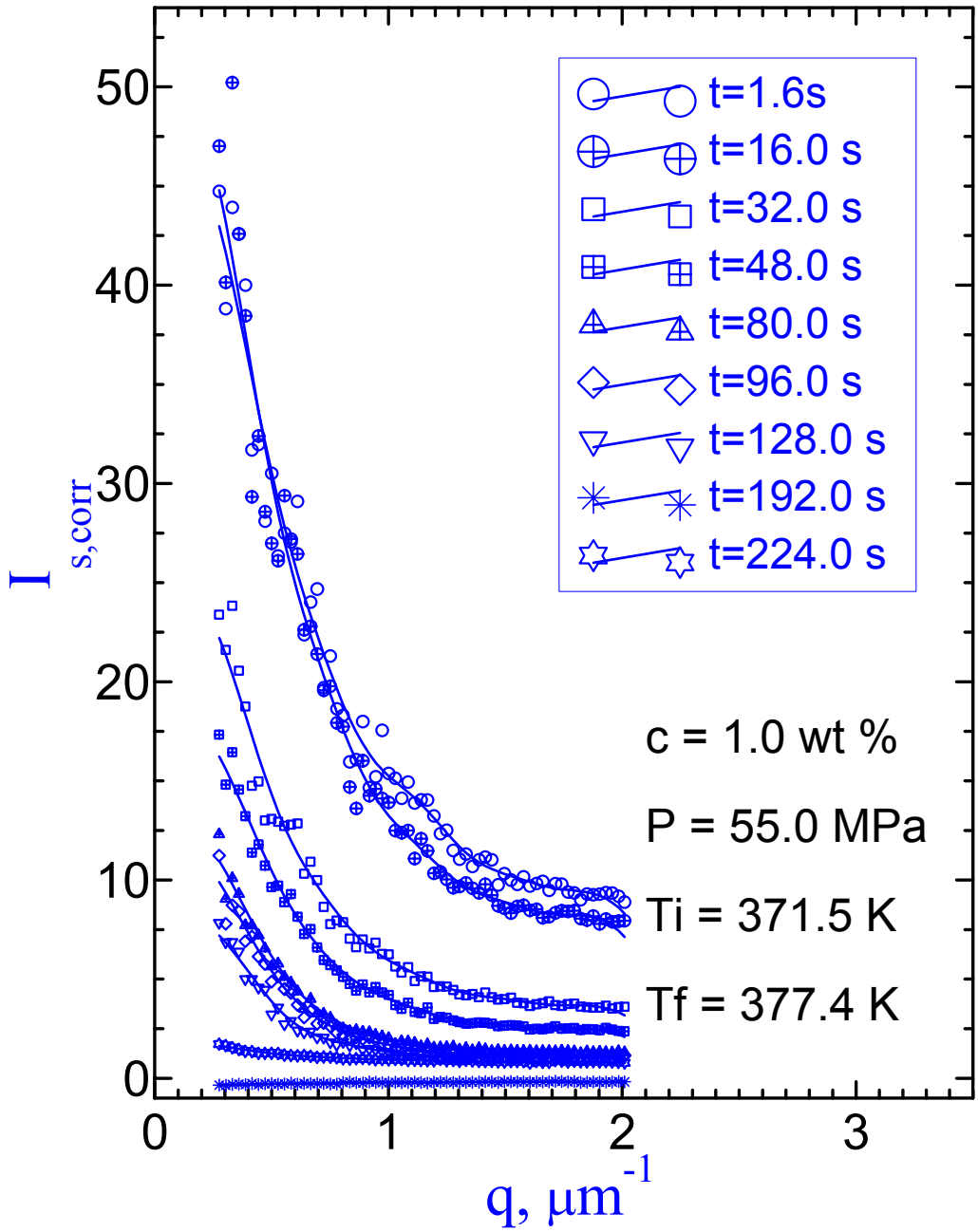

Figure 6.18. Variation of the corrected scattered light intensity $I_{s,\,corr}(q,t)$ versus wave number q at selected times during constant pressure heating of 1.0 wt % PE in n-pentane at 55 MPa.

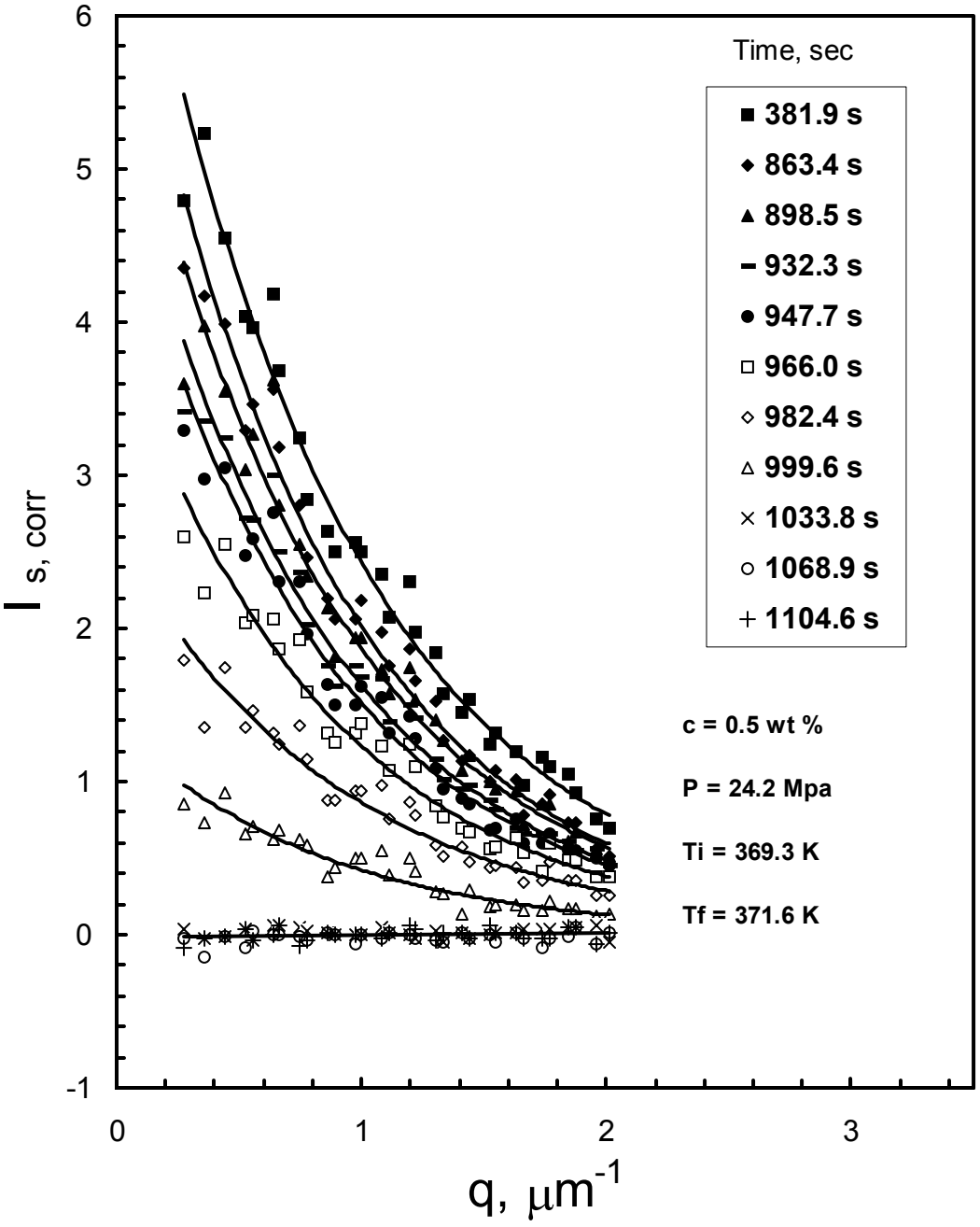

Figure 6.19. Variation of the corrected scattered light intensity $I_{s,\,corr}(q,t)$ versus wave number q at selected times during constant pressure heating of 0.5 wt % PE in n-pentane at 24 MPa.

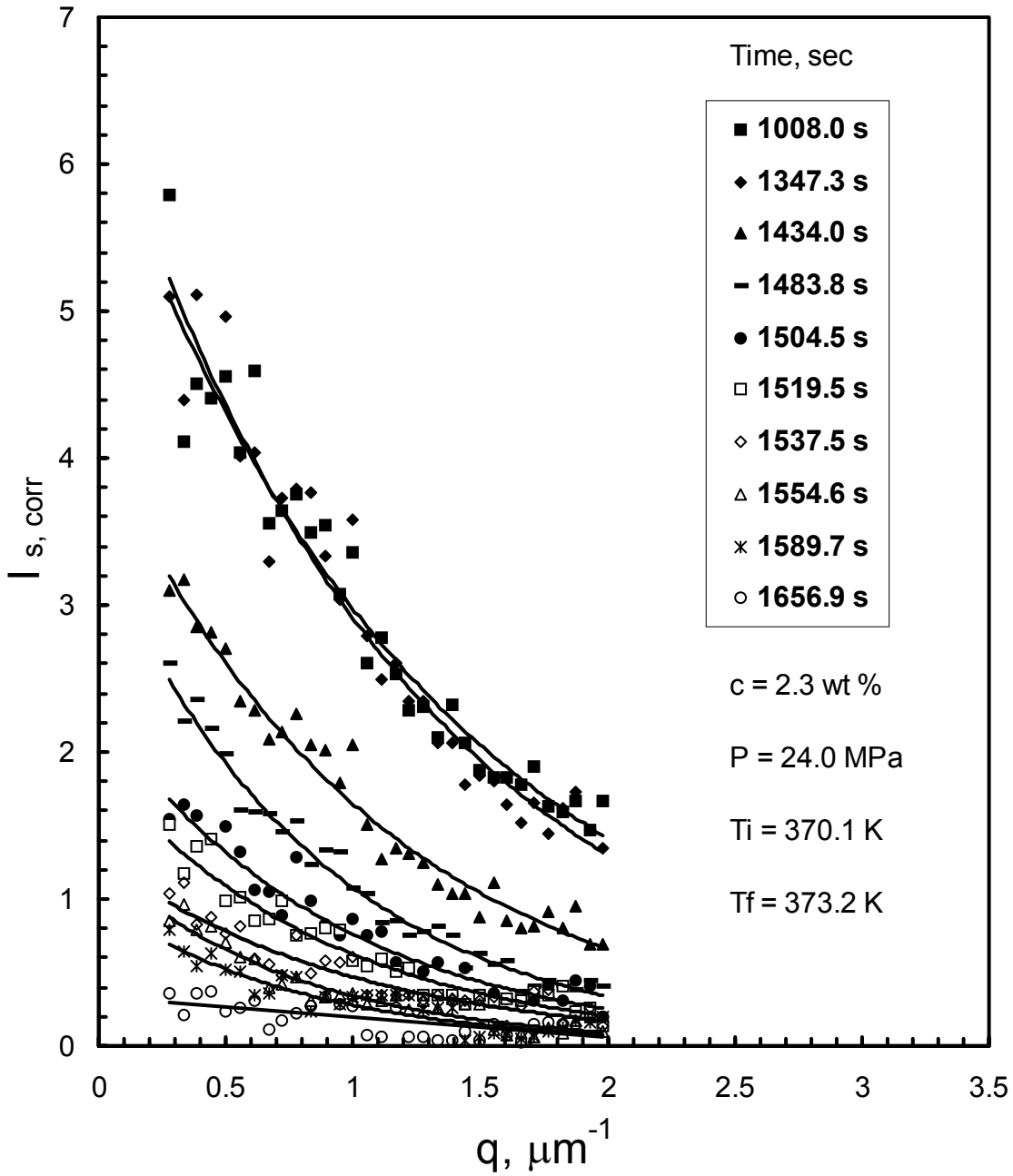

Figure 6.20. Variation of the corrected scattered light intensity $I_{s,\,corr}(q,t)$ versus wave number q at selected times during constant pressure heating of 2.3 wt % PE in n-pentane at 24 MPa.

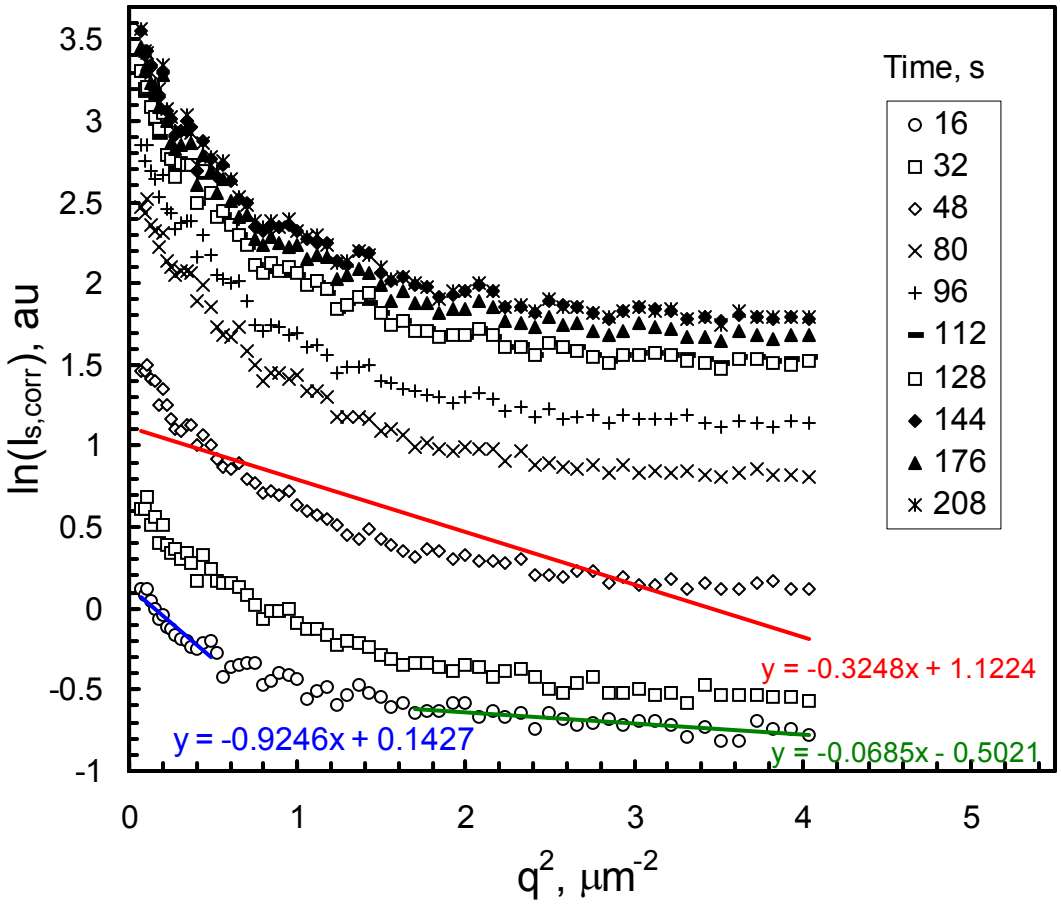

Figure 6.21. The evolution of the corrected scattered light intensities Ln(Is,corr) with time as a function of q^2 corresponding to data in Figure 6.1.

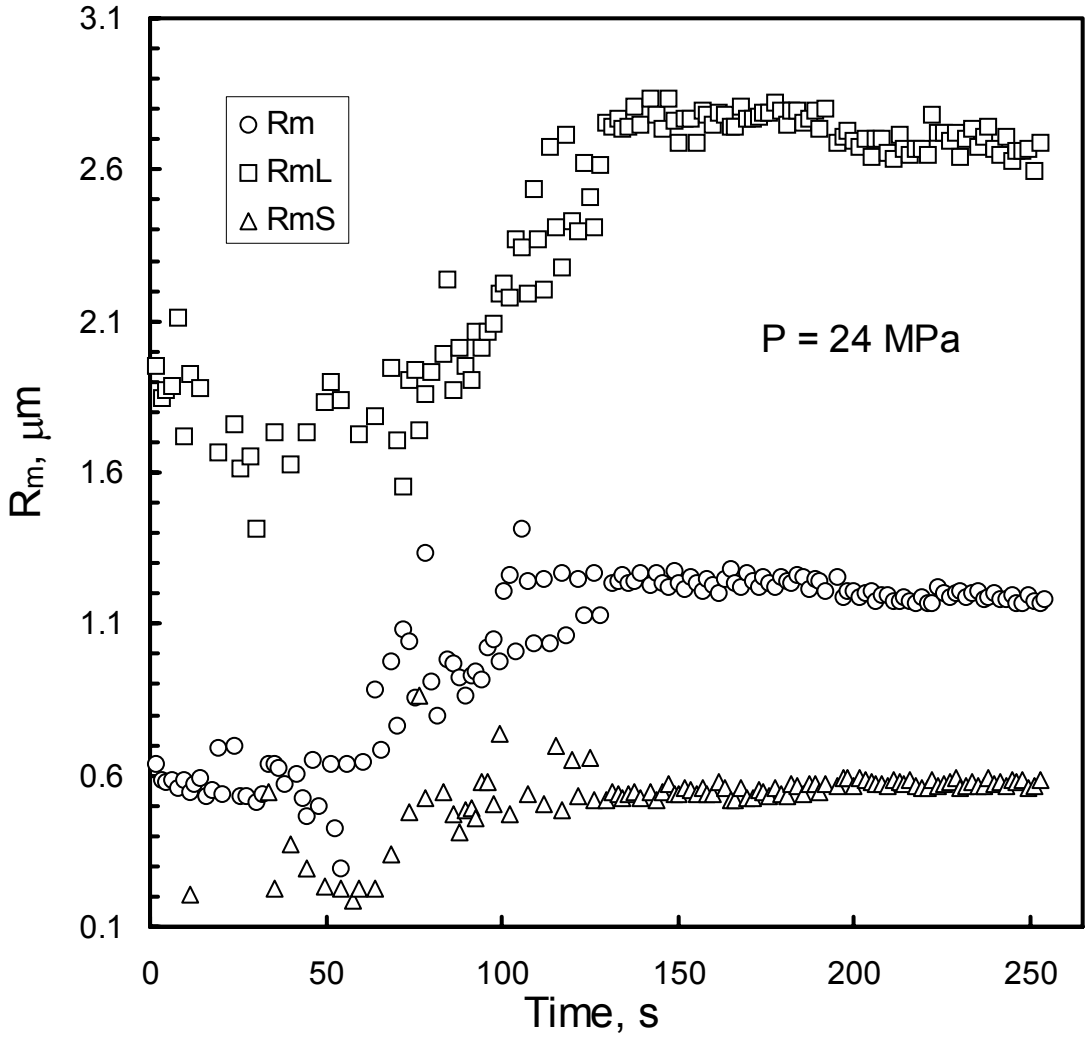

Figure 6.22. Evolution of the mean radii of particles during cooling process for 1.0 wt % solution at 23 MPa. R_m: overall mean radius determined from all scattering data; R_{mS}: mean particle radius determined using only scattering data at large wave numbers; R_{mL}: mean particle radius determined using only scattering data at small wave numbers.

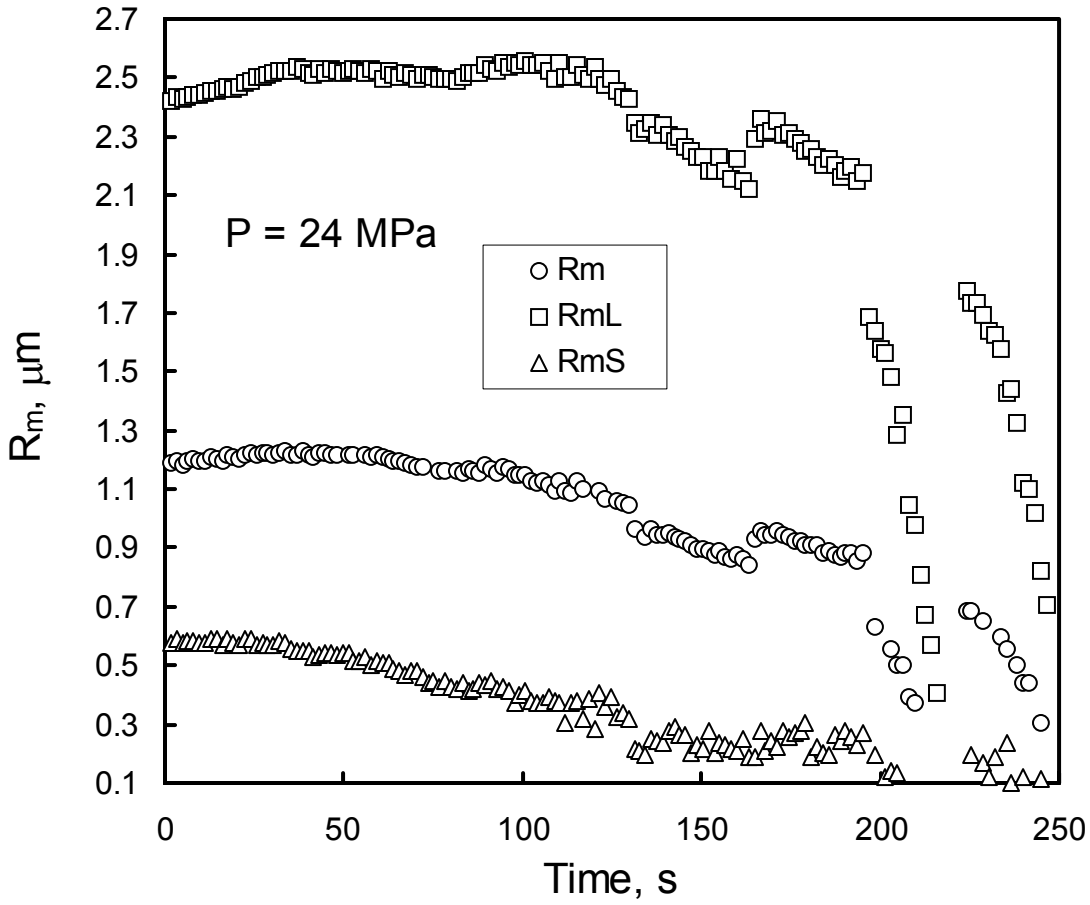

Figure 6.23. Evolution of the mean radii of particles during melting process for 1.0 wt % solution at 23 MPa. R_m: overall mean radius determined from all scattering data; R_{mS}: mean particle radius determined using only scattering data at large wave numbers; R_{mL}: mean particle radius determined using only scattering data at small wave numbers.

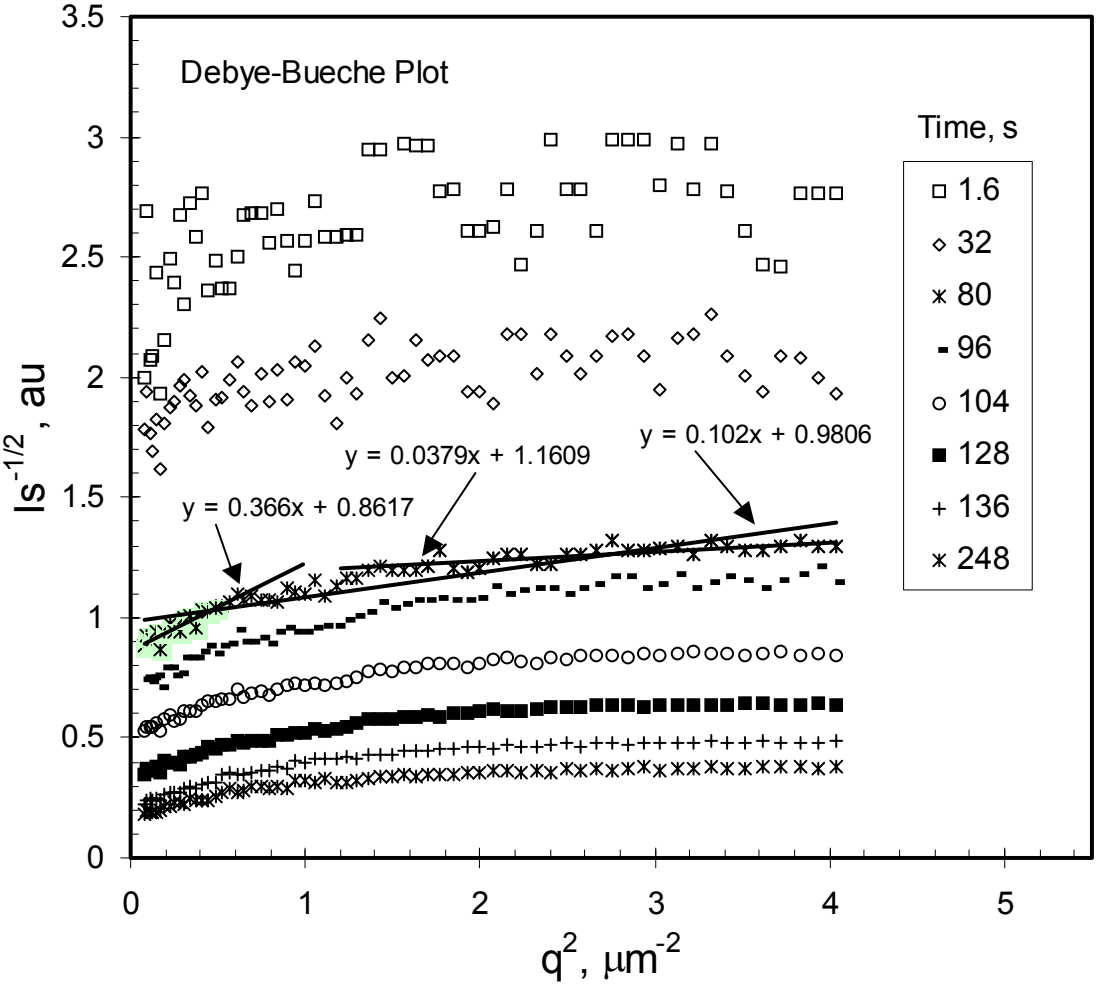

Figure 6.24. Debye-Bueche plot for 1.0 wt % PE in n-pentane at 23 MPa during constant pressure cooling process. The original data are shown in Figure 6.1.

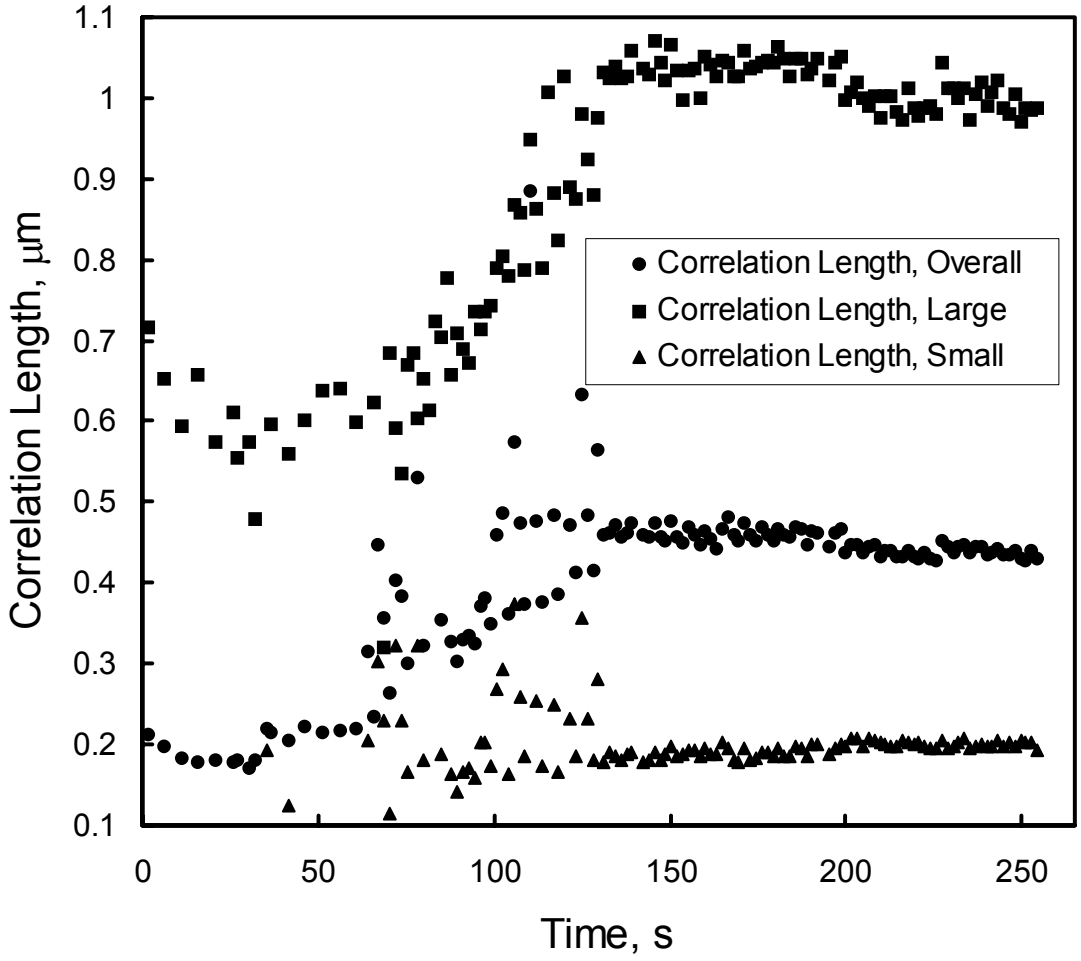

Figure 6.25. Correlation length calculated from Debye-Bueche plots as shown in Figure 6.24 for 1.0 wt % PE in n-pentane at 24 MPa during constant pressure cooling process.

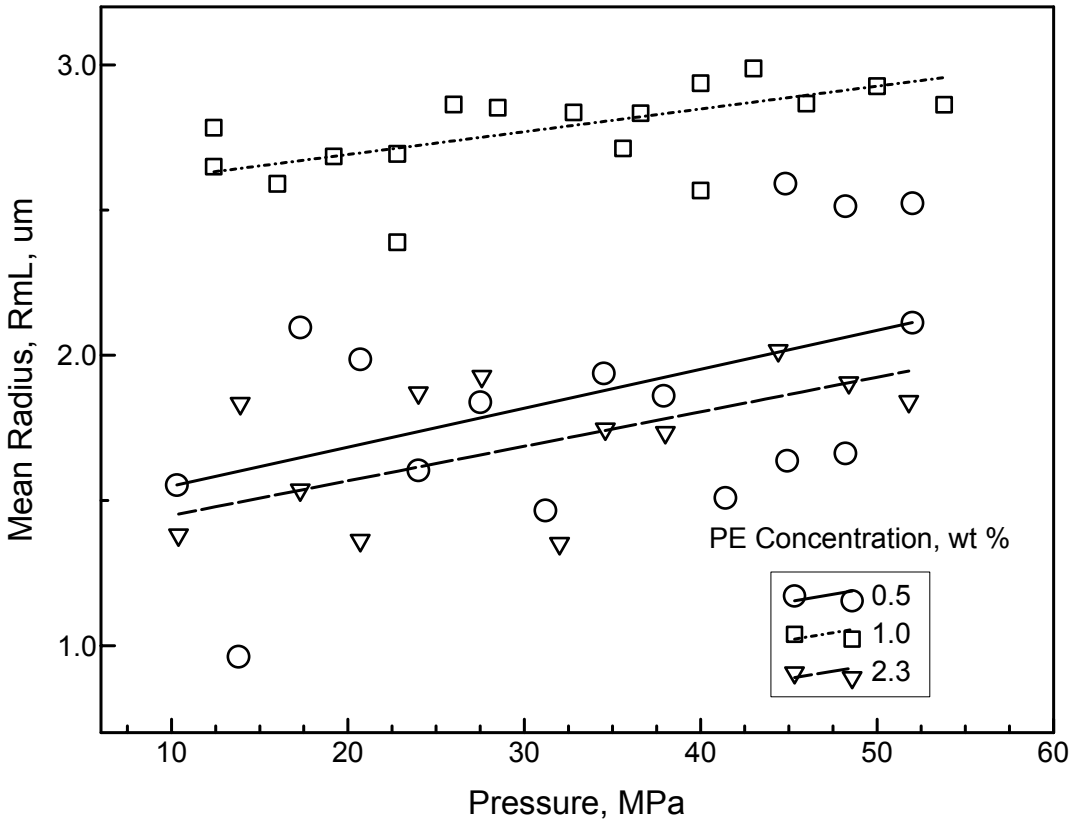

Figure 6.26. Variation of the equilibrium mean particle radius R_{mL} with crystallization pressure for PE solutions in n-pentane with 0.5, 1.0, 2.3 wt %, respectively.

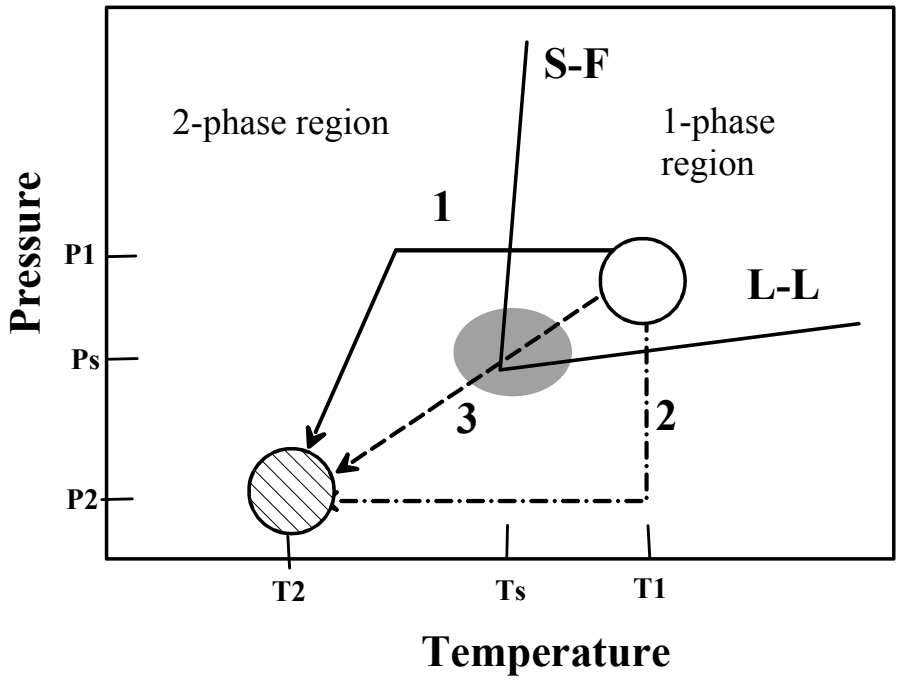

Figure 6.27. Schematic P-T diagram of the phase separation routes from homogenous region at P1 and T1 to the sample collection state P2 and T2. Route 1: constant pressure cooling followed by depressurization process. Route 2: depressurization first and followed by cooling process. Route 3: controlled cooling and pressure reduction process. S-F: solid-fluid phase boundary. L-L: liquid-liquid phase boundary. Open circle: the beginning state. Filled circle: the sample collection state.

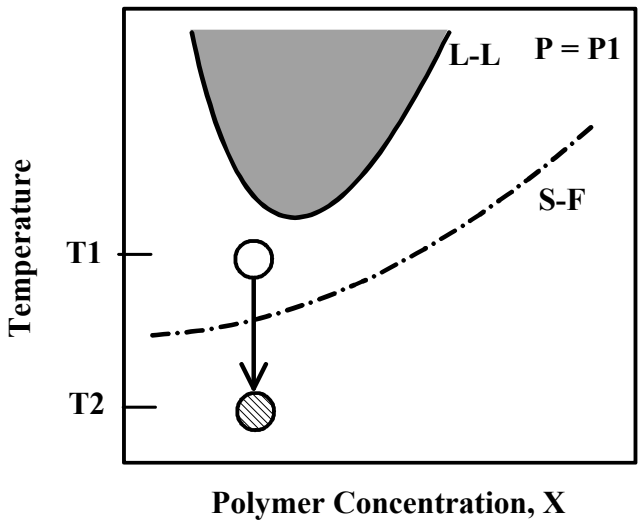

Figure 6.28. Schematic T-X phase diagram for Route 1 (Figure 6.27), constant pressure cooling (P = P1) followed by a depressurization process. S-F: solid-fluid phase boundary. The system shows LCST type of L-L phase boundary. Initially solution is homogenous at T = T1. The arrow shows the phase separation path (see Figure 2.3 e).

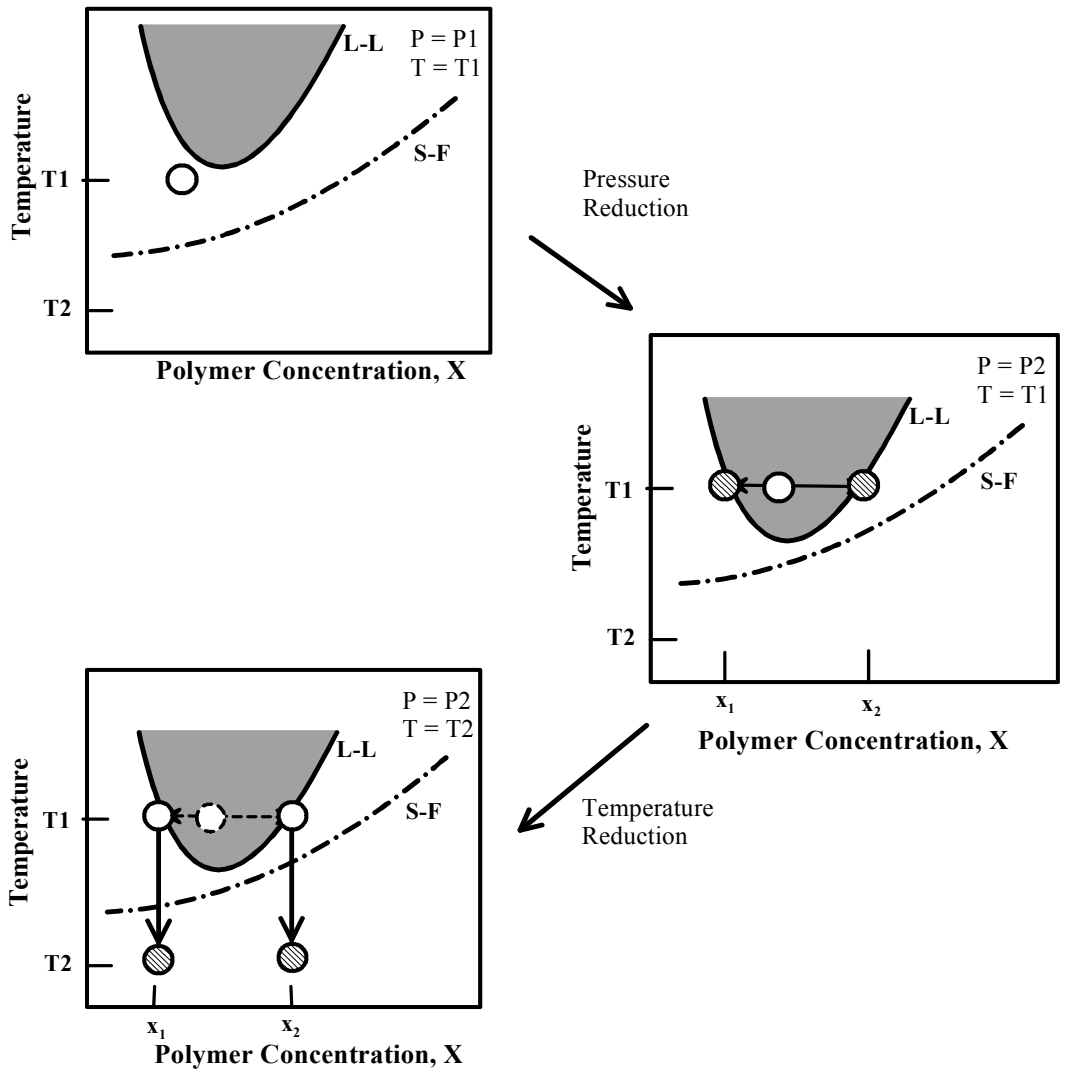

Figure 6.29. Schematic T-X phase diagram for Route 2 (Figure 6.27), depressurization first and followed by cooling process. The top diagram shows the state before pressure quench. With reduction of P at constant T, LCST phase boundary moves and the initially homogenous solution undergoes L-L phase separation with equilibrium phase composition of x1 and x2 for polymer-lean and polymer-rich phase. The middle diagram shows the state after pressure quench but before the cooling process. In the cooling step (the bottom diagram) that follows, polymer-rich and polymer-lean phases cross the S-F boundary, which lead to different particle size and morphology. Bonnett et al. (2003) reported a similar figure with a submerged UCST L-L phase boundary.

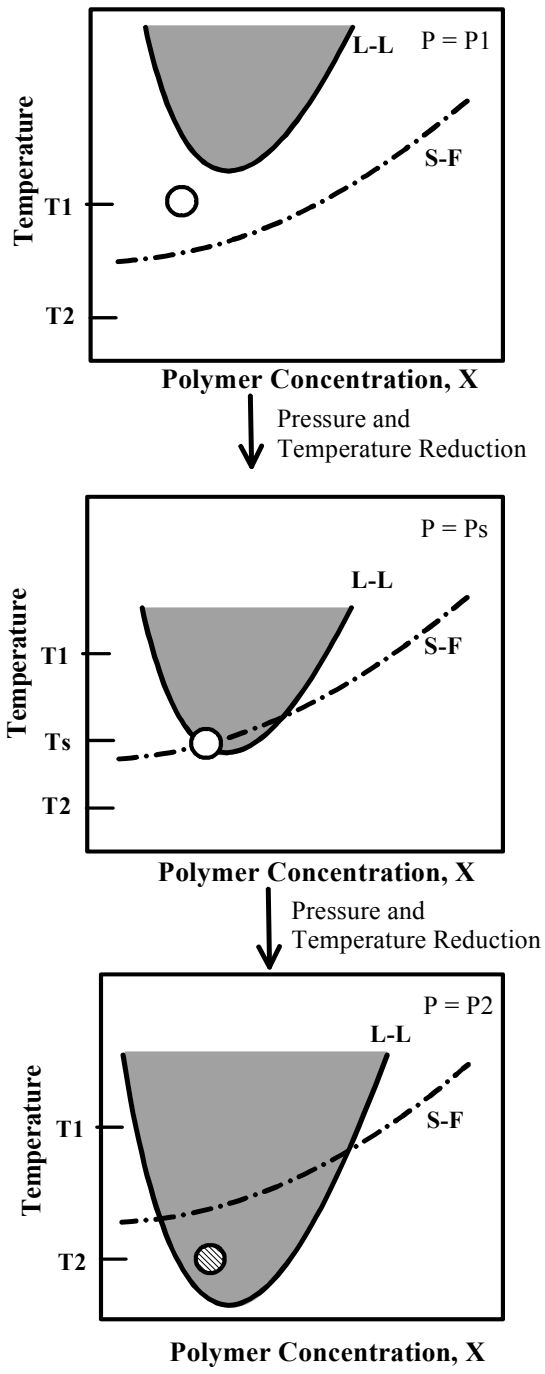

Figure 6.30. Schematic T-X phase diagram for Route 3 (Figure 6.27), the controlled cooling and pressure reduction process. The upper diagram shows the beginning state at T1 and P1. The middle curve shows the state in the shaded region of Figure 6.27 at Ts and Ps. The lower diagram shows the sample collection state at P2 and T2.

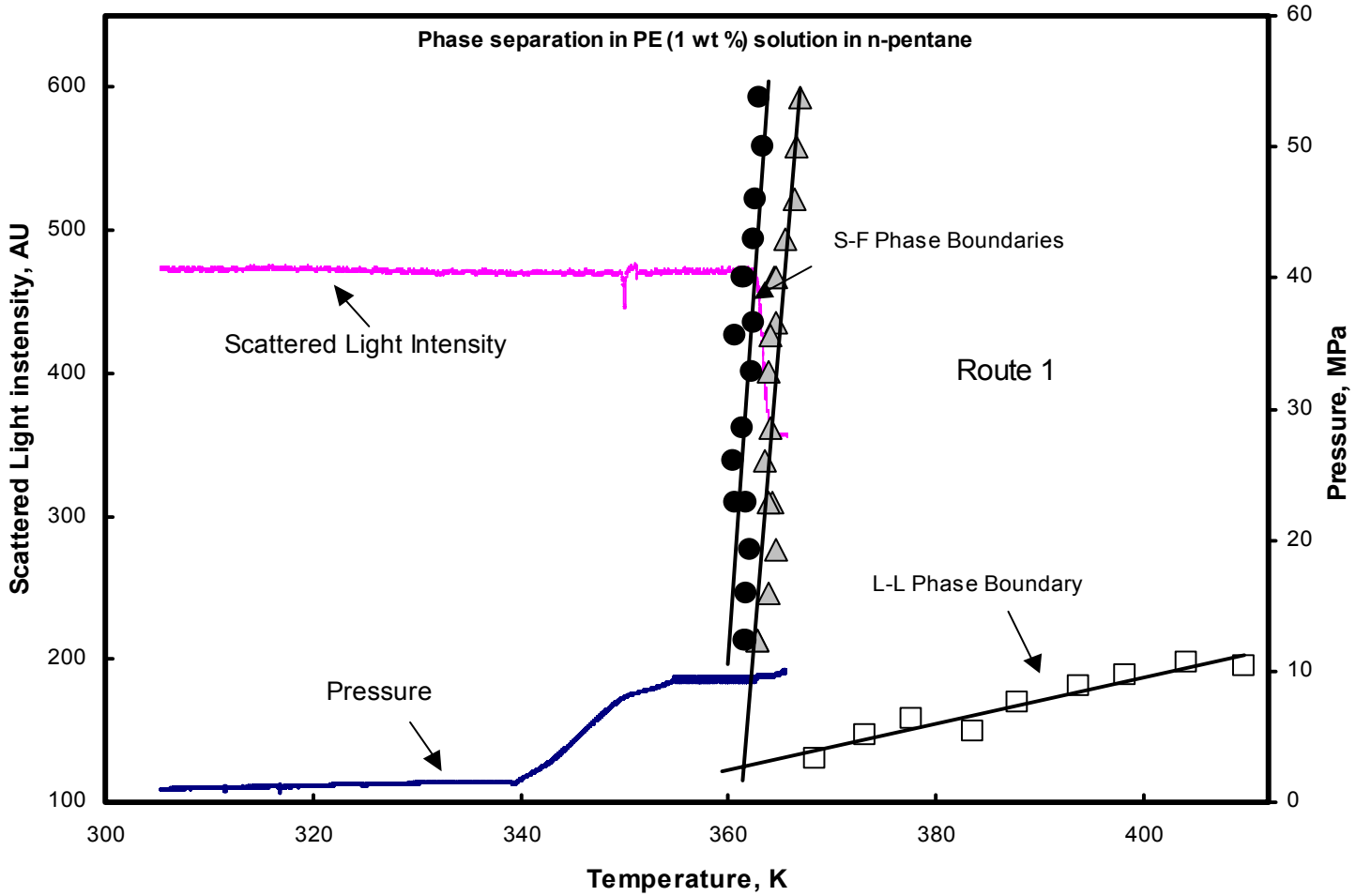

Figure 6.31. The phase separation process of route 1 followed by light scattering experiment of 1 wt % PE solution in n-pentane from 365 K to 305 K.

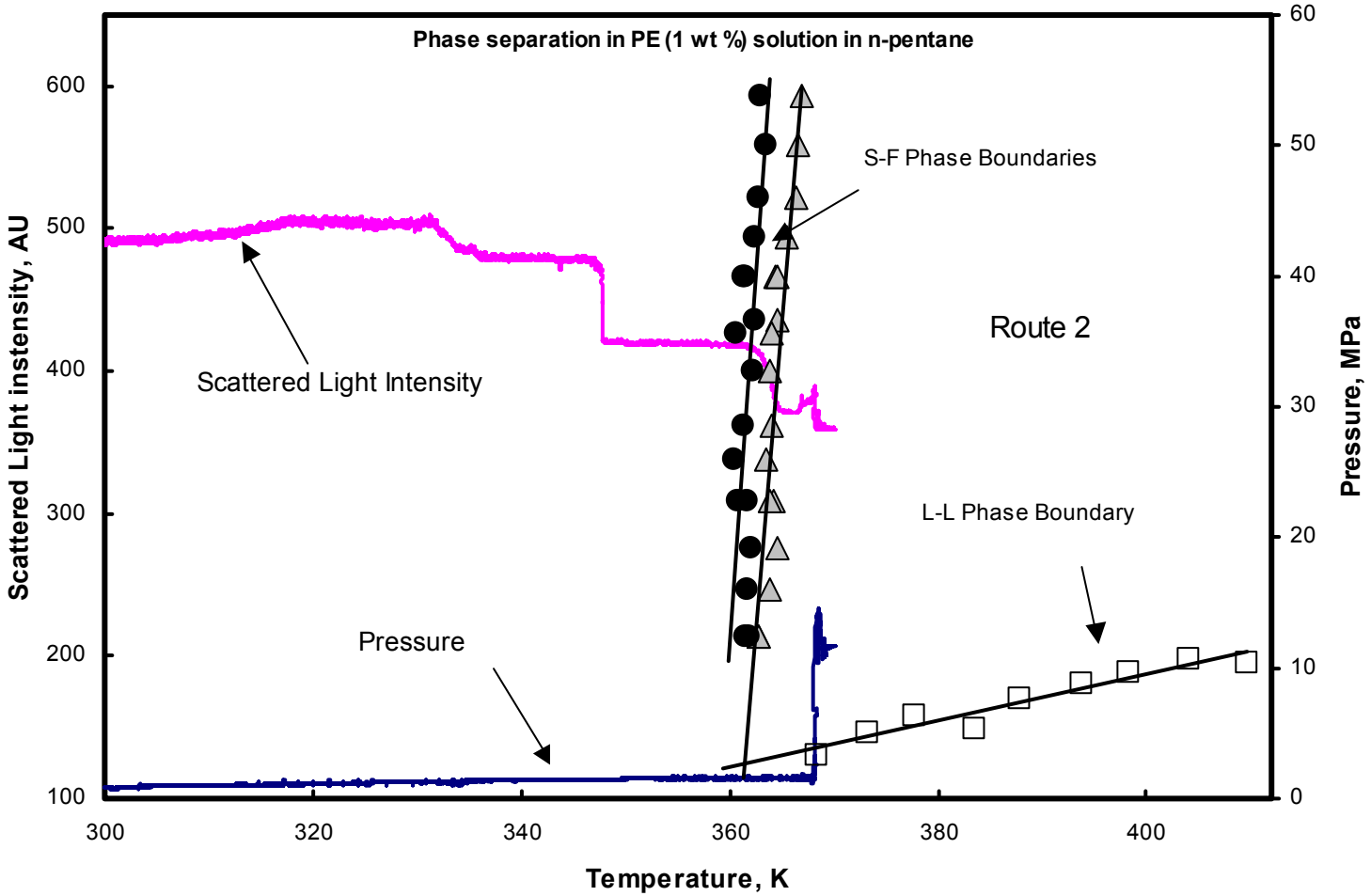

Figure 6.32. The phase separation process of route 2 followed by light scattering experiment of 1 wt % PE solution in n-pentane from 369 K to 300 K.

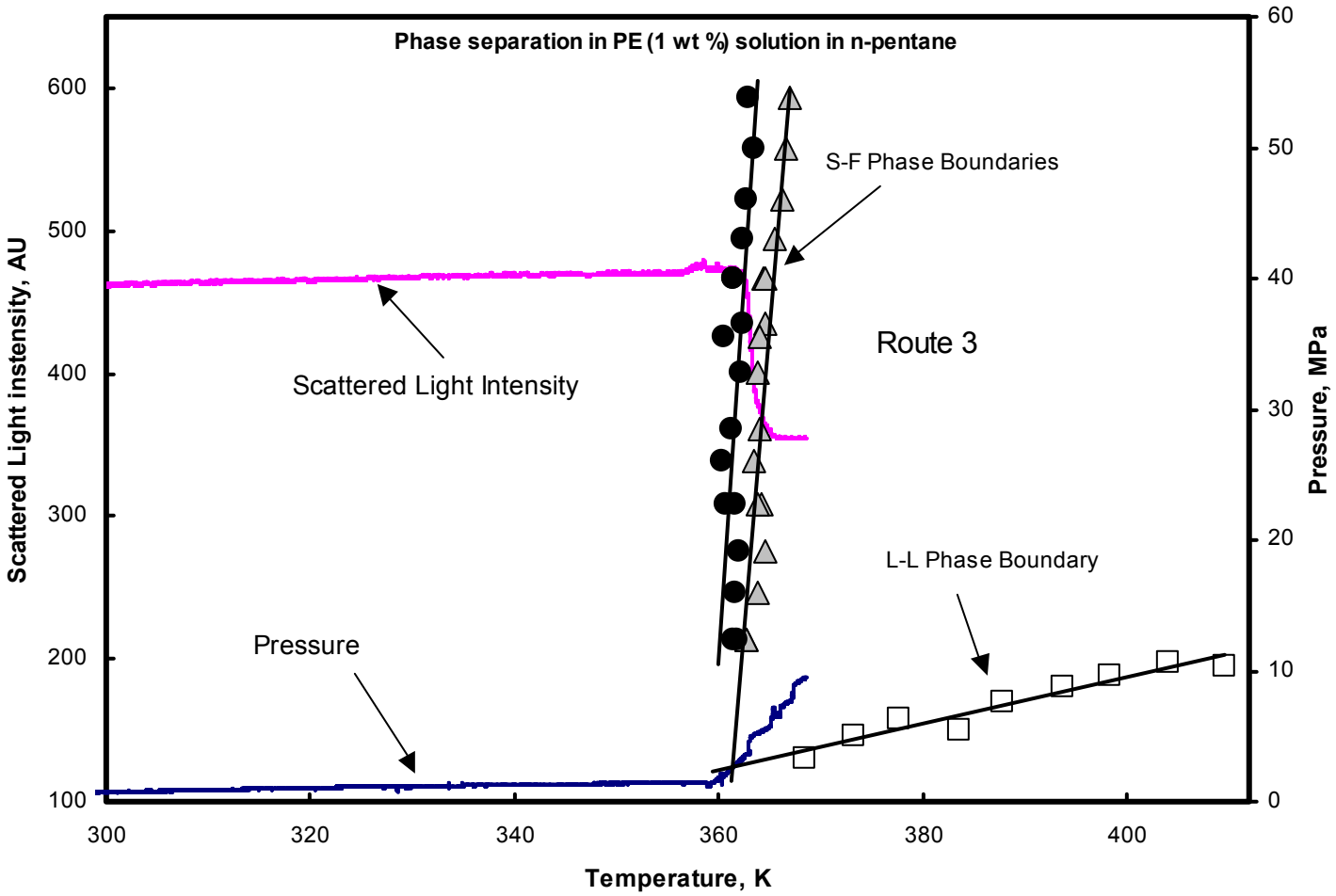

Figure 6.33. The phase separation process of route 3 followed by light scattering experiment of 1 wt % PE solution in n-pentane from 365 K to 300 K.

Chapter 7

Morphology and Thermal Properties of PE Crystals Formed in n-Pentane and n-Pentane + CO_2 Mixtures*

This chapter presents the results on the morphological and thermal properties PE samples crystallized in n-pentane or n-pentane + CO_2 mixtures. Figure 7.1 shows the process of the sample collection after constant pressure crystallization. While holding the pressure constant at a selected value, the solution is continually cooled until no further change in the scattered light intensity is observed with the reduction in temperature. Then the system is cooled to room temperature without further adjusting the pressure. Once the room temperature is reached, the system is depressurized to the ambient pressure. The PE crystals are then collected for microscopic and calorimetric characterizations. The PE samples crystallized from 1.0 and 2.3 wt % solutions were collected from the microreactor of the light scattering system after the constant pressure cooling process. The PE samples from 5 wt % solutions were collected from the view cell and the crystallization process was slightly different in that the solutions were held at a temperature below the S-F phase boundary for a certain time. The thermal and morphological properties of the samples collected after the light scattering experiments described in section 6.3 are also included in this chapter. The author has to give special thanks to Mr. Gerd Upper because of the collaborations on some works of this chapter.

**Portion of this chapter has appeared as: "*Upper, G. Beckel, D. Zhang, W., Kiran E. High Pressure Crystallization in Supercritical or Dense Fluids. in *Proceedings of the 6th International Symposium on Supercritical Fluids*, Versailles, France, April 28-30, 2003, Vol. 3 – Materials Processing, pp. 1509-1514."

A Perkin-Elmer Differential Scanning Calorimeter (Model: Diamond) was used to investigate the thermal properties of the collected PE sample. The samples were first heated from 0 ^{o}C to 160 ^{o}C, and then immediately cooled back to 0 ^{o}C, which was then followed by a second heating scan and a cooling scan. Scanning rates were chosen at 10 K/min or 20 K/min. The experiments were carried out in N_2 atmosphere. Prior to calorimetric analysis, the polyethylene samples were decanted and vacuum dried to remove n-pentane. A Leo® 1550 Field Emission Scanning Electron Microscope (FESEM) was used to examine the morphology of the PE particles. The samples were sputter-coated with 6 nm Gold-Platinum layer to reduce the electron charging effects using a Cressington® 208 HR sputter coater. Mr. Stephen McCartney offered help on sample preparation and microscope operation in the FESEM work.

7.1 Thermal Properties

7.1.1 Effect of Pressure

Figure 7.2 shows the DSC scans for the PE particles crystallized and recovered from the 1 wt % PE solution at 45 MPa. The scans are shifted along the y-axis for clarity. Three melting peaks were displayed at 122, 126 and 131 ^{o}C respectively in the first heating scan. The first melting peak appears as a shoulder. The cooling scan shows that there is only one crystallization peak. In the second heating scan, the multiple melting transitions are no longer observed; there is only one melting peak identified at 132 ^{o}C. The second cooling reproduces the first cooling scan extremely well with an identical crystallization peak temperature of 117 ^{o}C. The multiple melting peaks were observed in all the PE crystals formed in n-pentane solution under different pressures. They are

depicted in Figure 7.3 for the crystals obtained from 1 wt % solutions. The first DSC heating scan for the original PE sample is also shown for comparison. All the melting peaks are observed at lower temperatures than that of original PE sample, which was observed at 134 ^{o}C. The shoulder in the multiple melting peaks moves to lower temperatures, from 124 to 122 ^{o}C, as the crystallization pressure is increased. So does the second melting peak. The relative intensity of the melting peaks is observed to change as crystallization pressure changed. At the lowest crystallization pressure explored (14 MPa), the second melting peak is dominant and the appearance of the third peak is more like a shoulder instead of a peak. As the crystallization pressure increases to 23 MPa, the third peak becomes more significant. The intensity of the third melting peak increases further to become even larger than the second peak at the crystallization pressure around 34 MPa. The third melting peak becomes dominant as the crystallization pressure is increased to 45.

The percent crystallinities of these PE crystals are also included in Figure 7.3. They were calculated using the method of Mathot and Pijpers (1983; Upper, 2002). In this method, the heat of fusion ?h(T) is calculated from the area between the melting peak curve and the baseline, which is extrapolated from the heat flux above the melting temperature. Then the $?h(T)$ is divided by a reference value of the heat of fusion $?h'(T)$ for a completely crystalline PE sample at the same temperature. This reference value is calculated from the equation suggested by Mathot and Pijpers:

$$\Delta h'(T) = 293 - 0.3092\times10^{-5}\cdot(414.6-T)^{2}\cdot(414.6+2T) \quad [\mathrm{J/g}] \qquad (7.1)$$

The degree of crystallinity at a given temperature is then obtained from:

$$\text{Degree of Crystallinity} = \frac{\Delta h(T)}{\Delta h'(T)} \cdot 100\,\% \qquad (7.2)$$

For each sample, ?$h(T)$ is calculated at the crystallization peak temperature T_c observed in the cooling scan of the DSC scan. The results in Figure 7.3 show that the PE samples crystallized from n-pentane solution under pressure have a degree of crystallinity about 12 percent higher than that of the original PE sample.

Figure 7.4 shows the first DSC scans for the PE samples collected from 5 wt % solutions in n-pentane at selected pressures (Upper, 2002; Upper et al., 2003). The solutions were held at 90 ^{o}C for 60 minutes before further cooling and depressurization. Even though the heating rates are different, which is 10 K/min, multiple melting peaks were observed for all the samples. Except for the 52.1 MPa samples, a shoulder is observed around 122 ^{o}C, and two better resolved peaks appear around 126 and 130 ^{o}C. Again all these melting peaks appear at temperatures lower than the melting temperature of the original sample and that of the second heating scans. The crystallinity is in the range of 72 to 79 %.

Figure 7.5 shows the DSC results of PE samples collected from 5 wt % solution in 15 wt % CO_2 + 85 wt % n-pentane mixture (Upper, 2002; Upper et al., 2003). Except for the addition of CO_2, other conditions of the sample collection are as same as the samples shown in Figure 7.4. Features are similar to those observed in samples from the n-pentane solutions, with differences at 37.0 MPa and 40.8 MPa, where a broader peak is observed in place of the second and third peaks. The crystallinity is in the range of 72 % and 78 %.

Multiple melting peaks similar to those shown in Figures 7.2 and 7.5 have been previously observed in crystals formed under extreme pressure in melts (Miyata et al.,

1974; Tseng and Philips, 1985; Vanden Eynde et al., 2000; Yasuniwa et al., 1990; Aulov, 1994). In those studies, these melting peaks were attributed to the presence of folded chain crystals (FCC) and extended chain crystals (ECC) with the ECC being promoted in melt at high pressures. There are several possibilities for the occurrence of such multiple melting peaks. These are schematically presented in Figure 7.6. First, this could be due to the recrystallization that alters the fold length (Figure 7.6a). Secondly, it could arise from the secondary crystallization in the amorphous regions between the lamellae (Figure 7.6b). The multiple melting peaks could also be a sign of the presence of crystals with different lamellar thickness (Figure 7.6c). In the present case, the multiple peaks may be more likely due to the presence of different lamellar thickness. Figure 7.7 shows how the different lamellar thickness may develop during the constant pressure crystallization, followed by a depressurization stage. In the first stage of cooling to crystallization temperature, it is possible that some shorter chains remain in the solution and not crystallize. However, these shorter chains will crystallize in the final cooling and depressurization to the ambient conditions. The lamellar thickness depends on the rate of quench, and therefore in the final depressurization stage, the thickness may be smaller than the controlled cooling process. Thus it leads to at least two different crystal structures with different lamellar thickness and melting temperatures.

7.1.2 Comparison of Different Phase Separation Routes

As discussed in Chapter 6, the in-situ light scattering results show that the different phase separation routes result in different profiles of the scattered light intensity. There are three increments in the scattered light intensity during the phase separation via Route 2, which is a pressure quench followed by cooling process. The pressure quench

brings the system into the L-L phase separated region, from which the system is cooled down to room temperature for the sample recovery. There is only one scattered light intensity increase during the phase separation via Route 1 and 3.

The first heating scans of DSC measurements of the PE samples via these three routes are depicted in Figure 7.8. The DSC curves show the multiple melting peaks for the samples collected from Route 1 and Route 2. But there is only one melting peak observed for the sample of Route 3. As discussed above, the multiple melting peaks shown for Route 1 could be due to the existence of crystals with different lamellar thickness during the crystallization process. However, two well-defined melting peaks also appear in the sample of Route 2. Since the polymer solution was quenched to the L-L phase separated region and no further depressurization was posted on the system, the crystallization mechanism is different from the one shown in Figure 7.7. The double peaks could arise from the crystals formed in the two liquid phases formed after the pressure quench as shown in Figure 6.29. Because of the broad molecular weight distribution of the PE sample, these two solutions phases should have different concentrations, different molecular weight and different molecular weight distribution. The polymer-lean phase (upper phase) contains the more short chains, while the polymer-rich phase (lower phase) contains the more long chains. The crystallization temperature could also be different even though this is not thermodynamically true for the two equilibrium phases with equal chemical potential. The two crystallization temperatures have been observed in the light scattering experiments as shown in Figure 6.32, where there are two increases in the scattered light intensity during the cooling process at

around 363 K and 345 K, respectively. Therefore, crystals with different lamellar thickness are very likely to form in this system.

The melting behavior for the crystals formed from Route 3 is quite different from those of Route 1 and 2 because only one melting peak with a broad shoulder is identified. The single melting peak may arise from a single lamellar thickness. However, the broader shoulder suggests that either recrystallization happened during the heating scan or there are more than one lamellar thickness with continuous thickness distribution, or both take place. The other difference of the sample from Route 3 is the lower crystallinity of this sample, 70% compared to the 75 % for the other samples. This indicates that there may be more defects in the crystals formed via Route 3. These defects could be a result of the interplay of the S-F and L-L phase separations. As shown in Figure 6.30, the system approaches the intersection of the S-F and L-L phase boundary, and the crystallization starts from the L-L metastable region. In this region, the concentration fluctuation is not large enough to bring about L-L phase separation, but the fluctuations result in some polymer-rich clusters. The nucleation of crystals first takes place in these polymer-rich clusters. As the temperature and pressure is further reduced, the system is kept in the metastable region, and some defects from these fluid-like clusters may stay with the crystals. In other words, there is less time for the polymer chains to crystallize than from stable solution phases such as those of Route 1 and 2. This also means recrystallization during the heating scan is possible.

7.2 Morphology

7.2.1 Effect of Polymer Concentration

The FESEM images of PE samples crystallized from 0.5 (a), 1.0 (b), 2.3 (c), and 5.0 wt % (d) solutions at 23 MPa are presented in Figure 7.9. As shown in Figure 7.9a, the PE crystals formed in 0.5 wt % solution display plate-like lamellae. Several of these lamellae stack together to form an ellipsoidal shape. These ellipsoid structures have dimensions of about 6-15 μm in the short diameter and around 20 μm in the long diameter. Similar behavior was found for the PE crystals formed in 1.0 wt % solution (Figure 7.9b). But the dimensions are larger than that of 0.5 wt % solutions where the shorter diameter is around 10-20 μm and the longer diameter is between 20-35 μm. The FESEM image of particles formed from 2.3 wt % solution is depicted in Figure 7.9c. The plate-like lamellae do not aggregate to form an ellipsoid shape, but form a flower-like structure with an overall diameter up to 150 microns. These lamellae appear as growing from a nucleation point at their center. The thin lamellar leaflets are 5 micron wide and up to 70 microns long. The flower-like structures are not observed in crystals formed from 5 wt % solutions (Figure 7.9d). The ellipsoid structures together with some isolated flakes are shown in this image. The dimensions of the structures are smaller than that of 1 and 2.3 wt % solutions. Spherical morphologies were reported also in earlier studies on crystallization of polyethylene from 24 wt % solution in supercritical propane (Condo et al., 1992).

7.2.2 Effect of Pressure

The pressure effect on the morphology was studied with the PE crystals formed from 1.0 and 5.0 wt % solutions. For the 1.0 wt % solutions, crystallization experiments were repeated at 14, 23, 34, and 45 MPa. The samples were collected for FESEM characterization. These images are shown in Figures 7.9b and 7.10a-c. Ellipsoid structures are displayed in all these images. However, the dimensions and the stacking of lamellae are quite different. The particles formed under 14 MPa have the smallest dimensions with 3-5 μm in the short diameter and only around 10 μm in the long diameter (Figure 7.10a). It is very interesting that the size distribution is very narrow in this situation and each of the ellipsoid structures is formed from only a few lamellae. The ellipsoidal structures formed at 23 MPa (Figure 7.9b) are of twice larger dimensions in each diameter and consist of more lamellae. As the crystallization pressure goes to 34 MPa (Figure 7.10b), the ellipsoid dimension does not change much. As shown in Figure 7.10c, another 11 MPa increase on the crystallization pressure induces larger particle sizes, which are 40-45 μm in the long diameter and 20-30 μm in the short diameter. In general, it appears that increasing the crystallization pressure in the solution leads to larger particle sizes. These observations are consistent also with the results of light scattering experiments as discussed in Chapter 6 in spite of the difference in the actual value of the particle size.

The ellipsoidal structures that are observed in these micrographs may be formed via two different mechanisms. This is illustrated in Figure 7.11. In the first mechanism, it is envisioned that the plate-like lamellae that form via nucleation, stacking together, and then reshaping into the final ellipsoid structure. The second mechanism is similar to the

traditional mechanism of spherulite formation from polymer melts. Here, it is envisioned that at the earlier stage of crystallization, the lamellar growth is accompanied by lamellar branching which then leads to the ellipsoidal morphologies. In the lower part of Figure 7.11, several FESEM images are included to help visualize the outcome of these processes.

Comparison of predicted particle size from light scattering data and the FESEM micrographs shows that there is a significant difference in the particle sizes. Several reasons may lead to this difference. First, the in-situ light scattering measurements were carried out at the crystallization pressure during cooling from one phase region into the S-F two phase region (typically around 90 ^{o}C), while the particles for the FESEM characterization were collected after cooling the system down to room temperature, followed by a depressurization process. The extended cooling could result in further growth of particles. Also, the final depressurization process could have a significant effect on both the morphology and the size of the particles. Second, the scattering data were captured in the scattering cell area where the gap between two sapphire windows is only 250 microns. The sample collected for FESEM measurements were from the microreactor, which is a bulk solution phase compared to that of the scattering cell. In the scattering cell, the sapphire windows and the stainless steel wall may serve as a heterogeneous crystallization surface. From this surface, the crystals may grow with orientation while the crystals formed from the microreactor do not. This has been confirmed from the observation that a PE particle layer is formed on the sapphire windows and the cell wall. Finally, the structure during the earlier stage of crystallization

may be different from the final structure that was recovered after cooling and depressurizing to ambient condition.

The FESEM images of PE samples collected from 5 wt % solutions in n-pentane at 38, 40 and 53 MPa from the view-cell system (Upper et al., 2003) are shown in Figure 7.12. A mixture of the ellipsoid structures and a stacked lamellae structure with many stacked lamellae is the common feature. These stacked lamellae structures can be viewed as an elongated ellipsoid structure. The formation of this structure can be explained by the first mechanism shown in Figure 7.11, but without the reshaping stage because of the larger number of lamellae stacked up together. At 38 MPa, the length of the stacked lamellae can be more than 50 μm with diameter of 15 μm. Some isolated lamellae that are shown in this image seem to be the elements to form the pile of lamellae. At 40 MPa, the dimension of the stacked lamellae structures is shown to be larger than those at 38 MPa, where the length can be up to 150 μm with diameter about 20 μm. At 53 MPa, the length of the stacked lamellae structures is not larger than those of 40 MPa, but the diameter increases to about 30 μm. This is consistent with the observation of the particle size in the 1 wt % solutions where the size of the ellipsoid structure increases with increasing pressure.

7.2.3 Effect of Carbon Dioxide

Figure 7.13 shows the FESEM images of PE samples collected from 5 wt % solutions in 15 wt % CO2 and 85 wt % n-pentane at 37, 40, 45, and 52 MPa. The significant difference between these images and those from n-pentane is that stacked lamellae structure is not a preferred structure. There are only few short ones identified in

the 37 MPa sample with a much smaller size in both length and diameter. The length is around 20 μm while the diameter is less than 10 μm. The dominating structure in these conditions is the ellipsoid structure similar to those of 1 wt % solutions in n-pentane. The long diameters of the ellipsoid structures are around 10, 20, 8, and 10 μm for samples collected at 37 MPa, 40 45 and 52 MPa, respectively. It is clear that with the addition of CO_2, the overall dimensions of the agglomerated structure are getting smaller. This could result from the reduced solvent power in the presence of CO_2.

7.2.4 Comparison Different Phase Separation Routes

As discussed in Chapter 6 and the previous section of this chapter, the phase separation via different routes shows different features on the in-situ light scattering observations and on the thermal properties of the recovered samples. Figure 7.14 shows the morphologies of the PE particles collected after these three processes. In fact, the FESEM images discussed so far are for Route 1. However, one FESEM image is still selected and shown here for comparison with the morphology from other two routes. Figure 7.14a shows the simple ellipsoid structures that formed with only two lamellae, which is very similar to those of Figure 10a. The only difference noticed in the figure is the small particles that embedded into the carbon tape. These small particles may be those crystallized during the depressurization process as depicted in Figure 7.7.

The morphology of the PE particles collected after phase separation via Route 2 shows some differences from those of Route 1, as illustrated in Figure 7.14b. There are two groups of particles: one group has larger size with diameter from 10 to 20 μm and this group is dominating; and the other group is not only smaller in size (less than 5 μm

in diameter), but also fewer in amount. Besides, the particles have more spherical shape compared to the ellipsoidal shaped particles shown for that of Route 1. Another difference has to do with the arrangement of the lamellae forming the particles. For the particles from Route 1, the particles may be made of a few lamellae with very simple arrangement. But the particles formed via Route 2 are made of many lamellae even for the very small particles with very complex arrangements. Figure 7.14c shows the morphology of PE particles from Route 3, where three types of particles are also observed. One type is very similar to some particles observed in Figure 7.10 with diameter of 10-20 μm; another type with diameter about 50 μm is similar to the flower-like morphology observed in 2.3 wt % solutions; and some very small particles are shown on the left side.

These differences could be due to the phase separation process or only to the difference in the crystallization pressure. Even though the overall polymer concentration is kept the same for all these three routes, the environment where the crystals grow could be different due to the L-L phase separation before the crystallization starts. As discussed earlier for Route 2, the polymer solution is first phase separated into two liquid phases, and then the crystallization takes place in these two separated phases during the following cooling process. Therefore, two groups of particles could represent the particles formed in two separated phases. The first group particles with larger size and amount are from polymer-rich phase, while the second group with less in amount and smaller in size is from the polymer-lean phase. The multiple particle size and morphologies of Route 3 can be viewed as a result of the competition between S-F and L-L phase separations.

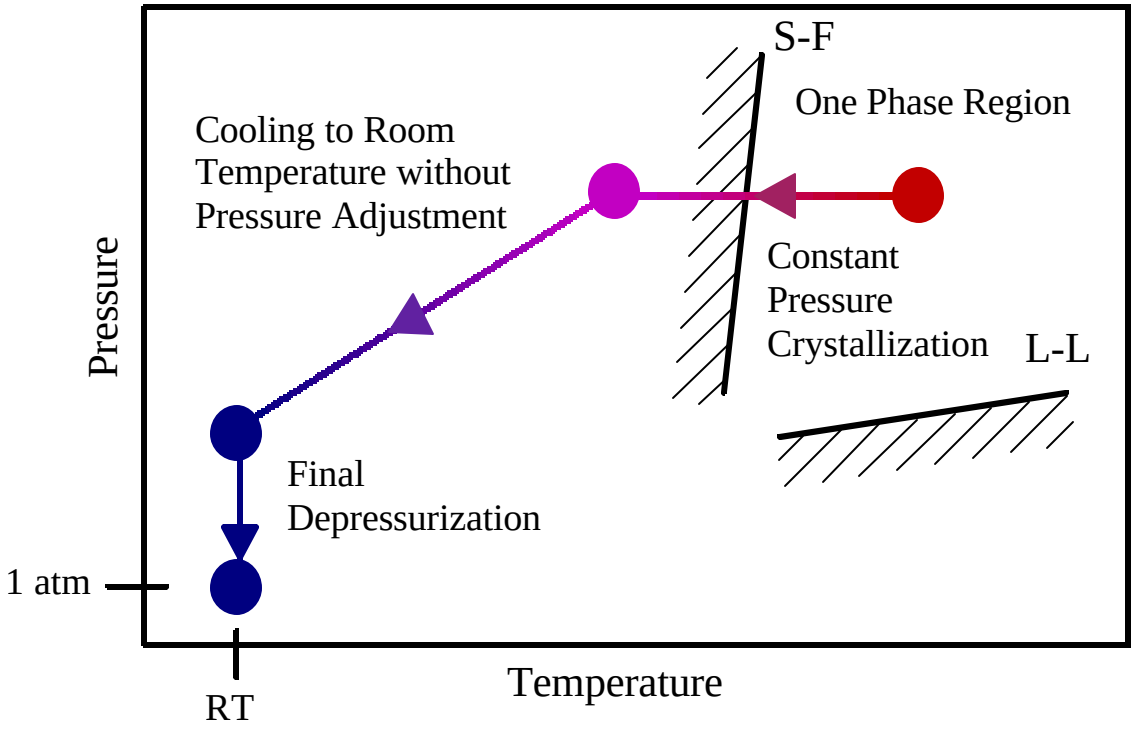

Figure 7.1. The sample collection process for PE crystals formed in n-pentane under high pressure.

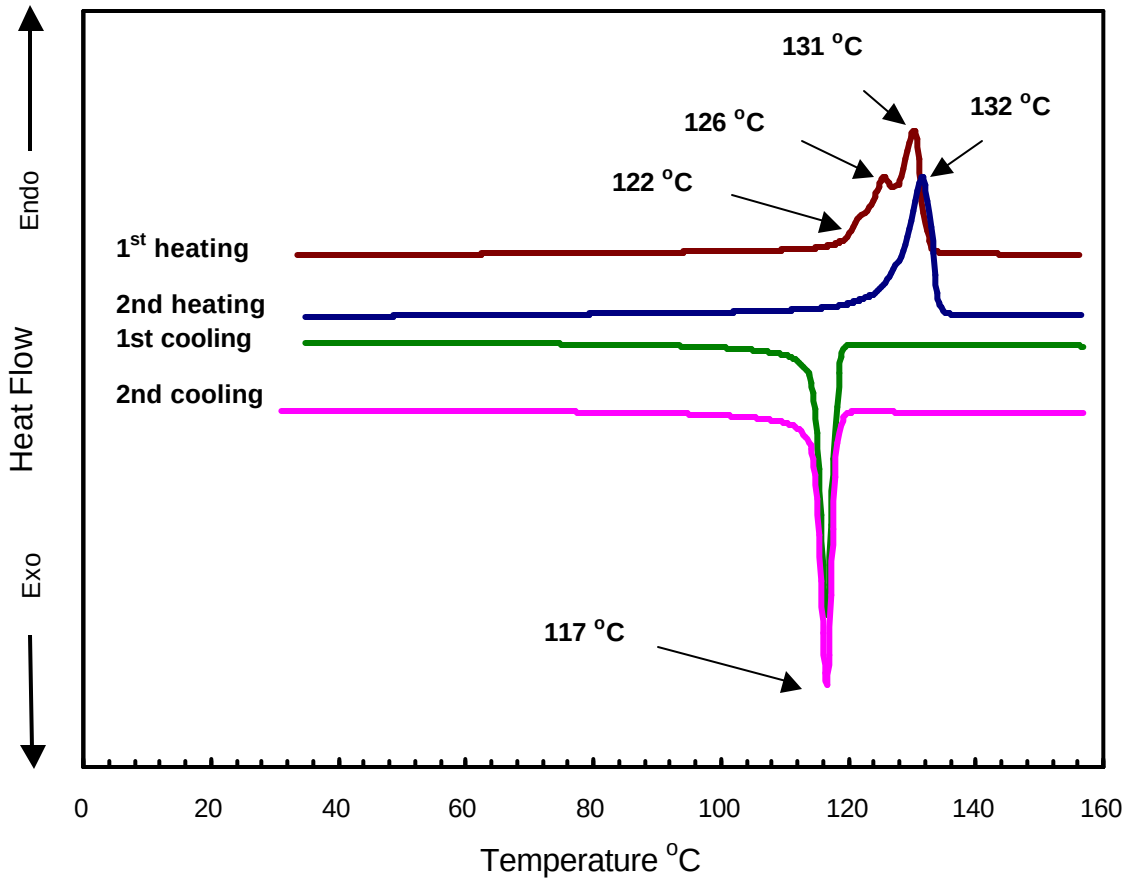

Figure 7.2. DSC scans of PE particles crystallized in 1 wt % solution in n-pentane at pressure 45 MPa. Heating/cooling rate: 20 K/min.

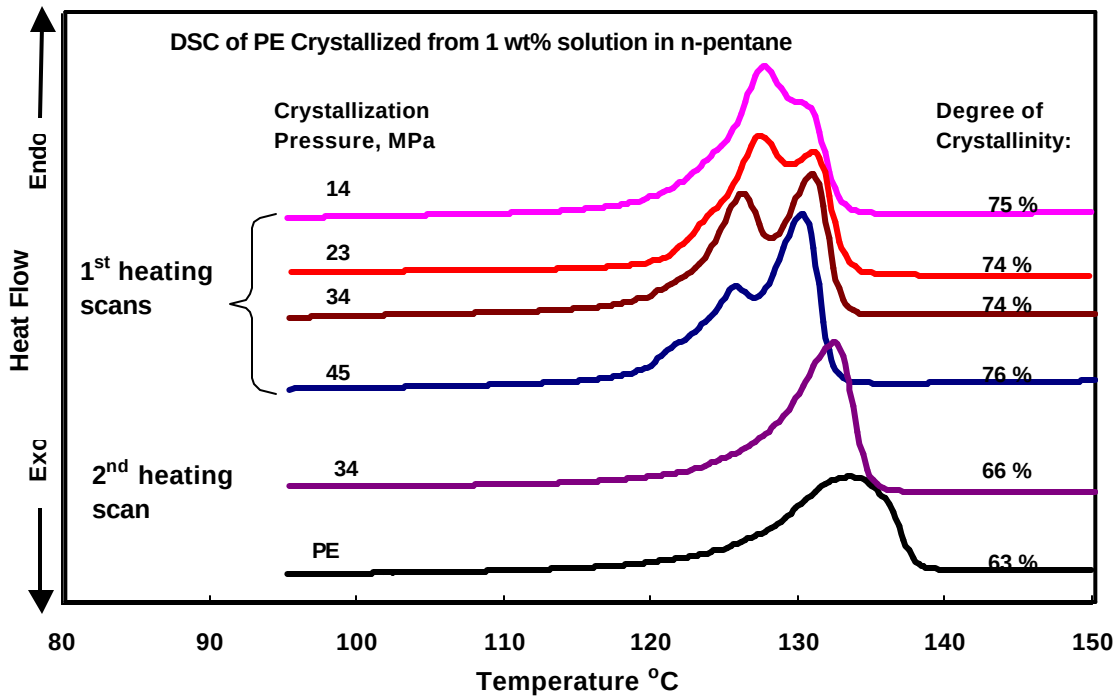

Figure 7.3. Comparison of DSC 1st heating scans of PE particles crystallized in 1.0 wt % solution in n-pentane at 14, 23, 34 and 45 MPa with the PE original sample. Heating rate: 20 K/min.

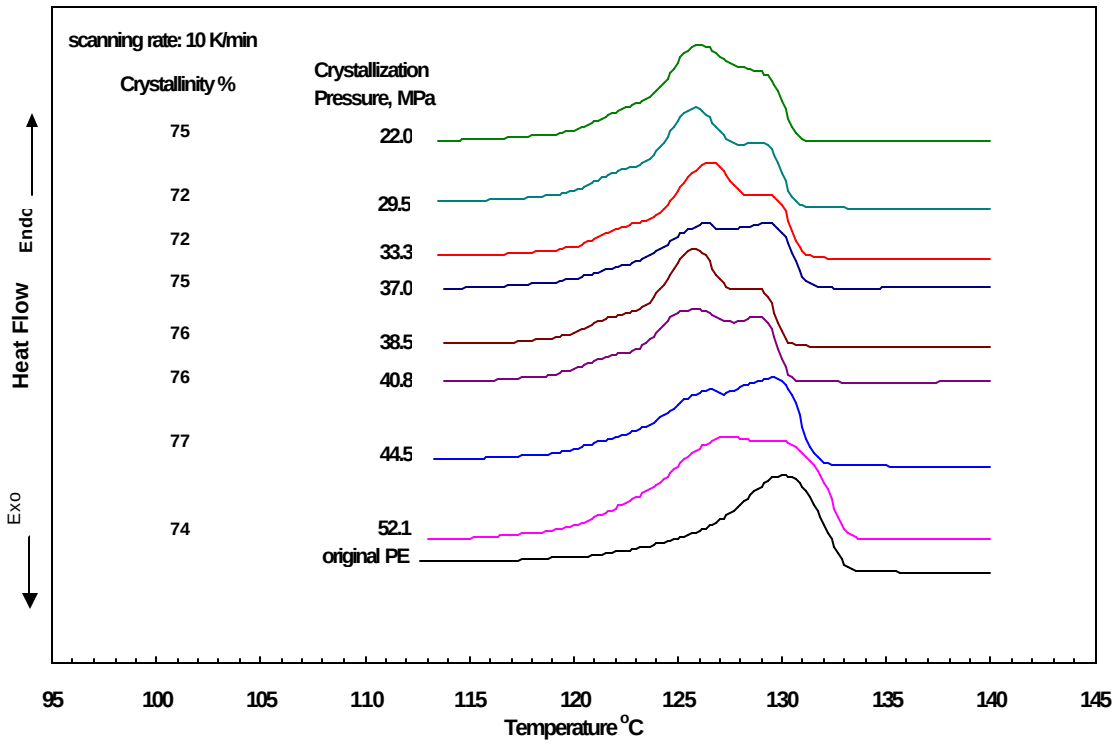

Figure 7.4. Comparison of DSC 1st heating scans of PE particles crystallized in 5.0 wt % solution in n-pentane at selected pressures with the PE original sample. Heating rate: 10 K/min (Upper, 2002; Upper et al. 2003).

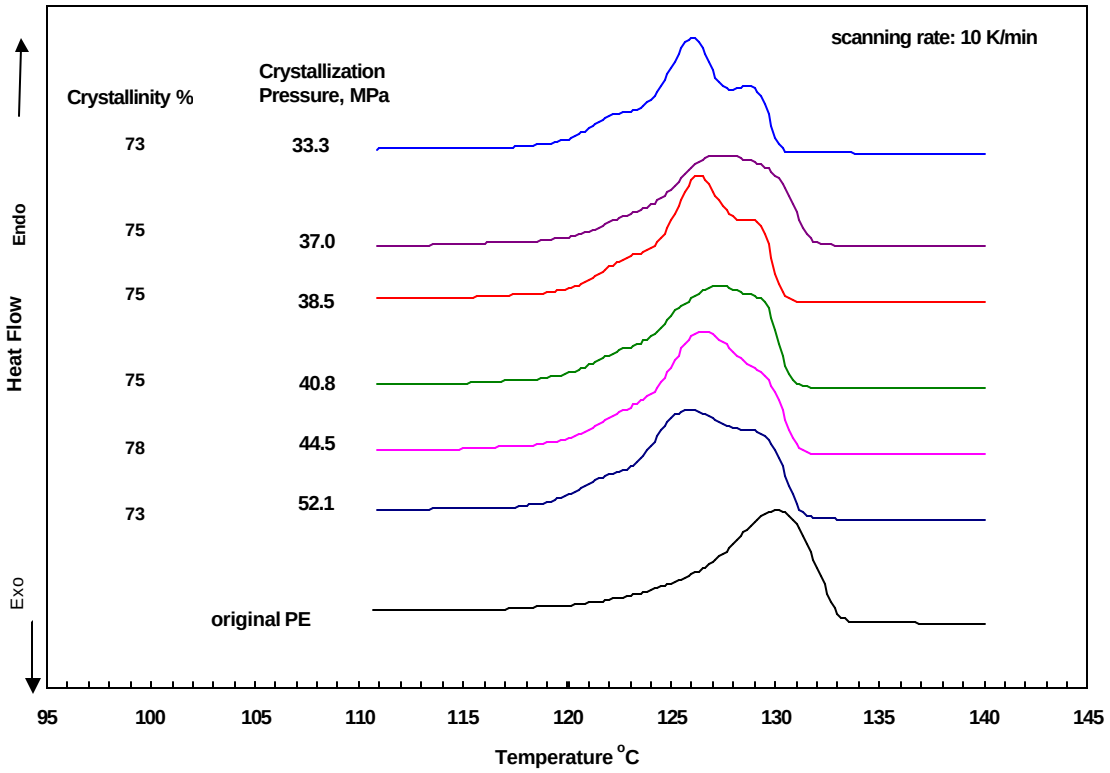

Figure 7.5. Comparison of DSC 1st heating scans of PE particles crystallized in 5.0 wt % solution in 15 wt % CO_2 + 85 wt % n-pentane at selected pressures with the PE original sample. Heating rate: 10 K/min (Upper, 2002; Upper et al. 2003).

a.

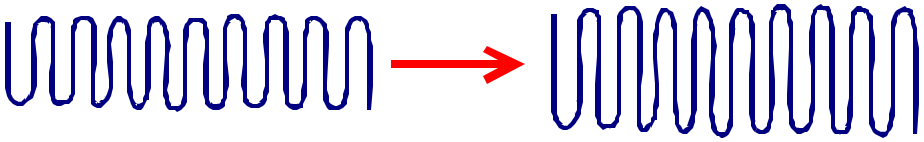

b.

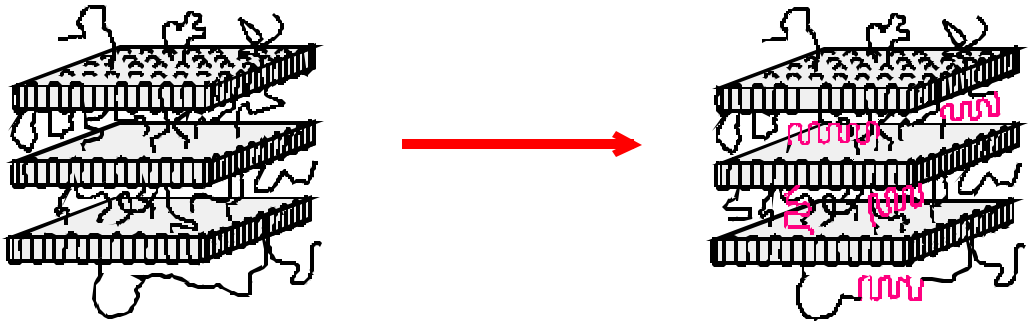

c.

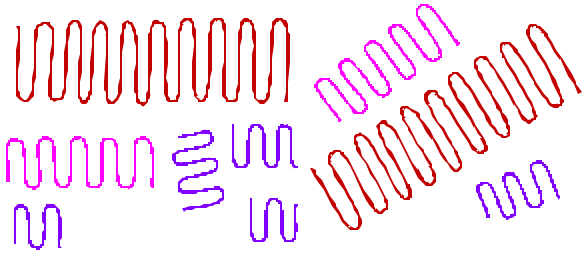

Figure 7.6. Schematic diagram showing the possible reasons for observation of multiple melting peaks in DSC scans. **a**. recrystallization and lamellar thickening; **b**. secondary crystallization in the amorphous region between lamellae; **c**. presence of crystals with difference lamellar thickness.

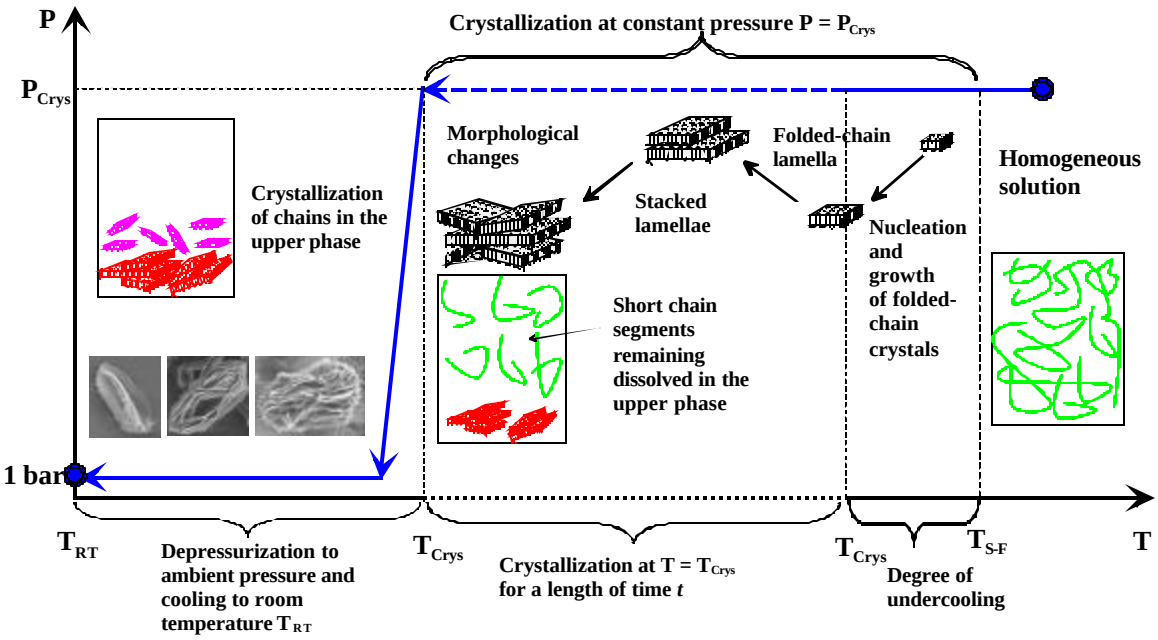

Figure 7.7. Schematic diagram showing constant pressure crystallization and the particle collection process that follows where the crystals with different sizes are developed. Initially the system is a homogenous solution. During constant pressure cooling, high molecular weight fractions are crystallized first, which shorter chains remain in solution, which crystallize in the final decompression stage.

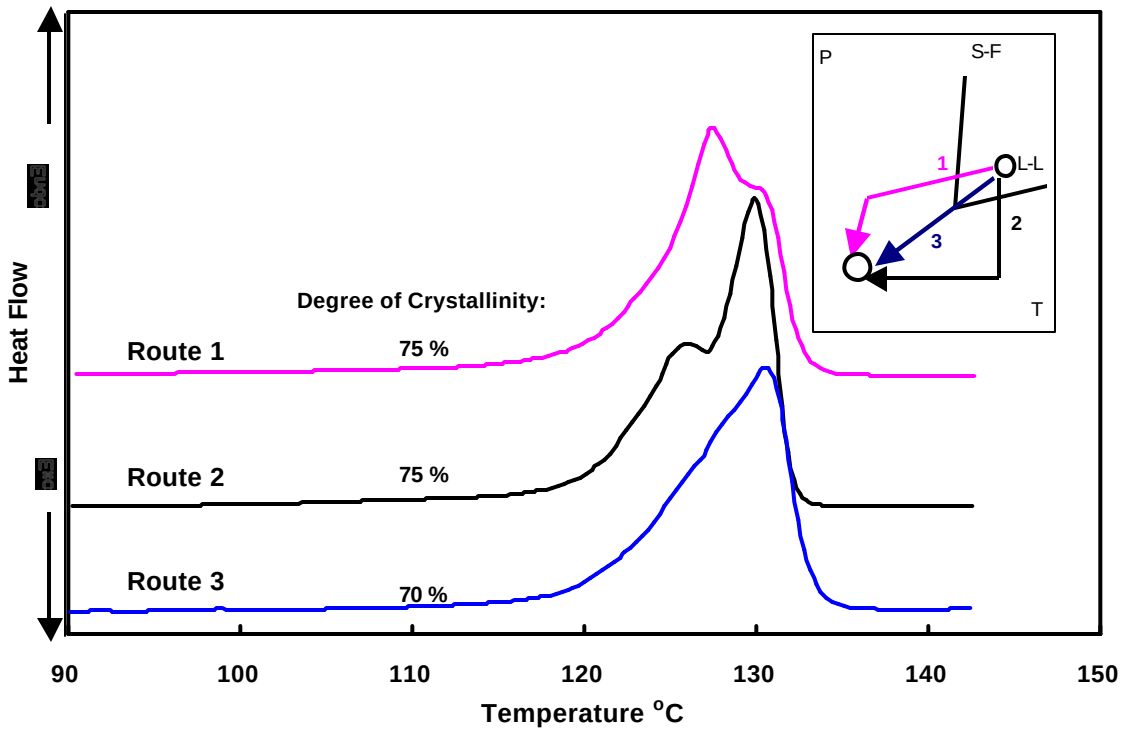

Figure 7.8. Comparison of DSC 1st heating scans of PE particles crystallized after light scattering experiments of 1 wt % PE solutions in n-pentane via three different routes: 1. constant pressure cooling process; 2. pressure quench followed by cooling process; and 3. controlled pressure and temperature reduction process. Heating rate: 20 K/min.

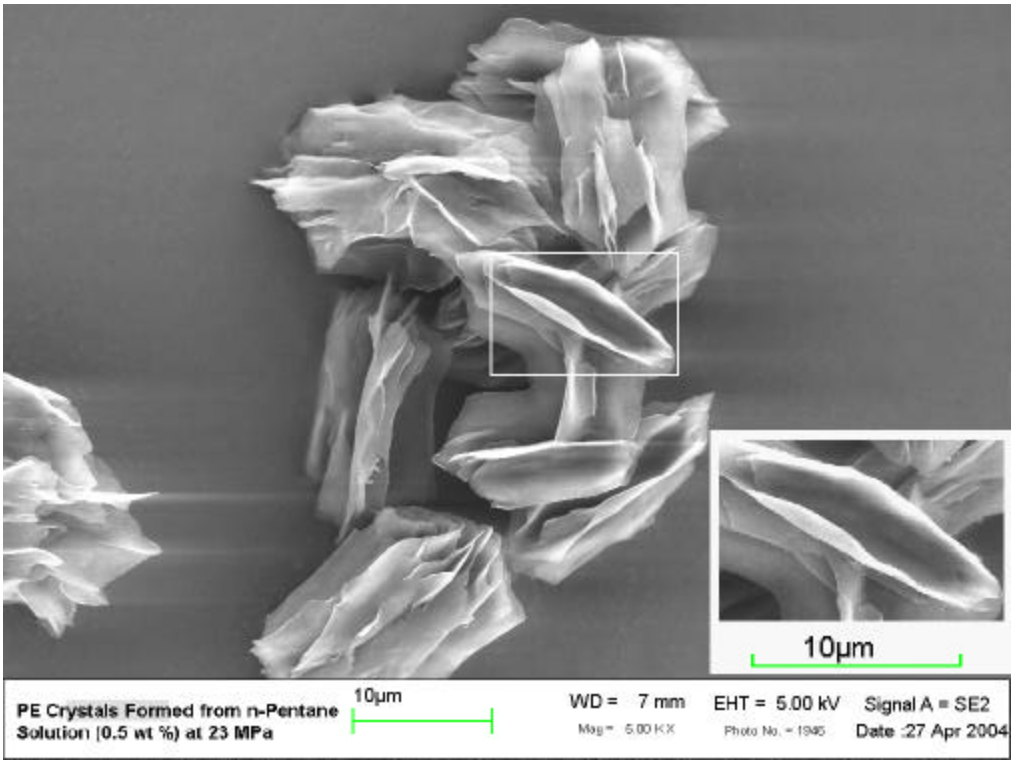
10µm
PE Crystals Formed from n-Pentane Solution (0.5 wt %) at 23 MPa
10µm
WD = 7 mm
Mag = 5.00 K X
EHT = 5.00 kV
Photo No. = 1945
Signal A = SE2
Date :27 Apr 2004

a

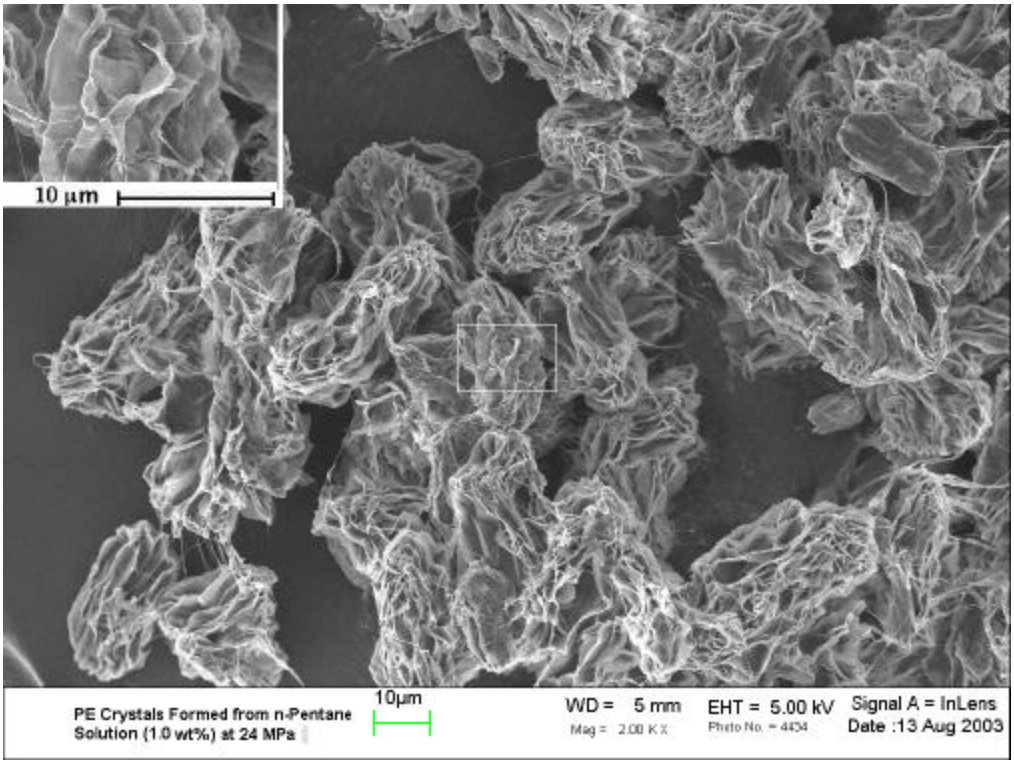
10 µm
PE Crystals Formed from n-Pentane Solution (1.0 wt%) at 24 MPa
10µm
WD = 5 mm
Mag = 2.00 K X
EHT = 5.00 kV
Photo No. = 4454
Signal A = InLens
Date :13 Aug 2003

b

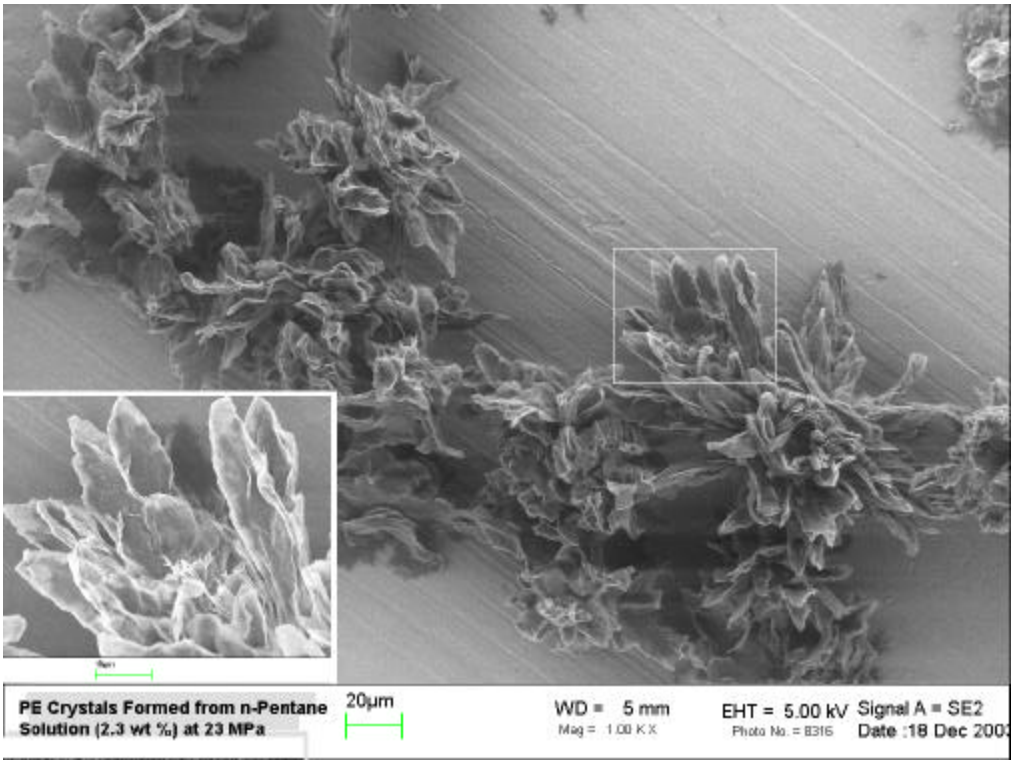

c

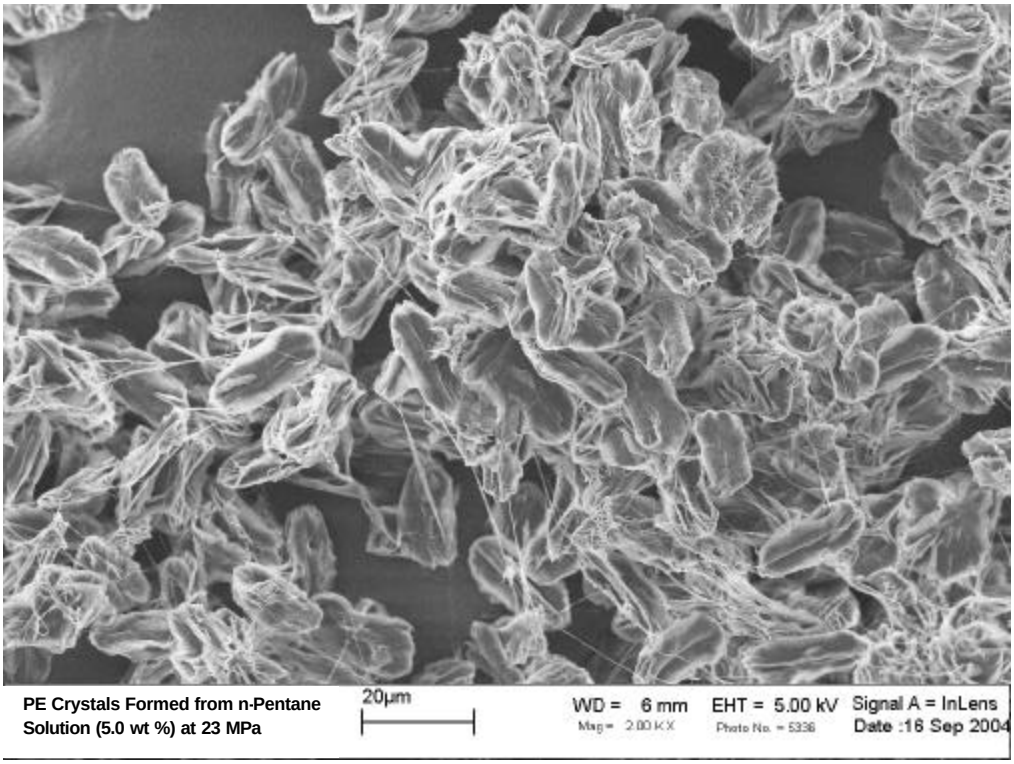

d

Figure 7.9. FESEM images of PE crystallized from n-pentane solutions [0.5 (**a**), 1.0 (**b**), 2.3 (**c**), and 5.0 wt % (**d**)] under constant pressure 23 MPa.

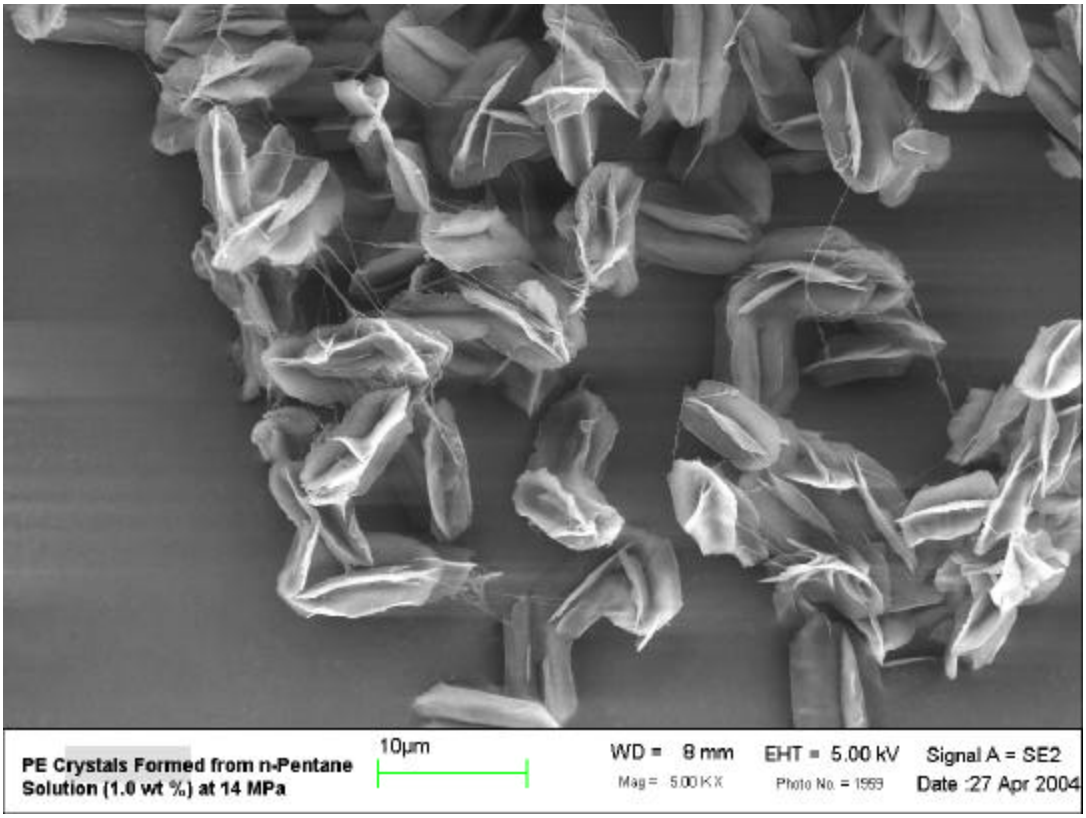
PE Crystals Formed from n-Pentane Solution (1.0 wt %) at 14 MPa
10µm
WD = 8 mm
Mag = 5.00 K X
EHT = 5.00 kV
Photo No. = 1969
Signal A = SE2
Date :27 Apr 2004

a

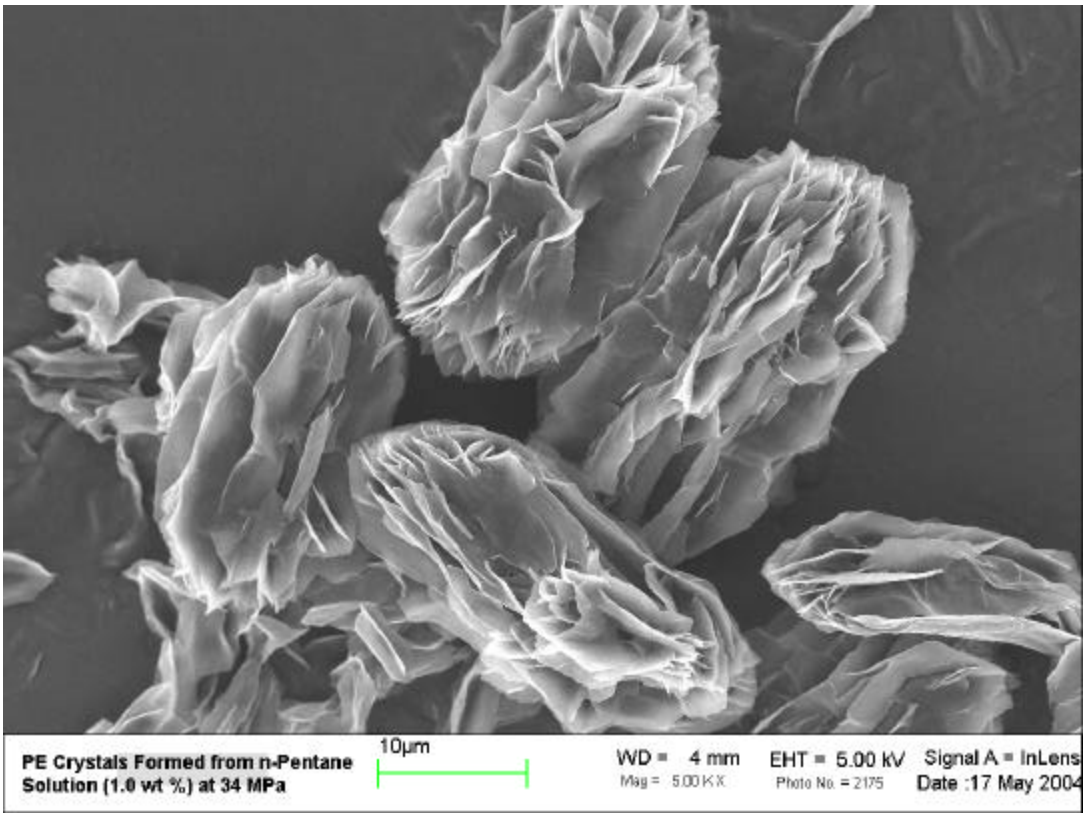
PE Crystals Formed from n-Pentane Solution (1.0 wt %) at 34 MPa
10µm
WD = 4 mm
Mag = 5.00 K X
EHT = 5.00 kV
Photo No. = 2175
Signal A = InLens
Date :17 May 2004

b

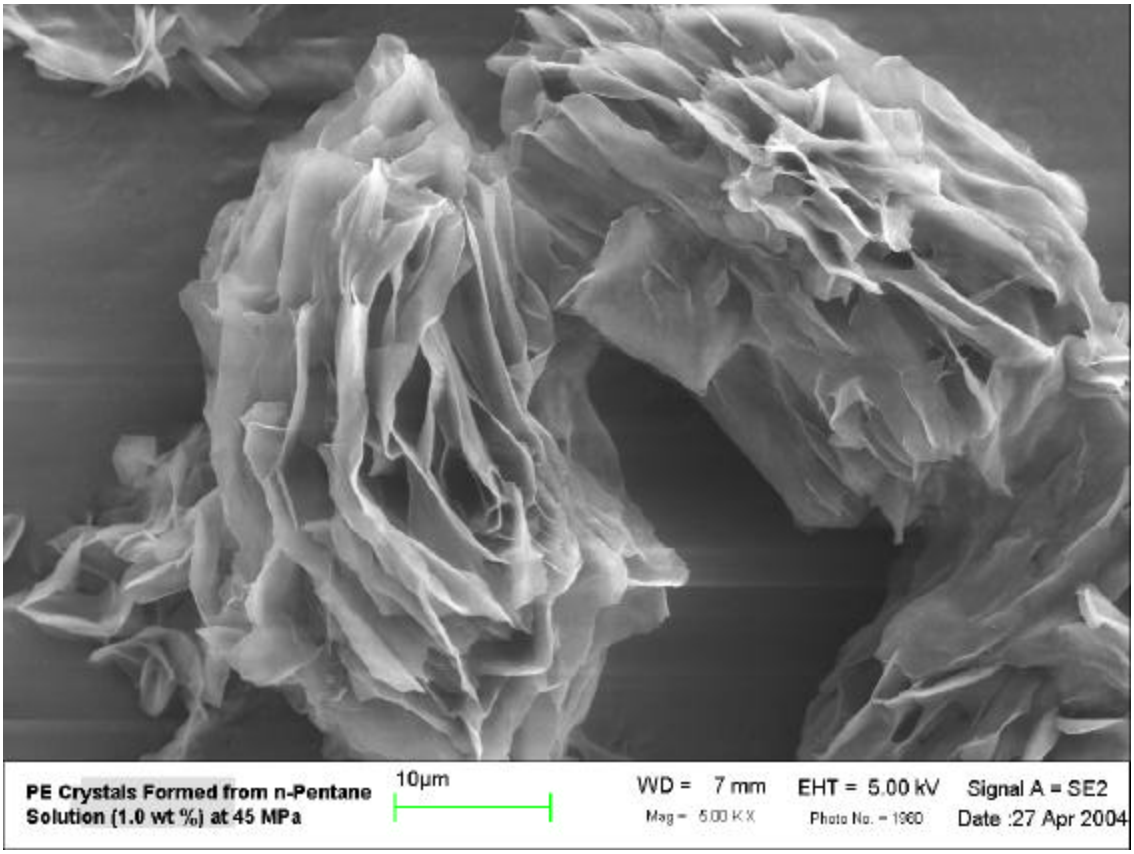

c

Figure 7.10. FESEM images of PE crystallized from 1.0 wt % n-pentane solutions under constant pressure of 14 (**a**), 34 (**b**) and 45 (**c**) MPa.

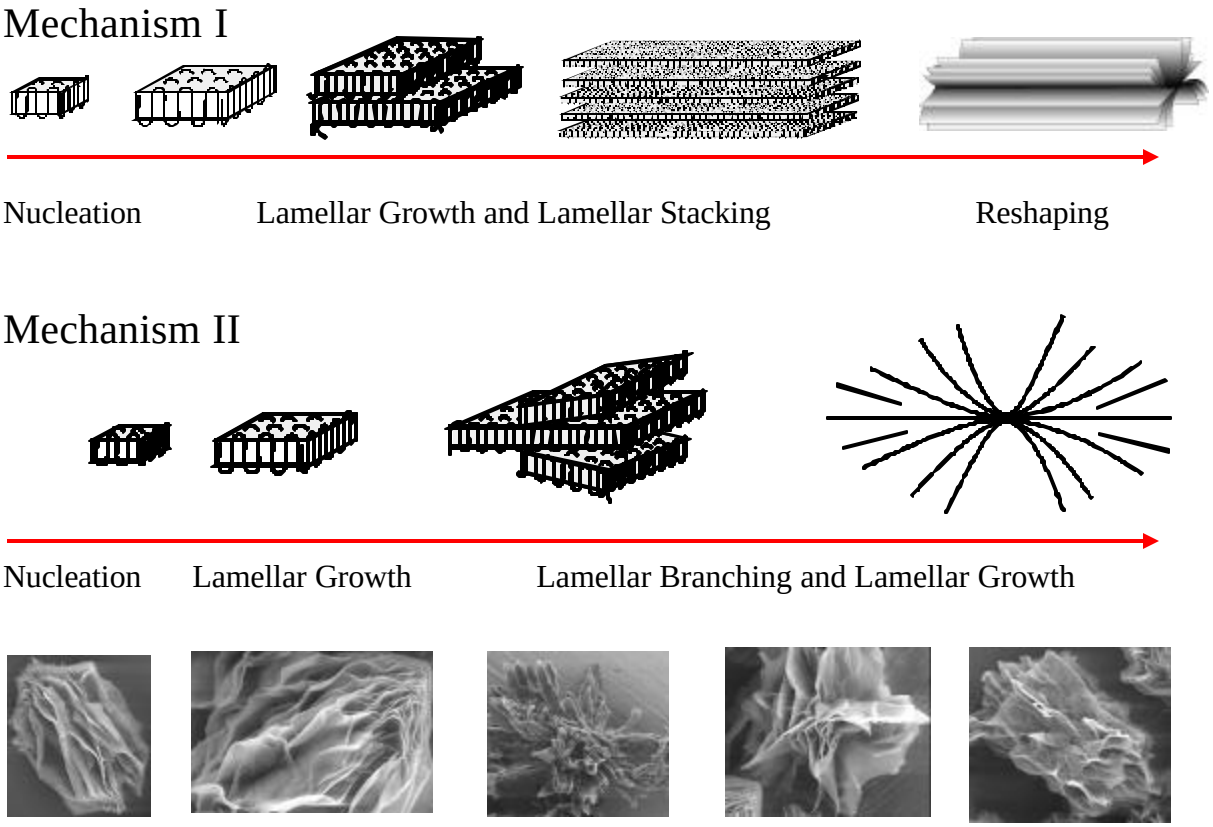

Figure 7.11. Schematic diagram for possible mechanisms for lamellar arrangements leading to ellipsoid structures.

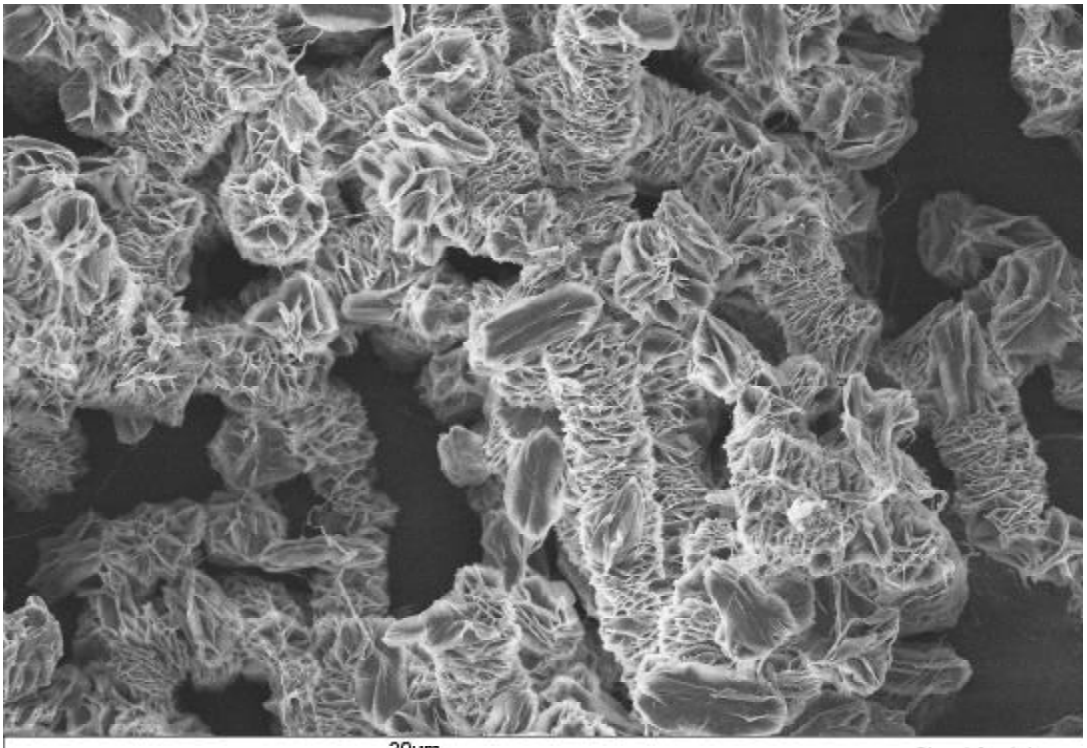

PE Crystals Formed from n-Pentane Solution (5.0 wt %) at 38 MPa

a

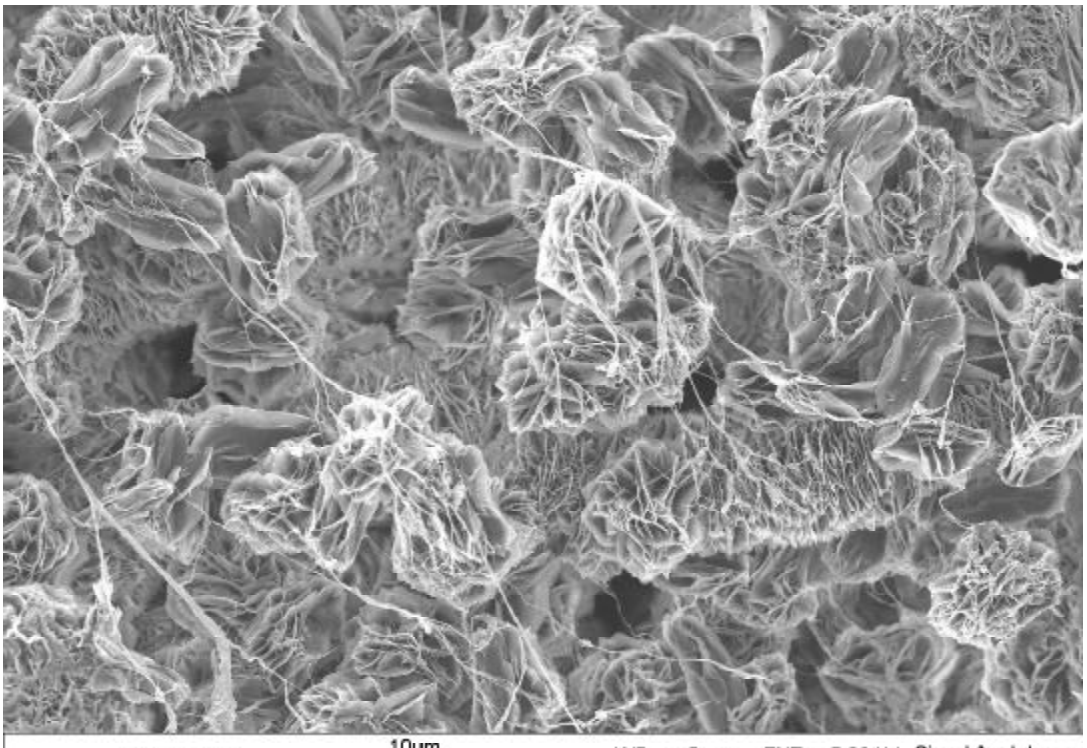

PE Crystals Formed from n-Pentane Solution (5.0 wt %) at 40 MPa

b

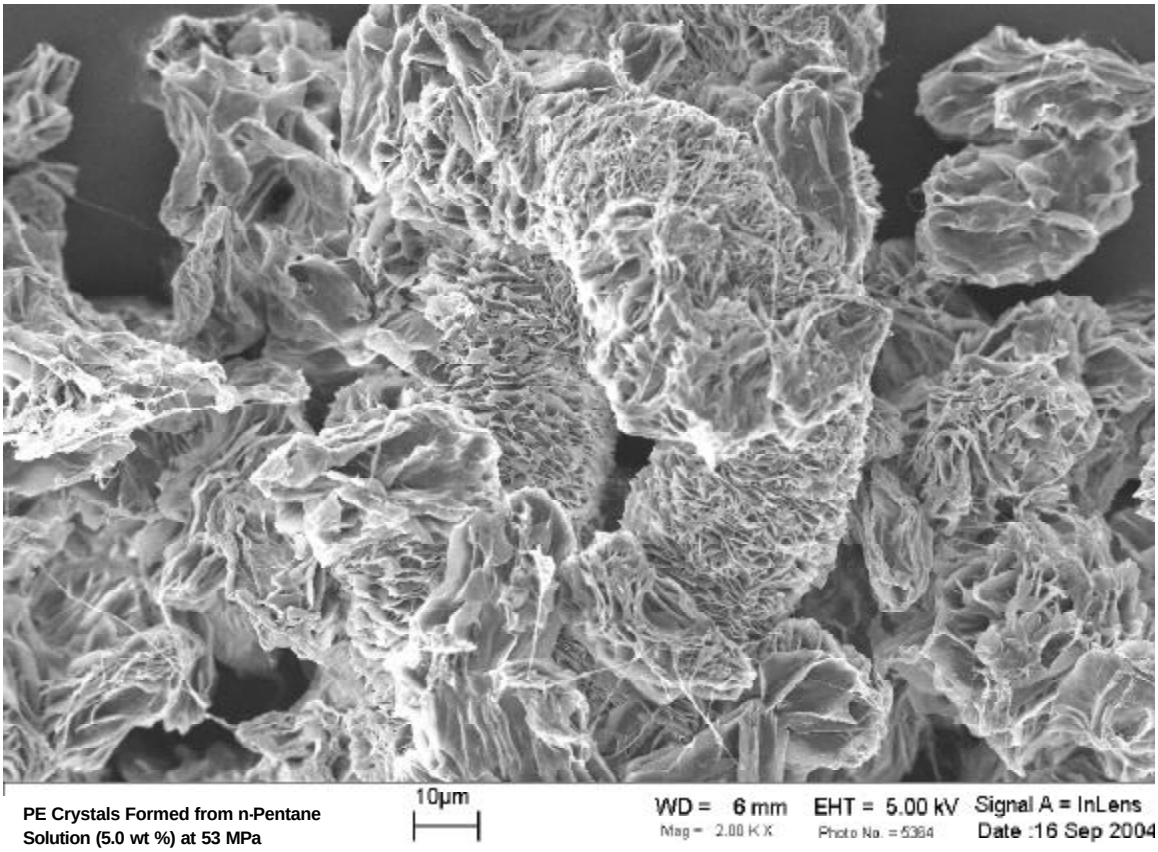

c

Figure 7.12. FESEM images of PE crystallized from 5.0 wt % n-pentane solutions under constant pressure of 38 (**a**), 40 (**b**) and 53 (**c**) MPa (Upper et al., 2005).

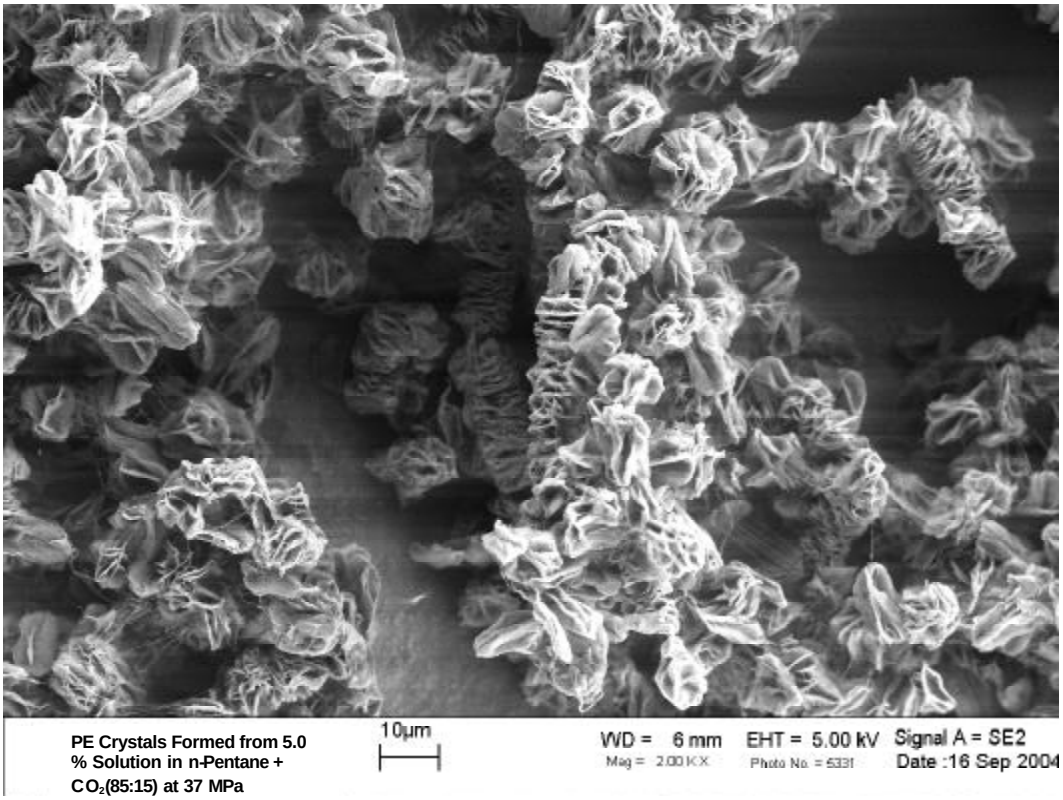

PE Crystals Formed from 5.0 % Solution in n-Pentane + CO_2(85:15) at 37 MPa

a

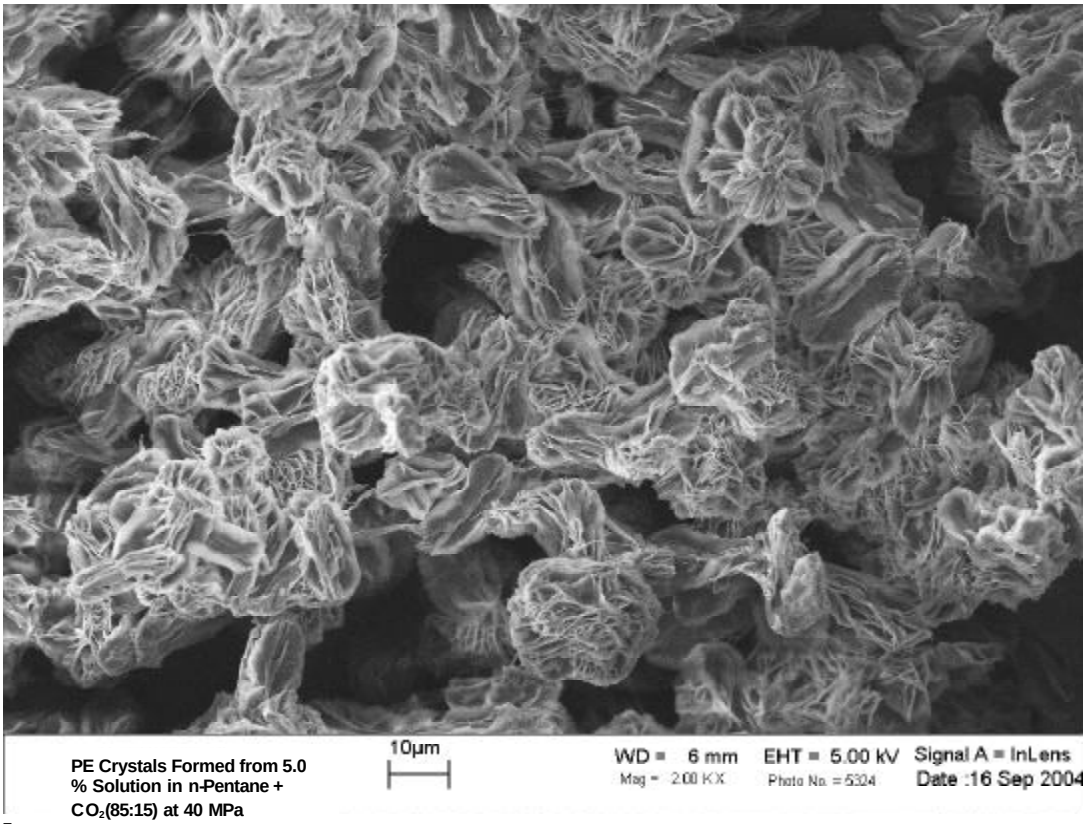

PE Crystals Formed from 5.0 % Solution in n-Pentane + CO_2(85:15) at 40 MPa

b

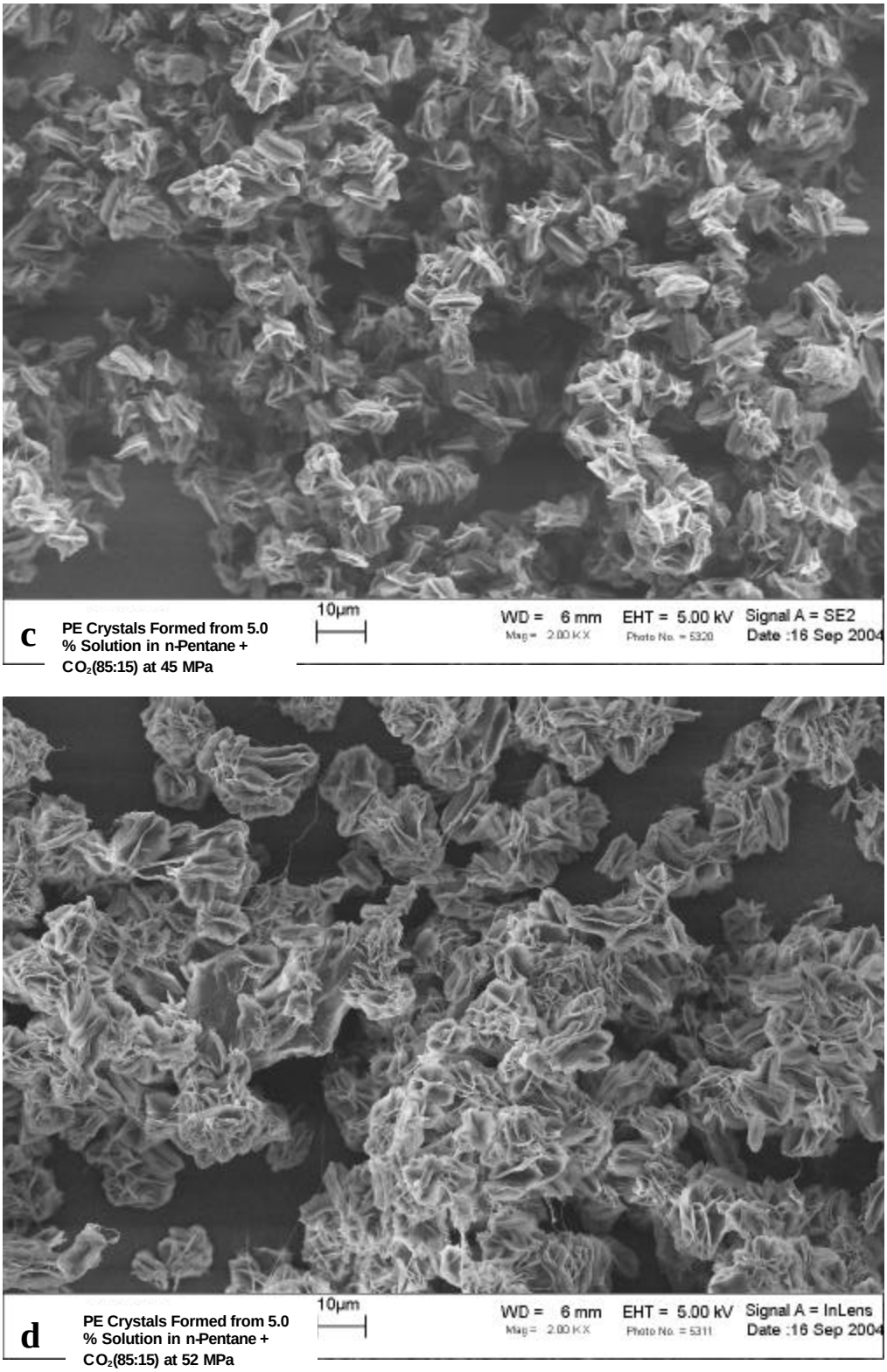

Figure 7.13. FESEM images of PE crystallized from 5.0 wt % solution in 15 wt % CO_2 + 85 wt % n-pentane solutions under constant pressure of 37 (**a**), 40 (**b**), 45 (**c**), and 52 (**d**) MPa (Upper et al., 2005).

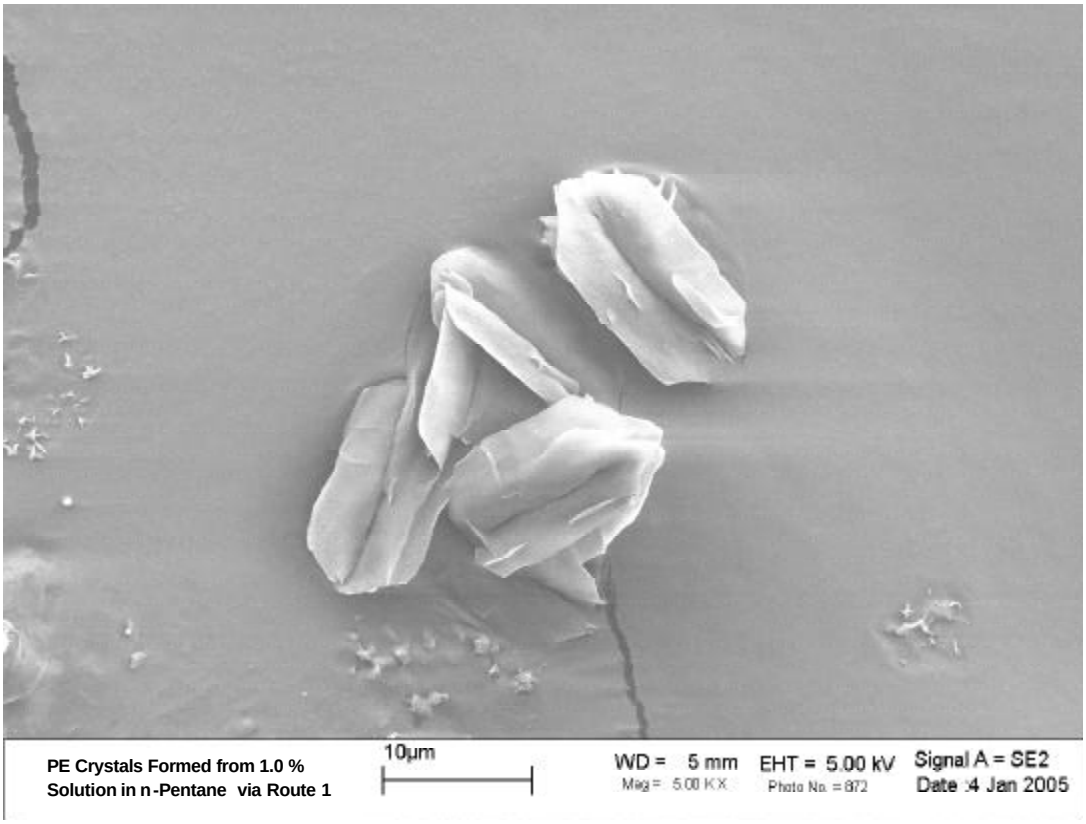
PE Crystals Formed from 1.0 %
Solution in n-Pentane via Route 1
10µm
WD = 5 mm
Mag = 5.00 KX
EHT = 5.00 kV
Photo No. = 872
Signal A = SE2
Date :4 Jan 2005

a

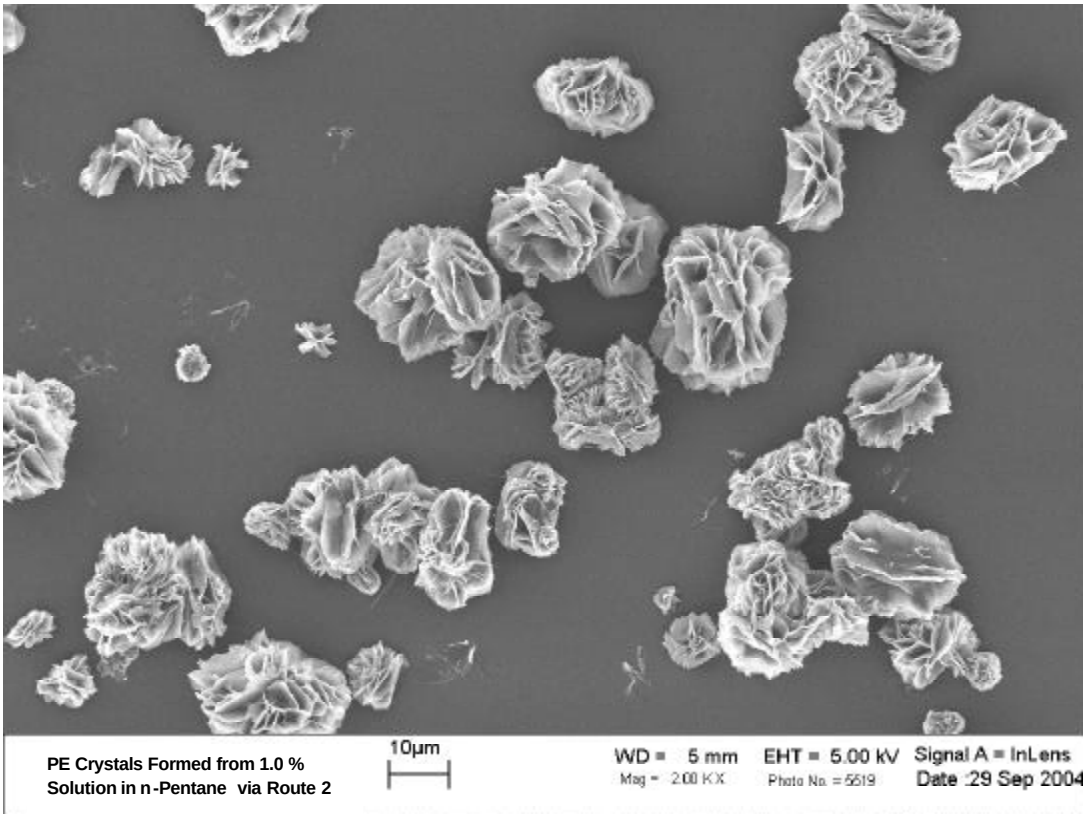
PE Crystals Formed from 1.0 %
Solution in n-Pentane via Route 2
10µm
WD = 5 mm
Mag = 2.00 KX
EHT = 5.00 kV
Photo No. = 5519
Signal A = InLens
Date :29 Sep 2004

b

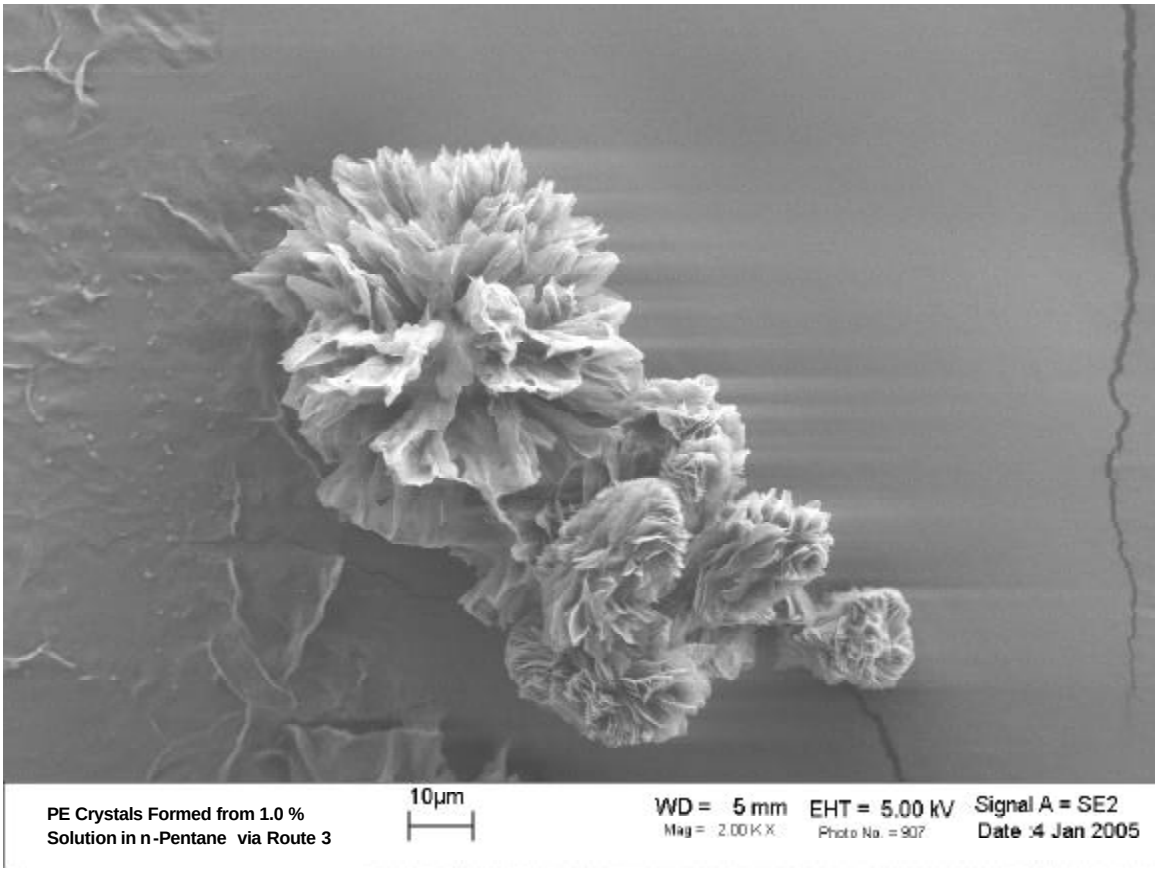

c

Figure 7.14. FESEM images of PE samples collected after phase separation via Route 1 (**a**), Route 2 (**b**) and Route 3 (**c**) in 1.0 wt % n-pentane solutions.

Chapter 8

Miscibility and Volumetric Properties of Polysulfone in THF + CO_2 Mixtures

The results of the miscibility and volumetric properties of polysulfone solutions in tetrahydrofuran + carbon dioxide mixtures investigated using high-pressure view cell are presented in this chapter. Tetrahydrofuran is a very good solvent for polysulfone and widely used in membrane formation processes. However, it is not an environmentally benign solvent. Carbon dioxide may be used to reduce the use of this solvent and serve as an alternative non-solvent to bring about phase separation for the membrane formation process. The miscibility of polysulfone in the THF + CO_2 solvent mixture was studied using the high-pressure view cell. With increasing amount of CO_2, the demixing pressure was found to be increased to higher pressures. Moreover, a very interesting phase behavior, multiple miscible windows, was observed in this system when the CO_2 content in the solvent mixture was increased. The multiple miscible windows reduce to a single miscible region at lower carbon dioxide levels. The volumetric properties of the system suggest that, in the region of reduced miscibility, the specific volume of the whole mixture is higher than in the region with miscibility. The numerical data of both phase boundary and density of this system are included in Appendix A.

---

*Portion of this chapter has appeared as: "Zhang, W., Kiran, E. Phase Behavior and Density of Polysulfone in Binary Fluid Mixtures of Tetrahydrofuran and Carbon Dioxide under High Pressure: Miscibility Windows**.** *Journal of Applied Polymer Science* (2002), 86(9), 2357-2362." and "Zhang, W., Kiran, E. *Journal of Chemical Thermodynamics* (2003), 35(4), 605-624."

8.1 Materials

The polysulfone polymers were obtained from Scientific Polymer Products. These samples were from two different batches with very similar molecular weights and molecular weight distributions. The molecular weights were Mw = 68,621, Mn = 37,978 and Mw = 60,206, Mn = 32,683. Tetrahydrofuran (purity > 99.5 %) was obtained from EM Science. Carbon dioxide was obtained from Air Products and Chemicals with a purity > 99.99%. The polymers and solvents were used without further purification.

8.2 The Phase Behavior of Polysulfone in Binary Fluid Mixtures of THF + CO_2 under High Pressures

8.2.1 Influence of CO_2 Concentration on Miscibility

The demixing conditions for 4.5 wt % polysulfone solutions in CO_2 + THF mixtures were first measured at different CO_2 contents. In these experiments polymer concentration was kept constant, and the solvent fluid concentrations were varied with CO_2 concentration ranging from 9.9 wt % to 13.9 wt % in the temperature range from 300 to 425 K. Figure 8.1 shows the demixing conditions in the P-T diagram as determined from the change in transmitted light intensities (see for example, Figure 3.4). The region above each P-T curve corresponds to the one-phase homogeneous region, while the lower pressure side of each curve is the phase-separated region. The increase in the CO_2 concentration in the solvent fluid mixture causes a remarkable increase in the demixing pressures. This effect is even greater at lower temperatures than that at higher temperatures. For example at 308 K, the shift is from about 16 to 67 MPa, but at 368 K, the shift is from about 31 to 65 MPa. For 9.9, 11.4 and 12.9 wt % CO_2 concentrations,

the system displays a LCST-type behavior (phase separation occurs upon increasing temperature) in the temperature range investigated. However, UCST-type behavior (miscibility rather than phase separation takes place upon increasing temperature) is observed at 13.9 wt % CO_2 solution as illustrated with the arrow in Figure 8.1. The CO_2 effect on the miscibility will be discussed further in next section with P-X and T-X phase diagrams cut at three different CO_2 levels: 8, 10 and 13 wt % of CO_2 in the solvent mixtures.

8.2.2 Influence of Polymer Concentration on Miscibility

Figure 8.2 shows the demixing curves for miscibility of polysulfone as a function of polymer concentration in a solvent mixture in which the ratio of the THF and carbon dioxide is kept constant at 87:13 by mass. (The fluid concentration was achieved in each experiment within an error margin of less than 0.03 wt %.) The polymer concentration range studied is from 0.28 to 4.99 wt %. At the polymer concentrations higher than 4.99 wt %, it is either unable to dissolve the polymer in the solvent mixture or impossible to mix the contents with the magnetic stirrer. It should be stressed that a homogenous solution was not achieved in the concentration range from 2.1 to 3.6 wt % in the pressure range studied. At 0.28 and 4.99 wt % polymer concentrations, both UCST-type and LCST-type phase behaviors were observed. At 0.28 wt % polysulfone concentration, the system shows UCST-type behavior at low temperatures (below 340 K), but shifts to LCST-type behavior as the temperature is increased (above 380 K). At 4.99 wt %, the crossover from UCST to LCST is shifted to the lower temperatures, to about 325 K. For the other polymer concentrations, only LCST-type phase behavior was observed in the temperature range investigated.

By taking a constant temperature or pressure cut of Figure 8.2, the pressure-polymer concentration (P-X) and temperature- polymer concentration (T-X) phase diagrams can be generated. Figure 8.3 shows the P-X curves at six temperatures in the range from 313 to 418 K. There are two separated miscibility domains shown at each temperature within this concentration range. For example at 418.3 K the first miscibility domain is at P > 57 MPa in the polymer concentration range of 0.3 – 2.1 wt %. The second domain is observed at concentrations greater than 3.6 wt % and at pressures greater than 55 MPa. Remarkably, the system is not miscible in the polymer concentration range from 2.1 to 3.6 wt %, and the demixing pressures increase extremely rapidly as illustrated by the dash lines in this figure.

Figure 8.4 shows the T-X curves at three pressures: 57, 55 and 53 MPa. Other than these three pressures, it is difficult to take constant pressure cuts that would include the data of most of the concentrations. Because the demixing pressure of 0.28 wt % is higher than 60 MPa for all the temperatures, it is not included in this diagram. Once again, the system is not completely miscible in the concentration range from 2.1 to 3.6 wt %. At 57 MPa, for 4.99 wt % solution, phase separation is encountered at two temperatures (filled and open triangle) which must be on the miscibility loop defining this region. A more complete picture of a miscibility loop with closure on the lower part of the loop can perhaps be observed but the present data would suggest the generation of more data at lower temperatures, going to sub-ambient conditions.

Figure 8.5 shows the P-T diagram of this ternary system in a solvent mixture with lower CO_2 level, (10 wt % instead of 13 wt %), for polymer concentrations in the range from 1.0 to 5.0 wt %. Figure 8.6 and 8.7 are the P-X and T-X phase diagrams generated

from Figure 8.5 by constant temperature and pressure cuts. The general features are similar to those observed in the 87:13 mixtures.

However, as shown in Figure 8.6, the two miscibility regions now partially merge, forming one region of miscibility with a local maximum in pressure below which the two-phase region could still be entered in the concentration range from about 2.0 to 3.6 wt %. This 'W'-type of phase boundary evolves from the 'double U'-type of phase boundary as the CO_2 level in the solvent mixture is reduced. In the T-X diagrams, the phase boundary at 40 MPa gives an 'M'-type of phase diagram, indicating that two homogeneous region merge at somewhere around 3.0 wt % polysulfone concentration. However, at the other pressures, the constant pressure cuts from the P-T diagram can only give two portions of curves, which means that either the potential merge temperature of the two separated one-phase regions is beyond the temperature range of measurement in the present study, or they still remain separated at this CO_2 level.

Since at the lower CO_2 level (10 wt %), the two isolated miscibility regions tend to merge into one region, it is very interesting to find out when these two regions completely merge into one. Therefore, the CO_2 level is further lowered to 8 % by mass in the solvent mixture. Figure 8.8 shows the P-T diagram for polymer concentrations in the range from 1.0 to 4.73 wt %. As discussed in the previous section, the demixing pressure decreases with decreasing the CO_2 content. The demixing pressures at this CO_2 level is observed in the range from 0 to about 40 MPa, while none of the demixing pressures for solutions with 13 wt % is lower than 40 MPa. Figure 8.9 shows the P-X diagram at several temperatures. Figure 8.10 shows the T-X phase diagram at 10, 20 and 30 MPa. In contrast to the double miscible regions observed in Figure 8.3 and 8.4 for 13 wt % CO_2

level and the partially merged double miscible regions in Figure 8.6 and 8.7 for 10 wt % CO_2 level, a single miscible region is observed at this CO_2 level.

Figures 8.11 and 8.12 offer a clearer comparison of these data and the merging of the miscibility regions with CO_2 level. These figures show pressure-composition phase diagrams at 313 and 418 K. The transition from a single miscible region to a 'W'-shape phase boundary, and then to ‘double U'-shape boundary with increasing CO_2 that results in two identifiable miscibility regions in the fluid mixture is clearly observed. Figure 8.13 summarizes this effect with a schematic diagram. In the pressure – polymer concentration domain (the upper diagram), with increasing CO_2 amounts in the solvent mixture, the miscibility of this polymer decreases, and the miscible region splits into two windows of miscibility. Even though it is not applicable to compare the T-X diagrams because of the demixing pressures occurring at quite different pressure ranges at these three CO_2 levels, the CO_2 effect on the T-X diagram is also shown in Figure 8.13 (the lower diagram). The increasing CO_2 content lowers the phase boundary, and reduces the miscible region.

8.3 The Volumetric Properties of Polysulfone in Binary Fluid Mixtures of THF + CO_2 under High Pressures

8.3.1 Volumetric Properties

Densities of the solutions with different polymer concentrations in the binary fluid mixture were also determined during the miscibility measurements. For each polymer solution, the densities were determined at 3.45 MPa intervals, starting at a high pressure in the one-phase conditions. For the measurements close to the phase separation

conditions, pressure intervals were adjusted so that the density data at the demixing condition could be determined.

Figure 8.14 shows the density of polymer solution containing 2.00 wt % polysulfone in the 87:13 mixture of THF + CO_2 at six temperatures: 301.8, 322.8, 344.8, 367.4, 398.8, and 422.4 K. The filled symbol in each curve represents the demixing condition at that temperature along the pressure reduction path. The densities of all these solutions increase almost linearly with pressure. Figure 8.15 shows the density of 2.00 wt % polysulfone in THF + CO_2 mixture with 10 wt % CO_2. Figure 8.16 shows the variation of the polymer solution density in solvent mixture with 8 wt % CO_2. The diagrams showing the variation of densities at other polymer concentrations are included in Appendix A. As shown in all the density results, there is no significant change in the overall mixture density noted across the phase separation point. This suggests that the coexisting phases must have very similar densities, which is often the case for liquid-liquid phase separation at high pressures where the coexisting liquid phases do not differ much in density.

Figure 8.17 shows the variations of specific volume with polymer concentration at 425 K at selected pressures of 35, 45, and 55 MPa, which exhibits a distinct increase in specific volume at an intermediate polymer concentration. Even though not shown, similar patterns were also observed at other temperatures. Comparison of Figure 8.17 and Figure 8.6 reveals that the pressure-composition diagram and the specific volume-composition diagram have similar patterns. In the polymer composition range of 0-2.0 and 3.0 –3.6 wt %, the specific volume and the demixing pressures decrease with polymer concentration, while in 2.0 – 3.0 and 3.6 – 5.0 wt % range, the specific volume

and the demixing pressure increase with the polymer concentration. This suggests that the miscibility between the polymer and solvent mixture improves with decreasing specific volume of the solutions but becomes worse with increasing specific volume. Volume expansion is a well-known factor that leads to phase separation. Reduction in the specific volume and improved miscibility in the present system may arise from specific interactions, such as hydrogen bonding between the polymer, THF and CO_2. The strength of such specific interactions may vary with polymer concentration, pressure, temperature or solvent composition.

8.3.2 Isothermal Compressibility

The isothermal compressibility of the solvent mixtures and polymer solutions was evaluated from the density vs. pressure data using the following equation:

$$\kappa(P,T) = \frac{-1}{V(P,T)}\left(\frac{\partial V(P,T)}{\partial P}\right)_T = \frac{1}{\rho(P,T)}\left(\frac{\partial \rho(P,T)}{\partial P}\right)_T$$

A 3rd order polynomial was used to fit each set of density vs. pressure data, and then differentiated to evaluate the isothermal compressibility at different pressures. Figure 8.18 shows the pressure dependence of isothermal compressibility at the selected temperatures for the 2.00 wt % polysulfone solution in THF and CO_2 mixture with 90:10 mass ratio. As expected, the isothermal compressibility decreases with pressure but increases with temperature. The compressibilities vary in the range from about 8 to 21 $\times$ 10^{-4} $(MPa)^{-1}$. Similar values were observed for other polymer concentrations. This is demonstrated in Figure 8.19, which shows the isothermal compressibility as a function of pressure for different polymer concentrations from 0 to 4.96 wt % at 423 K. The presence

of polymer in the solvent mixtures at these concentration levels (i.e. < 5 wt %) does not change the isothermal compressibility significantly. Evaluation at other temperatures did not show significant differences on the polymer concentration.

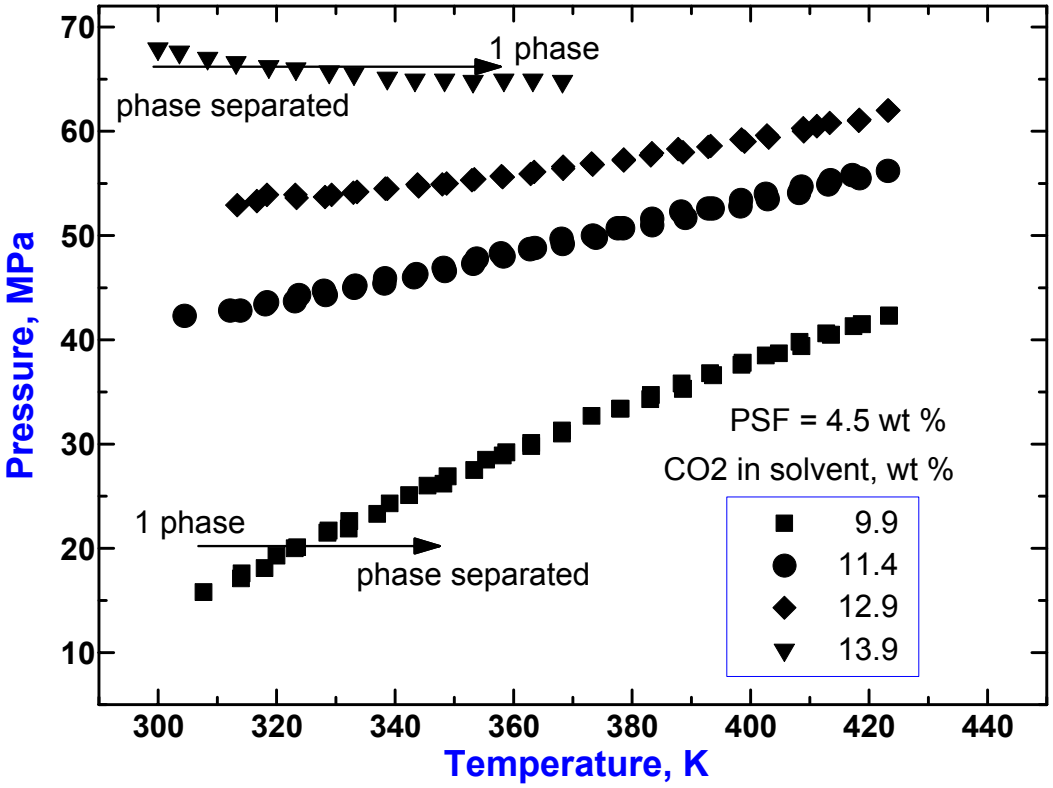

Figure 8.1. Variation of demixing pressures for 4.5 wt % polysulfone solutions in the THF/CO_2 binary solvents with CO_2 concentrations at 9.9, 11.4, 12.9, and 13.9 wt %.

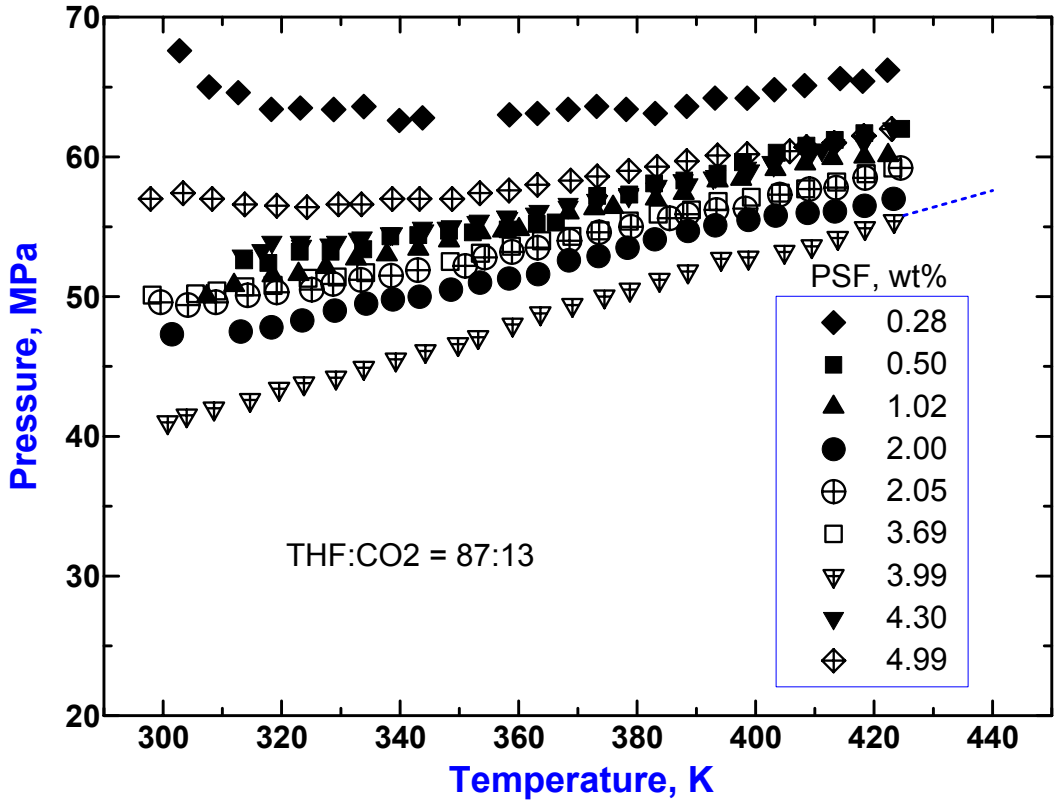

Figure 8.2. Variation of demixing pressures for polysulfone solutions in the THF/CO_2 binary solvents with THF:CO_2 = 87:13 at polymer concentrations of 0.28, 0.50, 1.02, 2.00, 2.05, 3.69, 3.99, 4.30, and 4.99 wt %.

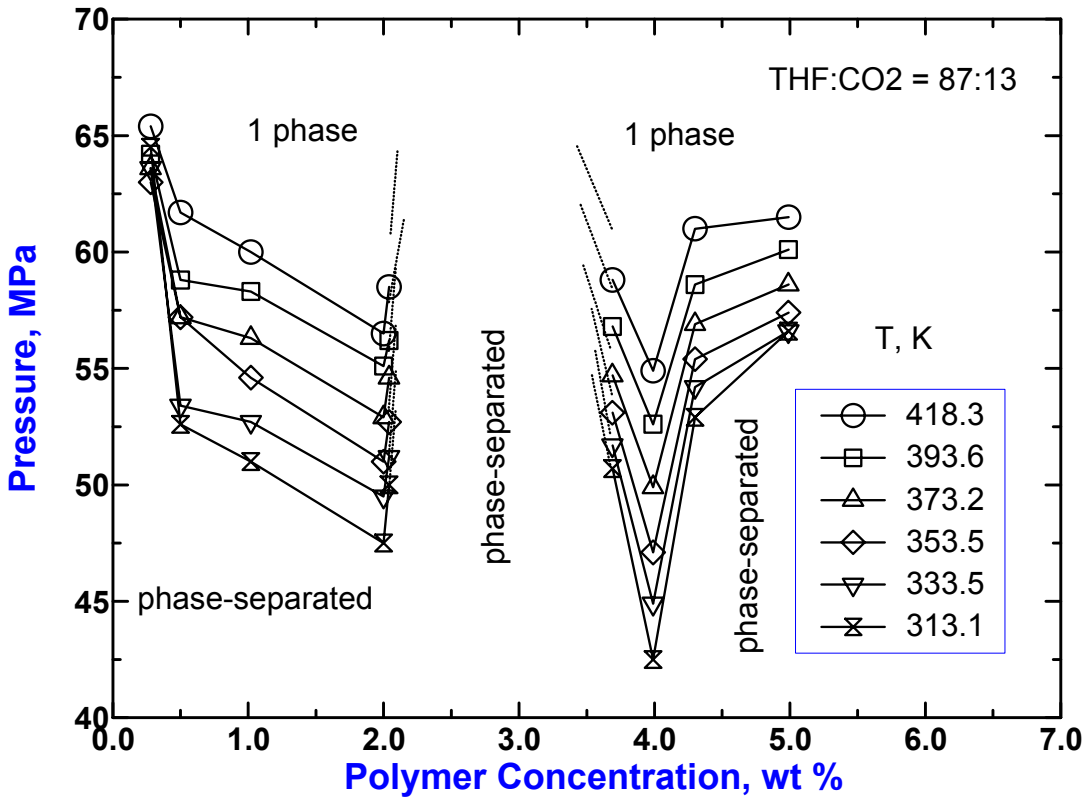

Figure 8.3. Variation of demixing pressures with polymer compositions for polysulfone solutions in the THF/CO_2 binary solvents with THF:CO_2 = 87:13 at temperatures of 313.1, 333.5, 353.5 373.2, 393.6 and 418.3 K.

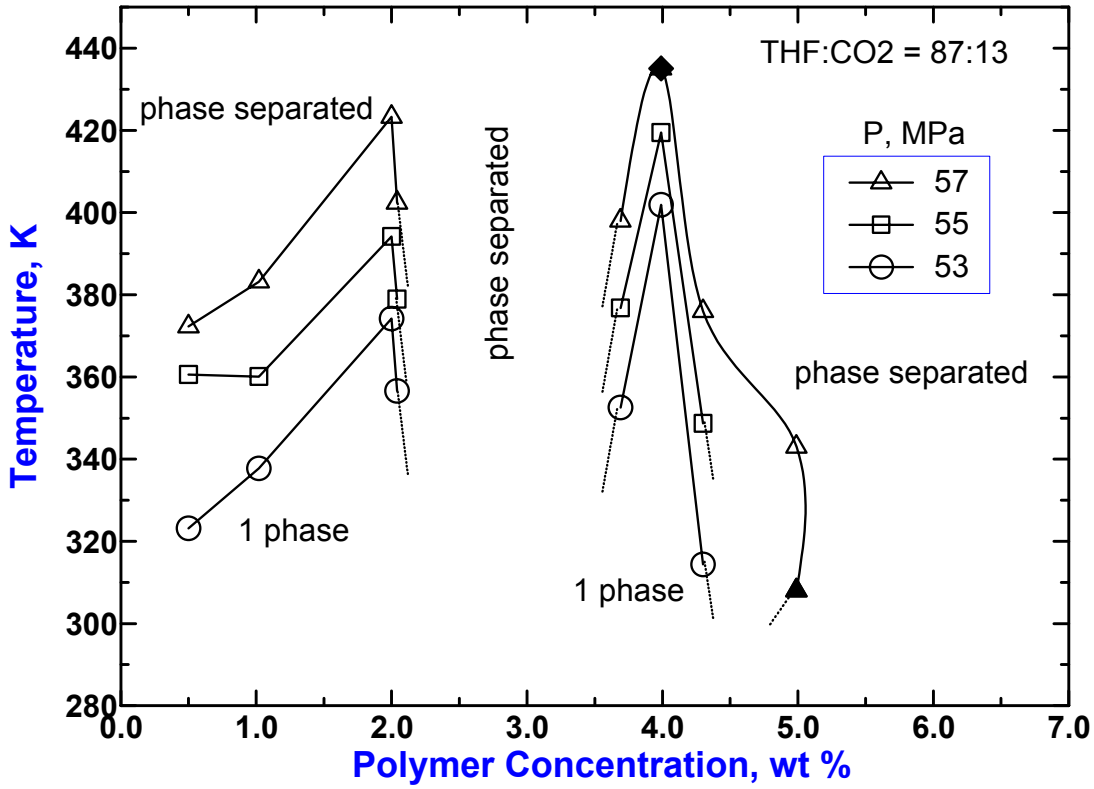

Figure 8.4. Temperature-Composition curves for polysulfone solutions in the THF/CO_2 binary solvents with THF:CO_2 = 87:13 at pressures of 53, 55, and 57 MPa. ▲: corresponds to a second phase separation point at 57 MPa at concentration 4.99 wt %. ♦ is an extrapolated point from the dotted portion of 3.99 wt % curve in Figure 8.2.

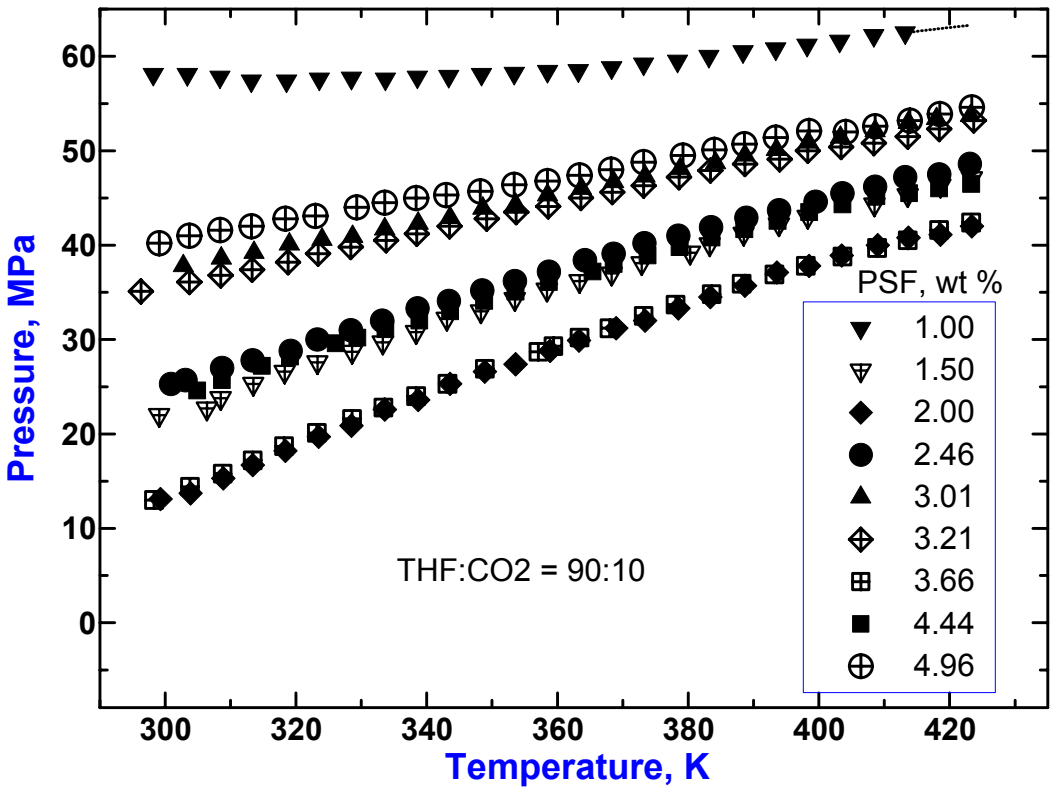

Figure 8.5. Variation of demixing pressures for polysulfone solutions in the THF/CO_2 binary solvents with THF:CO_2 = 90:10 at polymer concentrations of 1.00, 1.50, 2.00, 2.46, 3.01, 3.21, 3.66, 4.44, and 4.96 wt %.

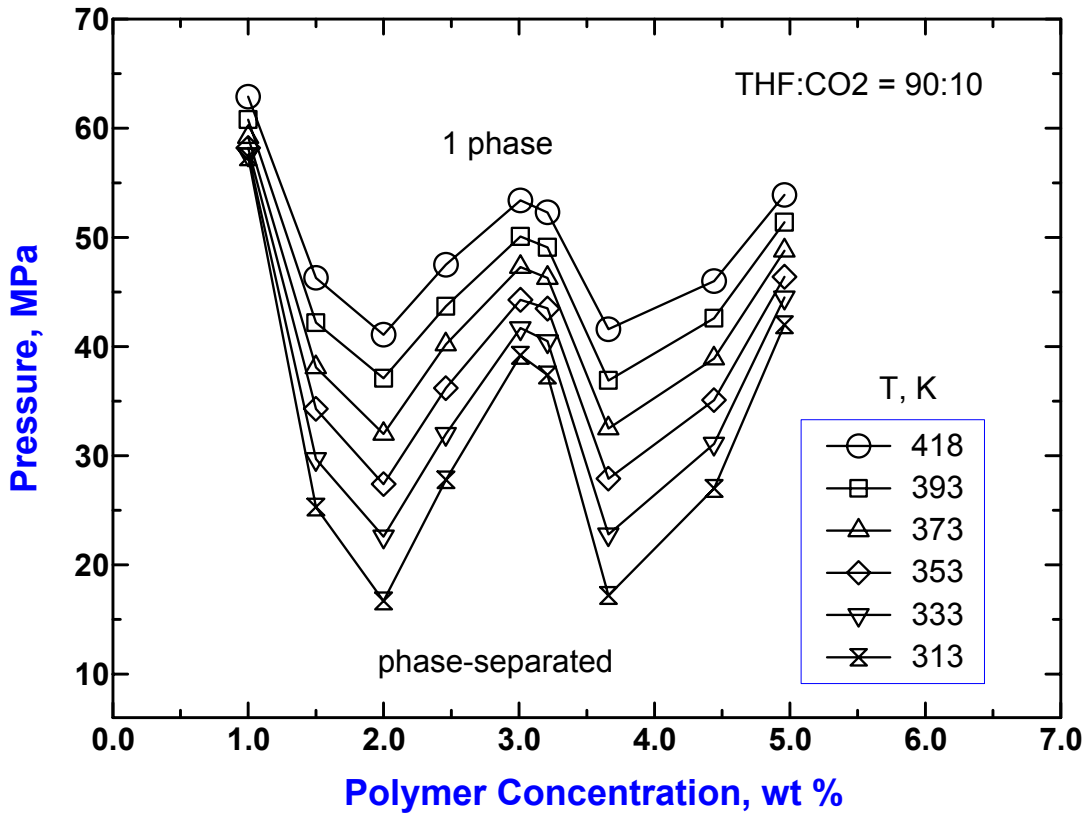

Figure 8.6. Variation of demixing pressures with polymer compositions for polysulfone solutions in the THF/CO_2 binary solvents with THF:CO_2 = 90:10 at temperatures of 313, 333, 353 373, 393 and 418 K.

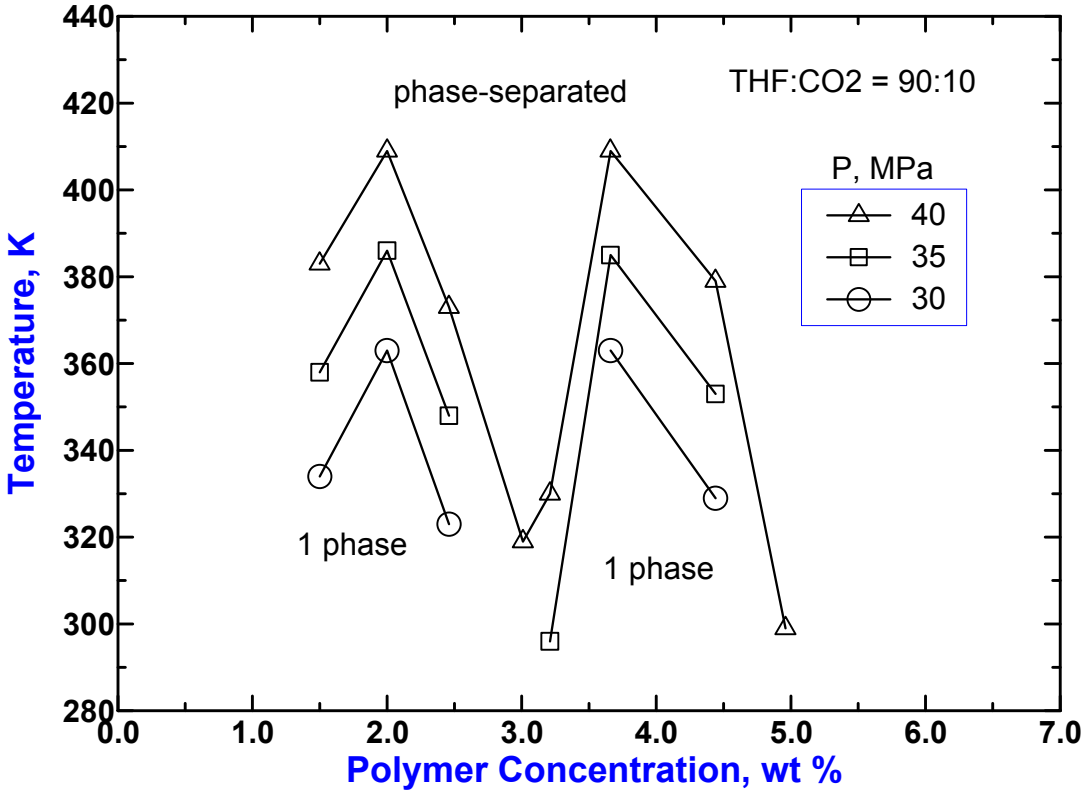

Figure 8.7. Temperature-Composition curves for polysulfone solutions in the THF/CO_2 binary solvents with THF:CO_2 = 90:10 at pressures of 30, 35, and 40 MPa.

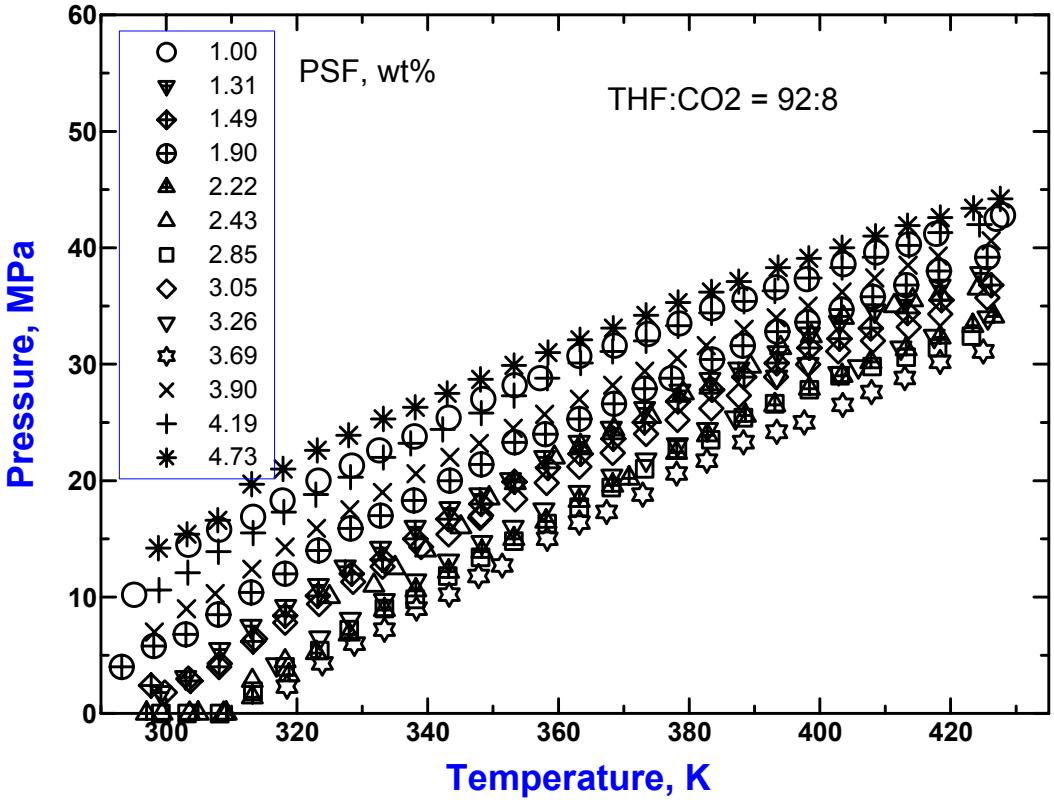

Figure 8.8. Variation of demixing pressures for polysulfone solutions in the THF/CO_2 binary solvents with THF:CO_2 = 92:8 at polymer concentrations of 1.00, 1.31, 1.49, 1.90, 2.22, 2.43, 2.85, 3.05, 3.26, 3.69, 3.90, 4.19, and 4.73 wt %.

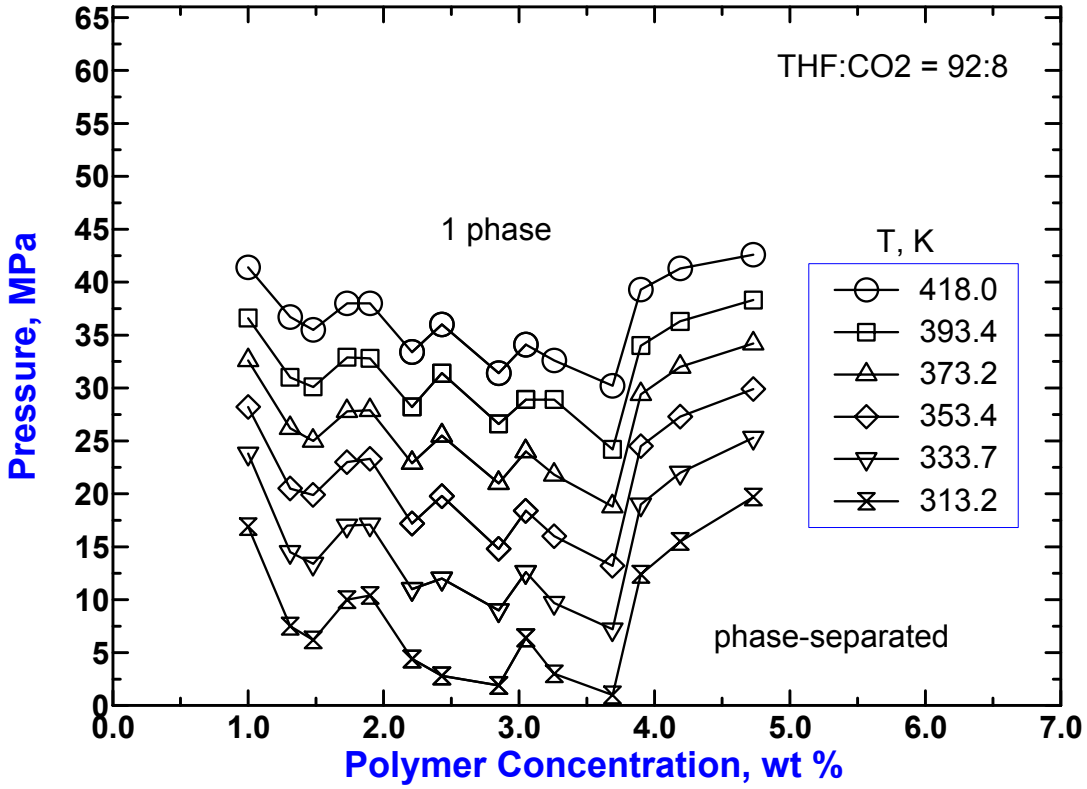

Figure 8.9. Variation of demixing pressures with polymer compositions for polysulfone solutions in the THF/CO_2 binary solvents with THF:CO_2 = 92:8 at temperatures of 313, 333, 353 373, 393 and 418 K.

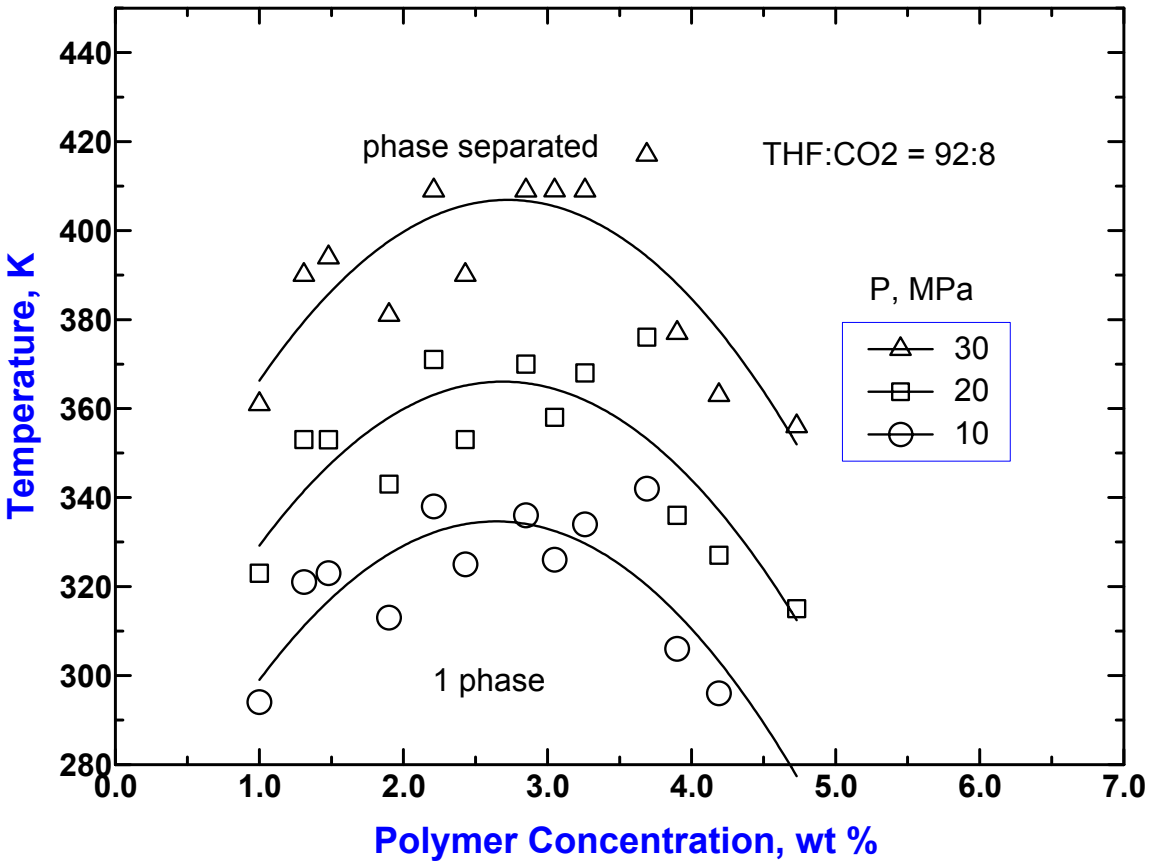

Figure 8.10. Temperature-Composition curves for polysulfone solutions in the THF/CO_2 binary solvents with THF:CO_2 = 92:8 at pressures of 10, 20, and 30 MPa.

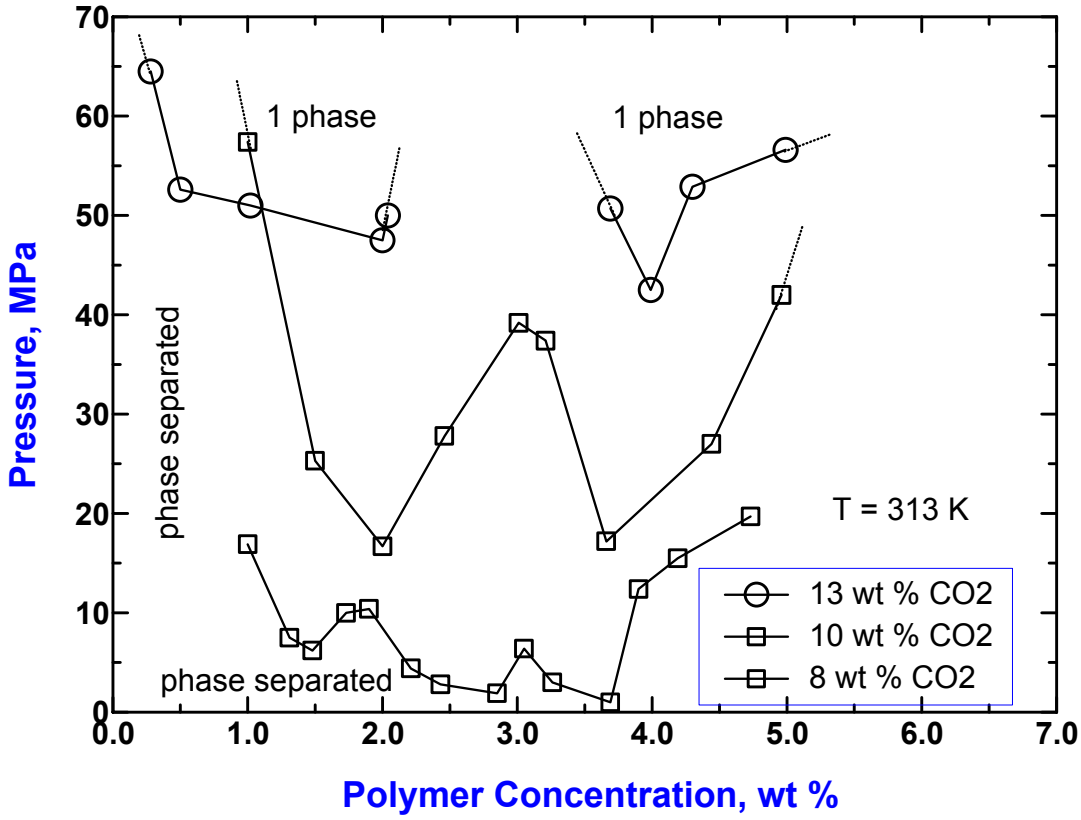

Figure 8.11. Comparison of demixing pressures as a function of polymer composition at 313 K for polysulfone +THF + CO_2 system with 8, 10 and 13 wt % CO_2 in the solvent mixtures.

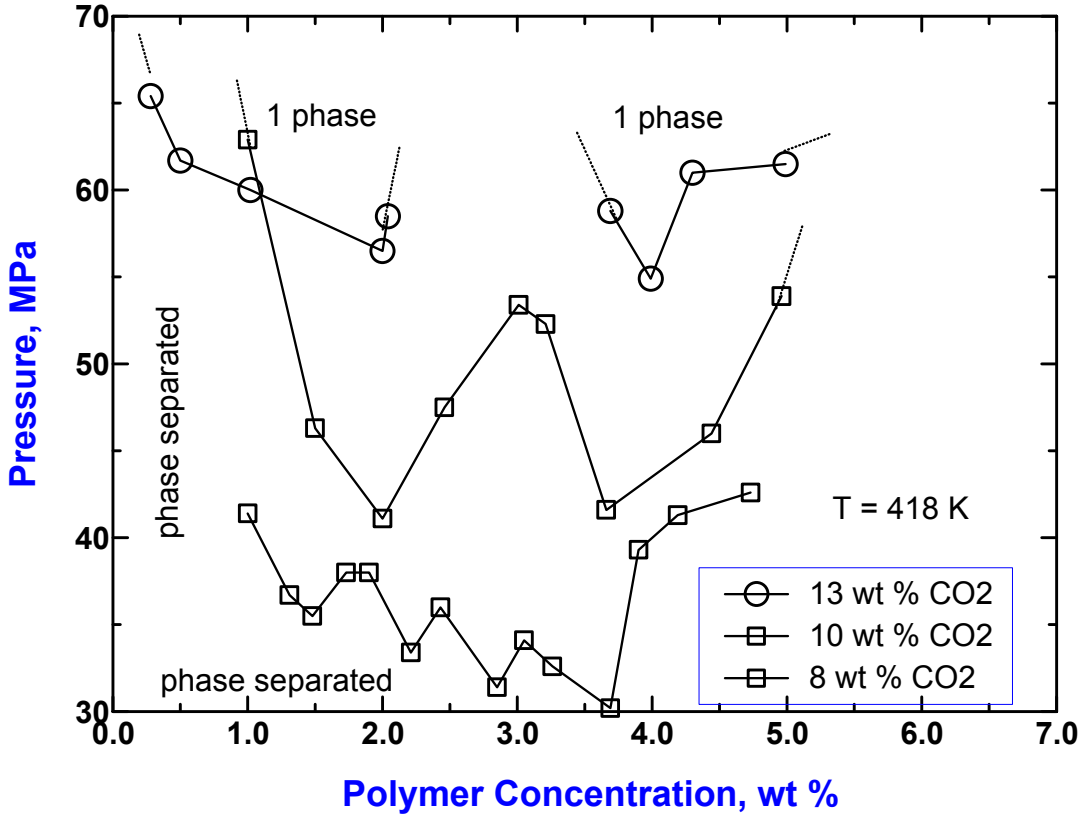

Figure 8.12. Comparison of demixing pressures as a function of polymer composition at 418 K for polysulfone +THF + CO_2 system with 8, 10 and 13 wt % CO_2 in the solvent mixtures.

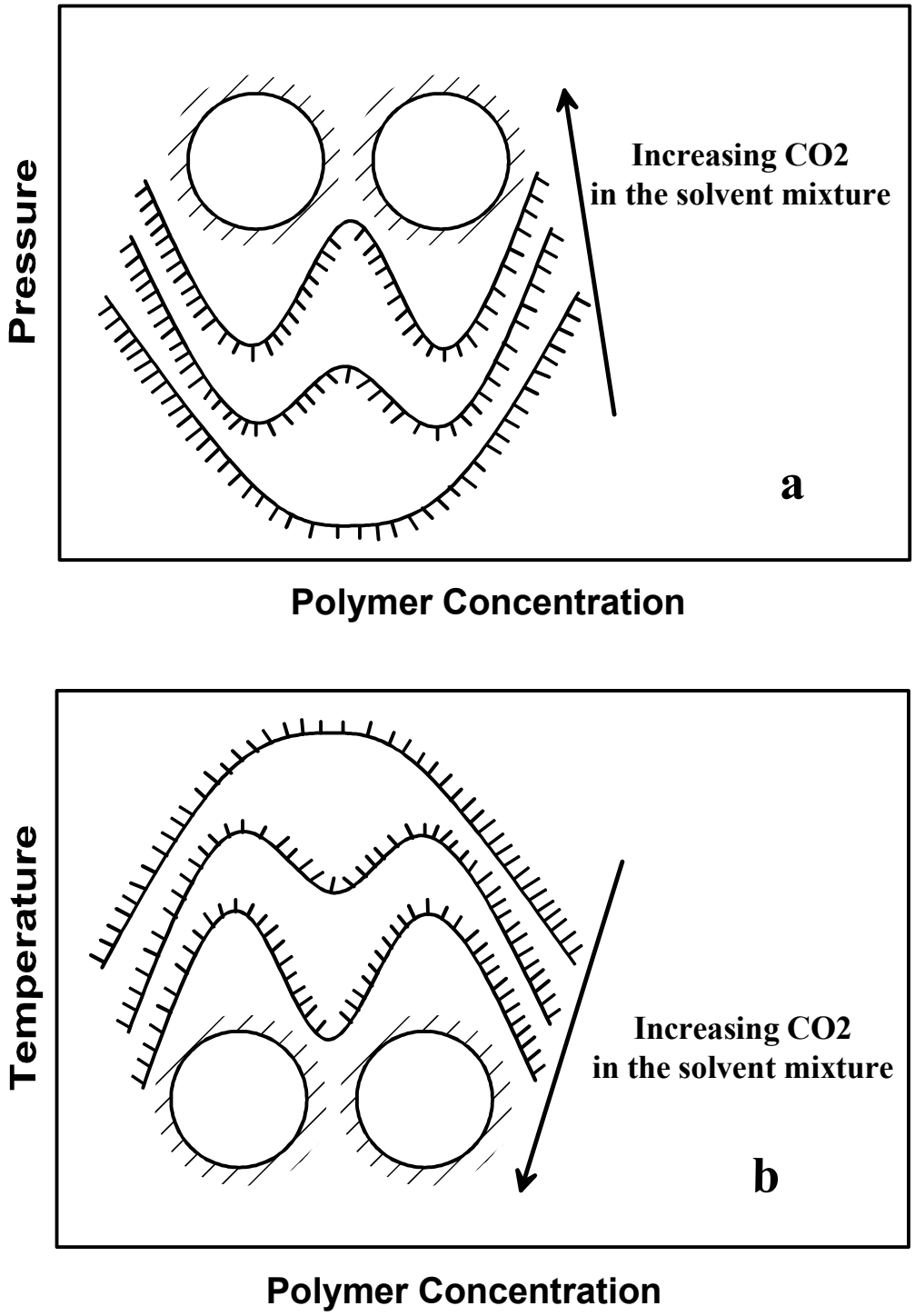

Figure 8.13. Schematic phase diagram for solutions of polysulfone in THF + CO_2 binary fluid mixtures. a: pressure vs. polymer concentration; b. temperature vs. polymer concentration.

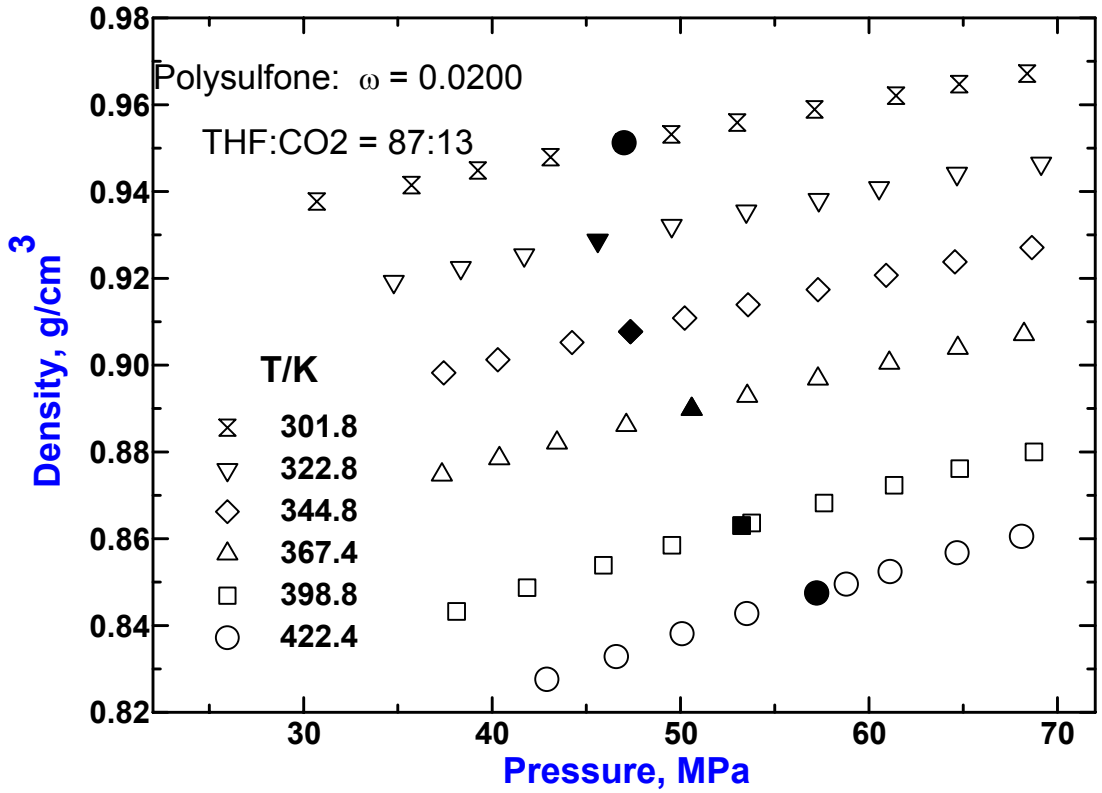

Figure 8.14. Pressure dependence of density for 2.00 wt % polysulfone solution in the THF and CO_2 solvent mixture (THF:CO_2 = 87:13) at 301.8, 322.8, 344.8, 367.4, 398.8, and 422.4 K. Filled data points are the densities at the phase separation points.

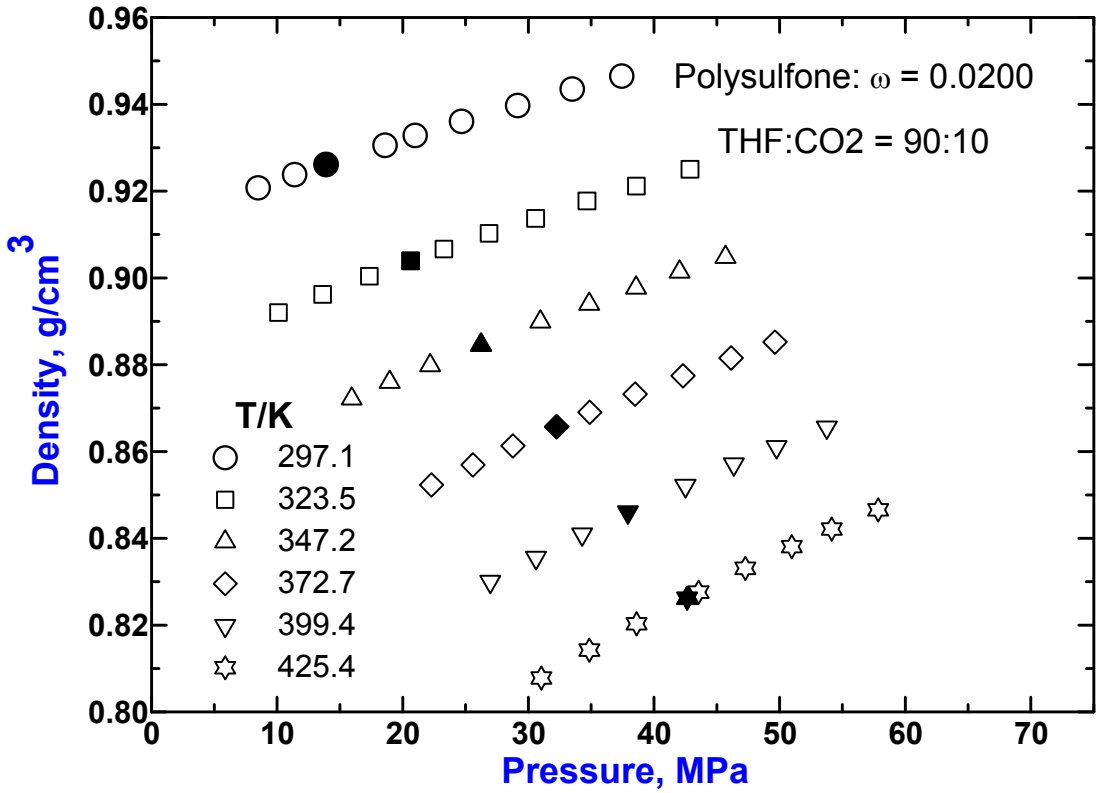

Figure 8.15. Pressure dependence of density for 2.00 wt % polysulfone solution in the THF and CO_2 solvent mixture (THF:CO_2 = 90:10) at 297.1, 323.5, 347.2, 372.7, 399.4, and 425.4 K. Filled data points are the densities at the phase separation points.

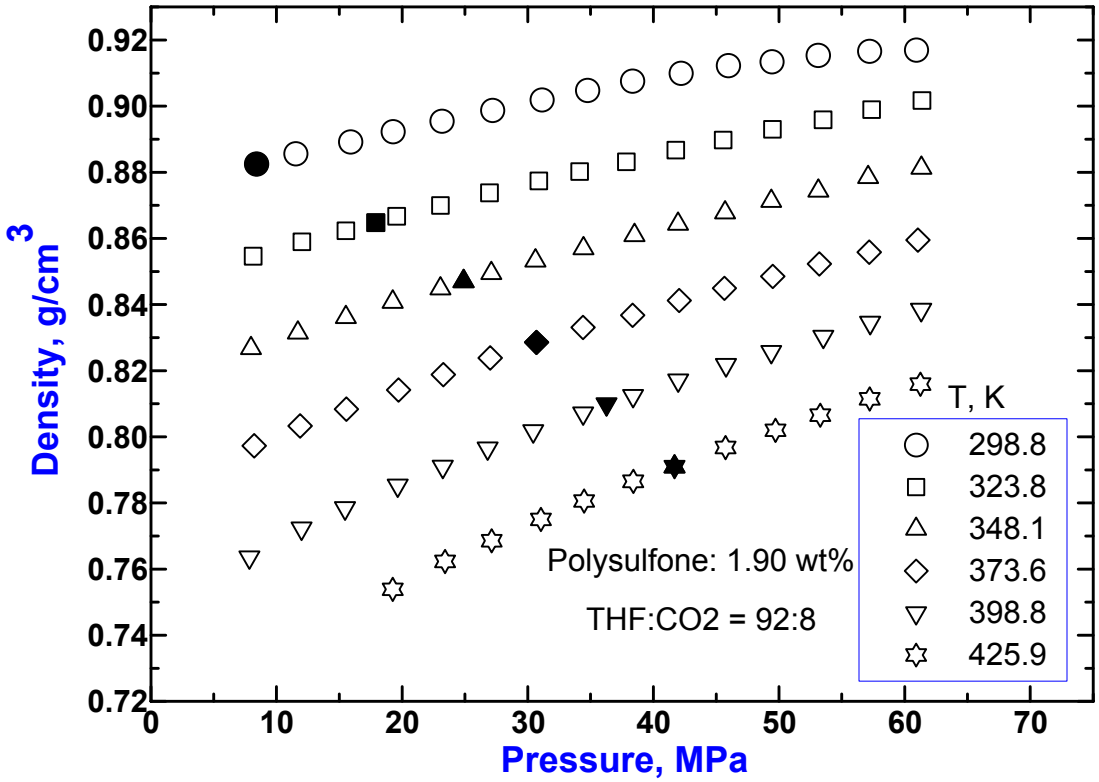

Figure 8.16. Pressure dependence of density for 1.90 wt % polysulfone solution in the THF and CO_2 solvent mixture (THF:CO_2 = 92:8) at 298.8, 323.3, 348.1, 373.6, 398.8, and 425.9 K. Filled data points are the densities at the phase separation points.

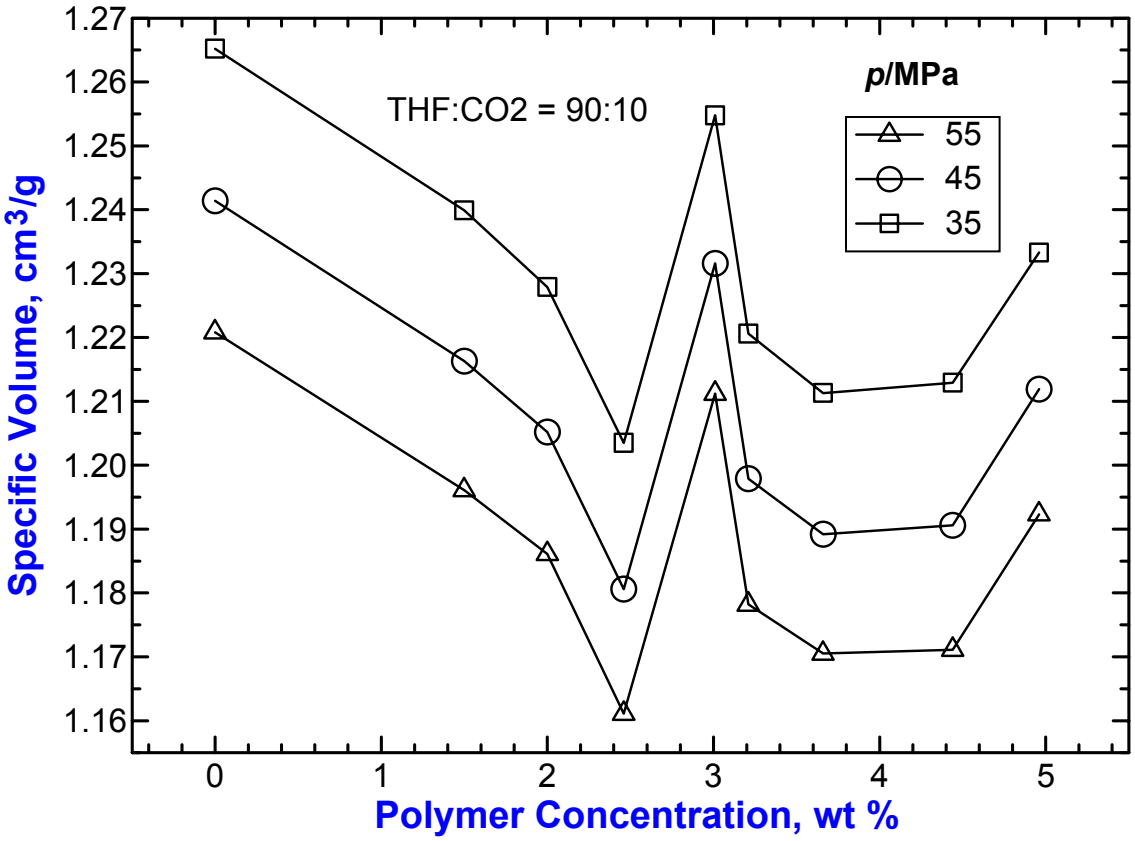

Figure 8.17. Variation of specific volume with polymer concentration at different pressures for polysulfone solutions in THF + CO_2 mixture (THF:CO_2 = 90:10) at 425 K.

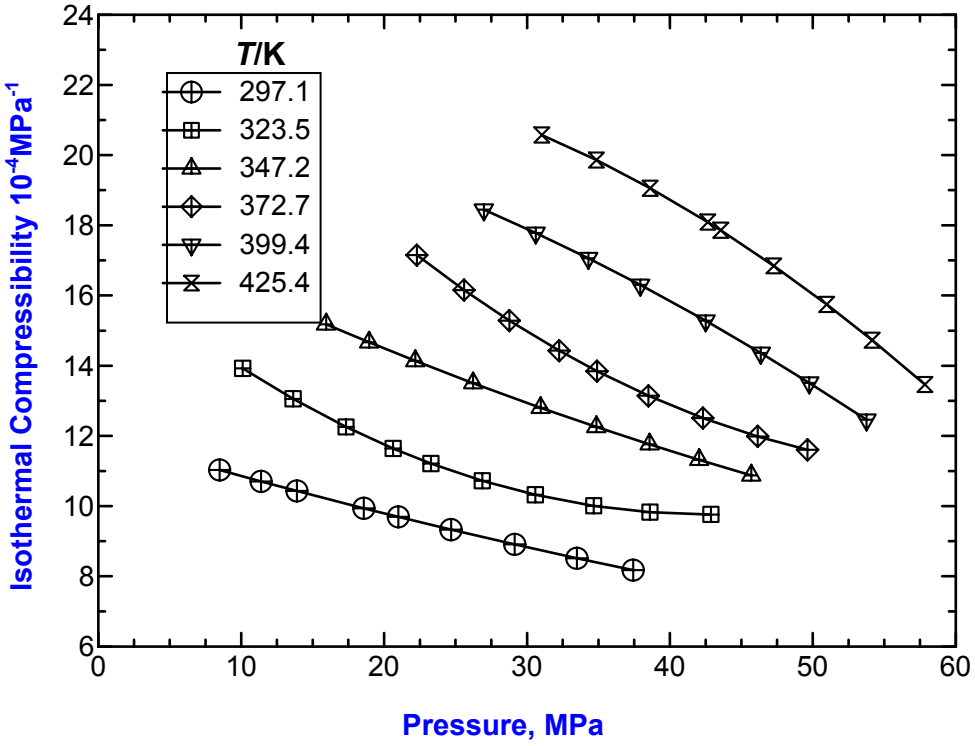

Figure 8.18. Variation of isothermal compressibility with pressure for 2.00 wt % polysulfone solution in the THF and CO_2 solvent mixture (THF:CO_2 = 90:10) at 297.1, 323.5, 347.2, 372.7, 399.4, and 425.4 K.

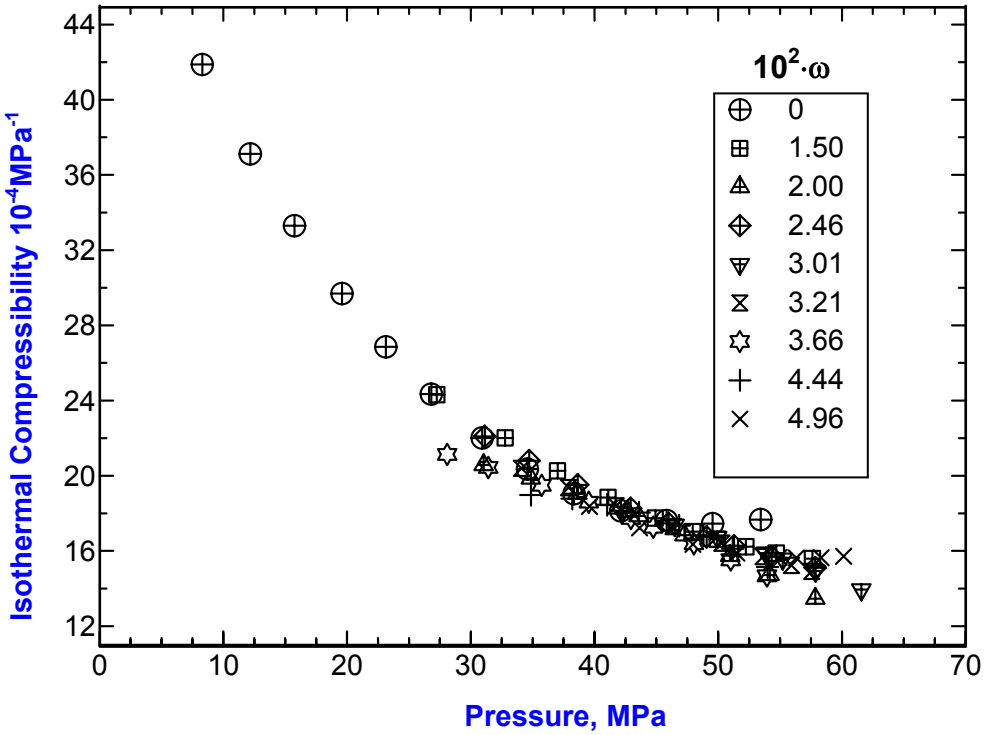

Figure 8.19. Pressure dependence of isothermal compressibility for different polysulfone solution in the THF and CO_2 solvent mixture (THF:CO_2 = 90:10) at 423 K.

Chapter 9

Kinetics of Pressure-Induced Phase Separation in PSF + THF + CO_2 Solutions

In this chapter, the experimental results on the kinetics of pressure-induced phase separation in solutions of polysulfone in THF + CO_2 are described. As discussed in Chapter 8, the polysulfone solutions in THF + CO_2 display multiple miscibility regions. Slow pressure reduction processes were used to determine the binodal envelope of this system at different compositions. At each concentration and temperature, several rapid pressure quenches with different depth were imposed on the system that is slightly above the binodal point. The time evolution of the phase-separating solutions was followed by light scattering experiments. The scattering patterns were used to determine the phase separation mechanism. The average new phase sizes are evaluated using the angular dependence of the scattered light intensity. The results for polysulfone solutions in THF and CO_2 solvent mixtures with mass ratio of 90:10 at several polysulfone concentrations are presented. Several concentrations and temperatures were selected for the rapid pressure quench experiments. The concentrations, temperatures and the pressure quench depths that have been tested are listed in Table 9.1.

Table 9.1. Polysulfone/THF/CO_2 solutions used in light scattering studies

Polysulfone Concentration, wt %	Temperature, K	Pressure Quench depth, MPa
1.99	372	2.3-6.8
2.61	368	0.7-5.8
2.87	363	0.22-4.7
2.87	374	0.5-3.48
3.13	363	0.4-2.96
3.20	323	0.74-5.1
3.26	323	0.82-0.99

9.1 Time Evolution of the Scattered Light Profiles

Figure 9.1 shows the variation of the temperature, pressure, the inverse of the averaged scattered light intensity, and the transmitted light intensity with time during a rapid pressure quench process in 2.87 wt % PSF solution at 363 K. The inverse of the averaged scattered light intensity is plotted as a function of the pressure in the lower curve. The start time (t_i) and end time (t_f) of the pressure quench can be found from the P-t curve, which determined to be 1.2 and 1.9 seconds. The temperature was maintained at 363 K during the whole process. The pressure quench depth is 0.22 MPa as determined from the lower curve on this figure. Figure 9.2 presents the scattered light intensity as a function of the wavenumber *q* at different times, from 0 to 24.8 seconds. The scattered light intensity shows monotonic decreasing with increasing q value without a distinct maximum. At each scattering angle, the scattered light intensity increases with time after the quench is imposed on the system. The number of seconds used to label the scattered light profiles are the total time elapsed from time zero. So the actual phase separation time is the total time minus the pre-quench time, which is 1.2 seconds in this case. For this shallow pressure quench experiment, the temperature is well maintained at the 363.1

K with little variations. However, the cooling effect during the pressure quenches plays a role for a deeper quenches as shown in Figure 9.3, for a quench depth of 2.4 MPa. The cooling effect brings the temperature down by about 0.2 K. The temperature recovers quickly in half seconds.

Figures 9.4 – 9.9 show the time evolution of the scattered light intensities for the same polymer solution after deeper pressure quenches from 0.53 MPa to 4.7 MPa. Similar features in the scattering profiles were found in these experiments in spite of the quench depth. It has been noted that the overall intensity of the scattered light increases with increasing the quench depth. For example, the scattered light intensity at q = 0.276 and near the end of process (around 25th second) increases from 7.2 (see Figure 9.2) at quench depth = 0.22 MPa, to 12.5 (see Figure 9.4) at quench depth = 0.53 MPa, and to about 200 (see Figure 9.9) at quench depth = 4.7 MPa.

The pressure quench experiments have been done on other concentrations and temperatures as listed in table 9.1. However, all of these scattering profiles display similar features. The scattered light intensity increases with time at all angles, and the scattering profiles show monotonic decrease with increasing scattering angles without maximum. This suggests that all the pressure quenches, no matter how deep they are, bring the system into the metastable region based on the scattering patterns. As mentioned in Chapter 8, this ternary system has unique phase behaviors with multiple miscible regions. It is not strange if the spinodal envelope is as irregular as the binodal envelope.

Even though the spinodal envelope could not be determined by the time evolution method, it can be determined using the extrapolation method. Figure 9.10 shows the

inverse of the scattered light intensity at q = 0.276 at 1 second after the pressure quench finishes, which is used as the rate of change in the scattered light intensity, versus the pressure quench depth in the 2.87 wt % polysulfone solution at 374 K. Extrapolation of the linear line to 1/Is = 0 indicates a metastable gap of 1.69 MPa. Similarly, the same method has been applied to the scattering data at 363 K in the same solution, which gives a metastable gap of 1.89 MPa. The metastable gaps determined for other concentrations are also included in Table 9.2.

Table 9.2. The metastable gap determined using the extrapolation method

PSF conc., wt %	Temperature, K	Metastable Gap, MPa
1.99	373	7.2 MPa
2.61	367	1.86
2.87	363	1.89
2.87	374	1.69
3.13	363	2.23
3.20	323	2.96

9.2 Particles Size Evolution

Equation 2.8 is used to evaluate the particle size in the phase separating system after pressure quenches. Figure 9.11 shows the evolution of the particle radius as a function of the time for 2.87 wt % solution after a 1.12 MPa pressure quench at 374 K. This figure reveals that the particles grow faster during the initial stage (the first 10 seconds), and then level off after the initial stage. A linear fit of the very early stage shows that the particle growth rate dR_{mL}/dt is about 0.46 μm/s. The particle size approaches a plateau value of 2.7 μm around the end of the experiment period. The

plateau particle radii have been identified for all other pressure quench experiments and they are plotted as a function of the quench depth in Figure 9.12. It is shown that the particle size is smaller at larger pressure quenches. This is reasonable because the larger the supersaturation, the smaller the particles are predicted. Similar phenomena have been found at other conditions of this system. Figure 9.13 shows that the particle growth rate dR_{mL}/dt in the initial stage as a function of the pressure quench depth in the 2.87 wt % solution at 374 K. The growth rate dR_{mL}/dt increases with increasing quench depth when the pressure quenches shallower than 1.65 MPa. But for deeper quenches than 1.65 MPa, the quench depth has no significant effect on the particle growth rate. The critical quench depth is very close to the metastable gap 1.69 MPa that is identified from the rate of change in the scattered light intensity versus pressure quench depth in Figure 9.6. This means that the particle size growth rate can also be effectively used to evaluate the metastable gap in addition to the inverse of the scattered light intensity.

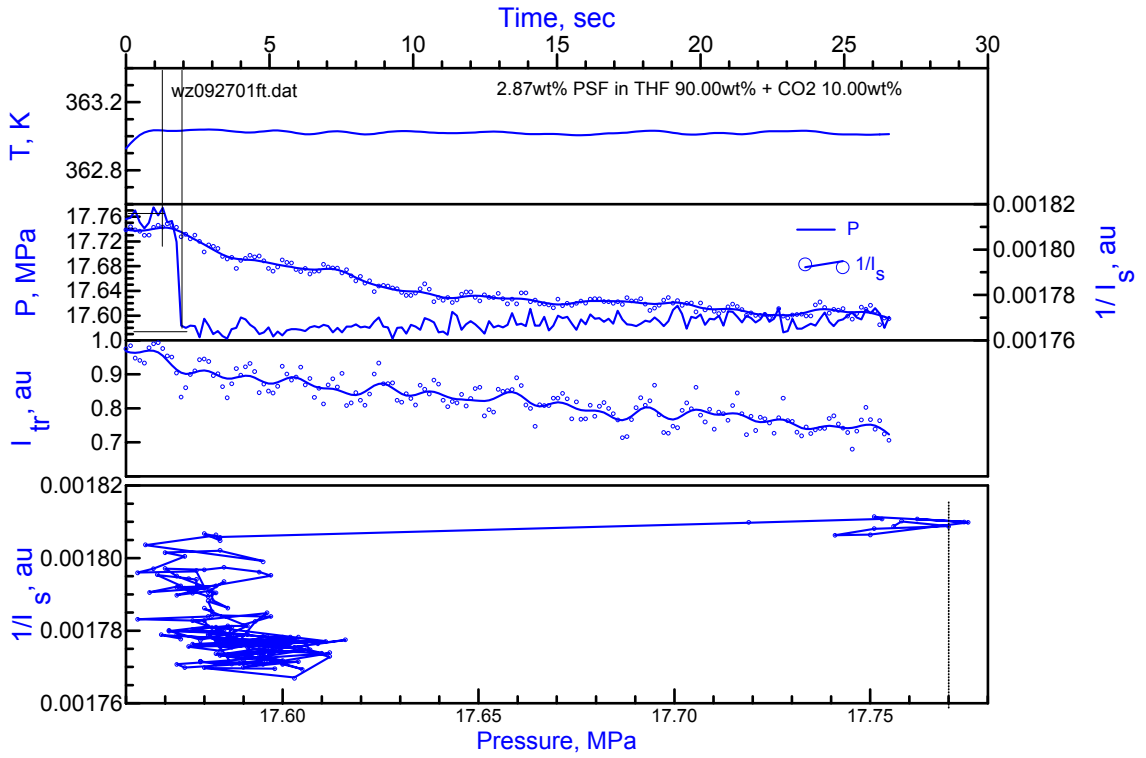

Figure 9.1. Variation of temperature (T), Pressure (P), transmitted light intensity (I_{tr}), and inverse averaged scattered light intensity (1/Is) with time during a fast pressure quench in 2.87 wt % solution of PSF in a mixture of THF (90 wt %) + CO_2 (10 wt %).

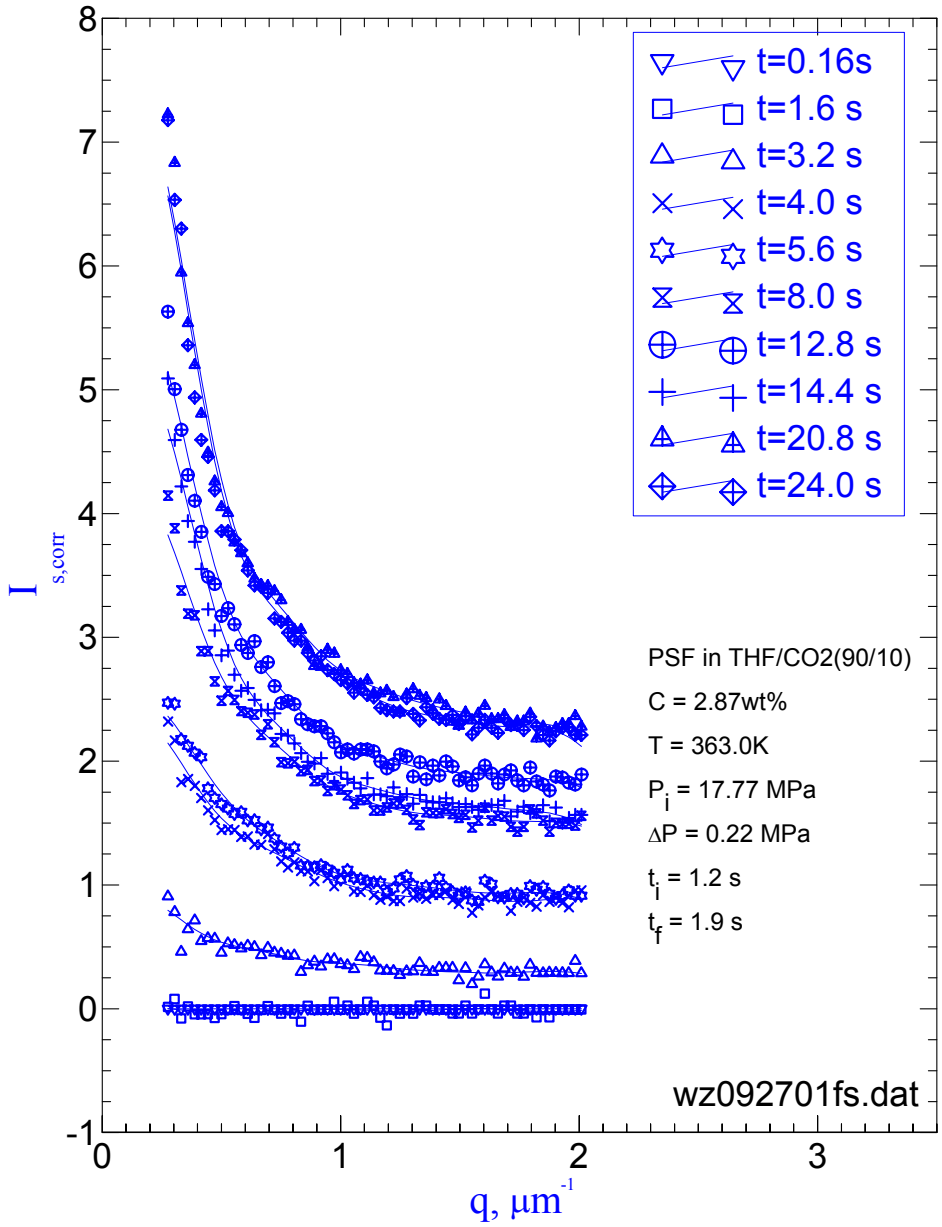

Figure 9.2. Time evolution of the scattered light intensities as a function of the wave number q after a pressure quench $\Delta P = 0.22$ MPa in 2.87 wt % solution of PSF in a mixture of THF (90 wt %) + CO_2 (10 wt %) at 363.0 K. The total observation time is 26 seconds. t_i: the time when the pressure quench starts; t_f: the time when the pressure quench ends.

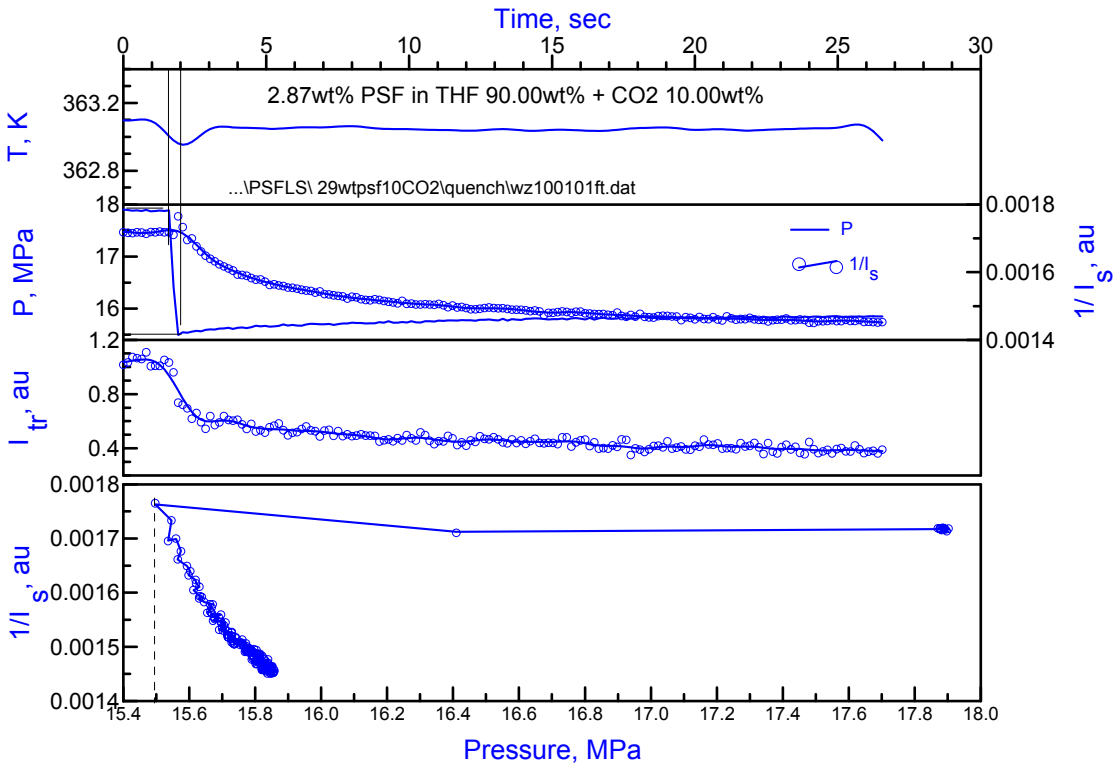

Figure 9.3. Variation of temperature (T), Pressure (P), transmitted light intensity (I_{tr}), and inverse averaged scattered light intensity ($1/I_s$) with time during a fast pressure quench in 2.87 wt % solution of PSF in a mixture of THF (90 wt %) + CO_2 (10 wt %).

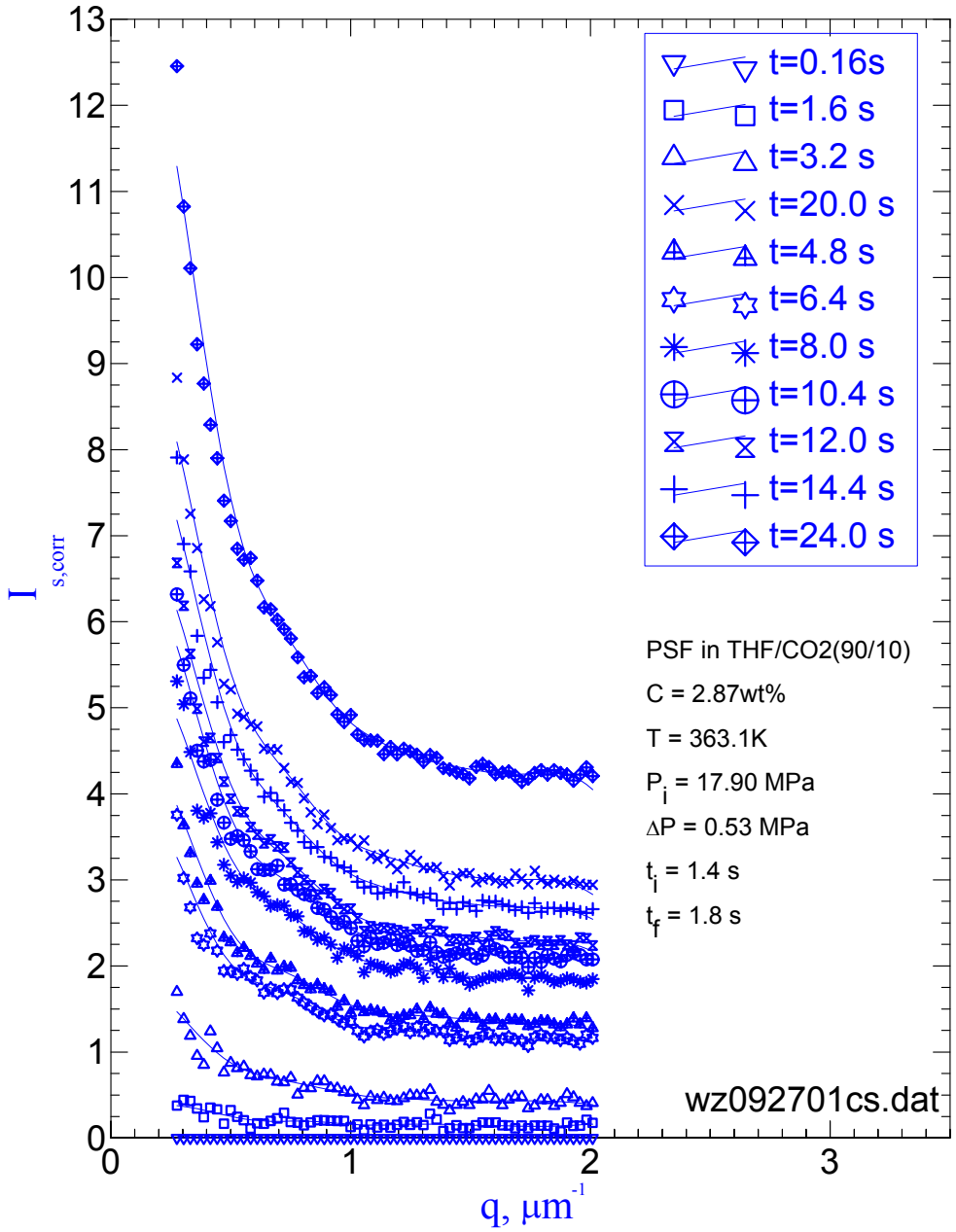

Figure 9.4. Time evolution of the scattered light intensities as a function of the wave number q after a pressure quench ΔP = 0.53 MPa in 2.87 wt % solution of PSF in a mixture of THF (90 wt %) + CO_2 (10 wt %) at 363.0 K. The total observation time is 26 seconds. t_i: the time when the pressure quench starts; t_f: the time when the pressure quench ends.

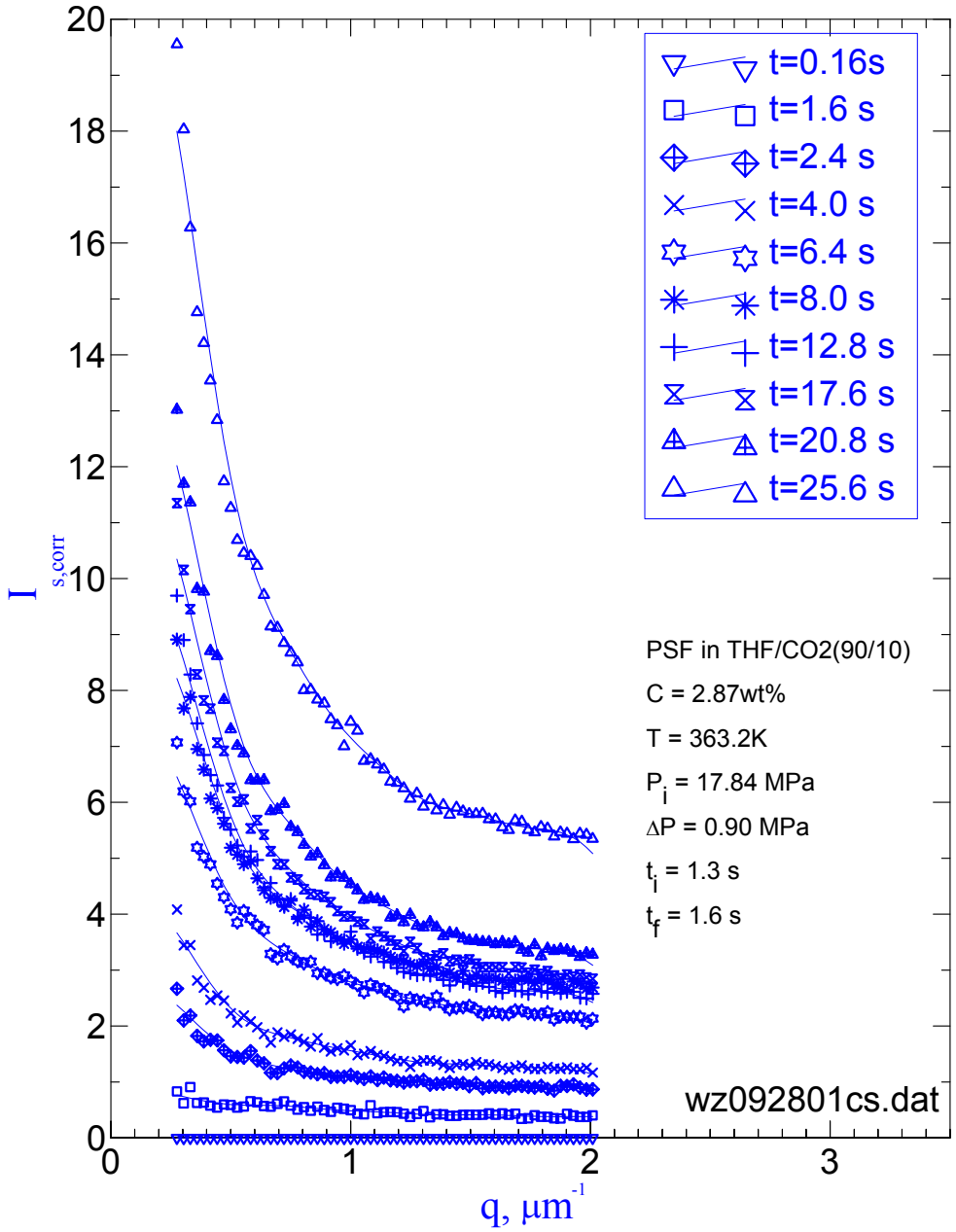

Figure 9.5. Time evolution of the scattered light intensities as a function of the wave number q after a pressure quench $\Delta P = 0.90$ MPa in 2.87 wt % solution of PSF in a mixture of THF (90 wt %) + CO_2 (10 wt %) at 363.0 K. The total observation time is 26 seconds. t_i: the time when the pressure quench starts; t_f: the time when the pressure quench ends.

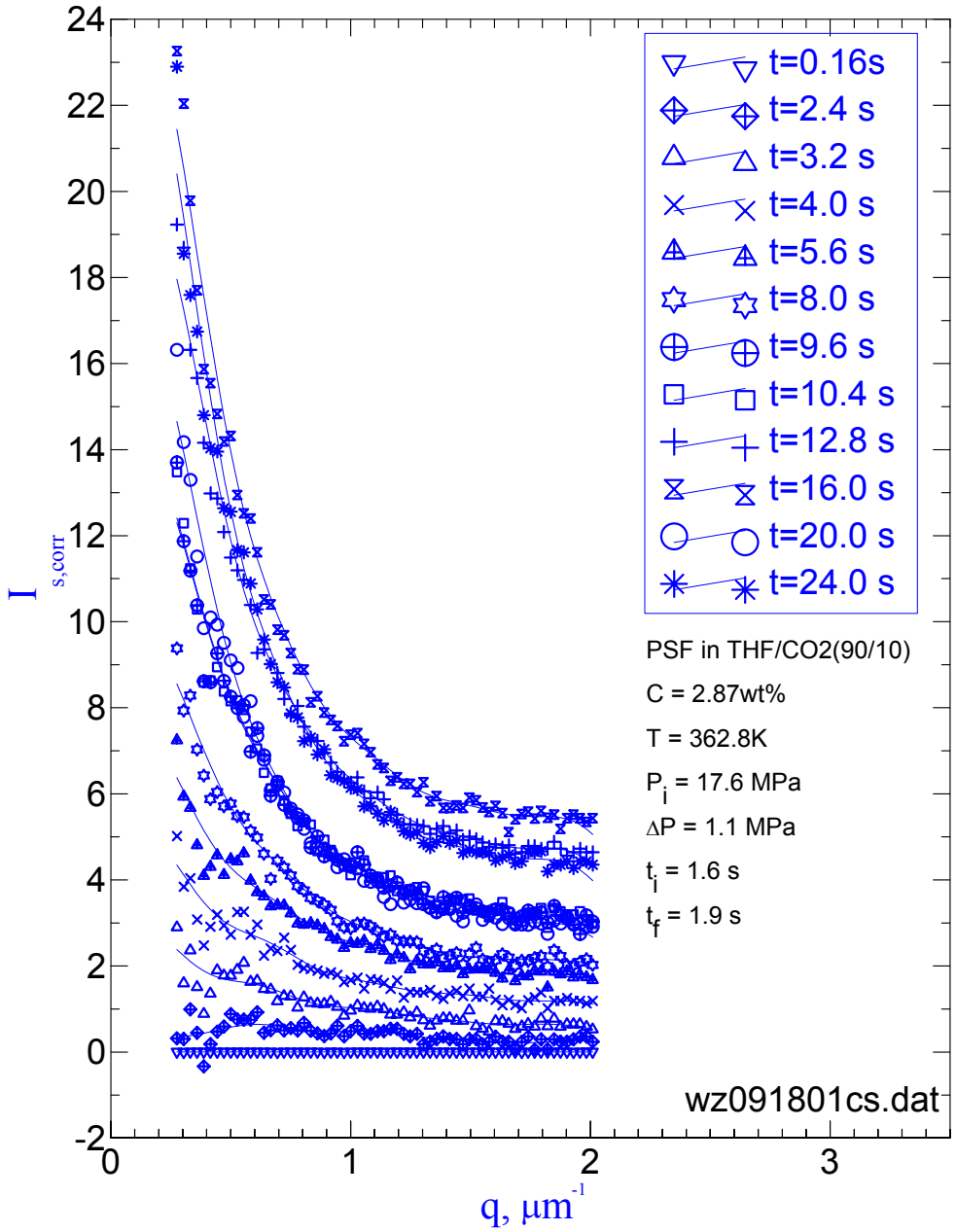

Figure 9.6. Time evolution of the scattered light intensities as a function of the wave number q after a pressure quench ΔP = 1.10 MPa in 2.87 wt % solution of PSF in a mixture of THF (90 wt %) + CO_2 (10 wt %) at 363.0 K. The total observation time is 26 seconds. t_i: the time when the pressure quench starts; t_f: the time when the pressure quench ends.

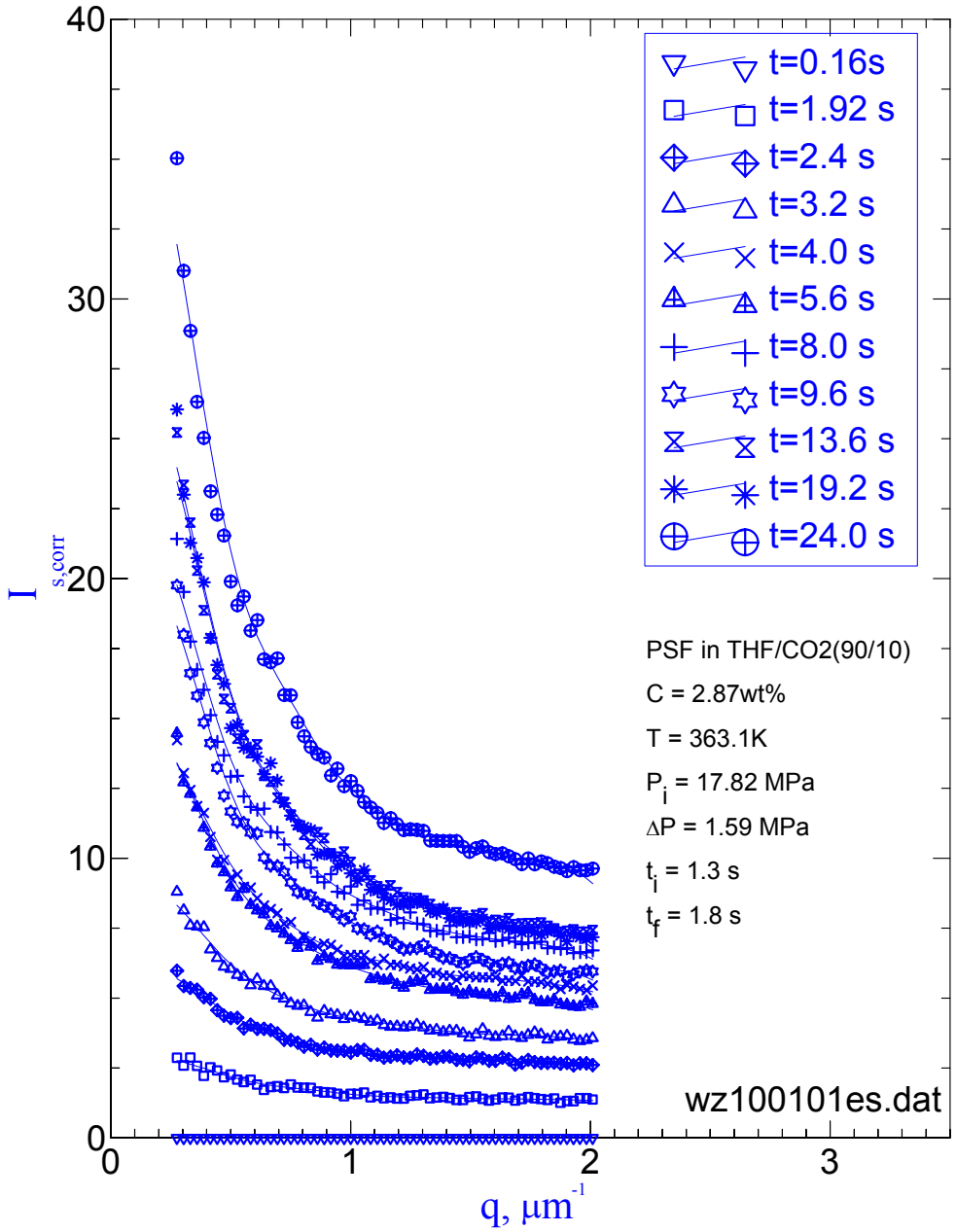

Figure 9.7. Time evolution of the scattered light intensities as a function of the wave number q after a pressure quench ΔP = 1.59 MPa in 2.87 wt % solution of PSF in a mixture of THF (90 wt %) + CO_2 (10 wt %) at 363.0 K. The total observation time is 26 seconds. t_i: the time when the pressure quench starts; t_f: the time when the pressure quench ends.

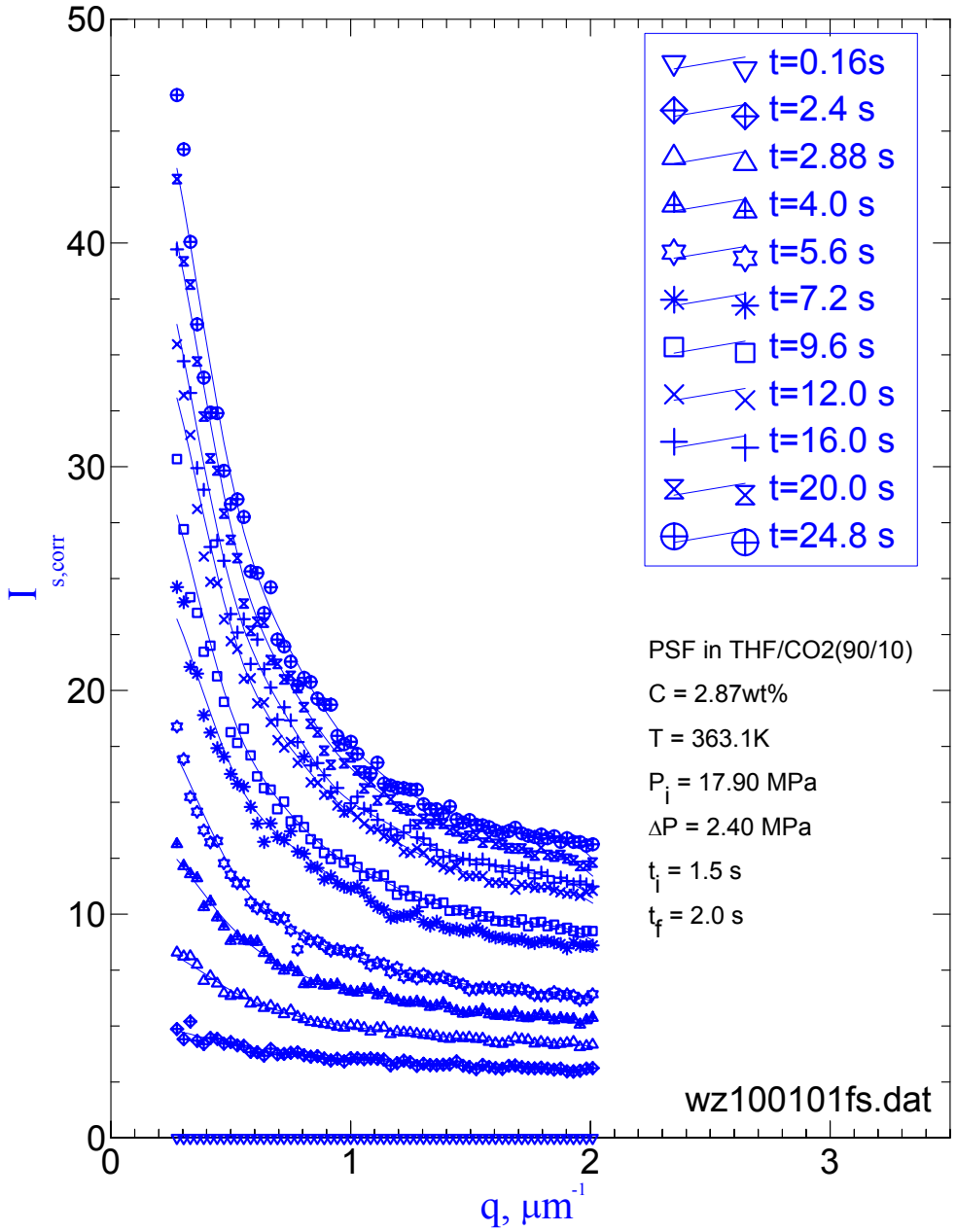

Figure 9.8. Time evolution of the scattered light intensities as a function of the wave number q after a pressure quench ΔP = 2.40 MPa in 2.87 wt % solution of PSF in a mixture of THF (90 wt %) + CO_2 (10 wt %) at 363.0 K. The total observation time is 26 seconds. t_i: the time when the pressure quench starts; t_f: the time when the pressure quench ends.

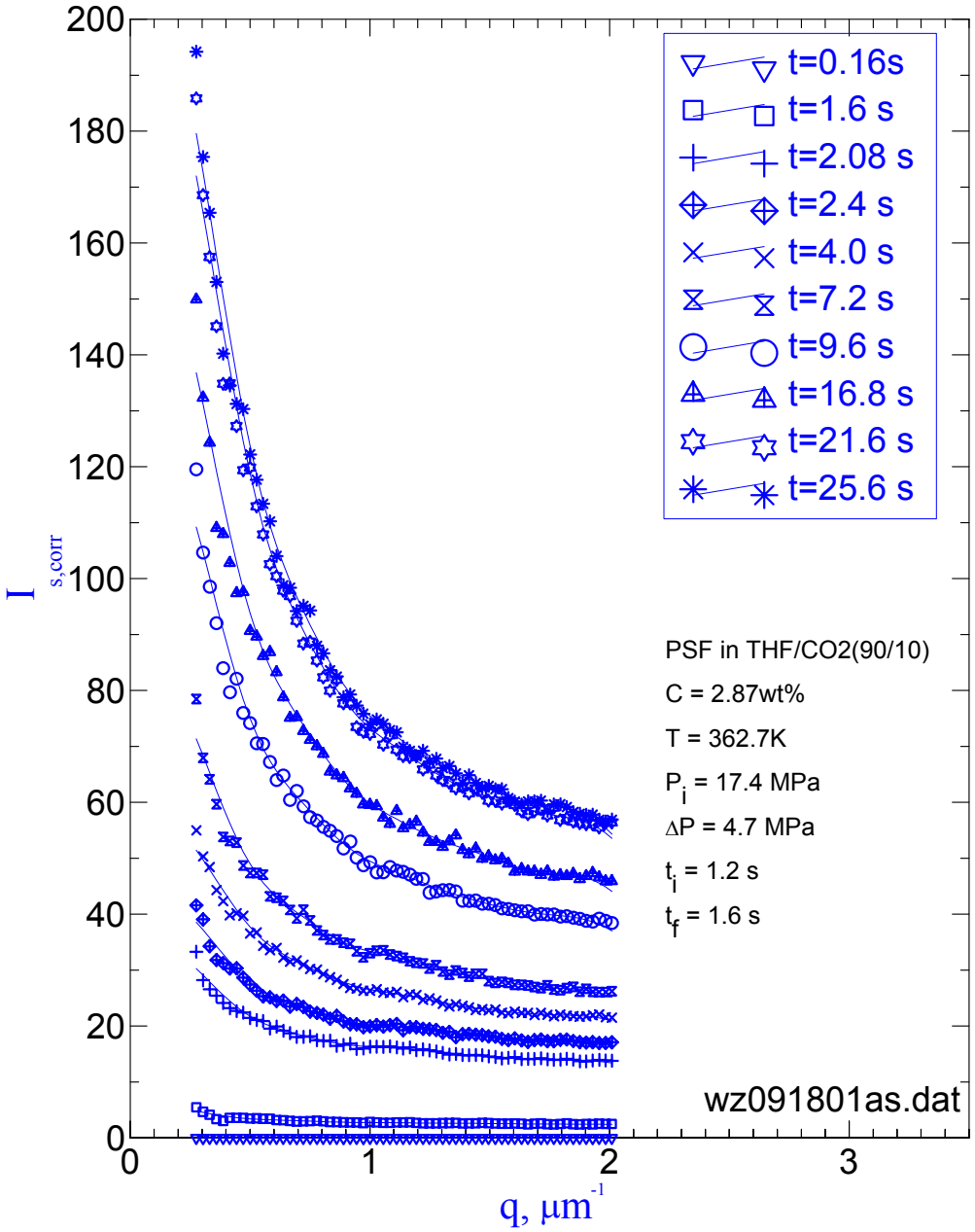

Figure 9.9. Time evolution of the scattered light intensities as a function of the wave number q after a pressure quench $\Delta P = 4.70$ MPa in 2.87 wt % solution of PSF in a mixture of THF (90 wt %) + CO_2 (10 wt %) at 363.0 K. The total observation time is 26 seconds. t_i: the time when the pressure quench starts; t_f: the time when the pressure quench ends.

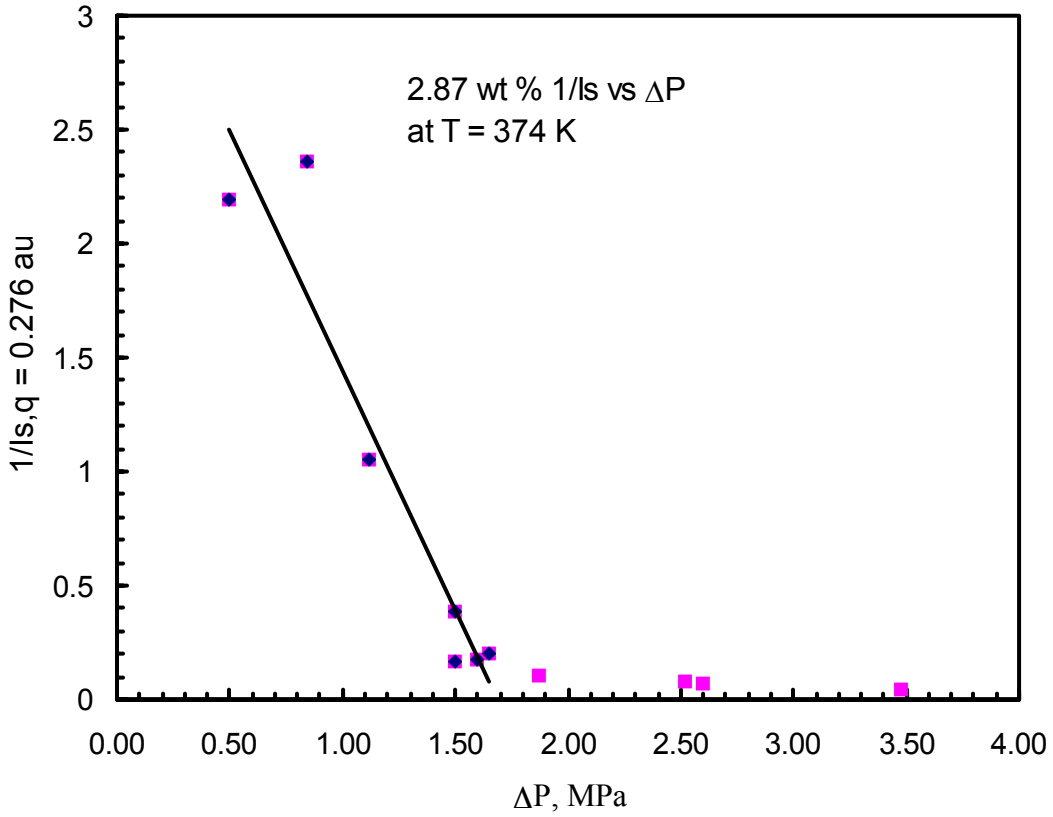

Figure 9.10. Variation of the inverse scattered light intensity at q = 0.276 at 1 second after pressure quench finishes ($1/I_{s,q=0.276}$) versus the quench depth ΔP in 2.87 wt % solution of PSF in a mixture of THF (90 wt %) + CO_2 (10 wt %) at 374 K.

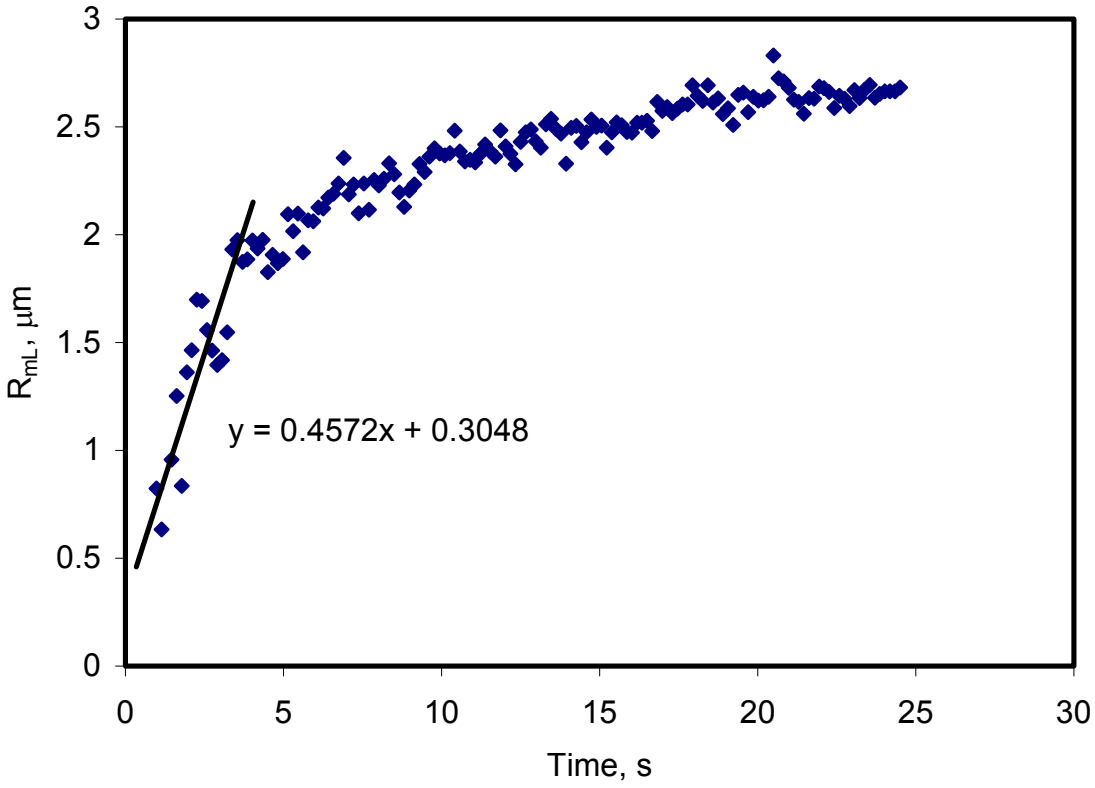

Figure 9.11. Evolution of the mean radii of particles evaluated from the scattered data at low scattering angles after a pressure quench ΔP = 1.12 MPa in 2.87 wt % solution of PSF in a mixture of THF (90 wt %) + CO_2 (10 wt %) at 374 K. The particle growth rate evaluated from the linear fit of the very earlier stage is 0.46 μm/s.

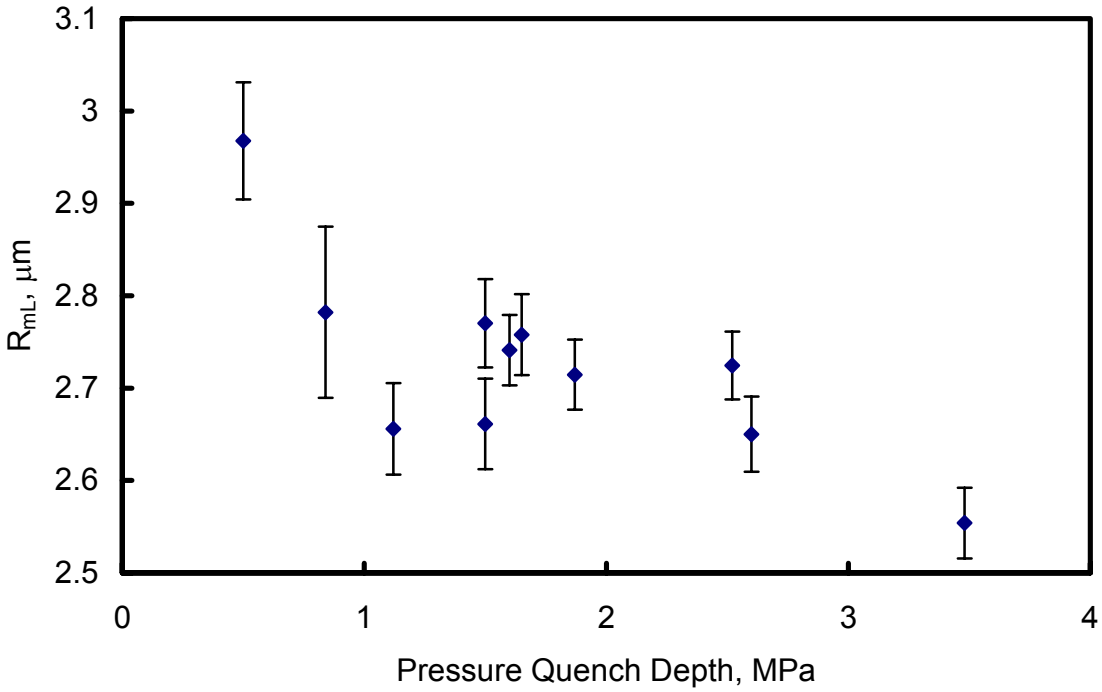

Figure 9.12. Variation of the plateau value of the mean particle radius as a function of the quench depth ΔP in 2.87 wt % solution of PSF in a mixture of THF (90 wt %) + CO_2 (10 wt %) at 374 K.

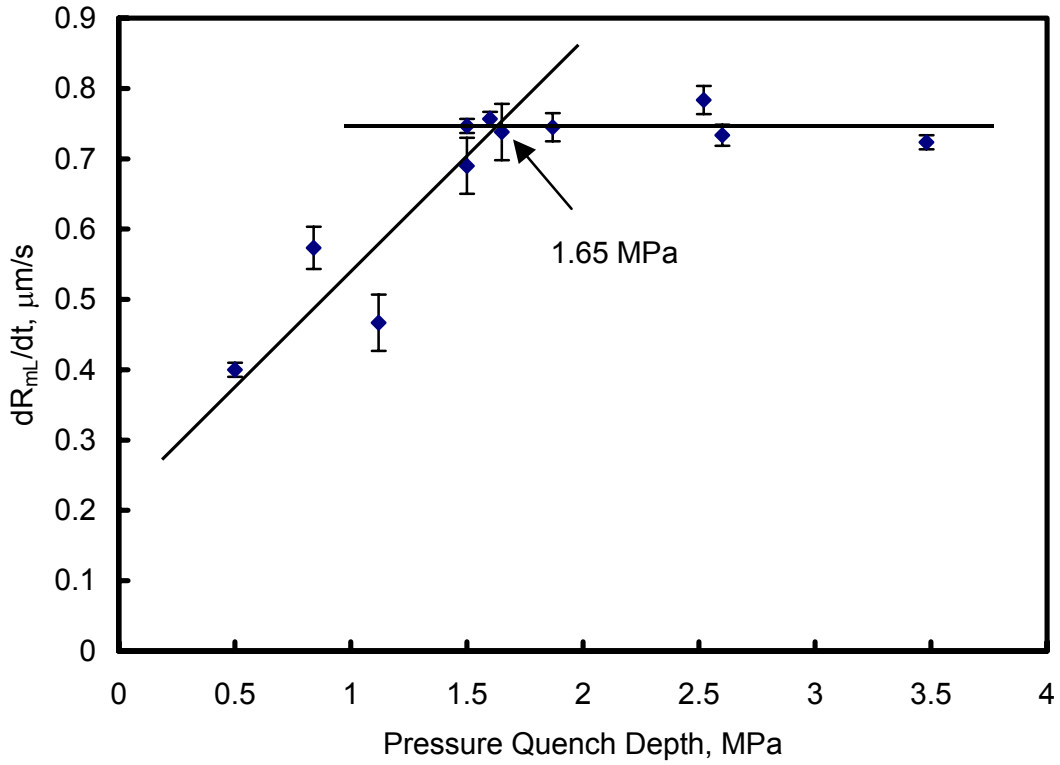

Figure 9.13. Variation particle growth rate dR_{mL}/dt as a function of the quench depth ΔP in 2.87 wt % solution of PSF in a mixture of THF (90 wt %) + CO_2 (10 wt %) at 374 K.

Chapter 10

Summary and Recommendations

The original goal of this thesis work was to study the phase behavior and phase separation kinetics of polymers in the binary mixtures of CO_2 and organic solvents to further the understanding on both the thermodynamics and dynamics aspects of miscibility and phase separation. Two model polymer-solvent systems were selected for this study: polyethylene + n-pentane + carbon dioxide and polysulfone + tetrahydrofuran + carbon dioxide. These polymers are industrially available polymers. The first system was selected to study both the solid-fluid and liquid-liquid phase separations, and the second system was selected for the importance of polysulfone as membrane formation polymer and the interest in developing new non-solvent systems. The following is a summary of the experimental investigations and some recommendations for further improvements.

10.1 Summary on the Miscibility of Polymers Solutions

Below are the highlights of our findings on the miscibility and the volumetric properties of PE in n-pentane + CO_2 and polysulfone in THF + CO_2 systems. For the PE in n-pentane and n-pentane + CO_2 system in the temperature range of 90 to 165 ^oC and at pressures up to 55 MPa, it has been found that:

1. The addition of CO_2 to PE + n-pentane system shifts the L-L phase boundary significantly to higher pressures, but moves the S-F phase boundary only slightly to higher temperatures. The S-F phase boundary which represents the

crystallization/melting temperatures was lowered by more than 10 ^{o}C compared to the crystallization/melting temperatures of the neat polyethylene samples determined by Differential Scanning Calorimetry (DSC).

2. The S-F phase boundary displays a unique sensitivity to the pressure-temperature conditions and moves to lower temperatures in the pressure range from 38 to 42 MPa in PE + n-pentane system. This effect, even though not as augmented, remains also in the solution in CO_2 + n-pentane. Competition between the pressure effect and the solvency effect is believed to cause this particular phenomenon.

For the polysulfone + THF + CO_2 system, the following observations have been made in the temperature range from 25 to 155 ^{o}C and pressure range up to 70 MPa.

1. The miscibility of polysulfone in THF + CO_2 is greatly reduced with increasing CO_2 content in the solvent mixtures. The LCST-type phase behavior at low CO_2 compositions is shifted to UCST-type phase behavior at higher CO_2 levels (up to 14 wt %). The phase boundary is pushed to higher pressures with increasing CO_2 content.

2. A unique phase behavior, multiple miscibility windows, was observed in this system. A 'U'-shaped phase boundary at 8 wt % CO_2 was observed to transfer to a "W"-shaped phase boundary at 10 wt % CO_2, which was further separated into a double 'U'-shaped phase boundary at 13 wt % CO_2.

3. The specific volumes of the polysulfone solutions were found to display a parallel variation to the changing pattern in the phase boundaries, which

means that the reduced miscibility is accompanied with an increase in the specific volume.

10.2 Summary on Phase Separation Kinetics

The phase separation kinetics in these polymer solutions were investigated using the time-resolved and angle-resolved light scattering techniques. Since the L-L phase separation kinetics in the polyethylene in n-pentane system has been extensively studied previously (Zhuang, 1995; Liu, 1999), in the present thesis the focus was on the S-F phase separation (crystallization and melting) in this system. The results on the crystallization and melting of PE in n-pentane can be summarized as follows:

1. The light scattering profiles reveal that the crystallization process is dominated by a nucleation and growth process that can be readily followed by time-resolved and angle-resolved light scattering. The evolution of the particle size (of the crystal phase) could be evaluated from the angular distribution of the scattered light intensity. In a majority of the experiments the particle growth process was observed to last for about 1 minute.

2. The particle size has a slight dependence on the crystallization pressure. This trend was confirmed by FESEM studies on the samples recovered after the cooling process. The particle sizes revealed by FESEM were much larger than those predicted from the scattering data.

The phase separation kinetics in the PSF solutions were conducted only in solvent mixtures with 90 wt % THF and 10 wt % CO_2. The results are highlighted by the following two points:

1. The scattering patterns suggest that nucleation and growth mechanism is the only mechanism for all the phase separation processes conducted at the selected conditions. This means that the metastable gap at these conditions is larger than the deepest pressure quenches applied to the system. However, using a multiple rapid pressure drop technique, a pressure that can be viewed as representing the spinodal point is identified from the rate of change of the scattered light intensity and the change of the particle growth rate with quench depth.

2. The particle size in the phase separating system shows a fast growth during the first few seconds. The results also reveal an inverse dependence of particle size on the quench depth.

10.3 Summary on the Morphological and Thermal Properties of PE Samples Recovered from n-Pentane and n-Pentane + CO_2

After constant pressure crystallization at selected pressures, the system was cooled down to room temperature and depressurized. Then PE samples were collected for morphological and thermal analysis. The thermal properties are summarized as follows:

1. All of the first DSC heating scans of the collected PE samples show multiple melting peaks, which reduced to only one during the second heating scans. The temperatures corresponding to the multiple melting peaks are lower than that of the original PE sample and that of second heating scan for all samples.

2. The relative strength of the melting peaks shows some pressure dependence on the crystallization pressure. The addition of CO_2 to the solution does not display much effect on the thermal properties.

3. It was observed that the overall crystallinity is increased by more than 10 % to about 75 % compared to the crystallinity of the original PE sample, which is about 63 %. This is due to the slow cooling rate during crystallization, the presence of solvent, and the application of pressure.

4. It is believed that the multiple melting peaks come from the presence of different crystal sizes because the crystallization process allows this to happen. During the constant pressure cooling process, the longer chains crystallize first, while the smaller ones stay in the solution, which then crystallize during further cooling and depressurization processes.

The microscopic results reveal that:

1. The prevailing morphology is the particles of agglomerated plate-like lamellae. The overall structure of the particles can be ellipsoid for most conditions. The exceptions are the particles collected from 5 wt % solutions in n-pentane after crystallized at pressures around 38-54 MPa where the stacked lamellae structure seems to be dominant. The addition of CO_2 lowers the solvent power and this stacked lamellae structure is no longer preferred.

2. The mechanism for the formation of such structures is proposed and it is readily valid for both types of structures. The plate like lamellae structures formed first, and then these lamellae aggregate to reduce the surface area.

Phase separation experiments were also carried out via two routes other than the constant pressure cooling pathway (Route 1). These two other routes are (a). the pressure quench into the liquid-liquid phase separated region followed by cooling process (Route 2); and (b). the controlled pressure and temperature reduction process (Route 3) that bring the system to the vicinity of the intersection of the S-F and L-L phase boundaries where the interplay of these two types of phase behaviors can be studied. The results, together with the phase separation kinetics results, are summarized as follows:

1. The scattered light intensity change during the phase separation process reveals that there are at least three transitions during the phase separation via Route 2. They are (1) the pressure quench induced L-L phase separation, (2) the crystallization in the polymer-rich phase that formed in L-L phase separation around the S-F phase boundary, and (3) the crystallization in the polymer-lean at a lower temperature. There is only one transition for each of Route 1 and 3 around the S-F phase boundary.

2. The DSC results show that there are three melting peaks for the sample of Route 1. There are two melting peaks for Route 2 represent the crystals formed from two different liquid phases. And there is only one melting peak for Route 3. The crystallinity of the sample from Route 3 is about 5 percent lower than those of Routes 1 and 2, indicating that there are more defects in the crystals formed in the L-L metastable region, which is the case in Route 3.

3. The FESEM results of the sample via Route 2 show two groups of particles both in spherical shape. The first group is believed to be from the polymer-rich phase because of the larger size and population, while the other group

must be obtained from the polymer-lean phase. Similar results are shown for Route 3 but the mechanism is not clear.

10.4 Recommendations

The present study has explored the miscibility and phase separation dynamics in two polymer solution systems. However, due to the time and experimental apparatus limitations, some aspects were not covered. The following suggestions should be considered in the future.

- Studies on higher polymer concentrations would be more interesting because the time scale of the phase separation would be longer for observations. This may require a new recirculation device because of the limitations of current equipment.
- Due to the nature of the polymer systems studied in present work, the CO_2 level is quite limited. Other polymer/solvent/CO_2 systems should be explored for higher CO_2 intake capability.
- Research should be continued on the morphological aspects of polymers processed in or with supercritical fluids.
- Future research should focus on developing a better understanding of the interplay of crystallization and liquid-liquid phase separations and how this interaction affects the polymer properties. This could be achieved by carrying out investigations on other semicrystalline polymer systems.

References

Anderson, V. J. and Lekkerkerker, H. N. W. (2002). Insights into phase transition kinetics from colloid science. *Nature*, *416*, 811.

Ariyapadi, M. V. and Nauman, E. B. (1989). Free energy of an inhomogeneous polymer-polymer-solvent system. *J. Polym. Sci.: Part B: Polym. Phys.*, *27*, 2637.

Ariyapadi, M. V. and Nauman, E. B. (1990). Gradient energy parameters for polymer - polymer-solvent systems and their application to spinodal decomposition in true ternary systems. *J. Polym. Sci.: Part B: Polym. Phys.*, *28*, 2395.

Ariyapadi, M. V. and Nauman, E. B. (1992). Free energy of an inhomogeneous polymer-polymer-solvent system. II. *J. Polym. Sci.: Part B: Polym. Phys.*, *30*, 533.

Aulov, V. A. (1994). Structural Aspects of Influence of High Pressure on Polyethylene. In A. L. Kovarskii. (Eds.), *High-pressure chemistry and physics of polymers*. (pp. 23). Boca Raton: CRC Press.

Bayraktar, Z. and Kiran, E. (2001). Polymer blending by pressure-induced swelling, impregnation and phase separation in supercritical fluids. Gradient blending and phase localization of poly(dimethylsiloxane) in polystyrene and polyethylene. *Proc. 2nd. Int. Meeting on High Pressure Chemical Engineering*, March 7-9, Hamburg, Germany.

Beckman, E. J. (2004). A challenge for green chemistry: designing molecules that readily dissolve in carbon dioxide. *Chemical Communications*(17), 1885-1888.

Binder, K. (1990). Spinodal Decomposition. In P. Haasen. (Eds.), *Materials Science and Technology, Vol. 5, Phase Transformations in Materials*. (pp. 405-472). Weinheim: VCH.

Binder, K. and Fratzl, P. (2001). Spinodal Decomposition. In G. Kostorz. (Eds.), *Phase Transformations in Materials*. (pp. 409-480). Weinheim: Wiley-VCH.

Blaum, G. and Wolf, B. A. (1976). The generation of true cosolvency by pressure. solubility limits of high molecular weight polystyrene in mixtures of acetone and diethylether. *Macromolecules*, *9*, 579.

Bonnett, P. E., Carpenter, K. J., Dawson, S. and Davey, R. J. (2003). Solution crystallization *via* a submerged liquid-liquid phase boundary: oiling out. *Chem. Commun.*, 698-699.

Bungert, B., Sadowski, G. and Arlt, W. (1997). Supercritical antisolvent fraction: measurements in the systems monodisperse and bidisperse polystyrene-cyclohexane-

carbon dioxide. *Fluid Phase Equilibria*, *139*, 349-359.

Cabral, J. T., Higgins, J. S., McLeish, T. C. B., Strausser, S. and Magonov, S. N. (2001). Bulk spinodal decomposition studied by atomic force microscopy and light scattering. *Macromolecules*, *34*, 3748.

Cahn, J. W. and Hilliard, J. E. (1958). Free free energy of a nonuniform system. I. Interfacial free energy. *J. Chem. Phys.*, *28*, 258.

Cahn, J. W. (1959). Free energy of a nonuniform system. II. Thermodynamic basis. *J. Chem. Phys.*, *30*(5), 1121.

Cahn, J. W. and Hilliard, J. E. (1959). Free energy of nonuniform system III. Nucleation in a two-component incompressible fluid. *J. Chem. Phys.*, *31*, 688.

Cahn, J. W. (1961). On spinodal decomposition. *Acta Metallurgica*, *9*, 795.

Chan, A. k. C., Russo, P. S. and Radosz, M. (2000). Fluid-liquid equilibria in poly(ethylene-cohexene-1) + propane: a light-scattering probe of cloud point pressure and critical polymer concentration. *Fluid Phase Equilibria*, *173*, 149.

Chen, X., Yasuda, K., Sato, Y., Takishima, S. and Masuoka, H. (2004). Measurement and correlation of phase equilibria of ethylene + n-hexane + metallocene polyethylene at temperatures between 373 and 473 K and at pressures up to 20 MPa. *Fluid Phase Equilibria*, *215*, 105.

Condo, P. D., Jr., Colman, E. J. and Ehrlich, P. (1992). Phase equilibria of linear polyethylene with supercritical propane. *Macromolecules*, *25*, 750.

Debenedetti, P. G. (1990). Homogeneous nucleation in supercritical fluids. *AIChE J.*, *36*, 1289.

Debye, P. and Bueche, A. M. (1949). Scattering by an inhomogenous solid. *J. Appl. Phys.*, *20*, 518.

Debye, P., Anderson, H. R. and Brumberger, H. (1957). Scattering by an Inhomogenous Solid. II. The correlation function and its application. *J. Appl. Phys.*, *28*, 679.

Debye, P. (1959). Angular dissymmetry of the critical opalescence in liquid mixtures. *J. Chem. Phys.*, *31*, 680.

Debye, P. and Woermann, D. (1960). Critical opalescence of polystyrene in cyclohexane. *J. Chem. Phys.*, *31*, 1746.

Debye, P., Woermann, D. and Chu, B. (1962). Critical opalescence of polystyrene in cyclohexane transmission measurements. *J. Chem. Phys.*, *80*(851).

Degiorgio, V., Corti, M. and Giglio, M. e. (1980). *Light Scattering in Liquids and Macromolecular Solutions*. New York: Plenum Press.

Derham, K. W., Goldsbrough, J. and Gordon, M. (1974). Pulse-induced critical scattering (PICS) from polymer solutions. *Pure and Appl. Chem.*, *38*, 97.

DeSimone, J. M., Guan, Z. and Elsbernd, C. S. (1992). Synthesis of fluoropolymers in supercritical carbon dioxide. *Science*, *257*, 945.

DeSimone, J. M. and Tumas, W. (2003). *Green Chemistry Using Liquid and Supercritical Carbon Dioxide*. New York: Oxford University Press.

Fang, J. and Kiran, E. (2005). Phase behavior and crystallization of poly(4-methyl-1-pentene) in n-pentane and in n-pentane/CO_2 at high pressures. *Research in Progress.*

Furukawa, H. (1985). A dynamic scaling assumption for phase separation. *Adv. Phys.*, *34*, 703.

Gauter, K., Peters, C. J., Scheidgen, A. L. and Schneider, G. M. (2000). Cosolvency effects, miscibility windows and two-phase lg holes in three-phase llg surfaces in ternary systems: a status report. *Fluid Phase Equilibria*, *171*, 127.

Graham, P. D., Pervan, A. J. and McHugh, A. J. (1997). The dynamics of thermal-induced phase separation in pmma solutions. *Macromolecules*, *30*, 1651.

Granasy, L. (1997). Nucleation and spinodal decomposition. *Solid State Phenomena*, *56*, 67.

Gregg, C. J., Stein, F. P., Morgan, C. K. and Radosz, M. (1994). A variable-volume optical pressure-volume-temperature cell for high-pressure cloud points, densities, and infrared spectra, applicable to supercritical fluid solutions of polymers up to 2 kbar. *J. Chem. Eng. Data*, *39*, 219.

Guan, Z. and DeSimone, J. M. (1994). Fluorocarbon-based heterophase polymeric materials. 1. Block copolymer surfactants for carbon dioxide applications. *Macromolecules*, *27*, 5527.

Gunton, J. D., Miguel, M. S. and Sahni, P. S. (1983). The Dynamics of First Order Phase Transitions. In C. Domb, Lebowitz, J. L. (Eds.), *Phase Transitions and Critical Phenomena, vol 8*. (pp. 267-466). London, San Diego, New York: Academic Press.

Gunton, J. D. (1999). Homogeneous nucleation. *J. Stat. Phys.*, *95*, 903.

Hammouda, B., Balsara, N. P. and Lefebvre, A. A. (1997). Small-angle neutron scattering from pressurized polyethylbutylene/polymethylbutylene blends.

Macromolecules, *30*, 5572.

Han, C. C., Okada, M., Muroga, Y., McCrakin, F. L., Bauer, B. J. and Tran-Cong, Q. (1986). Static and kinetic studies of polystyrene/poly(vinyl methyl ether) blends. *Polym. Eng. Sci.*, *26*, 3.

Hashimoto, T., Kumaki, J. and Kawai, H. (1983). Time-resolved light scattering studies on kinetics of phase separation and phase dissolution of polymer blends. 1. Kinetics of phase separation of a binary mixture of polystyrene and poly(vinyl methyl ether). *Macromolecules*, *16*, 641.

Hashimoto, T., Sasaki, K. and Kawai, H. (1984). Time-resolved light scattering studies on kinetics of phase separation and phase dissolution of polymer blends.2. Phase separation of ternary mixtures of polymer a, polymer b and solvent. *Macromolecules*, *17*, 2812.

Hashimoto, T., Itakura, M. and Shimidzu, N. (1986). Late stage spinodal decomposition of a binary polymer mixture. II. Scaling analyses on Qm(Tau) and Im(Tau). *J. Chem. Phys.*, *85*, 6773.

Hashimoto, T. (1987). Structure Formation in Polymer Mixtures by Spinodal Decomposition. In R. M. OTTENBRITE, L. A. UTRACKI and S. INOUE. (Eds.), *Current topics in polymer science. Volume 1 : Polymer chemistry and polymer physics : ionic polymerization. biological systems, spectrometric methods, liquid crystals.* (pp.). New York: Hanser Publishers.

Hashimoto, T. (1988). Dynamics in Spinodal Decomposition of Polymer Mixtures. *Phase Transitions*, *12*, 47.

Hatanaka, M. and Saito, H. (2004). In-situ investigation of liquid-liquid phase separation in polycarbonate/carbon dioxide system. *Macromolecules*, 7358 - 7363.

Hohne, G. W. H. and Blankenhorn, K. (1994). High pressure DSC investigations on n-alkanes, n-alkane mixtures and polyethylene. *Thermochim. Acta*, *238*, 351.

Hu, W. (2000). The melting point of chain polymers. *J. Chem. Phys.*, *113*, 3901.

Hu, W., Frenkel, D. and Mathot, V. B. F. (2003). Lattice model study of the thermodynamic interplay of polymer crystallization and liquid-liquid demixing. *J. Chem. Phys.*, *118*, 10343.

Hu, W. and Frenkel, D. (2004). Effect of metastable liquid-liquid demixing on the morphology of nucleated polymer crystals. *Macromolecules*, *37*, 4336-4338.

Huang, S. H. and Radosz, M. (1990). Equation of state for small, large, polydisperse and associating molecules. *Ind. Eng. Chem. Res.*, *29*, 2284.

Huglin, M. G. (1972). *Light Scattering From Polymer Solutions*. New York: Academic Press.

Inoue, T. and Ougizawa, T. (1989). Characterization of phase behavior in polymer blends by light scattering. *J. Macromol. Sci. - Chem. A*, *26*, 147.

Jiang, S., An, L., Jiang, B. and Wolf, B. A. (2003). Pressure effects on the thermodynamics of trans-decahydronaphthalene/polystyrene polymer solutions: application of the sanchez-lacombe lattice fluid theory. *Macromol. Chem. Phys.*, *204*, 692.

Johnston, K. P. and Lemert, R. M. (1996). Supercritical Fluid Technology: Theory and Application. In J. J. McKetta and G. E. Weismantel. (Eds.), *Encyclopedia of Chemical Processing and Design*. (pp. 1-45). New York: Marcel Dekker.

Joung, S. N., Park, J.-U., Kin, S. Y. and Yoo, K.-P. (2002). High-pressure phase behavior of polymer-solvent systems with addition of supercritical co2 at temperatures from 323.15 K to 503.15 K. *J. Chem. Eng. Data*, *47*, 270-273.

Kawai, H. and Strobl, G. (2004). Crystallization mechanism of syndiotactic polypropylene analyzed by time-dependent light scattering. *Macromolecules*, *37*, 2249.

Kawasaki, K. and Ohta, T. (1977). Theory of early stage spinodal decomposition in fluids near the critical point. I. *Progress. Theor. Phys.*, *57*, 826.

Kawasaki, K. and Ohta, T. (1978). Theory of early stage spinodal decomposition in fluids near the critical point. II. *Progress. Theor. Phys.*, *59*, 362.

Kazarian, S. G. (2000). Polymer processing with supercritical fluids. *Polymer Science, Ser. C*, *42*(1), 78.

Kiepen, F. and Borchard, W. (1988a). Critical opalescence of polymer solutions at high pressures. *Makromol. Chem.*, *189*, 2595.

Kiepen, F. and Borchard, W. (1988b). Pressure-pulse-induced critical scattering of oligostyrene in n-pentane. *Macromolecules*, *21*, 1784.

Kiepen, F. and Borchard, W. (1988c). Light scattering as tool for the determination of adiabatically performed temperature changes. *Makromol. Chem.*, *189*, 1543.

Kiran, E. (1994a). Polymer Formation, Modification and Processing in or with Supercritical Fluids. In E. Kiran and J. M. H. Levelt Sengers. (Eds.), *Supercritical Fluids Fundamentals for Applications*. (pp. 541-588). Dordrecht: Kluwer Academic Publishers.

Kiran, E. and Zhuang, W. (1994b). A new experimental method to study kinetics of

phase separation in high-pressure polymer solutions. Multiple rapid pressure-drop technique-MRPD. *J. Supercrit. Fluids*, *7*, 1.

Kiran, E., Xiong, Y. and Zhuang, W. (1994c). Effect of polydispersity on the demixing Pressures of Polyethylene in Near- and Supercritical Alkanes. *J. Supercrit. Fluids*, *7*, 283.

Kiran, E. (2000). Polymer miscibility and kinetics of pressure-induced phase separation in near-critical and supercritical fluids. In E. Kiran, Debenedetti, P. G.; Peters, C. J. (Eds.), *Supercritical Fluids: Fundamentals and Applications.(Proceedings of the NATO Advanced Study Institute, held 12-24 July 1998, Kemer, Antalya, Turkey.)*. (pp. 167-192). Dordrecht/Boston/London: Kluwer Academic Publisher.

Kiran, E. and Liu, K. (2002). The miscibility and phase behavior of polyethylene with poly(dimethylsiloxane) in near-critical n-pentane. *Korean J. Chem. Eng.*, *19*, 153.

Kleintjens, L. A. and Koningsveld, R. (1980). Liquid-liquid phase separation in multicomponent polymer systems. XIX. Mean-field lattice-gas treatment of the system n-alkane/linear-polyethylene. *Colloid and Polymer Science*, *258*, 711.

Klempner, D., Sperling, L. H. and Utracki., (Eds.). (1994). *Interpenetrating Polymer Networks*. Advances in Chemistry series: American Chemical Society.

Koberstein, J. T. and Stein, R. S. (1980). Small-angle light scattering from thin polymer films: multiple scattering from debye-bueche scatters. *J. Polym. Sci.: Polym. Phys. Ed.*, *18*, 199.

Kojima, J., Nakayama, Y., Takenaka, M. and Hashimoto, T. (1995). Apparatus for measuring time-resolved light scattering profiles from supercritical polymer solutions undergoing phase separation under high pressure. *Rev. Sci. Instrum.*, *66*, 4066.

Kojima, J., Nakayama, Y., Takenaka, M. and Hashimoto, T. (1999). Early stage spinodal decomposition in polymer solution under high pressure. *Macromolecules*, *32*, 1809.

Koningsveld, R. and Staverman, A. J. (1968). Liquid-liquid phase separation in multicomponent polymer solutions. III. Cloud-point curves. *J. Polym. Sci.: Part A-2*, *6*, 325.

Koningsveld, R., Stockmayer, W. H. and Nies, E. (2001). *Polymer Phase Diagrams: A Textbook.* Oxford: Oxford University Press.

Kuk, Y.-M., Lee, B.-C., Lee, Y. W. and Lim, J. S. (2001). Phase behavior of biodegradable polymers in dimethyl ether and dimethyl ether + carbon dioxide. *J. Chem. Eng. Data*, *46*, 1344-1348.

Kuwahara, N. and Kubota, K. (1992). Spinodal decomposition in a polymer solution. *Phys. Rev. A.*, *45*, 7385.

Langer, J. S., Bar-on, M. and Miller, H. D. (1975). New computational method in the theory of spinodal decomposition. *Phys. Rev. A.*, *11*, 1417.

Lee, J. M., Lee, B.-C. and Hwang, S.-J. (2000). Phase behavior of poly(L-lactide) in supercritical mixtures of carbon dioxide and chlorodifluoromethane. *J. Chem. Eng. Data*, *45*, 1162-1166.

Lefebvre, A. A., Lee, J. H., Jeon, H. S., Balsara, N. P. and Hammouda, B. (1999). Initial stages of nucleation in phase separating polymer blends. *J. Chem. Phys.*, *111*, 6082.

Lefebvre, A. A., Lee, J. H., Balsara, N. P. and Hammouda, B. (2000). Neutron scattering from pressurized polyolefin blends near the limits of metastability. *Macromolecules*, *33*, 7977.

Levelt Sengers, J. M. H. (1994). Critical Behavior of Fluids: Concepts and Applications. in. In E. Kiran and J. M. H. Levelt Sengers. (Eds.), *Supercritical Fluids Fundamentals for Application*. (pp.). Dordrecht: Kluwer Academic Publishers.

Liu, K. and Kiran, E. (1999). Kinetics of pressure-induced phase separation (PIPS) in solutions of polydimethylsiloxane in supercritical carbon dioxide: crossover from nucleation and growth to spinodal decomposition mechanism. *J. Supercrit. Fluids*, *16*, 59.

Liu, K. (1999) Master Thesis, *Kinetics of Pressure-Induced Phase Separation in Polymer Solutions by Time- and Angle-Resolved Light Scattering*, University of Maine, Orono, ME.

Liu, K. and Kiran, E. (2001). Pressure-induced phase separation in polymer solutions: kinetics of phase separation and crossover from nucleation and growth to spinodal decomposition in solutions of polyethylene in n-pentane. *Macromolecules*, *34*(9), 3060.

Luna-Barcenas, G., Mawson, S., Takishima, S., DeSimone, J. M., Sanchez, I. C. and Johnston, K. P. (1998). Phase behavior of poly(1,1-dihydroperfluorooctylacrylate) in supercritical carbon dioxide. *Fluid Phase Equilibria*, *146*, 325-337.

Luszczyk, M., Rebelo, L. P. N. and Van Hook, W. A. (1995). Isotope and pressure dependence of liquid-liquid equilibria in polymer solutions. 5. Measurements of solute and solvent isotope effects in polystyrene-acetone and polystyrene - methylcyclopent ane. 6. A continuous polydisperse thermodynamic interpretation of demixing measurements in polystyrene-acetone and polystyrene- methylcyclopentane solutions. *Macromolecules*, *28*, 745-767.

Maguey, J., Van Nuland, T. and Navard, P. (2001). Small angle light scattering investigation of polymerization induced phase separation mechanisms. *Polymer*, *42*, 4353.

Mathot, V. B. F. and Pijper, M. F. J. (1983). Heat capacity, enthalpy and crystallinity for a linear polyethylene obtained by DSC. *J. Thermal Analysis*, *28*, 349.

Matsuyama, H., Kudari, S., Kiyofuji, H. and Kitamura, Y. (2000). Kinetic studies of thermally induced phase separation in polymer-diluent system. *J. Appl. Polym. Sci.*, *76*, 1028-1036.

Mayer, W. and Woermann, D. (1990). Kinetics of liquid-liquid phase separation in a binary mixture with miscibility gap: study of non-critical mixtures of 2,6-dimethyl pyridine/water near the lower critical point. *J. Chem. Phys.*, *93*, 4349.

Mchugh, M. A. (2003). Solubility of Polymers in Supercritical Carbon Dioxide. In J. M. DeSimone and W. Tumas. (Eds.), *Green Chemistry Using Liquid and Supercritical Carbon Dioxide*. (pp. 125-133). New York: Oxford University Press.

Metz, U. and Schneider, G. M. (1990a). Pressure-jump experiments for the study of the kinetics of phase separation in the binary system ethene/hexane.I. Transient light scattering measurements. *Ber. Bunsenges. Phys. Chem.*, *94*, 452.

Metz, U. and Schneider, G. M. (1990b). Pressure-jump experiments for the study of the kinetics of phase separation in the binary system ethene/hexane. II. Measurements of pressure induced temperature changes. *Ber. Bunsenges. Phys. Chem.*, *94*, 447.

Miyata, S., Arikawa, T. and Sakaoku, K. (1974). Crystallization of polyethylene from xylene solutions under high pressure. *Analytical Calorimetry*, *3*, 603.

Nakata, M. and Kawate, K. (1992). Kinetics of nucleation in a dilute polymer solution. *Phys. Rev. Lett.*, *68*, 2176.

Okada, M. and Han, C. C. (1986). Experimental study of thermal fluctuations in spinodal decomposition of a binary polymer mixture. *J. Chem. Phys.*, *85*, 5317.

Olabisi, O., Robeson, L. M. and Shaw, M. T. (1979). *Polymer-Polymer Miscibility*. New York: Academic Press.

Olmsted, P. D., Poon, W. C. K., Mcleish, T. C. B., Terrill, N. J. and Ryan, A. J. (1998). Spinodal-assisted crystallization in polymer melts. *Phys. Rev. Lett.*, *81*(2), 373-376.

Pogodina, N. V., Siddiquee, S. K., van Egmond, J. W. and Winter, H. H. (1999). Correlation of rheology and light scattering in isotactic polypropylene during early stages of crystallization. *Macromolecules*, *32*, 1167.

Pöhler, H. and Schneider, G. M. (1995). Fluid phase equilibria of binary and ternary mixtures of supercritical carbon dioxide with tetradecanoic acid and docosane up to 43 MPa and 393 K: Cosolvency effect and miscibility windows. *Fluid Phase Equilibria*,

110, 151.

Pressl, K., Kriechbaum, M., Steinhart, M. and Laggner, P. (1997). High pressure cell for small- and wide-angle x-ray scattering. *Rev. Sci. Instrum.*, *68*, 4588.

Puri, S. and Binder, K. (2001). Power laws and crossovers in off-critical surface-directed spinodal decomposition. *Phys. Rev. Lett.*, *86*, 1797.

Quednau, J. and Schneider, G. M. (1989). A new high-pressure cell for differential pressure-jump experiments using optical detection. *Rev. Sci. Instrum.*, *60*, 3685.

Sasaki, T., Miyazaki, A., Sugiura, S. and Okada, K. (2002). Crystallization of poly(ethylene oxide) from solutions of different solvents. *Polym. J.*, *34*(11), 794.

Scheidgen, A. L. and Schneider, G. M. (2000). Fluid phase equilibria of (carbon dioxide + a 1-alkanol + an alkane) up to 100 MPa and T = 393 K: Cosolvency effect, miscibility windows, and holes in the critical surface. *J. Chem. Thermodynamics*, *32*, 1183.

Schneider, G. M., Scheidgen, A. L. and Klante, D. (2000). Complex phase equilibrium phenomena in fluid mixtures up to 2 GPa-cosolvency, holes, windows, closed loops, high-pressure immiscibility, barotropy, and related effects. *Ind. Eng. Chem. Res.*, *39*, 4476.

Scholte, T. G. (1972). Light scattering of concentrated polydisperse polymer solutions. *J. Polym. Sci.: Part C*, *39*, 281.

Scott, R. L. and Van Konynenburg, P. H. (1970). Static properties of solutions. 2. Van der Waals and related models for hydrocarbon mixtures. *Discussions of the Faraday Society*, *49*, 87-97.

Sear, R. P. (2001). Nucleation of noncritical phase in fluid near a critical point. *J. Chem. Phys.*, *114*(7), 3170.

Sengers, L. V. (1994). Effects of Critical Fluctuations on the Thermodynamic and Transport Properties of Supercritical Fluids. In E. Kiran and J. M. H. Levelt Sengers. (Eds.), *Supercritical Fluids Fundamentals for Application*. (pp.). Dordrecht: Kluwer Academic Publishers.

Shang, M., Matsuyama, H., Maki, T., Teramoto, M. and Lioyd, D. R. (2003). Effect of crystallization and liquid-liquid phase separation on phase-separation kinetics in poly(ehtylene-covinyl alcohol)/glycerol solution. *J. Polym. Sci.: Part B: Polym. Phys.*, *41*, 194-201.

Sieber, M. and Woermann, D. (1991). Study of non-equilibrium states of a homogeneous 2-butoxyethanol/water mixture of critical composition in the vicinity of its lower critical point using fast pressure jumps. *Ber. Bunsenges. Phys. Chem.*, *95*(1), 15.

Siggia, E. (1979). Late stages of spinodal decomposition in binary mixtures. *Phys. Rev. A.*, *20*, 595.

Stanley, H. E. (1971). *Introduction to Phase Transition and Critical Phenomena*. Oxford: Oxford University Press.

Stein, R. S. and Rhodes, M. B. (1960). Photographic light scattering by polyethylene films. *J. Appl. Phys.*, *31*, 1873.

Steinhart, M., Kriechbaum, M., Pressl, K., Amenitsch, H., Laggner, P. and Bernstorff, S. (1999). High-pressure instrument for small-and wide-angle x-ray scattering. II. Time-resolved experiments. *Rev. Sci. Instrum.*, *70*, 1540.

Steinhoff, B., Rullmann, M., Kuhne, L. and Alig, I. (1997). Phase separation kinetics in a binary mixture of polyethylene glycol and polypropylene glycol studied by light scattering after a pressure jump: pinning of domain growth by hydrogen bond structures. *J. Chem. Phys.*, *107*, 5217.

Szydlowski, J. and Van Hook, W. A. (1991). Glass capillary optical cell to determine the pressure dependence of polymer-solvent phase transitions at near critical conditions by light scattering. *J. Polym. Sci., Polym. Phys. Ed.*, *29*, 1437.

Szydlowski, J., Rebelo, L. P. and Van Hook, W. A. (1992). A new apparatus for detection of phase equilibria in polymer solvent systems by light scattering. *Rev. Sci. Instrum.*, *63*, 1717-1725.

Tahara, D., Fukao, K., Miyamoto, Y. (2002) Light scattering studies on crystallization in polyethylene terephthalate. *Polymer 43*, 7461.

Takeno, H., Iwata, M., Takenaka, M. and Hashimoto, T. (2000). Combined light scattering and laser scanning confocal microscopy studies of a polymer mixture involving a percolation-to-cluster transition. *Macromolecules*, *33*, 9657.

Talanquer, V. and Oxtoby, D. W. (1998). Crystal nucleation in presence of metastable critical point. *J. Chem. Phys.*, *109*(1), 223.

Tanaka, H. (1990). Transition from metastability to instability in binary liquid mixture. *Phys. Rev. Lett.*, *65*, 3136.

Tseng, H. T. and Phillips, P. J. (1985). Crystallization kinetics of linear polyethylene at elevated pressures. *Macromolecules*, *18*, 1565.

Upper, G. (2002) Master Thesis, *Investigations for the phase behaviour of asymmetrical mixtures from polymers and supercritical fluids.*, University of Karlsruhe, Karlsruhe, Germany.

Upper, G., Beckel, D., Zhang, W. and Kiran, E. (2003). High pressure crystallization in supercritical or dense fluids. *Proceedings of the 6th International Symposium on Supercritical Fluids*, Versailles, France.

Upper, G., Beckel, D., Zhang, W. and Kiran, E. (2005). High-Pressure Crystallization of Polyethylene in n-Pentane and n-Pentane + Carbon Dioxide Fluid Mixtures. *To be submitted to Journal of Supercritical Fluids*.

Utracki, L. A. (1994). Thermodynamics and Kinetics of Phase Separation. In D. Klempner, L. H. Sperling and L. A. Utracki. (Eds.), *Interpenetrating Polymer Networks, Advances in Chemistry 239,*. (pp. 77-123). Washington DC: American Chemical Society.

Van den Broecke, P. and Berghmans, H. (1990). Thermoreversible gelation of solutions of vinyl polymers. *Macromolecular Symposia*, *39*, 59.

Vanden Eynde, S., Mathot, V. B. F., Hohne, G. W. H., Schawe, J. W. K. and Reynaers, H. (2000). Thermal behaviour of homogeneous ethylene-1-octene copolymers and linear polyethylene at high pressures. *Polymer*, *41*, 3411.

Wagner, R., Kampmann, R. and Voorhees, P. W. (2002). Homogeneous Second-Phase Precipitation. In G. Kostorz. (Eds.), *Phase Transformations in Materials*. (pp.). Weinheim: Wiley-VCH.

Watkins, J. J., Krukonis, V. J., Condo, P. D., Jr., Pradhan, D. and Ehrlich, P. (1991). Fractionation of high-density polyethylene in propane by isothermal pressure profiling and isobaric temperature profiling. *J. Supercrit. Fluids*, *4*, 24.

Weidner, E., Knez, Z., Wiesmet, V. and Kokol, K. (1997a). Phase equilibrium (solid-liquid-gas) in the system of polyethyleneglycols-nitrogen. *ITSSF 97, 4th Conf. On SCF and their Application*, 409.

Weidner, E., Wiesmet, V., Knez, Z. and Skerget, M. (1997b). Phase equilibrium (solid-liquid-gas) in polyethyleneglycol-carbon dioxide systems. *J. Supercrit. Fluids*, *10*, 139.

Weidner, E. and Wiesmet, V. (1999). Phase equilibrium (solid-liquid-gas) in binary systems of polyethylenglycols, polyethylenglycoldimethylether with carbon dioxide, propane and nitrogen. *CISF 99, 5th Conf. on SCF and their Application*, 521.

Wells, P. A., de Loos, T. W. and Kleintjens, L. A. (1993). Pressure pulsed induced critical scattering: spinodal and binodal curves for the system polystyrene + methylcyclohexane. *Fluid Phase Equilibria*, *106*, 185.

Wells, P. A., de Loos, T. W. and Kleintjens, L. A. (1995). Experimental determination of the spinodal P-T-x surface for the system 2-butoxyethanol/water using the 'PPICS' apparatus. *Fluid Phase Equilibria*, *106*, 185.

Wenzel, J., Limbach, U., Bressonik, G. and Schneider, G. M. (1980). Kinetics of phase separation in binary liquid mixtures. *J. Phys. Chem.*, *84*, 1991.

Woenckhaus, J., Kohling, R., Winter, R., Thiyagarajan, P. and Finet, S. (2000). High pressure-jump apparatus for kinetic studies of protein folding reactions using small-angle synchroton x-ray scattering technique. *Rev. Sci. Instrum.*, *71*, 3895.

Wolde, P. R. t. and Frenkel, D. (1997). Enhancement of protein crystal nucleation by critical density fluctuations. *Science*, *277*(5334), 1975-1978.

Wolf, B. A. and Molinari, R. J. (1973). True cosolvency: acetone/diethylether/polystyrene. *Die Makromolekulare Chemie*, *173*, 241.

Wolf, B. A. and Blaum, G. (1976). Pressure influence on true cosolvency: measured and calculated solubility limits of polystyrene in mixtures of acetone and diethylether. *Makromol. Chem.*, *177*, 1073.

Wong, N.-C. and Knobler, C. M. (1978). Light scattering studies of phase separation in isobutyric acid + water mixtures. *J. Chem. Phys.*, *69*, 725.

Wong, N.-C. and Knobler, C. M. (1979). Pressure-jump studies in supercritical mixtures. *Phys. Rev. Lett.*, *43*, 1733.

Wong, N.-C. and Knobler, C. M. (1981). Light scattering studies of phase separation in isobutyric acid + water mixtures: Hydrodynamic effects. *Phys. Rev. A.*, *24*, 3205.

Xie, Y., Ludwig Jr., K. F., Bansil, R., Gallagher, P. D., Konak, C. and Morales, G. (1996). Time-resolved small-angle X-ray scattering studies of spinodal decomposition kinetics in a semidilute polystyrene-dioctyl phthalate solution. *Macromolecules*, *29*, 6150.

Xiong, Y. and Kiran, E. (1994). High pressure phase behavior in polyethylene/n-butane binary and polyethylene/n-butane/carbon dioxide ternary systems. *J. Appl. Polym. Sci.*, *53*, 1179.

Xiong, Y. and Kiran, E. (1995). Miscibility, density and viscosity of poly(dimethylsiloxane) in supercritical carbon dioxide. *Polymer*, *36*, 4817.

Xiong, Y. and Kiran, E. (1998). High-pressure light scattering apparatus to study pressure-induced phase separation in polymer solutions. *Rev. Sci. Instrum.*, *69*, 1463.

Xiong, Y. (1998) Ph. D. Thesis, *Kinetics of pressure induced phase separation in polymer solutions: A time- and angle-resolved light scattering study*, University of Maine, Orono.

Xiong, Y. and Kiran, E. (2000). Kinetics of pressure-induced phase separation (PIPS) in polystyrene + methylcyclohexane solutions at high pressure. *Polymer*, *41*, 3759.

Yasuniwa, M., Yamaguchi, M., Nakamura, A. and Tsubakihara, S. (1990). Melting and crystallization of solution-crystallized ultrahigh-molecular-weight polyethylene under high pressure. *Polym. J.*, *22*, 411.

Yazdi, A. V., Lepilleur, C., Singley, E. J., Liu, W., Adamsky, F. A., Enick, R. M. and Beckman, E. J. (1996). Highly carbon dioxide soluble surfactants, dispersants and chelating agents. *Fluid Phase Equilibria*, *117*, 297-303.

Zhang, W. and Kiran, E. (2002a). Phase behavior and density of polysulfone in binary fluid mixtures of tetrahydrofuran and carbon dioxide under high pressure: Miscibility windows. *J. Appl. Polym. Sci.*, *86*(9), 2357.

Zhang, W. and Kiran, E. (2002b). Miscibility of polymer in binary fluid mixture at high pressures: polysulfone + THF + CO_2. *Proceedings of the 4th International Symposium on High Pressure Technology and Chemical Engineering - High Pressure in Venice*, September 22-25, Venice, Italy.

Zhang, W., Dindar, C., Bayraktar, Z. and Kiran, E. (2003). Phase behavior, density, and crystallization of polyethylene in n-pentane and in n-pentane/CO2 at high pressures. *J. Appl. Polym. Sci.*, *89*, 2201.

Zhang, W. and Kiran, E. (2003). PVT behavior and miscibility of the ternary system polysulfone + THF +CO_2 at high pressures. *J. Chem. Thermodynamics*, *35*, 605-624.

Zhang, W. and Kiran, E. (2005). High-Pressure Crystallization and Melting Kinetics of Polyethylene in n-Pentane. *To be submitted to Polymer.*

Zhuang, W. (1995) Ph. D. Thesis, *Miscibility, demixing and kinetics of phase separation of polymers in near and supercritical fluids by light scattering*, University of Maine, Orono, Maine.

Zhuang, W. and Kiran, E. (1996). An automated high pressure PVT apparatus for continuous recording density and isothermal compressibility of fluids. *Rev. Sci. Instrum.*, *67*, 244.

Zhuang, W. and Kiran, E. (1998). Kinetics of pressure-induced phase separation (PIPS) from polymer solutions by time-resolved light scattering. Polyethylene + n-pentane. *Polymer*, *39*(13), 2903.

Appendix A

Data Tables of the Phase Behavior and Volumetric Properties

The numerical data on the phase boundaries and densities of two polymer systems at high pressures are included in this section. Table A.1 gives the solid-fluid phase boundary of PE solutions in *n*-pentane or *n*-pentane + CO_2 binary mixtures. Table A.2 gives the liquid-liquid phase boundary of the PE solutions in *n*-pentane or *n*-pentane + CO_2 binary mixtures. Table A.3 includes the density data that were measured during the constant pressure cooling path for PE solutions in *n*-pentane or *n*-pentane + CO_2 binary mixtures. Table A.4 includes the density data that were measured during the pressure reduction path for the PE solutions in *n*-pentane or *n*-pentane + CO_2 binary mixtures.

Table A.5 gives the liquid-liquid phase boundary of the polysulfone solutions in THF + CO_2 binary mixtures. Table A.6 gives the density data of the binary mixtures of THF + CO_2. Table A.7-9 includes the density data tables for the polysulfone solutions in THF + CO_2 binary mixtures with 8, 10 and 13 wt % CO_2, respectively.

Table A.1. The crystallization and melting temperatures of PE in *n*-pentane and *n*-pentane + CO_2 mixtures at high pressures. These data are measured during the constant pressure cooling, variable pressure and temperature, and constant pressure heating paths.

Polyethylene: 0.51 wt %, *n*-Pentane:CO2 = 100:0

$T_{c,\ initial}$ and $T_{c,final}$ at P (Constant Pressure Cooling Path)			$T_{m,\ initial}$ and $T_{m,final}$ at P (Constant Pressure Heating Path)		
P/MPa	$T_{C,\ initial}$/K	$T_{C,\ final}$/K	P/MPa	$T_{m,\ initial}$/K	$T_{m,\ final}$/K
10.30	363.3	362.0	10.40	368.0	370.4
13.80	363.8	362.5	10.60	367.7	369.8
17.30	364.0	362.5	13.90	367.8	370.5
20.70	363.4	362.0	14.00	368.0	370.3
24.00	363.6	361.9	17.50	368.3	370.6
27.50	364.0	362.2	17.60	368.3	371.0
31.20	364.0	362.5	20.80	368.5	370.7
34.50	364.6	363.3	24.20	369.3	371.6
37.90	364.6	362.8	24.30	368.3	370.6
41.40	364.4	364.0	27.60	369.0	371.7
44.80	365.0	364.0	31.20	370.0	371.9
44.90	365.0	364.3	34.60	370.4	372.4
48.20	365.8	364.3	38.20	369.7	371.6
52.00	367.2	365.6	38.30	370.9	372.2
52.00	367.3	365.7	41.50	371.4	373.2
			44.80	370.2	371.8
			44.90	370.8	373.0
			48.30	371.4	372.3
			48.40	371.7	373.3
			51.90	373.1	374.3
			52.00	371.7	373.4

Polyethylene: 1.0 wt %, *n*-Pentane:CO2 = 100:0

$T_{c,\ initial}$ and $T_{c,final}$ at P (Constant Pressure Cooling Path)			$T_{m,\ initial}$ and $T_{m,final}$ at P (Constant Pressure Heating Path)		
P/MPa	$T_{C,\ initial}$/K	$T_{C,\ final}$/K	P/MPa	$T_{m,\ initial}$/K	$T_{m,\ final}$/K
12.40	362.8	361.5	12.40	366.7	369.9
12.40	362.8	361.8	12.50	365.1	367.8
16.00	363.9	361.7	15.40	367.1	370.4
19.20	364.5	362.0	18.80	366.2	368.9
22.80	364.2	361.7	19.00	367.2	370.1
22.80	363.8	360.7	18.90	367.0	369.9
26.00	363.5	360.4	22.70	366.3	369.4
28.50	364.0	361.3	22.30	367.7	371.4
32.80	363.9	362.2	26.40	367.2	370.4
36.60	364.6	362.4	26.40	367.2	370.4
35.60	364.0	360.6	29.30	367.6	370.5
40.00	364.4	361.4	32.10	367.6	370.7
40.00	364.5	361.5	32.40	368.3	371.3
43.00	365.5	362.4	32.20	368.0	371.2
46.00	366.3	362.7	36.00	366.8	369.6
50.00	366.6	363.4	38.80	368.5	371.2
53.80	366.9	362.9	40.00	368.7	372.0
			42.50	368.6	372.2
			47.20	370.3	376.2
			49.60	371.6	377.3
			49.00	370.4	373.3
			53.20	372.1	375.4
			55.00	371.5	377.4

(Table A.1 continued)

Polyethylene: 2.3 wt %, *n*-Pentane:CO2 = 100:0

$T_{c,\ initial}$ and $T_{c,final}$ at P (Constant Pressure Cooling Path)			$T_{m,\ initial}$ and $T_{m,final}$ at P (Constant Pressure Heating Path)		
P/MPa	$T_{C,\ initial}$/K	$T_{C,\ final}$/K	P/MPa	$T_{m,\ initial}$/K	$T_{m,\ final}$/K
10.40	365.8	364.0	10.50	370.0	372.0
13.90	365.8	363.5	14.00	370.0	371.7
17.30	365.0	362.2	17.30	369.0	371.4
20.70	365.8	364.1	20.80	370.1	373.1
24.00	365.7	362.7	24.00	370.1	373.2
27.60	367.4	364.3	27.70	370.1	374.6
32.00	367.2	363.7	34.60	370.1	373.1
34.60	365.8	363.9	38.10	370.1	374.6
38.00	365.8	364.0	42.60	373.0	376.0
44.40	367.2	365.7	45.10	371.6	374.6
48.40	368.7	365.7	48.40	373.0	374.7
51.80	367.4	365.6	51.80	372.9	376.1

PE conc. 4.4 %
n-Pentane:CO2 = 86:14

$T_{c,\ initial}$ and $T_{c,final}$ at P (Constant Pressure Cooling Path)		
P/MPa	$T_{C,\ initial}$/K	$T_{C,\ final}$/K
57.16	379.8	376.9
53.40	379.5	376.2
49.57	380.1	376.5
45.81	380.1	376.4
41.98	379.4	376.2
38.18	379.5	376.2
34.40	380.1	376.5

PE conc. 4.1 %
n-Pentane:CO2 = 81:19

$T_{c,\ initial}$ and $T_{c,final}$ at P (Constant Pressure Cooling Path)		
P/MPa	$T_{C,\ initial}$/K	$T_{C,\ final}$/K
57.20	380.2	377.2
53.40	380.1	377.0
49.60	380.5	377.1
45.77	379.7	376.6
41.97	379.8	376.4

Polyethylene: 1.0 wt %, *n*-Pentane:CO2 = 100:0

$T_{c,\ initial}$ and $T_{c,final}$ at P (Constant Pressure Cooling Path)		
P/MPa	$T_{C,\ initial}$/K	$T_{C,\ final}$/K
7.86	374.7	371.0
11.64	375.7	371.1
15.46	374.3	370.9
19.20	374.5	371.5
23.04	376.2	372.2
26.75	376.5	372.5
30.56	375.8	372.6
34.40	376.7	373.0
35.10	377.3	373.0
36.64	376.7	373.0
38.20	375.2	372.5
39.70	375.9	372.3
41.16	376.0	372.5
41.90	377.7	373.7
45.75	377.5	374.0
49.50	377.8	374.2
53.30	377.0	374.0

$T_{c,\ initial}$ and $T_{c,final}$ at P_i and P_f (Variable P and T Cooling Path)			
P_i/MPa	$T_{c,\ initial}$/K	P_f/MPa	$T_{c,\ final}$/K
7.63	376.8	6.21	372.4
7.85	387.5	6.88	383.9
13.65	374.3	12.36	371.0
25.60	374.7	24.00	371.4
33.34	376.2	31.75	372.7
38.32	378.7	36.13	373.7
40.42	376.7	39.00	373.5
46.80	379.0	44.90	374.5

Table A.2. The liquid-liquid phase boundary of PE in *n*-pentane and *n*-pentane + CO_2 mixtures at high pressures. The demixing pressures were measured during the pressure reduction paths at a constant T. P_i and P_f are the incipient demixing pressure and demixing pressure at $I_{tr} = 0$ conditions.

Polyethylene: 0.5 wt %
n-Pentane:CO2 = 100:0

T/K	P_i/MPa	P_f/MPa
373.4	5.20	1.60
377.9	7.30	1.70
381.0	7.70	1.80
388.0	7.60	3.20
393.3	9.40	3.60
398.2	9.90	1.80
399.8	10.20	5.60

Polyethylene: 1.0 wt %
n-Pentane:CO2 = 100:0

T/K	P_i/MPa	P_f/MPa
368.4	3.30	0.80
373.2	5.10	0.80
377.7	6.40	0.90
383.5	5.40	1.20
387.9	7.60	1.20
393.8	8.80	2.20
398.3	9.70	3.00
404.1	10.70	6.00
409.6	10.40	4.00

Polyethylene: 2.3 wt %
n-Pentane:CO2 = 100:0

T/K	P_i/MPa	P_f/MPa
368.6	7.10	2.00
373.1	8.00	4.00
375.2	7.90	1.60
377.4	9.20	5.90
381.8	9.40	4.00
383.4	9.30	6.30
387.8	9.90	5.70
387.9	9.90	9.00
393.6	11.40	8.30
395.3	11.00	7.50
398.2	12.20	9.40
401.1	12.00	8.90

Polyethylene: 5.0 wt %
n-Pentane:CO2 = 100:0

T/K	P_i/MPa	P_f/MPa
378.4	6.25	5.25
382.1	7.61	5.86
389.0	8.53	7.13
398.4	9.96	8.13
402.9	10.54	9.11
407.8	11.10	9.73
413.3	12.00	10.28
418.4	12.29	11.30
423.4	13.78	12.33
427.1	14.41	12.97
433.4	14.56	13.73
438.3	15.03	14.23

Polyethylene: 4.4 %
n-Pentane:CO2 = 86:14

T/K	P_i/MPa	P_f/MPa
383.8	32.15	31.35
388.3	32.25	31.30
393.6	32.69	31.75
398.0	33.00	32.25
403.6	33.40	32.75
408.5	33.80	33.10
413.6	34.20	33.50
418.5	34.50	33.80
423.2	34.90	34.25
428.4	35.30	34.60
434.4	35.70	35.10
438.5	36.40	35.40

Polyethylene: 4.1 %
n-Pentane:CO2 = 81:19

T/K	P_i/MPa	P_f/MPa
393.4	38.80	38.00
398.2	39.10	38.30
403.4	39.25	38.50
408.3	39.50	38.80
413.6	39.90	39.20
418.5	40.10	39.40
423.6	40.30	39.80
428.3	40.60	39.90
433.5	40.90	40.20
438.4	41.20	40.40

Table A.3. The density of PE solutions in *n*-pentane or *n*-pentane + CO_2 mixtures at high pressures. These data are measured during the constant pressure cooling path.

Polyethylene: 5.0 wt %, *n*-Pentane:CO2 = 100:0

	T/K	ρ/g.cm^3	T/K	ρ/g.cm^3	T/K	ρ/g.cm^3	T/K	ρ/g.cm^3	T/K	ρ/g.cm^3
P/MPa	**49.47**		**45.68**		**40.76**		**39.63**		**36.60**	
	384.3	0.6274	384.4	0.6258	385.9	0.6237	389.5	0.6153	390.8	0.6112
	382.3	0.6288	381.9	0.6272	383.8	0.6237	387.5	0.6162	388.5	0.6124
	380.1	0.6302	380.3	0.6282	381.3	0.6237	385.5	0.6175	386.6	0.6136
	377.8	0.6318	377.9	0.6301	379.5	0.6251	383.5	0.6188	384.1	0.6153
	375.6	0.6331	376.7	0.6310	377.6	0.6260	381.6	0.6201	382.7	0.6162
	373.5	0.6342	375.7	0.6318	376.1	0.6269	379.6	0.6216	381.0	0.6176
	372.8	0.6348	374.4	0.6324	375.5	0.6274	377.5	0.6230	378.5	0.6195
	371.3	0.6354	373.7	0.6328	374.3	0.6282	375.7	0.6245	377.0	0.6204
			372.6	0.6336	373.4	0.6286	374.2	0.6255	375.6	0.6216
					372.1	0.6297	373.3	0.6261	374.5	0.6222
					371.4	0.6303	372.1	0.6270	373.8	0.6228
							370.9	0.6279	372.7	0.6238
							370.2	0.6286	371.7	0.6245
									371.1	0.6252

	T/K	ρ/g.cm^3	T/K	ρ/g.cm^3	T/K	ρ/g.cm^3	T/K	ρ/g.cm^3	T/K	ρ/g.cm^3
P/MPa	**34.33**		**30.55**		**26.76**		**22.98**		**19.20**	
	386.8	0.6109	390.4	0.6031	385.6	0.6022	386.8	0.5939	389.5	0.5850
	384.3	0.6122	388.8	0.6040	383.4	0.6025	385.9	0.5945	387.7	0.5863
	382.8	0.6134	385.8	0.6062	381.6	0.6037	384.9	0.5953	385.7	0.5875
	380.9	0.6145	383.0	0.6083	379.8	0.6051	383.6	0.5964	384.7	0.5890
	378.7	0.6161	380.8	0.6098	378.3	0.6066	382.3	0.5973	383.0	0.5901
	376.6	0.6179	379.4	0.6109	376.9	0.6077	381.7	0.5978	381.1	0.5916
	375.6	0.6187	377.1	0.6128	375.6	0.6085	379.5	0.5995	379.9	0.5926
	374.6	0.6195	376.1	0.6135	374.5	0.6094	378.2	0.6007	378.6	0.5939
	373.6	0.6201	375.0	0.6143	373.7	0.6101	377.3	0.6016	377.4	0.5950
	372.5	0.6209	373.3	0.6155	372.7	0.6109	376.0	0.6027	376.3	0.5961
	371.5	0.6216	372.7	0.6161	372.1	0.6115	374.1	0.6041	374.8	0.5973
	371.0	0.6221	371.6	0.6171	371.2	0.6123	373.3	0.6048	373.5	0.5983
			370.8	0.6178	370.8	0.6128	371.7	0.6062	372.8	0.5990
							371.4	0.6066	371.9	0.5998
							370.8	0.6071	371.4	0.6003
									370.8	0.6009
									370.5	0.6013

	T/K	ρ/g.cm^3	T/K	ρ/g.cm^3	T/K	ρ/g.cm^3
P/MPa	**15.41**		**11.63**		**7.85**	
	385.7	0.5811	387.3	0.5719	385.5	0.5641
	384.0	0.5820	385.8	0.5730	384.6	0.5650
	382.7	0.5832	384.9	0.5739	382.8	0.5664
	381.4	0.5844	383.2	0.5754	381.5	0.5679
	380.2	0.5854	381.5	0.5770	379.5	0.5699
	378.6	0.5870	380.0	0.5784	378.3	0.5710
	377.1	0.5882	378.9	0.5797	377.0	0.5724
	376.1	0.5892	377.3	0.5810	376.0	0.5737
	374.9	0.5904	376.2	0.5821	374.9	0.5750
	373.8	0.5914	374.9	0.5836	373.9	0.5759
	372.6	0.5925	373.9	0.5847	372.7	0.5771
	371.5	0.5934	373.1	0.5854	371.6	0.5783
	370.6	0.5943	372.0	0.5863	371.2	0.5790
	369.8	0.5951	371.0	0.5871	370.5	0.5797
	369.2	0.5957	370.3	0.5879	369.4	0.5806
			369.9	0.5882		

(Table A.3 continued)

Polyethylene: 4.4 wt %, *n*-Pentane:CO2 = 86:14

	T/K	ρ/g.cm^3	T/K	ρ/g.cm^3	T/K	ρ/g.cm^3	T/K	ρ/g.cm^3	T/K	ρ/g.cm^3	T/K	ρ/g.cm^3	T/K	ρ/g.cm^3
P/MPa	**57.16**		**53.40**		**49.67**		**45.80**		**41.98**		**38.18**		**34.40**	
	389.4	0.7225	394.7	0.7070	393.7	0.7016	393.8	0.6944	394.7	0.6857	393.2	0.6767	392.0	0.6732
	387.6	0.7237	392.1	0.7094	392.0	0.7027	391.8	0.6960	393.0	0.6870	391.2	0.6795	390.0	0.6745
	386.3	0.7249	390.0	0.7114	390.4	0.7044	390.3	0.6975	391.6	0.6884	388.7	0.6821	388.8	0.6758
	384.3	0.7262	388.1	0.7128	388.8	0.7057	388.6	0.6989	390.0	0.6899	386.6	0.6844	387.5	0.6774
	382.9	0.7275	386.6	0.7139	387.2	0.7071	387.4	0.7002	388.7	0.6912	385.1	0.6859	385.6	0.6795
	381.8	0.7287	383.7	0.7167	385.5	0.7089	386.0	0.7017	387.7	0.6922	383.5	0.6875	384.1	0.6809
	380.6	0.7299	382.4	0.7181	383.7	0.7108	384.6	0.7031	386.6	0.6931	381.6	0.6897	383.0	0.6823
	379.2	0.7314	381.5	0.7189	382.7	0.7118	383.7	0.7041	385.1	0.6947	379.7	0.6920	380.9	0.6848
	378.0	0.7327	380.2	0.7200	381.3	0.7129	382.5	0.7052	383.8	0.6961	378.4	0.6932	380.4	0.6853
	376.5	0.7340	379.3	0.7209	379.2	0.7150	381.0	0.7062	382.0	0.6982	377.5	0.6944	378.7	0.6873
	375.6	0.7347	378.1	0.7221	378.4	0.7158	380.0	0.7075	380.8	0.6991	376.1	0.6960	377.0	0.6894
			377.3	0.7230	377.4	0.7169	379.0	0.7086	378.6	0.7018	375.4	0.6970	376.4	0.6902
			376.2	0.7241	376.5	0.7178	378.0	0.7100	377.5	0.7028	374.6	0.6980	375.8	0.6908
			375.4	0.7251	375.8	0.7186	377.0	0.7109	376.7	0.7039				
			374.8	0.7256	375.1	0.7192	376.5	0.7113	376.1	0.7047				
							375.5	0.7123	375.4	0.7055				
							375.1	0.7126	374.9	0.7058				

Polyethylene: 4.1 wt %, *n*-Pentane:CO2 = 81:19

	T/K	ρ/g.cm^3	T/K	ρ/g.cm^3	T/K	ρ/g.cm^3	T/K	ρ/g.cm^3	T/K	ρ/g.cm^3
P/MPa	**57.16**		**53.40**		**49.57**		**45.80**		**41.98**	
	396.6	0.7146	392.9	0.7106	394.6	0.7012	390.9	0.6980	393.8	0.6878
	395.0	0.7157	391.1	0.7121	391.9	0.7035	389.1	0.6991	392.8	0.6883
	393.5	0.7171	389.1	0.7139	390.6	0.7047	387.7	0.7000	391.3	0.6898
	391.6	0.7188	387.5	0.7151	389.3	0.7059	386.5	0.7012	390.2	0.6908
	390.1	0.7201	385.9	0.7169	387.6	0.7075	385.4	0.7023	389.3	0.6919
	388.3	0.7215	384.4	0.7181	386.2	0.7089	383.9	0.7039	388.2	0.6931
	386.8	0.7229	382.9	0.7195	384.9	0.7104	383.0	0.7050	387.2	0.6941
	385.4	0.7245	381.6	0.7205	383.1	0.7121	382.0	0.7061	386.1	0.6952
	383.4	0.7261	380.7	0.7214	381.4	0.7139	381.0	0.7071	384.9	0.6966
	381.6	0.7276	379.7	0.7226	380.1	0.7152	380.2	0.7077	383.7	0.6978
	379.9	0.7294	378.5	0.7239	379.2	0.7162	379.5	0.7085	382.6	0.6991
	378.6	0.7307	377.6	0.7248	378.5	0.7172	378.3	0.7100	381.6	0.7002
	377.6	0.7318	376.8	0.7256	377.7	0.7180	377.5	0.7110	379.8	0.7020
	377.0	0.7323	376.0	0.7265	377.1	0.7189	376.6	0.7122	378.8	0.7031
	375.8	0.7334	375.4	0.7269	376.5	0.7195	375.5	0.7131	377.7	0.7044
					376.0	0.7199			376.7	0.7056
									375.6	0.7067

Table A.4. The density of PE solutions in *n*-pentane or *n*-pentane + CO_2 mixtures at high pressures. These data are measured during the pressure reduction path.

Polyethylene: 4.4 wt %, *n*-Pentane:CO2 = 86:14

	P/MPa	ρ/g.cm^3	P/MPa	ρ/g.cm^3	P/MPa	ρ/g.cm^3	P/MPa	ρ/g.cm^3	P/MPa	ρ/g.cm^3
T/K	**397.5**		**403.4**		**408.3**		**413.5**		**417.8**	
	49.5	0.6977	49.5	0.6927	49.5	0.6850	49.5	0.6798	49.5	0.6735
	45.7	0.6913	45.7	0.6830	45.7	0.6807	45.7	0.6754	45.7	0.6688
	41.9	0.6840	41.9	0.6777	41.9	0.6727	41.9	0.6677	41.9	0.6605
	38.1	0.6760	38.1	0.6698	38.1	0.6647	38.1	0.6585	38.2	0.6516
	33.0	0.6641	33.4	0.6580	33.8	0.6537	34.2	0.6484	34.5	0.6419
	32.3	0.6614	32.8	0.6555	33.1	0.6508	33.6	0.6457	33.7	0.6394
	30.5	0.6572	30.5	0.6498	30.5	0.6439	30.5	0.6373	30.5	0.6307
	26.8	0.6471	26.8	0.6397						

	P/MPa	ρ/g.cm^3	P/MPa	ρ/g.cm^3	P/MPa	ρ/g.cm^3	P/MPa	ρ/g.cm^3
T/K	**423.9**		**428.3**		**433.2**		**438.6**	
	49.5	0.6706	49.5	0.6655	49.5	0.6600	49.6	0.6539
	45.7	0.6632	45.8	0.6576	45.7	0.6523	45.7	0.6477
	41.9	0.6542	41.9	0.6485	42.0	0.6435	41.9	0.6387
	38.1	0.6445	38.1	0.6390	38.2	0.6333	38.1	0.6288
	34.9	0.6362	35.3	0.6305	35.7	0.6237	36.4	0.6218
	34.3	0.6338	34.6	0.6291	35.1	0.6230	35.4	0.6193
	30.5	0.6238	34.4	0.6290	34.5	0.6235	34.3	0.6179
			30.5	0.6186	30.6	0.6121	30.5	0.6068

Polyethylene: 4.1 wt %, *n*-Pentane:CO2 = 81:19

	P/MPa	ρ/g.cm^3	P/MPa	ρ/g.cm^3	P/MPa	ρ/g.cm^3	P/MPa	ρ/g.cm^3	P/MPa	ρ/g.cm^3
T/K	**398.3**		**403.3**		**408.4**		**413.2**		**418.2**	
	49.5	0.7011	49.5	0.6946	49.5	0.6889	49.5	0.6838	49.5	0.6779
	45.7	0.6931	45.7	0.6876	45.7	0.6812	45.7	0.6759	45.7	0.6699
	41.9	0.6852	41.9	0.6787	41.9	0.6723	41.9	0.6674	41.9	0.6611
	39.1	0.6787	39.2	0.6724	39.5	0.6667	39.9	0.6624	40.1	0.6563
	38.3	0.6765	38.4	0.6703	38.8	0.6651	39.2	0.6605	39.3	0.6540
	34.3	0.6672	34.3	0.6605	34.3	0.6540	34.3	0.6481	38.1	0.6509

	P/MPa	ρ/g.cm^3	P/MPa	ρ/g.cm^3	P/MPa	ρ/g.cm^3	P/MPa	ρ/g.cm^3
T/K	**422.8**		**427.9**		**432.7**		**438.2**	
	49.5	0.6714	49.5	0.6654	49.5	0.6603	49.5	0.6558
	45.7	0.6631	45.7	0.6573	45.7	0.6518	45.7	0.6472
	41.9	0.6543	41.9	0.6480	41.9	0.6428	41.2	0.6358
	40.3	0.6501	40.6	0.6449	40.9	0.6399	40.4	0.6332
	39.7	0.6486	39.9	0.6430	40.2	0.6379	38.1	0.6309
	38.1	0.6445	38.1	0.6385	38.1	0.6327		

Table A.5. The liquid-liquid phase boundary of polysulfone in THF + CO_2 mixtures at high pressures. These data are measured during the pressure reduction paths.

4.5 wt % Polysulfone in THF/CO_2

THF/CO_2: 90.1/9.9		THF/CO_2: 88.6/11.4		THF/CO_2: 87.1/12.9		THF/CO_2: 86.1/13.9	
T/K	P_i/MPa	T/K	P_i/MPa	T/K	P_i/MPa	T/K	P_i/MPa
307.7	15.8	304.5	42.3	303.7	51.4	300.0	67.9
314.0	17.1	312.2	42.8	307.6	52.1	303.6	67.6
318.0	18.1	318.4	43.6	313.4	52.9	308.4	67.0
320.0	19.3	323.8	44.3	316.7	53.3	313.2	66.6
323.5	20.1	328.0	44.7	297.8	53.5	318.7	66.2
328.6	21.5	333.3	45.2	323.4	53.6	323.3	66.0
328.8	21.7	338.3	45.9	328.2	53.7	328.9	65.7
332.3	22.6	343.6	46.3	333.0	54.1	333.1	65.5
337.0	23.3	348.2	46.9	338.4	54.5	338.7	65.1
339.1	24.3	353.8	47.8	338.7	54.5	343.4	64.9
342.4	25.1	357.9	48.3	344.0	54.7	348.4	64.9
345.5	26.0	363.6	48.8	348.0	54.9	353.2	64.8
348.9	26.9	368.1	49.7	353.0	55.3	358.4	64.9
353.4	27.5	373.4	50.0	358.2	55.6	363.3	64.9
355.4	28.5	377.6	50.7	362.9	55.9	368.3	64.8
358.8	29.2	383.4	51.6	368.4	56.4		
363.0	30.1	388.3	52.3	373.4	56.8		
368.2	31.3	392.9	52.6	378.6	57.3		
373.2	32.7	398.4	53.4	383.2	57.7		
378.0	33.4	402.6	54.0	388.6	58.0		
383.1	34.3	408.6	54.7	392.9	58.5		
388.6	35.3	413.5	55.3	398.5	59.2		
393.7	36.6	417.2	55.8	402.8	59.6		
398.5	37.6	423.2	56.2	408.9	60.3		
402.6	38.5			411.2	60.5		
404.8	38.7			413.4	60.8		
408.6	39.4			418.4	61.1		
413.6	40.5			423.3	62.0		
417.4	41.3						
418.8	41.5						
423.4	42.3						

Polysulfone Solution in THF/CO_2 = 92:8

Polysulfone: 1.00 wt %		Polysulfone: 1.31 wt %		Polysulfone: 1.49 wt %		Polysulfone: 1.90 wt %		Polysulfone: 2.22 wt %	
T/K	P_i/MPa	T/K	P_i/MPa	T/K	P_i/MPa	T/K	P_i/MPa	T/K	P_i/MPa
288.8	10.8	299.2	1.8	297.7	2.4	293.2	4.0	309.2	0.0
293.0	12.4	303.0	3.1	303.7	2.8	298.1	5.8	313.2	1.4
298.2	13.9	308.2	5.5	308.1	4.0	303.0	6.8	318.8	3.3
303.2	15.2	313.0	7.5	313.3	6.2	308.0	8.5	323.0	5.2
308.2	16.6	318.3	9.2	318.2	8.4	313.0	10.4	328.0	6.8
313.2	18.4	323.3	11.0	323.2	10.1	318.2	12.0	333.4	8.9
318.5	19.2	327.4	12.6	328.4	12.0	323.3	14.0	338.2	10.6
323.8	21.0	332.8	14.2	333.1	13.2	328.2	15.9	343.2	12.2
328.4	21.8	338.1	16.0	338.1	15.0	332.8	17.0	348.3	13.9
332.8	23.1	343.4	17.6	343.2	16.7	337.9	18.3	353.2	15.0
338.3	24.4	348.0	18.8	348.2	18.0	343.4	20.0	358.1	16.5
343.2	25.7	352.7	20.1	353.3	19.9	348.2	21.4	363.2	18.3
349.1	27.0	357.9	22.0	358.4	21.1	353.3	23.3	368.3	19.6
353.4	28.4	363.2	23.3	363.4	22.3	358.0	24.0	370.8	20.2
358.5	29.8	368.1	24.5	368.4	23.6	363.2	25.3	378.1	22.4

(Table A.5 continued)

Polysulfone: 1.00 wt %		Polysulfone: 1.31 wt %		Polysulfone: 1.49 wt %		Polysulfone: 1.90 wt %		Polysulfone: 2.22 wt %	
T/K	P_i/MPa	T/K	P_i/MPa	T/K	P_i/MPa	T/K	P_i/MPa	T/K	P_i/MPa
363.2	30.6	373.2	26.2	373.2	25.0	368.5	26.6	382.8	23.9
368.3	31.8	378.6	27.7	378.3	26.8	373.2	27.9	388.6	25.6
373.2	34.0	383.2	28.7	383.5	27.8	377.3	28.8	393.1	26.5
378.4	34.8	387.6	29.6	388.4	28.9	383.5	30.4	398.4	27.9
383.8	35.6	393.6	31.0	393.4	30.1	388.2	31.6	403.4	29.0
388.4	36.6	398.4	32.6	398.4	31.4	393.5	32.8	407.8	30.2
393.4	38.0	403.0	33.6	403.0	32.2	398.1	33.6	413.2	31.3
398.4	38.6	408.4	34.6	407.8	33.1	403.3	34.7	418.4	32.3
403.2	39.5	413.2	35.5	413.4	34.4	408.1	35.8	423.4	33.3
408.8	40.0	418.4	36.7	418.6	35.5	413.2	36.8	426.6	34.1
413.3	41.1	424.6	37.8	426.2	36.8	418.2	38.0		
418.2	41.7					425.6	39.2		
423.8	42.2								
428.0	42.8								

Polysulfone Solution in THF/CO_2 = 92:8

Polysulfone: 2.43 wt %		Polysulfone: 2.85 wt %		Polysulfone: 3.05 wt %		Polysulfone: 3.26 wt %		Polysulfone: 3.69 wt %	
T/K	P_i/MPa	T/K	P_i/MPa	T/K	P_i/MPa	T/K	P_i/MPa	T/K	P_i/MPa
308.8	0.0	308.2	0.0	299.8	1.8	316.9	4.2	318.5	2.3
313.2	2.8	313.3	1.9	303.4	3.0	323.5	6.5	323.9	4.3
318.2	4.5	318.2	4.0	308.2	4.3	328.2	8.1	328.8	6.0
325.0	10.0	323.5	5.4	313.6	6.4	333.4	9.7	333.4	7.2
331.8	11.0	328.0	7.2	318.2	7.8	338.2	11.4	338.3	9.0
335.0	12.5	333.4	9.0	323.4	9.4	343.2	13.1	343.3	10.2
339.7	14.0	338.1	9.8	328.6	11.3	348.3	14.7	347.8	11.8
345.1	16.0	343.1	11.8	333.1	12.6	353.1	16.0	351.4	12.7
349.4	18.5	348.1	13.4	339.0	14.3	357.8	17.5	358.3	15.0
353.4	19.8	353.2	14.8	343.2	15.4	363.2	19.0	363.2	16.4
359.4	22.0	358.3	16.3	348.0	16.8	368.2	20.4	367.4	17.3
363.4	23.0	363.2	17.7	348.2	17.0	373.4	21.8	372.9	18.8
368.5	24.4	368.1	19.4	353.4	18.4	378.2	23.1	378.1	20.6
374.1	25.5	373.2	21.0	358.2	19.8	382.8	24.4	382.7	21.7
379.1	27.5	378.2	22.7	363.2	21.2	387.1	25.4	388.3	23.3
383.2	28.0	383.3	23.5	368.3	22.4	393.4	28.9	393.4	24.2
389.4	29.8	388.3	25.4	373.4	24.0	398.2	30.0	397.6	25.0
394.0	31.4	393.1	26.6	378.2	25.2	402.9	29.2	403.5	26.5
398.7	32.4	398.4	27.8	383.4	26.2	405.9	29.8	407.9	27.6
403.6	34.0	403.1	29.0	387.6	27.3	412.4	31.4	413.0	28.8
411.4	35.0	408.0	29.8	393.3	28.9	417.5	32.4	418.4	30.2
414.2	35.5	413.2	30.6	398.2	30.0	425.7	34.0	425.0	31.1
418.4	36.0	418.0	31.4	402.8	31.1				
424.2	36.5	423.2	32.4	408.1	32.0				
				413.6	33.2				
				418.4	34.3				
				425.6	35.7				

(Table A.5 continued)

Polysulfone Solution in THF/CO_2 = 92:8

Polysulfone: 3.90 wt %		Polysulfone: 4.19 wt %		Polysulfone: 4.73 wt %	
T/K	P_i/MPa	T/K	P_i/MPa	T/K	P_i/MPa
298.2	7.0	298.9	10.6	298.8	14.2
303.1	9.0	303.3	12.1	303.2	15.4
307.5	10.3	308.0	13.9	307.9	16.6
313.1	12.4	313.3	15.5	313.1	19.7
318.2	14.3	318.0	17.3	317.9	21.0
323.0	15.9	322.9	18.8	323.1	22.6
328.1	17.5	328.2	20.3	327.9	23.9
333.1	19.0	333.2	22.0	333.2	25.3
338.2	20.6	337.4	23.2	338.1	26.3
343.4	22.0	342.3	24.4	343.0	27.5
347.9	23.2	348.2	25.8	348.1	28.7
353.1	24.5	353.2	27.3	353.2	29.9
357.9	25.7	358.3	28.8	358.4	31.0
363.2	27.0	363.4	30.1	363.3	32.1
368.3	28.2	368.3	31.1	368.4	33.1
373.2	29.4	373.4	32.0	373.4	34.2
378.2	30.5	378.3	33.3	378.3	35.3
382.6	31.6	383.4	34.4	383.4	36.2
388.4	33.0	388.4	35.4	387.6	37.1
393.3	34.0	393.1	36.3	393.6	38.3
398.2	35.0	398.4	37.4	398.3	39.1
403.4	36.2	403.4	38.3	403.4	40.0
408.4	37.4	408.4	39.2	408.5	41.0
413.5	38.5	413.6	40.2	413.4	41.9
418.1	39.3	418.4	41.3	418.4	42.6
426.2	40.6	424.4	42.0	423.5	43.4
				427.6	44.2

Polysulfone Solution in THF/CO_2 = 90:10

Polysulfone: 1.00 wt %		Polysulfone: 1.50 wt %		Polysulfone: 2.00 wt %		Polysulfone: 2.46 wt %		Polysulfone: 3.01 wt %	
T/K	P_i/MPa	T/K	P_i/MPa	T/K	P_i/MPa	T/K	P_i/MPa	T/K	P_i/MPa
298.2	58.1	299.1	22.0	299.3	13.1	300.9	25.3	302.8	37.8
303.4	58.1	306.4	22.7	303.9	13.7	303.1	25.7	308.6	38.6
308.4	57.8	308.5	23.8	308.9	15.3	308.7	27.0	313.6	39.2
313.2	57.4	313.5	25.3	313.4	16.7	313.4	27.8	319.0	40.1
318.6	57.4	318.3	26.6	318.4	18.2	319.2	28.8	324.0	40.6
323.6	57.6	323.3	27.6	323.5	19.7	323.3	30.0	328.7	40.9
328.5	57.7	328.6	28.7	328.5	20.9	328.4	31.0	333.6	41.7
333.7	57.6	333.3	29.7	333.6	22.6	333.2	32.0	338.7	42.3
338.6	57.8	338.4	30.8	338.7	23.6	338.6	33.3	343.6	42.9
343.4	57.9	343.1	32.2	343.6	25.3	343.4	34.1	348.6	43.9
348.4	58.1	348.3	33.0	348.9	26.6	348.5	35.2	353.6	44.3
353.4	58.2	353.5	34.3	353.6	27.4	353.5	36.2	358.5	45.3
358.5	58.4	358.4	35.3	358.9	28.8	358.7	37.2	363.7	46.0
363.2	58.5	363.4	36.2	363.3	29.9	364.2	38.4	368.6	46.7
368.3	58.8	368.3	37.0	369.0	31.2	368.6	39.1	373.4	47.3
373.2	59.2	372.9	38.1	373.4	32.0	373.3	40.2	378.8	48.1
378.4	59.5	380.3	39.2	378.5	33.3	378.5	41.0	384.2	48.7
383.2	60.0	383.3	40.1	383.4	34.5	383.5	41.9	388.7	49.5
388.4	60.5	388.5	41.2	388.7	35.7	388.9	42.9	393.5	50.1
393.4	60.8	393.9	42.2	393.6	37.1	393.9	43.7	398.4	50.9
398.2	61.2	398.3	43.0	398.5	37.8	399.5	44.6	403.3	51.4
403.2	61.6	408.5	44.3	403.5	38.9	403.6	45.5	408.6	52.1

(Table A.5 continued)

Polysulfone: 1.00 wt %		Polysulfone: 1.50 wt %		Polysulfone: 2.00 wt %		Polysulfone: 2.46 wt %		Polysulfone: 3.01 wt %	
T/K	P_i/MPa	T/K	P_i/MPa	T/K	P_i/MPa	T/K	P_i/MPa	T/K	P_i/MPa
408.4	62.2	413.6	45.3	409.0	40.0	408.6	46.2	413.7	53.0
413.2	62.5	418.6	46.3	413.7	40.8	413.2	47.2	418.0	53.4
		423.4	47.1	418.6	41.1	418.4	47.5	423.2	53.7
				423.4	42.0	423.1	48.6		

Polysulfone Solution in THF/CO_2 = 90:10

Polysulfone: 3.21 wt %		Polysulfone: 3.66 wt %		Polysulfone: 4.44 wt %		Polysulfone: 4.96 wt %	
T/K	P_i/MPa	T/K	P_i/MPa	T/K	P_i/MPa	T/K	P_i/MPa
296.3	35.1	298.3	13.0	304.9	24.6	299.1	40.2
303.7	36.1	303.8	14.4	308.7	25.7	303.7	41.0
308.5	36.8	308.8	15.8	314.8	27.2	308.4	41.6
313.3	37.4	313.4	17.2	319.1	28.2	313.2	42.0
318.8	38.2	318.2	18.7	326.1	29.6	318.4	42.8
323.4	39.1	323.2	20.1	329.4	30.2	323.0	43.1
328.4	39.8	328.6	21.6	333.7	31.1	329.3	44.0
333.8	40.5	333.4	22.8	338.9	32.0	333.6	44.5
338.5	41.2	338.4	24.0	343.6	33.0	338.4	45.0
343.5	42.0	343.2	25.3	348.8	34.1	343.0	45.3
349.2	42.8	348.9	26.9	353.6	35.1	348.2	45.7
353.7	43.5	357.1	28.7	358.7	36.1	353.4	46.4
358.6	44.1	359.4	29.3	365.4	37.2	358.5	46.8
363.6	45.0	363.4	30.2	368.6	38.0	363.4	47.4
368.4	45.6	368.0	31.2	373.8	38.9	368.2	48.0
373.2	46.3	373.2	32.5	378.7	39.8	373.2	48.8
378.6	47.2	378.1	33.7	383.6	40.8	379.2	49.5
383.4	47.9	383.6	34.8	388.6	41.7	384.0	50.1
388.7	48.6	388.2	35.9	393.7	42.6	388.6	50.7
394.0	49.1	393.2	36.9	398.5	43.5	393.4	51.4
398.3	50.0	398.0	37.8	403.6	44.3	398.5	52.1
403.4	50.4	403.6	38.8	408.8	45.2	404.1	52.0
408.4	50.8	408.9	39.7	413.8	45.5	408.6	52.6
413.6	51.5	413.6	40.5	418.4	46.0	413.9	53.2
418.4	52.3	418.4	41.6	423.3	46.5	418.5	53.9
423.7	53.2	423.3	42.4			423.4	54.6

Polysulfone Solution in THF/CO_2 = 87:13

Polysulfone: 0.28 wt %		Polysulfone: 0.50 wt %		Polysulfone: 1.02 wt %		Polysulfone: 2.00 wt %		Polysulfone: 2.05 wt %	
T/K	P_i/MPa	T/K	P_i/MPa	T/K	P_i/MPa	T/K	P_i/MPa	T/K	P_i/MPa
302.8	67.6	313.7	52.6	307.4	50.0	301.5	47.3	299.6	49.6
307.8	65.0	317.8	52.4	312.0	50.8	313.1	47.5	304.2	49.4
312.7	64.6	323.1	53.2	318.5	51.5	318.3	47.8	308.9	49.6
318.3	63.4	328.3	53.2	322.9	51.6	323.5	48.3	314.3	50.1
323.2	63.5	333.8	53.4	327.5	52.1	329.0	49.0	319.2	50.3
328.8	63.4	338.4	54.3	332.6	52.7	334.3	49.5	325.1	50.5
333.9	63.6	343.1	54.4	337.8	53.0	338.8	49.8	328.7	50.9
339.9	62.6	348.3	54.7	343.1	53.4	343.3	50.0	333.4	51.2
343.8	62.8	352.3	54.6	348.3	54.0	348.6	50.5	338.5	51.5
358.5	63.0	358.2	54.8	353.6	54.6	353.5	51.0	343.0	51.9
363.2	63.1	363.1	55.2	357.4	54.7	358.4	51.3	351.0	52.2
368.4	63.4	366.3	55.3	360.1	54.8	363.3	51.6	354.3	52.8
373.2	63.6	373.3	57.2	368.5	56.0	368.5	52.6	358.9	53.2
378.2	63.4	378.7	57.3	372.8	56.3	373.5	52.9	363.2	53.5
383.1	63.1	382.9	58.1	376.0	56.4	378.4	53.5	368.6	54.0

(Table A.5 continued)

Polysulfone: 0.28 wt %		Polysulfone: 0.50 wt %		Polysulfone: 1.02 wt %		Polysulfone: 2.00 wt %		Polysulfone: 2.05 wt %	
T/K	P_i/MPa	T/K	P_i/MPa	T/K	P_i/MPa	T/K	P_i/MPa	T/K	P_i/MPa
388.4	63.6	388.0	58.3	383.2	57.0	383.0	54.1	373.6	54.6
393.2	64.2	393.6	58.8	387.9	57.4	388.6	54.7	379.0	55.0
398.6	64.2	397.9	59.6	393.6	58.3	393.2	55.1	385.5	55.6
403.2	64.8	403.6	60.3	397.6	58.4	398.8	55.5	388.5	55.9
408.3	65.1	408.6	60.8	403.4	59.1	403.4	55.8	393.4	56.2
414.3	65.6	413.4	61.2	408.4	59.5	408.8	56.0	398.3	56.3
418.1	65.4	418.4	61.7	413.0	59.9	413.4	56.1	404.1	57.3
422.3	66.2	424.6	62.0	418.4	60.0	418.4	56.5	409.1	57.7
				422.4	60.1	423.3	57.0	413.6	57.8
								418.5	58.5
								424.5	59.2

Polysulfone Solution in THF/CO_2 = 87:13

Polysulfone: 3.69 wt %		Polysulfone: 3.99 wt %		Polysulfone: 4.30 wt %		Polysulfone: 4.99 wt %	
T/K	P_i/MPa	T/K	P_i/MPa	T/K	P_i/MPa	T/K	P_i/MPa
298.2	50.1	300.8	41.0	303.7	51.4	297.9	57.0
305.5	50.2	304.0	41.5	307.6	52.1	303.4	57.4
309.1	50.4	308.6	42.0	313.4	52.9	308.3	57.0
313.8	50.7	314.7	42.6	316.7	53.3	313.8	56.6
318.6	50.8	319.6	43.4	323.4	53.6	319.2	56.5
324.5	51.3	323.8	43.8	329.3	53.9	324.3	56.4
329.4	51.4	329.2	44.2	333.6	54.2	329.6	56.6
334.2	51.7	333.9	44.9	338.7	54.5	333.5	56.6
348.5	52.5	339.3	45.5	344.0	54.7	338.7	57.0
353.6	53.1	344.3	46.1	348.7	55.0	343.3	57.0
358.8	53.6	349.8	46.6	353.0	55.3	348.8	57.0
363.9	54.0	353.2	47.1	358.2	55.6	353.5	57.4
369.0	54.3	359.0	48.0	362.9	55.9	358.4	57.6
373.8	54.7	363.7	48.8	368.4	56.4	363.2	58.0
378.7	55.4	369.1	49.4	373.4	56.8	368.8	58.3
383.6	55.9	374.5	50.0	378.6	57.2	373.3	58.6
389.2	56.2	378.8	50.5	383.2	57.7	378.6	59.0
393.7	56.8	383.8	51.2	388.6	58.0	383.4	59.3
399.3	57.1	388.6	51.8	393.3	58.6	388.4	59.7
404.2	57.4	394.2	52.7	398.5	59.2	393.6	60.1
408.5	57.7	398.8	52.8	402.8	59.6	398.6	60.2
413.7	58.2	404.9	53.2	408.9	60.3	405.8	60.4
418.7	58.8	409.5	53.6	411.2	60.5	408.6	60.7
423.2	59.2	413.9	54.2	413.4	60.8	413.3	61.0
		418.5	54.9	418.4	61.1	418.3	61.5
		423.4	55.4	423.2	62.0	423.0	62.0

Table A.6. Density ρ of THF and THF + CO2 with a mass fraction at 100:0, 92:8, 90:10 and 87:13 at pressure P.

THF:CO_2 = 100:0

	P/MPa	ρ/g.cm^3	P/MPa	ρ/g.cm^3	P/MPa	ρ/g.cm^3	P/MPa	ρ/g.cm^3	P/MPa	ρ/g.cm^3	P/MPa	ρ/g.cm^3
T/K	**302.4**		**322.9**		**347.2**		**373.8**		**399.5**		**425.5**	
	53.26	0.9495	53.29	0.9310	54.00	0.9123	53.91	0.8911	53.57	0.8699	53.95	0.8469
	49.47	0.9493	49.61	0.9295	49.15	0.9091	49.96	0.8876	49.80	0.8662	49.90	0.8420
	46.02	0.9489	46.02	0.9275	45.62	0.9063	46.29	0.8841	46.02	0.8619	45.61	0.8367
	42.42	0.9475	42.39	0.9249	41.91	0.9031	42.41	0.8805	42.12	0.8575	41.88	0.8322
	37.51	0.9458	38.58	0.9219	38.30	0.9000	38.38	0.8763	38.36	0.8532	38.31	0.8275
	33.95	0.9437	34.63	0.9188	34.56	0.8968	34.41	0.8721	34.74	0.8488	34.45	0.8223
	30.78	0.9415	30.93	0.9158	30.92	0.8934	30.84	0.8681	30.83	0.8440	30.79	0.8172
	26.46	0.9386	27.26	0.9126	27.22	0.8900	27.32	0.8641	26.98	0.8389	26.88	0.8112
	23.28	0.9364	23.46	0.9093	23.62	0.8864	23.27	0.8593	23.50	0.8342	23.30	0.8054
	19.29	0.9335	19.61	0.9060	19.58	0.8824	19.64	0.8547	19.58	0.8285	19.49	0.7989
	15.79	0.9306	15.82	0.9023	15.91	0.8785	16.03	0.8501	15.91	0.8228	15.71	0.7921
	11.95	0.9271	12.06	0.8988	12.02	0.8740	11.95	0.8448	11.93	0.8163	11.80	0.7844
	8.30	0.9238	8.22	0.8949	8.07	0.8691	8.23	0.8397	8.30	0.8100	8.06	0.7761

THF:CO_2 = 92:8

	P/MPa	ρ/g.cm^3	P/MPa	ρ/g.cm^3	P/MPa	ρ/g.cm^3	P/MPa	ρ/g.cm^3	P/MPa	ρ/g.cm^3	P/MPa	ρ/g.cm^3
T/K	**302.2**		**323.3**		**347.4**		**373.7**		**399.4**		**425.9**	
	53.35	0.9370	53.29	0.9181	53.70	0.8936	53.81	0.8660	53.51	0.8398	53.44	0.8147
	49.62	0.9368	49.68	0.9157	49.62	0.8897	49.43	0.8617	49.53	0.8352	49.68	0.8098
	45.98	0.9350	46.17	0.9127	45.90	0.8862	45.67	0.8579	45.85	0.8308	46.00	0.8048
	42.19	0.9324	42.22	0.9094	42.16	0.8824	41.78	0.8536	41.99	0.8260	42.09	0.7993
	38.19	0.9295	38.49	0.9061	38.33	0.8786	38.34	0.8495	38.34	0.8213	38.27	0.7937
	34.60	0.9268	34.63	0.9025	34.40	0.8746	34.54	0.8450	34.41	0.8160	34.56	0.7879
	30.75	0.9236	30.81	0.8988	30.91	0.8705	30.78	0.8411	30.65	0.8105	30.67	0.7815
	27.26	0.9205	27.07	0.8952	27.11	0.8662	26.85	0.8352	27.03	0.8052	26.80	0.7748
	23.27	0.9171	23.32	0.8913	23.18	0.8615	23.08	0.8301	23.21	0.7992	23.12	0.7677
	19.41	0.9136	19.42	0.8873	19.33	0.8569	19.42	0.8250	19.36	0.7926	19.62	0.7605
	15.72	0.9103	15.25	0.8828	15.72	0.8522	15.78	0.8195	15.64	0.7858	15.55	0.7512
	11.74	0.9064	11.77	0.8789	11.70	0.8470	11.82	0.8134	11.87	0.7785	11.54	0.7409
	8.34	0.9029	8.41	0.8749	8.24	0.8422	8.26	0.8072	8.09	0.7705	8.21	0.7315

THF:CO_2 = 90:10

	P/MPa	ρ/g.cm^3	P/MPa	ρ/g.cm^3	P/MPa	ρ/g.cm^3	P/MPa	ρ/g.cm^3	P/MPa	ρ/g.cm^3	P/MPa	ρ/g.cm^3
T/K	**301.9**		**323.8**		**347.7**		**373.7**		**400.0**		**425.2**	
	53.63	0.9476	53.54	0.9238	53.69	0.8991	53.70	0.8709	53.42	0.8423	53.44	0.8172
	49.84	0.9467	49.56	0.9211	49.58	0.8953	49.62	0.8667	49.59	0.8377	49.54	0.8119
	45.87	0.9442	45.55	0.9176	45.46	0.8912	45.91	0.8627	45.83	0.8330	45.83	0.8068
	42.43	0.9423	41.96	0.9145	42.13	0.8879	42.08	0.8585	42.04	0.8282	42.13	0.8014
	37.93	0.9391	38.41	0.9113	38.38	0.8841	38.15	0.8539	38.33	0.8232	38.35	0.7957
	34.45	0.9366	34.75	0.9081	34.27	0.8796	34.39	0.8493	34.75	0.8180	34.58	0.7897
	30.54	0.9337	30.89	0.9041	30.53	0.8757	30.71	0.8446	30.85	0.8124	30.92	0.7834
	27.11	0.9310	27.08	0.9006	26.93	0.8718	27.07	0.8398	26.90	0.8065	26.81	0.7759
	23.05	0.9275	23.59	0.8969	23.28	0.8672	23.09	0.8344	23.15	0.8003	23.14	0.7690
	19.61	0.9243	19.55	0.8928	19.51	0.8627	19.56	0.8292	19.46	0.7939	19.60	0.7617
	15.79	0.9207	15.83	0.8887	15.61	0.8574	15.83	0.8234	15.64	0.7870	15.75	0.7523
	12.08	0.9171	11.87	0.8842	12.21	0.8528	12.08	0.8173	12.05	0.7793	12.18	0.7429
	8.58	0.9136	8.53	0.8801	8.60	0.8477	8.52	0.8111	8.23	0.7710	8.30	0.7313

(Table A.6 continued)

THF:CO_2 = 87:13

	P/MPa	ρ/g.cm^3	P/MPa	ρ/g.cm^3	P/MPa	ρ/g.cm^3	P/MPa	ρ/g.cm^3	P/MPa	ρ/g.cm^3	P/MPa	ρ/g.cm^3
T/K	**302.6**		**323.7**		**348.2**		**373.6**		**399.7**		**425.1**	
	53.32	0.9429	53.70	0.9258	53.57	0.9001	53.84	0.8737	53.61	0.8464	53.45	0.8213
	49.57	0.9420	49.54	0.9226	49.69	0.8965	49.65	0.8692	49.69	0.8417	49.81	0.8164
	45.87	0.9400	45.80	0.9192	46.13	0.8931	45.90	0.8652	45.98	0.8370	45.91	0.8109
	42.05	0.9383	42.03	0.9160	42.35	0.8891	42.11	0.8604	42.29	0.8321	42.14	0.8051
	38.40	0.9356	38.57	0.9125	38.40	0.8849	38.35	0.8557	38.57	0.8268	38.32	0.7990
	34.71	0.9326	34.63	0.9089	34.63	0.8807	34.33	0.8506	34.62	0.8212	34.75	0.7933
	30.89	0.9294	30.92	0.9052	30.81	0.8765	30.60	0.8459	31.08	0.8155	30.81	0.7860
	27.11	0.9259	27.29	0.9013	27.11	0.8721	27.07	0.8409	26.99	0.8087	26.83	0.7777
	23.28	0.9220	23.40	0.8971	23.20	0.8674	23.36	0.8356	23.34	0.8023	23.20	0.7702
	19.58	0.9186	19.39	0.8926	19.54	0.8626	19.61	0.8298	19.39	0.7947	19.65	0.7621
	15.66	0.9145	15.78	0.8885	15.87	0.8576	15.72	0.8235	15.75	0.7873	16.66	0.7548
	11.97	0.9107	12.12	0.8840	11.93	0.8520	12.08	0.8172	11.68	0.7780	12.16	0.7419
	8.52	0.9072	8.04	0.8790	8.53	0.8468	8.45	0.8104	8.04	0.7694		

Table A.7. Density ρ of polysulfone solution in THF + CO_2 mixture with a mass fraction 92:8 at pressure P.

Polysulfone: 1.00 wt %, THF:CO_2 = 92:8

	P/MPa	ρ/g.cm^3	P/MPa	ρ/g.cm^3	P/MPa	ρ/g.cm^3	P/MPa	ρ/g.cm^3	P/MPa	ρ/g.cm^3	P/MPa	ρ/g.cm^3
T/K	**292.0**		**321.3**		**349.0**		**373.4**		**399.5**		**425.5**	
	34.74	0.9257	41.82	0.8988	46.50	0.8747	46.88	0.8494	49.48	0.8260	53.57	0.8088
	31.14	0.9229	38.36	0.8960	42.45	0.8710	43.25	0.8456	46.06	0.8222	49.86	0.8040
	27.33	0.9199	34.67	0.8927	38.36	0.8670	39.33	0.8412	42.19	0.8175	46.21	0.7989
	23.44	0.9168	30.81	0.8891	34.69	0.8633	35.76	0.8370	38.58	0.8129	42.90	0.7941
	19.84	0.9135	27.09	0.8857	30.87	0.8591	33.02	0.8338	35.01	0.8083	39.15	0.7888
	16.21	0.9104	23.19	0.8818	27.76	0.8556	29.60	0.8295	31.00	0.8026	35.25	0.7830
	15.07	0.9093	20.74	0.8794	24.07	0.8515	26.16	0.8251	27.91	0.7982	31.63	0.7772
	11.43	0.9059	17.90	0.8766	20.69	0.8474	22.83	0.8207				
	8.66	0.9035	15.00	0.8737	16.90	0.8428						
			12.58	0.8712								

Polysulfone: 1.31 wt %, THF:CO_2 = 92:8

	P/MPa	ρ/g.cm^3	P/MPa	ρ/g.cm^3	P/MPa	ρ/g.cm^3	P/MPa	ρ/g.cm^3	P/MPa	ρ/g.cm^3	P/MPa	ρ/g.cm^3
T/K	**298.0**		**323.5**		**348.9**		**373.6**		**399.8**		**425.3**	
	61.07	0.9412	61.07	0.9306	61.35	0.9112	61.04	0.8895	60.82	0.8665	61.27	0.8452
	56.86	0.9412	56.28	0.9295	57.12	0.9080	57.11	0.8861	56.84	0.8623	57.31	0.8404
	53.25	0.9411	53.38	0.9278	53.47	0.9047	53.67	0.8826	52.95	0.8582	53.17	0.8352
	49.47	0.9411	49.49	0.9249	49.58	0.9014	49.50	0.8783	49.54	0.8542	49.62	0.8307
	46.05	0.9404	46.01	0.9222	45.88	0.8978	45.97	0.8745	45.68	0.8496	46.05	0.8261
	41.90	0.9391	41.81	0.9186	42.01	0.8944	42.19	0.8704	41.89	0.8449	41.88	0.8200
	38.30	0.9379	38.08	0.9156	38.19	0.8905	38.61	0.8663	38.26	0.8402	39.70	0.8167
	34.52	0.9365	34.35	0.9120	34.26	0.8867	34.56	0.8613	34.63	0.8351	37.81	0.8140
	30.92	0.9354	30.38	0.9084	30.89	0.8829	30.81	0.8567	31.04	0.8301	34.18	0.8085
	27.03	0.9328	26.68	0.9046	27.29	0.8791	29.26	0.8546	27.03	0.8242	30.62	0.8026
	23.48	0.9300	23.05	0.9013	22.83	0.8738	26.89	0.8517	23.17	0.8181	27.11	0.7963
	19.70	0.9267	19.56	0.8974	19.46	0.8698	23.27	0.8467	19.43	0.8119	23.25	0.7890
	15.70	0.9233	15.66	0.8934	15.48	0.8649	19.73	0.8417	16.03	0.8057	19.39	0.7810
	11.90	0.9196	11.59	0.8891	10.87	0.8587	15.79	0.8359	11.51	0.7971	15.74	0.7733
	8.07	0.9160	7.81	0.8844	7.20	0.8532	11.67	0.8294	7.73	0.7890	12.05	0.7643
	5.79	0.9135					7.99	0.8231			7.73	0.7523

Polysulfone: 1.49 wt %, THF:CO_2 = 92:8

	P/MPa	ρ/g.cm^3	P/MPa	ρ/g.cm^3	P/MPa	ρ/g.cm^3	P/MPa	ρ/g.cm^3	P/MPa	ρ/g.cm^3	P/MPa	ρ/g.cm^3
T/K	**299.4**		**323.1**		**348.4**		**373.3**		**399.6**		**425.5**	
	61.32	0.9564	61.33	0.9349	60.94	0.9127	61.06	0.8910	61.34	0.8684	61.07	0.8452
	57.28	0.9537	57.15	0.9319	57.08	0.9096	56.95	0.8873	57.17	0.8639	57.18	0.8406
	53.29	0.9509	53.44	0.9293	53.51	0.9062	53.24	0.8836	53.37	0.8596	53.38	0.8358
	49.54	0.9484	49.81	0.9263	49.50	0.9027	49.40	0.8798	49.46	0.8552	49.62	0.8309
	45.42	0.9455	45.68	0.9228	45.72	0.8990	45.80	0.8759	45.64	0.8505	45.87	0.8259
	42.03	0.9428	41.79	0.9196	42.10	0.8957	42.11	0.8719	41.97	0.8461	42.03	0.8205
	38.00	0.9397	38.19	0.9165	38.11	0.8917	38.30	0.8674	38.23	0.8412	38.42	0.8151
	34.75	0.9370	34.35	0.9130	34.33	0.8878	34.62	0.8632	34.60	0.8361	34.57	0.8091
	30.81	0.9335	30.78	0.9098	30.71	0.8840	30.70	0.8582	33.26	0.8342	30.80	0.8028
	26.65	0.9301	27.01	0.9060	26.73	0.8794	27.01	0.8535	30.78	0.8306	27.03	0.7961
	22.97	0.9270	23.28	0.9024	22.91	0.8750	23.04	0.8482	27.01	0.8251	23.22	0.7887
	19.21	0.9235	19.48	0.8983	20.22	0.8720	19.39	0.8428	23.17	0.8190	19.27	0.7806
	15.22	0.9200	15.77	0.8947	19.12	0.8707	15.72	0.8374	19.41	0.8124	15.63	0.7725
	11.93	0.9170	13.79	0.8923	15.66	0.8661	11.68	0.8310	15.61	0.8054	11.71	0.7626
	8.13	0.9131	11.68	0.8899	12.05	0.8617	8.12	0.8252	11.86	0.7981	7.84	0.7512
	5.32	0.9103	7.62	0.8855	8.00	0.8562			7.88	0.7893		

(Table A.7 continued)

Polysulfone: 1.73 wt %, THF:CO_2 = 92:8

	P/MPa	ρ/g.cm^3	P/MPa	ρ/g.cm^3	P/MPa	ρ/g.cm^3	P/MPa	ρ/g.cm^3	P/MPa	ρ/g.cm^3	P/MPa	ρ/g.cm^3
T/K	**299.1**		**323.3**		**348.4**		**373.1**		**398.8**		**425.1**	
	61.05	0.9421	61.31	0.9222	61.11	0.8995	61.22	0.8787	61.25	0.8560	61.04	0.8334
	56.73	0.9394	57.64	0.9195	57.29	0.8963	57.34	0.8753	57.41	0.8521	57.15	0.8288
	53.21	0.9374	53.29	0.9161	53.28	0.8928	53.42	0.8713	53.32	0.8476	53.32	0.8242
	49.22	0.9349	49.58	0.9129	49.46	0.8895	49.62	0.8675	49.58	0.8434	49.60	0.8193
	45.68	0.9324	45.89	0.9099	45.67	0.8860	45.67	0.8634	45.89	0.8390	45.75	0.8141
	41.97	0.9297	42.50	0.9071	41.97	0.8824	42.05	0.8596	42.28	0.8344	42.01	0.8086
	38.49	0.9273	38.38	0.9034	38.11	0.8787	38.34	0.8555	38.33	0.8294	41.07	0.8072
	34.48	0.9240	34.33	0.9000	34.29	0.8748	34.56	0.8509	35.97	0.8262	38.20	0.8029
	30.96	0.9212	30.81	0.8963	30.70	0.8709	30.67	0.8463	34.33	0.8239	34.37	0.7968
	26.98	0.9180	26.73	0.8927	26.80	0.8670	30.02	0.8454	30.66	0.8189	30.69	0.7908
	22.87	0.9145	22.94	0.8889	24.23	0.8639	27.07	0.8415	27.37	0.8139	26.76	0.7837
	19.19	0.9111	19.05	0.8853	22.76	0.8623	23.25	0.8365	23.09	0.8071	23.35	0.7775
	15.60	0.9080	17.27	0.8832	19.27	0.8581	19.42	0.8312	19.22	0.8007	19.37	0.7693
	12.01	0.9047	15.15	0.8811	15.54	0.8535	15.68	0.8256	15.45	0.7940	15.68	0.7611
	10.48	0.9031	11.78	0.8776	11.90	0.8488	11.85	0.8196	11.74	0.7868	11.82	0.7514
	6.45	0.8994	7.39	0.8722	8.10	0.8436	7.92	0.8130	8.19	0.7793	8.07	0.7409

Polysulfone: 1.90 wt %, THF:CO_2 = 92:8

	P/MPa	ρ/g.cm^3	P/MPa	ρ/g.cm^3	P/MPa	ρ/g.cm^3	P/MPa	ρ/g.cm^3	P/MPa	ρ/g.cm^3	P/MPa	ρ/g.cm^3
T/K	**298.8**		**323.8**		**348.1**		**373.6**		**398.8**		**425.9**	
	60.94	0.9170	61.38	0.9017	61.34	0.8813	61.07	0.8595	61.32	0.8385	61.26	0.8159
	57.21	0.9166	57.37	0.8989	57.09	0.8785	57.18	0.8559	57.26	0.8345	57.22	0.8115
	53.12	0.9154	53.51	0.8959	53.14	0.8744	53.21	0.8523	53.54	0.8303	53.29	0.8065
	49.44	0.9134	49.48	0.8930	49.38	0.8713	49.50	0.8485	49.39	0.8257	49.73	0.8020
	45.97	0.9122	45.57	0.8897	45.72	0.8678	45.66	0.8449	45.79	0.8218	45.75	0.7967
	42.21	0.9099	41.79	0.8867	41.97	0.8644	42.07	0.8412	41.99	0.8171	41.69	0.7909
	38.34	0.9076	37.85	0.8832	38.49	0.8610	38.34	0.8368	38.40	0.8124	38.40	0.7865
	34.77	0.9048	34.14	0.8802	34.45	0.8569	34.40	0.8331	36.28	0.8099	34.49	0.7806
	31.15	0.9019	30.89	0.8774	30.62	0.8533	30.70	0.8286	34.41	0.8071	31.06	0.7750
	27.20	0.8987	26.96	0.8738	27.11	0.8494	27.01	0.8239	30.43	0.8017	27.14	0.7685
	23.18	0.8954	23.05	0.8699	24.90	0.8470	23.28	0.8188	26.81	0.7965	23.43	0.7623
	19.28	0.8923	19.58	0.8667	23.06	0.8448	19.72	0.8142	23.25	0.7910	19.26	0.7539
	15.91	0.8892	17.91	0.8648	19.25	0.8408	15.57	0.8084	19.66	0.7853		
	11.54	0.8856	15.53	0.8623	15.53	0.8361	11.88	0.8033	15.46	0.7785		
	8.41	0.8825	12.03	0.8589	11.71	0.8315	8.23	0.7974	11.99	0.7723		
			8.15	0.8546	7.98	0.8267			7.85	0.7636		

Polysulfone: 2.22 wt %, THF:CO_2 = 92:8

	P/MPa	ρ/g.cm^3	P/MPa	ρ/g.cm^3	P/MPa	ρ/g.cm^3	P/MPa	ρ/g.cm^3	P/MPa	ρ/g.cm^3	P/MPa	ρ/g.cm^3
T/K	**299.5**		**332.5**		**348.0**		**373.9**		**399.6**		**426.3**	
	60.94	0.9340	61.46	0.9137	61.13	0.8925	61.35	0.8712	61.42	0.8502	61.48	0.8273
	56.87	0.9316	57.41	0.9108	57.22	0.8894	57.06	0.8673	57.18	0.8457	57.02	0.8220
	53.25	0.9293	53.17	0.9076	53.46	0.8864	53.08	0.8635	53.29	0.8418	53.48	0.8178
	49.56	0.9265	49.65	0.9049	49.69	0.8831	49.59	0.8600	49.53	0.8375	49.81	0.8132
	45.80	0.9238	45.80	0.9019	45.76	0.8796	45.64	0.8560	45.87	0.8334	45.83	0.8080
	41.97	0.9208	42.08	0.8989	41.97	0.8759	41.90	0.8521	42.05	0.8288	57.02	0.8220
	38.49	0.9181	37.93	0.8956	38.23	0.8725	38.42	0.8483	38.53	0.8243	53.48	0.8178
	34.55	0.9151	34.03	0.8922	34.56	0.8687	34.64	0.8442	34.52	0.8190	35.54	0.7931
	30.92	0.9124	30.89	0.8895	30.81	0.8650	30.81	0.8394	30.93	0.8142	34.23	0.7909
	26.84	0.9091	27.21	0.8863	26.88	0.8608	26.83	0.8349	29.33	0.8117	30.78	0.7854
	22.93	0.9057	23.17	0.8824	23.28	0.8568	23.25	0.8302	26.95	0.8083	27.11	0.7792
	19.39	0.9029	19.31	0.8786	19.39	0.8524	19.50	0.8250	23.21	0.8026	23.40	0.7724
	15.96	0.8997	15.75	0.8749	15.60	0.8480	15.87	0.8201	19.54	0.7967	19.50	0.7650

(Table A.7 continued)

	P/MPa	ρ/g.cm^3	P/MPa	ρ/g.cm^3	P/MPa	ρ/g.cm^3	P/MPa	ρ/g.cm^3	P/MPa	ρ/g.cm^3	P/MPa	ρ/g.cm^3
T/K	**299.5**		**332.5**		**348.0**		**373.9**		**399.6**		**426.3**	
	11.84	0.8962	12.08	0.8712	11.67	0.8431	12.08	0.8143	15.64	0.7900	15.41	0.7563
	8.29	0.8928	8.32	0.8668	7.84	0.8381	8.10	0.8079	11.97	0.7835	12.16	0.7483
			7.20	0.8655					8.13	0.7756	8.23	0.7377

Polysulfone: 2.85 wt %, THF:CO_2 = 92:8

	P/MPa	ρ/g.cm^3	P/MPa	ρ/g.cm^3	P/MPa	ρ/g.cm^3	P/MPa	ρ/g.cm^3	P/MPa	ρ/g.cm^3	P/MPa	ρ/g.cm^3
T/K	**299.1**		**322.1**		**347.7**		**372.5**		**399.0**		**426.7**	
	45.77	0.9726	45.96	0.9312	46.08	0.9211	45.61	0.8993	45.80	0.8737	46.91	0.8477
	42.05	0.9700	42.54	0.9290	41.97	0.9180	41.84	0.8954	41.87	0.8689	42.13	0.8411
	38.30	0.9667	38.18	0.9263	38.03	0.9141	38.17	0.8913	38.12	0.8642	38.00	0.8349
	34.48	0.9640	34.32	0.9230	34.26	0.9107	34.41	0.8870	34.57	0.8593	34.79	0.8299
	30.66	0.9610	30.62	0.9198	30.70	0.9067	30.70	0.8822	30.68	0.8538	31.00	0.8234
	26.68	0.9575	26.99	0.9165	26.99	0.9029	27.11	0.8778	28.16	0.8503	26.95	0.8164
	22.75	0.9542	22.98	0.9127	23.13	0.8985	22.98	0.8724	26.69	0.8479	23.17	0.8092
	18.78	0.9507	19.49	0.9094	19.57	0.8943	21.69	0.8704	22.94	0.8421	19.56	0.8019
	15.26	0.9472	15.91	0.9054	15.79	0.8895	19.24	0.8666	18.55	0.8348	15.58	0.7929
	11.86	0.9443	12.01	0.9014	14.66	0.8881	15.47	0.8613	15.04	0.8287	11.80	0.7840
	7.92	0.9404	7.25	0.8960	11.67	0.8846	11.71	0.8554	9.65	0.8179	7.92	0.7730
			4.28	0.8926	8.00	0.8798	8.11	0.8494				

Polysulfone: 3.05 wt %, THF:CO_2 = 92:8

	P/MPa	ρ/g.cm^3	P/MPa	ρ/g.cm^3	P/MPa	ρ/g.cm^3	P/MPa	ρ/g.cm^3	P/MPa	ρ/g.cm^3	P/MPa	ρ/g.cm^3
T/K	**299.9**		**324.9**		**350.1**		**373.4**		**400.8**		**425.3**	
	45.98	0.9731	45.90	0.9493	45.95	0.9255	46.06	0.9023	46.05	0.8754	49.47	0.8567
	42.15	0.9705	42.31	0.9464	42.39	0.9221	41.97	0.8982	42.20	0.8707	45.74	0.8517
	38.27	0.9676	38.33	0.9430	38.48	0.9180	38.34	0.8941	38.42	0.8659	42.20	0.8465
	34.25	0.9643	34.60	0.9397	34.75	0.9141	34.63	0.8898	34.61	0.8606	38.46	0.8409
	30.59	0.9614	31.04	0.9363	30.69	0.9097	30.76	0.8848	31.91	0.8567	37.14	0.8389
	26.31	0.9578	27.14	0.9326	26.83	0.9056	27.06	0.8802	30.62	0.8547	34.47	0.8345
	23.06	0.9550	23.32	0.9288	22.98	0.9009	26.13	0.8789	26.98	0.8491	30.78	0.8283
	19.42	0.9517	19.57	0.9249	19.89	0.8970	23.32	0.8751	23.00	0.8428	27.11	0.8215
	15.87	0.9485	15.78	0.9209	15.60	0.8915	19.64	0.8698	19.26	0.8365	23.05	0.8139
	12.08	0.9448	12.46	0.9166	11.71	0.8865	15.72	0.8641	15.87	0.8302	19.27	0.8061
	8.30	0.9410	7.77	0.9110	7.00	0.8796	12.00	0.8582	11.71	0.8218	15.15	0.7968
	3.72	0.9363					8.23	0.8517	8.15	0.8137	9.66	0.7820

Polysulfone: 3.26 wt %, THF:CO_2 = 92:8

	P/MPa	ρ/g.cm^3	P/MPa	ρ/g.cm^3	P/MPa	ρ/g.cm^3	P/MPa	ρ/g.cm^3	P/MPa	ρ/g.cm^3	P/MPa	ρ/g.cm^3
T/K			**317.6**		**348.5**		**373.9**		**399.1**		**425.5**	
			45.76	0.9493	46.06	0.9198	45.74	0.8953	46.15	0.8718	46.79	0.8473
			42.07	0.9465	42.04	0.9158	42.31	0.8914	42.07	0.8667	42.00	0.8409
			38.35	0.9435	38.14	0.9121	38.30	0.8873	38.38	0.8621	38.42	0.8355
			34.62	0.9400	34.45	0.9082	34.35	0.8825	34.54	0.8570	35.46	0.8307
			30.40	0.9365	30.54	0.9038	30.62	0.8782	30.89	0.8517	31.04	0.8235
			26.84	0.9332	26.90	0.8998	26.76	0.8731	29.70	0.8501	27.11	0.8168
			23.06	0.9296	23.09	0.8953	23.71	0.8691	26.73	0.8455	23.09	0.8094
			19.21	0.9256	19.25	0.8904	20.03	0.8642	22.88	0.8395	19.24	0.8017
			15.57	0.9220	17.00	0.8882	16.21	0.8586	19.24	0.8335	16.04	0.7940
			11.86	0.9181	14.47	0.8849	12.03	0.8524	15.53	0.8271	11.71	0.7835
			8.16	0.9137	11.68	0.8813			11.93	0.8203		
			6.48	0.9121	7.70	0.8763						

(Table A.7 continued)

Polysulfone: 3.69 wt %, THF:CO_2 = 92:8

T/K	P/MPa	ρ/g.cm^3	P/MPa	ρ/g.cm^3	P/MPa	ρ/g.cm^3	P/MPa	ρ/g.cm^3	P/MPa	ρ/g.cm^3	P/MPa	ρ/g.cm^3
	323.8				348.5				371.6		397.6		425.0	
			45.74	0.9279	45.74	0.9048	45.76	0.8833	45.74	0.8594	45.79	0.8335
			42.07	0.9249	42.09	0.9013	41.97	0.8793	42.01	0.8551	41.97	0.8282
			38.49	0.9220	38.46	0.8980	37.84	0.8750	38.29	0.8503	38.36	0.8229
			34.56	0.9182	34.33	0.8936	34.41	0.8709	34.38	0.8454	34.41	0.8172
			30.43	0.9149	30.70	0.8903	30.70	0.8667	30.63	0.8404	32.59	0.8145
			26.98	0.9115	26.92	0.8860	26.76	0.8620	26.46	0.8343	29.56	0.8095
			23.09	0.9079	22.94	0.8817	23.34	0.8572	23.16	0.8291	25.97	0.8035
			19.45	0.9042	19.20	0.8773	20.03	0.8528	19.21	0.8228	21.46	0.7953
			15.49	0.9001	15.60	0.8731	16.32	0.8477	15.64	0.8169		
			11.09	0.8953	13.59	0.8703	12.12	0.8414				
			7.92	0.8920	11.31	0.8676						
			5.56	0.8893	8.41	0.8635						

Polysulfone: 3.90 wt %, THF:CO_2 = 92:8

T/K	P/MPa	ρ/g.cm^3	P/MPa	ρ/g.cm^3	P/MPa	ρ/g.cm^3	P/MPa	ρ/g.cm^3	P/MPa	ρ/g.cm^3	P/MPa	ρ/g.cm^3
	298.6		323.2		348.0		372.9		399.2		426.1	
	60.98	0.9240	60.82	0.9089	61.33	0.8896	61.35	0.8685	61.02	0.8458	61.41	0.8241
	57.28	0.9236	57.04	0.9074	57.13	0.8862	57.20	0.8645	57.07	0.8418	57.26	0.8195
	53.44	0.9223	53.29	0.9060	53.24	0.8829	53.44	0.8613	53.16	0.8375	53.37	0.8147
	49.67	0.9213	49.43	0.9031	49.50	0.8796	49.53	0.8572	49.56	0.8336	49.69	0.8098
	45.74	0.9206	45.90	0.9006	45.67	0.8762	45.72	0.8537	45.83	0.8293	45.90	0.8047
	42.01	0.9192	42.20	0.8977	42.02	0.8728	42.19	0.8498	42.16	0.8251	42.24	0.7997
	38.30	0.9183	38.53	0.8946	38.15	0.8691	38.23	0.8457	38.42	0.8204	38.49	0.7942
	34.43	0.9166	34.37	0.8909	34.79	0.8657	34.66	0.8414	37.36	0.8191	34.30	0.7877
	30.85	0.9151	30.77	0.8877	30.66	0.8615	31.89	0.8382	34.37	0.8149	30.59	0.7819
	26.99	0.9127	27.03	0.8844	26.92	0.8574	30.71	0.8367	30.51	0.8096	27.14	0.7760
	23.28	0.9102	23.28	0.8809	26.01	0.8564	26.80	0.8320	26.58	0.8038	22.88	0.7680
	19.33	0.9069	19.50	0.8768	22.60	0.8527	23.36	0.8275	23.09	0.7988	19.50	0.7610
	15.63	0.9039	15.75	0.8731	19.19	0.8486	19.42	0.8219	19.42	0.7927	15.75	0.7530
	12.16	0.9007	11.55	0.8686	15.11	0.8437	15.33	0.8164	15.57	0.7860	11.78	0.7434
	7.96	0.8968	8.07	0.8647	11.54	0.8394	11.62	0.8108	11.78	0.7786	7.17	0.7312
					7.88	0.8342	8.11	0.8051	7.96	0.7706		

Polysulfone: 4.19 wt %, THF:CO_2 = 92:8

T/K	P/MPa	ρ/g.cm^3	P/MPa	ρ/g.cm^3	P/MPa	ρ/g.cm^3	P/MPa	ρ/g.cm^3	P/MPa	ρ/g.cm^3	P/MPa	ρ/g.cm^3
	298.2		324.0		348.8		374.4		399.3		426.7	
	61.07	0.9426	61.42	0.9202	61.23	0.8982	61.19	0.8758	61.29	0.8546	61.89	0.8319
	56.97	0.9402	56.95	0.9163	57.32	0.8951	57.18	0.8724	57.03	0.8503	57.49	0.8271
	52.95	0.9375	52.87	0.9133	53.48	0.8918	53.44	0.8688	53.25	0.8463	53.70	0.8224
	49.43	0.9348	49.47	0.9108	49.79	0.8887	49.62	0.8649	49.39	0.8420	49.54	0.8171
	45.67	0.9321	46.02	0.9081	45.95	0.8852	45.72	0.8608	45.97	0.8379	45.83	0.8121
	42.05	0.9295	41.94	0.9048	42.20	0.8816	42.05	0.8567	42.17	0.8333	44.03	0.8094
	38.19	0.9264	38.08	0.9013	38.08	0.8775	38.26	0.8525	39.12	0.8295	41.67	0.8061
	34.33	0.9235	34.56	0.8982	34.45	0.8739	34.37	0.8480	38.36	0.8285	38.30	0.8012
	30.66	0.9206	30.62	0.8947	30.81	0.8701	34.05	0.8477	34.60	0.8235	34.19	0.7946
	26.83	0.9174	26.52	0.8908	28.66	0.8675	30.70	0.8436	30.37	0.8175	31.04	0.7895
	23.25	0.9144	23.09	0.8876	26.95	0.8657	26.87	0.8388	26.61	0.8120	27.03	0.7825
	19.69	0.9114	22.30	0.8869	23.42	0.8617	23.36	0.8343	23.28	0.8068	23.44	0.7756
	15.56	0.9073	19.58	0.8840	19.42	0.8569	19.54	0.8289	19.70	0.8009	19.73	0.7676
	15.04	0.9068	15.78	0.8803	15.98	0.8526	15.64	0.8231	16.06	0.7943	15.79	0.7583
	11.85	0.9043	11.92	0.8759	12.12	0.8478	12.01	0.8171	11.71	0.7857	11.71	0.7488
	8.10	0.9004	8.26	0.8717	8.00	0.8421	8.26	0.8105	7.70	0.7769	8.15	0.7385

(Table A.7 continued)

Polysulfone: 4.73 wt %, THF:CO_2 = 92:8

	P/MPa	ρ/g.cm^3	P/MPa	ρ/g.cm^3	P/MPa	ρ/g.cm^3	P/MPa	ρ/g.cm^3	P/MPa	ρ/g.cm^3	P/MPa	ρ/g.cm^3
T/K	**299.6**		**324.5**		**349.0**		**373.8**		**398.8**		**427.1**	
	61.22	0.9553	61.38	0.9329	61.39	0.9114	61.46	0.8893	61.49	0.8683	61.51	0.8434
	57.03	0.9524	57.30	0.9300	57.15	0.9078	57.24	0.8853	57.27	0.8638	57.26	0.8384
	53.14	0.9493	53.17	0.9265	53.24	0.9043	53.24	0.8815	53.51	0.8597	53.14	0.8335
	49.47	0.9470	49.28	0.9236	49.54	0.9008	50.00	0.8783	49.59	0.8552	49.58	0.8286
	45.80	0.9442	45.67	0.9206	45.53	0.8973	45.76	0.8740	45.89	0.8507	45.80	0.8235
	41.97	0.9411	42.05	0.9172	41.97	0.8937	41.90	0.8699	42.09	0.8459	42.13	0.8183
	38.46	0.9384	38.08	0.9139	38.27	0.8902	38.38	0.8657	40.65	0.8438	38.57	0.8132
	34.77	0.9357	34.56	0.9107	34.56	0.8862	36.30	0.8633	38.33	0.8409	34.14	0.8064
	30.69	0.9322	30.61	0.9070	31.46	0.8830	34.23	0.8607	34.14	0.8350	30.66	0.8002
	26.99	0.9292	27.03	0.9035	30.62	0.8821	30.32	0.8561	30.17	0.8295	26.68	0.7931
	23.21	0.9257	25.89	0.9023	26.67	0.8774	26.50	0.8511	26.91	0.8247	22.94	0.7856
	21.85	0.9244	23.25	0.8997	22.97	0.8733	23.02	0.8470	23.25	0.8191	19.42	0.7782
	19.24	0.9221	19.08	0.8955	19.27	0.8690	19.35	0.8417	19.69	0.8131	15.64	0.7706
	15.38	0.9187	15.32	0.8914	15.10	0.8636	15.53	0.8358	15.75	0.8057	12.08	0.7616
	11.55	0.9152	11.71	0.8876	12.05	0.8599	12.05	0.8302	11.67	0.7985	7.85	0.7489
	7.81	0.9113	7.85	0.8834	8.11	0.8544	7.96	0.8238	8.00	0.7902		

Table A.8. Density ρ of polysulfone solution in THF + CO_2 mixture with a mass fraction 90:10 at pressure P.

Polysulfone: 1.50 wt %, THF:CO_2 = 90:10

	P/MPa	ρ/g.cm^3	P/MPa	ρ/g.cm^3	P/MPa	ρ/g.cm^3	P/MPa	ρ/g.cm^3	P/MPa	ρ/g.cm^3	P/MPa	ρ/g.cm^3
T/K	299.2		323.3		348.5		373.3		398.4		424.5	
	45.58	0.9440	46.00	0.9208	49.64	0.9001	50.26	0.8776	54.63	0.8592	57.62	0.8394
	40.83	0.9401	41.97	0.9174	45.77	0.8965	46.18	0.8732	51.14	0.8553	54.69	0.8358
	35.17	0.9357	37.35	0.9131	42.28	0.8930	42.77	0.8693	47.04	0.8502	52.24	0.8324
	29.78	0.9305	33.01	0.9092	38.72	0.8894	39.21	0.8653	44.02	0.8466	49.92	0.8292
	25.72	0.9276	29.34	0.9055	35.66	0.8862	35.08	0.8602	40.04	0.8414	47.95	0.8264
	23.93	0.9259	25.48	0.9017	34.60	0.8849	31.70	0.8560	35.01	0.8345	44.92	0.8222
	20.45	0.9224	21.68	0.8978	30.85	0.8807	27.62	0.8508	30.01	0.8272	41.10	0.8164
	16.39	0.9189	17.77	0.8936	26.53	0.8758	23.73	0.8455	25.74	0.8205	37.02	0.8100
	12.20	0.9147	13.41	0.8885	22.77	0.8714					32.78	0.8027

Polysulfone: 2.00 wt %, THF:CO_2 = 90:10

	P/MPa	ρ/g.cm^3	P/MPa	ρ/g.cm^3	P/MPa	ρ/g.cm^3	P/MPa	ρ/g.cm^3	P/MPa	ρ/g.cm^3	P/MPa	ρ/g.cm^3
T/K	297.1		323.5		347.2		372.7		399.4		425.4	
	37.43	0.9465	42.87	0.9251	45.70	0.9047	49.63	0.8852	53.76	0.8656	57.85	0.8465
	33.49	0.9436	38.61	0.9211	42.05	0.9014	46.14	0.8816	49.76	0.8610	54.16	0.8421
	29.15	0.9398	34.67	0.9178	38.58	0.8977	42.31	0.8774	46.36	0.8571	50.97	0.8380
	24.68	0.9361	30.59	0.9137	34.85	0.8940	38.49	0.8732	42.50	0.8521	47.27	0.8331
	21.00	0.9328	26.88	0.9103	30.96	0.8899	34.90	0.8690	37.93	0.8460	43.56	0.8275
	18.58	0.9306	23.28	0.9067	26.23	0.8846	32.25	0.8657	34.29	0.8409	42.66	0.8262
	13.89	0.9261	20.64	0.9039	22.19	0.8798	28.77	0.8613	30.62	0.8355	38.62	0.8202
	11.40	0.9238	17.34	0.9004	18.96	0.8759	25.60	0.8569	26.98	0.8300	34.86	0.8142
	8.49	0.9208	13.64	0.8962	15.94	0.8721	22.29	0.8523			31.04	0.8078
			10.11	0.8919								

Polysulfone: 2.46 wt %, THF:CO_2 = 90:10

	P/MPa	ρ/g.cm^3	P/MPa	ρ/g.cm^3	P/MPa	ρ/g.cm^3	P/MPa	ρ/g.cm^3	P/MPa	ρ/g.cm^3	P/MPa	ρ/g.cm^3
T/K	301.2		323.2		345.6		372.4		399.2		425.0	
	53.48	0.9776	52.41	0.9544	52.86	0.9331	53.15	0.9086	54.55	0.8849	57.83	0.8650
	49.54	0.9745	47.58	0.9504	47.94	0.9285	49.20	0.9046	51.38	0.8813	54.32	0.8603
	45.34	0.9712	41.98	0.9453	43.48	0.9241	45.49	0.9003	48.71	0.8780	51.28	0.8562
	42.01	0.9686	37.84	0.9416	38.99	0.9196	41.74	0.8960	46.01	0.8745	49.06	0.8530
	37.95	0.9649	33.91	0.9380	35.73	0.9159	40.57	0.8944	45.07	0.8733	45.98	0.8486
	34.29	0.9618	30.78	0.9350	31.95	0.9119	37.37	0.8905	42.32	0.8696	42.92	0.8439
	30.31	0.9585	26.76	0.9309	28.09	0.9073	33.69	0.8859	38.43	0.8642	38.64	0.8371
	27.11	0.9553	23.03	0.9270	24.38	0.9031	30.28	0.8814	34.60	0.8588	34.72	0.8306
	26.39	0.9546	19.58	0.9233	21.20	0.8992	27.00	0.8768	30.97	0.8532	31.13	0.8242
	23.32	0.9520	15.85	0.9191								
	19.58	0.9482										
	15.79	0.9445										

Polysulfone: 3.01 wt %, THF:CO_2 = 90:10

	P/MPa	ρ/g.cm^3	P/MPa	ρ/g.cm^3	P/MPa	ρ/g.cm^3	P/MPa	ρ/g.cm^3	P/MPa	ρ/g.cm^3	P/MPa	ρ/g.cm^3
T/K	303.1		320.0		347.8		372.1		397.0		424.3	
	53.29	0.9356	57.95	0.9209	57.06	0.8967	58.19	0.8766	59.53	0.8555	61.57	0.8337
	50.21	0.9333	53.44	0.9176	52.95	0.8931	54.00	0.8724	56.62	0.8526	57.86	0.8292
	47.69	0.9313	49.37	0.9142	49.80	0.8901	50.11	0.8684	52.72	0.8481	55.22	0.8259
	44.06	0.9285	45.27	0.9108	46.07	0.8867	47.52	0.8655	50.90	0.8462	53.85	0.8241
	40.99	0.9261	41.48	0.9077	43.79	0.8844	43.83	0.8614	47.42	0.8419	49.92	0.8189
	38.63	0.9240	38.64	0.9053	40.01	0.8806	40.35	0.8574	42.96	0.8364	46.48	0.8141
	35.01	0.9210	34.54	0.9017	36.64	0.8770	36.79	0.8533	39.09	0.8314	42.21	0.8079
	30.89	0.9175	30.70	0.8982	32.74	0.8729			35.71	0.8268		
	26.84	0.9138	26.61	0.8944	28.77	0.8685						
	23.20	0.9107										

(Table A.8 continued)

Polysulfone: 3.21 wt %, THF:CO_2 = 90:10

T/K	P/MPa	ρ/g.cm^3	P/MPa	ρ/g.cm^3	P/MPa	ρ/g.cm^3	P/MPa	ρ/g.cm^3	P/MPa	ρ/g.cm^3	P/MPa	ρ/g.cm^3
	296.4		324.8		349.4		375.5		400.0		426.3	
	56.87	0.9715	58.70	0.9464	56.98	0.9221	57.43	0.8980	57.65	0.8762	57.55	0.8520
	52.53	0.9682	54.16	0.9428	53.40	0.9189	53.78	0.8944	54.91	0.8729	55.92	0.8499
	45.15	0.9627	49.96	0.9392	49.86	0.9155	50.37	0.8909	53.02	0.8707	53.63	0.8470
	42.03	0.9604	46.02	0.9357	46.74	0.9125	47.35	0.8874	50.68	0.8679	50.29	0.8425
	37.85	0.9570	42.36	0.9323	43.71	0.9095	43.99	0.8836	46.63	0.8629	46.34	0.8367
	36.29	0.9556	40.41	0.9305	40.31	0.9060	39.74	0.8786	42.39	0.8573	41.75	0.8300
	31.87	0.9520	36.31	0.9268	36.08	0.9015	35.54	0.8736	37.98	0.8517	37.90	0.8241
	26.35	0.9473	31.52	0.9222	31.57	0.8967	31.04	0.8680	33.39	0.8452	34.10	0.8177
	22.19	0.9436	25.41	0.9161	26.99	0.8915						
	17.67	0.9394										

Polysulfone: 3.66 wt %, THF:CO_2 = 90:10

T/K	P/MPa	ρ/g.cm^3	P/MPa	ρ/g.cm^3	P/MPa	ρ/g.cm^3	P/MPa	ρ/g.cm^3	P/MPa	ρ/g.cm^3	P/MPa	ρ/g.cm^3
	298.6		323.6		348.6		373.8		398.8		423.7	
	38.18	0.9554	41.90	0.9342	45.68	0.9132	46.02	0.8900	50.79	0.8716	53.95	0.8530
	32.44	0.9508	37.51	0.9300	41.07	0.9088	41.89	0.8854	46.28	0.8661	51.02	0.8493
	28.24	0.9472	33.59	0.9265	36.87	0.9044	37.67	0.8802	42.81	0.8617	48.04	0.8452
	23.40	0.9431	29.16	0.9223	33.02	0.9004	34.26	0.8763	39.82	0.8578	44.76	0.8406
	18.90	0.9391	24.89	0.9180	29.90	0.8969	33.14	0.8747	38.42	0.8558	42.95	0.8380
	13.79	0.9342	20.94	0.9139	27.45	0.8943	29.10	0.8696	34.52	0.8507	39.55	0.8326
	10.87	0.9312	17.24	0.9100	22.41	0.8880	25.10	0.8643	30.40	0.8446	35.73	0.8267
	8.14	0.9284	14.17	0.9064	19.16	0.8842	20.67	0.8584	26.42	0.8387	31.42	0.8198
			10.43	0.9024	14.42	0.8783	16.84	0.8527	23.47	0.8339	28.09	0.8139

Polysulfone: 4.44 wt %, THF:CO_2 = 90:10

T/K	P/MPa	ρ/g.cm^3	P/MPa	ρ/g.cm^3	P/MPa	ρ/g.cm^3	P/MPa	ρ/g.cm^3	P/MPa	ρ/g.cm^3	P/MPa	ρ/g.cm^3
	308.3		321.7		346.9		372.2		398.6		426.0	
	52.72	0.9612	52.04	0.9489	53.25	0.9264	53.17	0.9018	54.16	0.8772	53.98	0.8525
	48.62	0.9581	48.02	0.9457	48.45	0.9220	49.62	0.8983	51.05	0.8735	51.17	0.8488
	44.32	0.9546	44.02	0.9422	44.66	0.9183	46.45	0.8950	47.19	0.8689	48.81	0.8455
	39.86	0.9508	39.21	0.9382	40.73	0.9142	42.73	0.8909	43.98	0.8646	46.84	0.8426
	35.16	0.9468	34.70	0.9341	37.81	0.9111	37.18	0.8842	42.43	0.8626	43.60	0.8378
	30.89	0.9429	31.04	0.9306	31.99	0.9046	34.45	0.8811	38.31	0.8572	41.03	0.8339
	27.38	0.9400	26.31	0.9258	28.13	0.9002	31.12	0.8767	35.07	0.8526	38.20	0.8296
	22.97	0.9357	23.17	0.9228	24.21	0.8957	27.29	0.8719	31.39	0.8475	34.86	0.8243
	19.47	0.9325	19.77	0.9192	20.20	0.8909						
	15.94	0.9290	16.21	0.9152								
	12.35	0.9254	12.24	0.9108								

Polysulfone: 4.96 wt %, THF:CO_2 = 90:10

T/K	P/MPa	ρ/g.cm^3	P/MPa	ρ/g.cm^3	P/MPa	ρ/g.cm^3	P/MPa	ρ/g.cm^3	P/MPa	ρ/g.cm^3	P/MPa	ρ/g.cm^3
	299.2		323.2		348.9		374.8		400.8		425.3	
	56.01	0.9527	57.15	0.9347	57.45	0.9113	58.09	0.8885	59.45	0.8663	60.14	0.8454
	50.90	0.9496	53.62	0.9320	53.51	0.9079	54.01	0.8845	56.28	0.8631	58.32	0.8432
	46.48	0.9464	49.44	0.9286	50.21	0.9048	51.24	0.8814	53.48	0.8597	56.31	0.8405
	42.88	0.9439	45.68	0.9253	47.99	0.9027	49.24	0.8791	52.00	0.8579	54.91	0.8385
	40.37	0.9420	42.96	0.9231	46.06	0.9007	45.52	0.8752	48.29	0.8534	51.51	0.8341
	35.69	0.9383	37.43	0.9179	42.04	0.8968	41.33	0.8703	45.11	0.8494	47.95	0.8293
	31.19	0.9347	33.08	0.9140	38.30	0.8929	37.09	0.8654	41.44	0.8449	43.64	0.8235
	26.98	0.9308	28.88	0.9098	33.84	0.8883	32.02	0.8593	38.08	0.8405	39.59	0.8174

Table A.9. Density ρ of polysulfone solution in THF + CO_2 mixture with a mass fraction 87:13 at pressure P.

Polysulfone: 0.28 wt %, THF:CO_2 = 87:13

T/K	P/MPa	ρ/g.cm^3	P/MPa	ρ/g.cm^3	P/MPa	ρ/g.cm^3	P/MPa	ρ/g.cm^3	P/MPa	ρ/g.cm^3	P/MPa	ρ/g.cm^3
			323.3		347.8		372.6		398.0		422.3	
			68.69	0.8906	69.40	0.8816	69.67	0.8654	68.53	0.8451	69.27	0.8260
			64.98	0.8883	66.88	0.8797	66.34	0.8627	66.05	0.8428	67.05	0.8237
			60.89	0.8856	64.19	0.8778	63.50	0.8601	64.60	0.8413	66.11	0.8221
			57.11	0.8831	61.04	0.8756	60.90	0.8576	60.97	0.8377	63.10	0.8194
			53.55	0.8806	58.32	0.8734	57.41	0.8546	57.64	0.8345	59.76	0.8156
			50.49	0.8783	53.94	0.8700	53.63	0.8511	53.48	0.8300	56.04	0.8113
			46.36	0.8752	50.06	0.8664	50.07	0.8478	49.69	0.8257	52.41	0.8069
					46.05	0.8630	46.06	0.8438	45.80	0.8214	48.60	0.8021

Polysulfone: 0.50 wt %, THF:CO_2 = 87:13

T/K	P/MPa	ρ/g.cm^3	P/MPa	ρ/g.cm^3	P/MPa	ρ/g.cm^3	P/MPa	ρ/g.cm^3	P/MPa	ρ/g.cm^3	P/MPa	ρ/g.cm^3
	306.6				341.7		373.6		390.4		414.7	
	67.97	0.9214			68.13	0.8999	67.63	0.8722	67.11	0.8571	66.17	0.8342
	64.58	0.9194			64.55	0.8969	64.03	0.8689	63.95	0.8538	63.28	0.8309
	60.77	0.9168			60.17	0.8932	60.69	0.8654	61.21	0.8507	60.85	0.8279
	57.26	0.9142			57.18	0.8907	57.16	0.8618	59.15	0.8485	57.54	0.8241
	54.89	0.9124			55.46	0.8890	53.39	0.8579	56.14	0.8448	54.82	0.8202
	51.03	0.9097			52.18	0.8864	49.53	0.8538	53.10	0.8414	51.90	0.8165
	47.01	0.9065			49.01	0.8833	45.88	0.8497	49.69	0.8372	49.09	0.8127
	42.96	0.9032			45.49	0.8798			45.95	0.8326	45.65	0.8080
									42.70	0.8284		

Polysulfone: 1.02 wt %, THF:CO_2 = 87:13

T/K	P/MPa	ρ/g.cm^3	P/MPa	ρ/g.cm^3	P/MPa	ρ/g.cm^3	P/MPa	ρ/g.cm^3	P/MPa	ρ/g.cm^3	P/MPa	ρ/g.cm^3
	306.7		323.3		353.6		373.2		397.7		422.5	
	71.13	0.9528	70.40	0.9461	70.60	0.9201	70.52	0.9033	69.67	0.8801	70.74	0.8597
	67.10	0.9522	66.85	0.9454	66.67	0.9192	66.36	0.9006	65.58	0.8782	67.16	0.8570
	63.50	0.9514	63.00	0.9427	62.83	0.9153	62.50	0.8969	61.51	0.8737	64.45	0.8540
	60.10	0.9503	59.23	0.9396	58.89	0.9122	58.87	0.8935	57.71	0.8697	61.44	0.8503
	56.75	0.9479	55.25	0.9362	54.46	0.9076	55.75	0.8905	53.70	0.8646	60.82	0.8494
	53.37	0.9453	51.37	0.9329	50.12	0.9030	53.32	0.8877	50.07	0.8599	57.40	0.8452
	49.16	0.9420	47.70	0.9298	45.91	0.8984	50.02	0.8841	46.61	0.8549	53.62	0.8403
	46.50	0.9392	44.02	0.9265	43.15	0.8946	46.17	0.8797	42.28	0.8496	49.78	0.8348
	42.55	0.9364	40.14	0.9231			42.47	0.8754			46.17	0.8292
	38.72	0.9331										

Polysulfone: 2.00 wt %, THF:CO_2 = 87:13

T/K	P/MPa	ρ/g.cm^3	P/MPa	ρ/g.cm^3	P/MPa	ρ/g.cm^3	P/MPa	ρ/g.cm^3	P/MPa	ρ/g.cm^3	P/MPa	ρ/g.cm^3
	301.8		322.8		344.8		367.4		398.8		422.4	
	68.39	0.9672	69.14	0.9465	68.65	0.9271	68.23	0.9071	68.76	0.8800	68.10	0.8606
	64.79	0.9648	64.68	0.9441	64.56	0.9238	64.72	0.9039	64.83	0.8761	64.68	0.8568
	61.44	0.9621	60.54	0.9409	60.92	0.9207	61.08	0.9005	61.34	0.8723	61.12	0.8525
	57.12	0.9589	57.34	0.9381	57.30	0.9174	57.30	0.8968	57.62	0.8682	58.80	0.8496
	53.01	0.9559	53.50	0.9354	53.59	0.9139	53.55	0.8928	53.78	0.8637	57.22	0.8475
	49.51	0.9532	49.53	0.9321	50.22	0.9109	50.60	0.8898	53.25	0.8630	53.51	0.8428
	47.01	0.9513	45.61	0.9287	47.35	0.9077	47.12	0.8862	49.55	0.8585	50.08	0.8382
	43.11	0.9479	41.71	0.9254	44.24	0.9052	43.46	0.8821	45.91	0.8539	46.59	0.8329
	39.25	0.9449	38.34	0.9224	40.31	0.9012	40.39	0.8785	41.86	0.8487	42.90	0.8276
	35.73	0.9415	34.79	0.9192	37.43	0.8983	37.34	0.8748	38.12	0.8433		
	30.70	0.9377										

(Table A.9 continued)

Polysulfone: 2.04 wt %, THF:CO_2 = 87:13

	P/MPa	ρ/g.cm^3	P/MPa	ρ/g.cm^3	P/MPa	ρ/g.cm^3	P/MPa	ρ/g.cm^3	P/MPa	ρ/g.cm^3	P/MPa	ρ/g.cm^3
T/K	**298.5**		**321.0**		**347.6**		**373.3**		**397.7**		**425.6**	
	66.11	0.9638	65.72	0.9509	66.32	0.9276	66.30	0.9051	66.17	0.8831	64.64	0.8563
	62.40	0.9617	62.13	0.9483	64.11	0.9257	63.39	0.9024	63.45	0.8802	61.19	0.8521
	59.42	0.9597	58.49	0.9454	60.82	0.9230	60.82	0.8998	60.88	0.8774	60.02	0.8506
	56.35	0.9576	54.46	0.9421	57.68	0.9201	58.02	0.8970	58.26	0.8743	56.92	0.8468
	52.87	0.9551	51.40	0.9396	53.46	0.9160	54.76	0.8935	56.96	0.8728	53.97	0.8428
	49.54	0.9525	50.04	0.9386	52.45	0.9150	51.55	0.8902	53.25	0.8685	50.56	0.8379
	47.80	0.9511	46.57	0.9357	49.62	0.9122	47.76	0.8859	49.73	0.8641		
	44.32	0.9489	42.43	0.9321	46.10	0.9089	44.20	0.8817	45.98	0.8593		
	41.14	0.9463	38.80	0.9286	42.77	0.9055						
	38.36	0.9438										
	35.24	0.9410										
	31.95	0.9384										
	28.39	0.9352										
	25.48	0.9325										
	22.22	0.9295										
	19.05	0.9267										
	15.75	0.9235										

Polysulfone: 3.69 wt %, THF:CO_2 = 87:13

	P/MPa	ρ/g.cm^3	P/MPa	ρ/g.cm^3	P/MPa	ρ/g.cm^3	P/MPa	ρ/g.cm^3	P/MPa	ρ/g.cm^3	P/MPa	ρ/g.cm^3
T/K	**301.5**		**322.6**		**347.6**		**372.6**		**398.8**		**424.6**	
	64.90	0.9608	64.83	0.9392	64.90	0.9187	64.83	0.8961	64.86	0.8729	64.79	0.8538
	60.36	0.9578	60.93	0.9363	61.19	0.9157	61.08	0.8926	61.72	0.8698	62.78	0.8512
	56.57	0.9547	57.34	0.9334	58.05	0.9128	57.56	0.8892	59.87	0.8677	60.66	0.8483
	53.82	0.9526	53.78	0.9306	54.72	0.9099	54.19	0.8856	56.77	0.8643	59.38	0.8462
	50.77	0.9502	51.21	0.9283	52.49	0.9076	50.79	0.8822	53.73	0.8609	57.26	0.8432
	47.20	0.9474	48.97	0.9266	49.31	0.9046	47.12	0.8781	49.92	0.8573	53.59	0.8383
	44.02	0.9449	45.83	0.9238	46.06	0.9015	43.60	0.8742	47.57	0.8535	50.56	0.8341
	40.69	0.9422	42.31	0.9207	42.77	0.8981	41.14	0.8714	44.43	0.8493	46.40	0.8285
			38.61	0.9174	39.10	0.8944						
					35.42	0.8907						

Polysulfone: 3.99 wt %, THF:CO_2 = 87:13

	P/MPa	ρ/g.cm^3	P/MPa	ρ/g.cm^3	P/MPa	ρ/g.cm^3	P/MPa	ρ/g.cm^3	P/MPa	ρ/g.cm^3	P/MPa	ρ/g.cm^3
T/K	**299.5**		**323.6**		**347.1**		**373.0**		**397.8**		**424.2**	
	64.03	0.9496	64.70	0.9327	64.83	0.9134	65.21	0.8919	64.82	0.8695	64.64	0.8468
	60.74	0.9478	60.89	0.9303	61.04	0.9104	60.32	0.8874	60.57	0.8651	61.00	0.8428
	57.26	0.9457	57.02	0.9275	57.11	0.9071	57.15	0.8839	57.37	0.8616	57.45	0.8384
	53.55	0.9431	53.32	0.9247	53.78	0.9039	53.59	0.8802	52.57	0.8560	55.75	0.8364
	49.92	0.9404	49.30	0.9214	50.07	0.9006	49.47	0.8757	49.65	0.8525	53.26	0.8333
	45.68	0.9374	45.22	0.9178	46.21	0.8967	46.05	0.8721	45.51	0.8475	49.62	0.8282
	42.05	0.9345	43.03	0.9158	42.50	0.8930	42.40	0.8681	42.13	0.8431	45.91	0.8232
	39.36	0.9323	38.87	0.9124	38.76	0.8892	38.75	0.8637	38.61	0.8383	41.97	0.8176
	35.43	0.9290	34.71	0.9085	34.86	0.8852						
	31.81	0.9260	31.46	0.9051								
	28.30	0.9232										

(Table A.9 continued)

Polysulfone: 4.30 wt %, THF:CO_2 = 87:13

	P/MPa	ρ/g.cm^3	P/MPa	ρ/g.cm^3	P/MPa	ρ/g.cm^3	P/MPa	ρ/g.cm^3	P/MPa	ρ/g.cm^3	P/MPa	ρ/g.cm^3
T/K	**298.9**		**323.2**				**363.1**					
	68.44	0.9439	68.25	0.9359			68.08	0.9021				
	64.60	0.9438	64.64	0.9333			64.61	0.8991				
	60.80	0.9436	60.93	0.9306			60.85	0.8956				
	57.10	0.9431	57.11	0.9273			57.13	0.8920				
	53.04	0.9410	53.15	0.9238			53.93	0.8889				
	50.52	0.9393	51.16	0.9224			49.72	0.8847				
	45.55	0.9355	49.50	0.9209			45.82	0.8807				
	42.28	0.9331	45.76	0.9179			41.94	0.8766				
	38.32	0.9301	41.85	0.9146			38.23	0.8725				
	34.87	0.9271	38.24	0.9112			34.57	0.8680				
	30.74	0.9239	34.51	0.9078								
	27.35	0.9208	30.74	0.9041								
	23.36	0.9174										

Polysulfone: 4.30 wt %, THF:CO_2 = 87:13

	P/MPa	ρ/g.cm^3	P/MPa	ρ/g.cm^3	P/MPa	ρ/g.cm^3	P/MPa	ρ/g.cm^3	P/MPa	ρ/g.cm^3	P/MPa	ρ/g.cm^3
T/K	**302.9**		**323.3**		**348.3**		**373.5**		**398.8**		**425.3**	
	65.11	0.9825	65.30	0.9584	65.76	0.9362	64.89	0.9131	64.98	0.8910	64.67	0.8657
	60.82	0.9797	61.57	0.9556	63.09	0.9340	62.96	0.9113	62.86	0.8887	63.26	0.8640
	57.75	0.9775	59.06	0.9537	60.21	0.9315	60.58	0.9091	60.85	0.8865	62.22	0.8627
	54.01	0.9745	56.19	0.9513	56.23	0.9277	57.60	0.9059	59.68	0.8851	60.14	0.8602
	51.17	0.9724	54.84	0.9502	52.80	0.9246	54.01	0.9024	56.27	0.8813	57.65	0.8570
	46.97	0.9694	51.58	0.9476	49.49	0.9215	51.05	0.8990	53.38	0.8778	53.85	0.8522
	43.71	0.9663	48.16	0.9446	46.37	0.9184	47.80	0.8954	49.58	0.8731	51.24	0.8488
			44.62	0.9415			44.02	0.8911	46.18	0.8688	47.93	0.8443
			40.94	0.9381								

Appendix B

Volumetric Properties of Polysulfone Solutions in THF + CO_2

In Chapter 8, Figures 8.14-16 show the pressure dependence of 2.0 wt % polysulfone solutions in THF + CO_2 on the polymer concentration at 13, 10 and 8 wt % CO_2 levels. The variation of density as a function of the pressure at other polymer concentrations are included in this section. Table B.1 is a summary of the polymer solution compositions and figure numbers in Appendix B.

Table B.1. The polymer and solvent mixture conditions of Figures in Appendix B.

THF:CO2, by mass	PSF Concentration, wt %	Figure number
87:13	0.28	B.1
	0.50	B.2
	1.02	B.3
	2.04	B.4
	3.69	B.5
	3.99	B.6
	4.30	B.7
	4.99	B.8
90:10	1.50	B.9
	2.46	B.10
	3.01	B.11
	3.21	B.12
	3.66	B.13
	4.44	B.14
	4.96	B.15
92:8	1.00	B.16
	1.49	B.17
	2.22	B.18
	3.05	B.19
	3.69	B.20
	4.19	B.21
	4.73	B.22

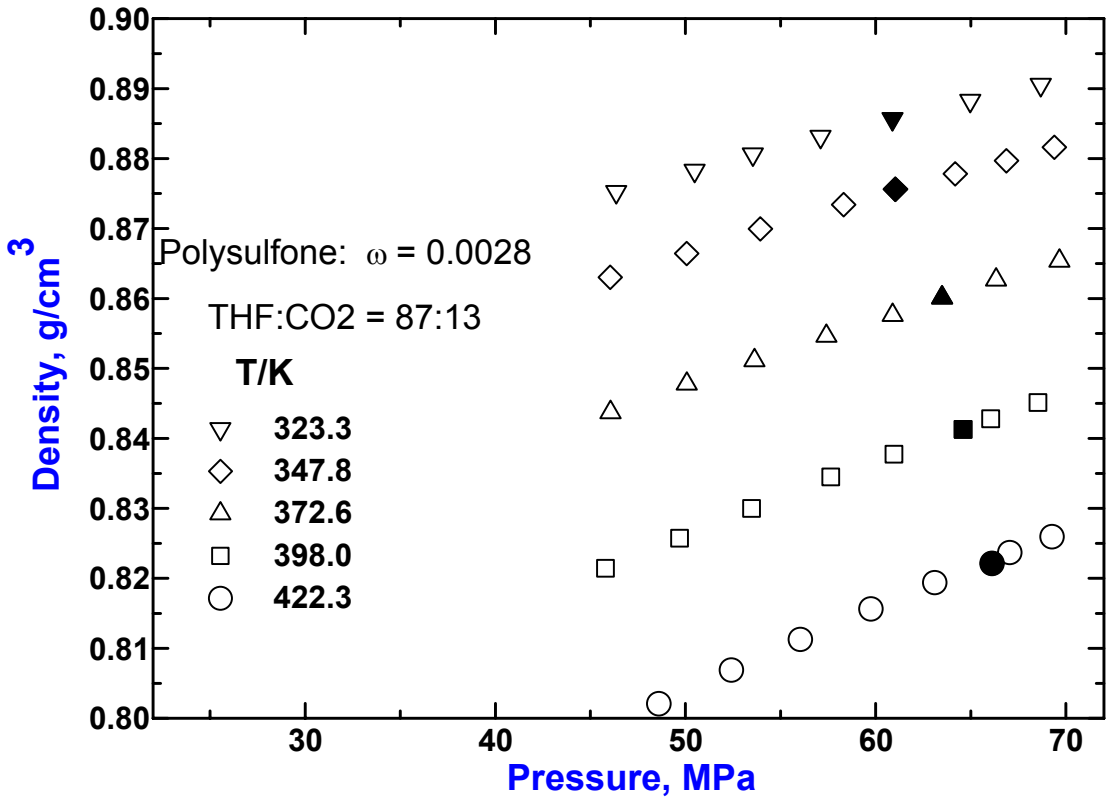

Figure B.1. Pressure dependence of density for 0.28 wt % polysulfone solution in the THF and CO_2 solvent mixture (THF:CO_2 = 87:13) at 323.3, 347.8, 372.6, 398.0, and 422.3 K. Filled data points are the densities at the phase separation points.

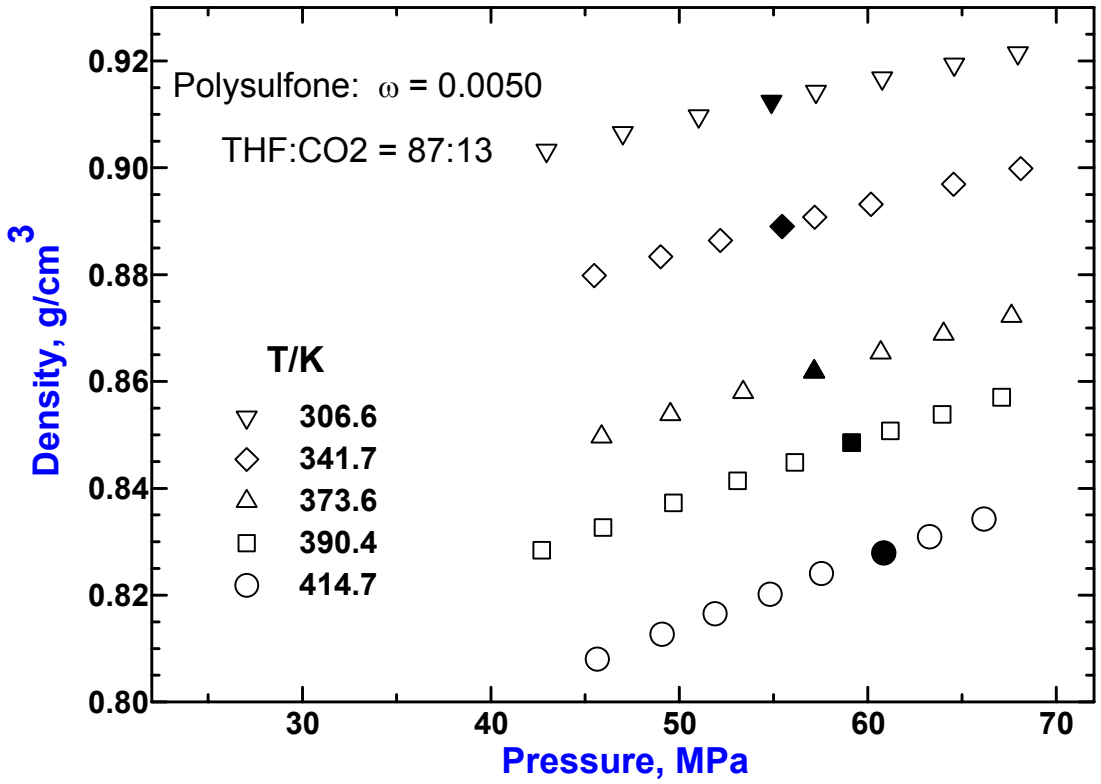

Figure B.2. Pressure dependence of density for 0.50 wt % polysulfone solution in the THF and CO_2 solvent mixture (THF:CO_2 = 87:13) at 306.6, 341.7, 373.6, 390.4, and 414.7 K. Filled data points are the densities at the phase separation points.

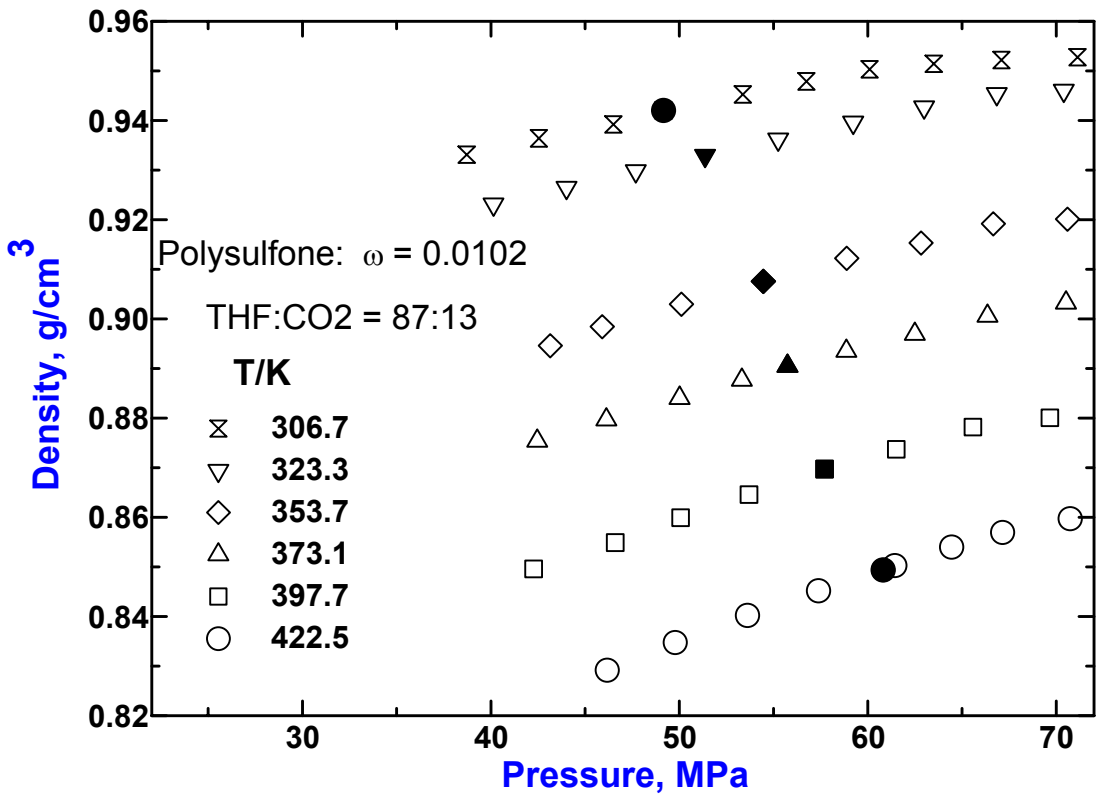

Figure B.3. Pressure dependence of density for 1.02 wt % polysulfone solution in the THF and CO_2 solvent mixture (THF:CO_2 = 87:13) at 306.7, 323.3, 353.7, 373.1, 397.7, and 422.5 K. Filled data points are the densities at the phase

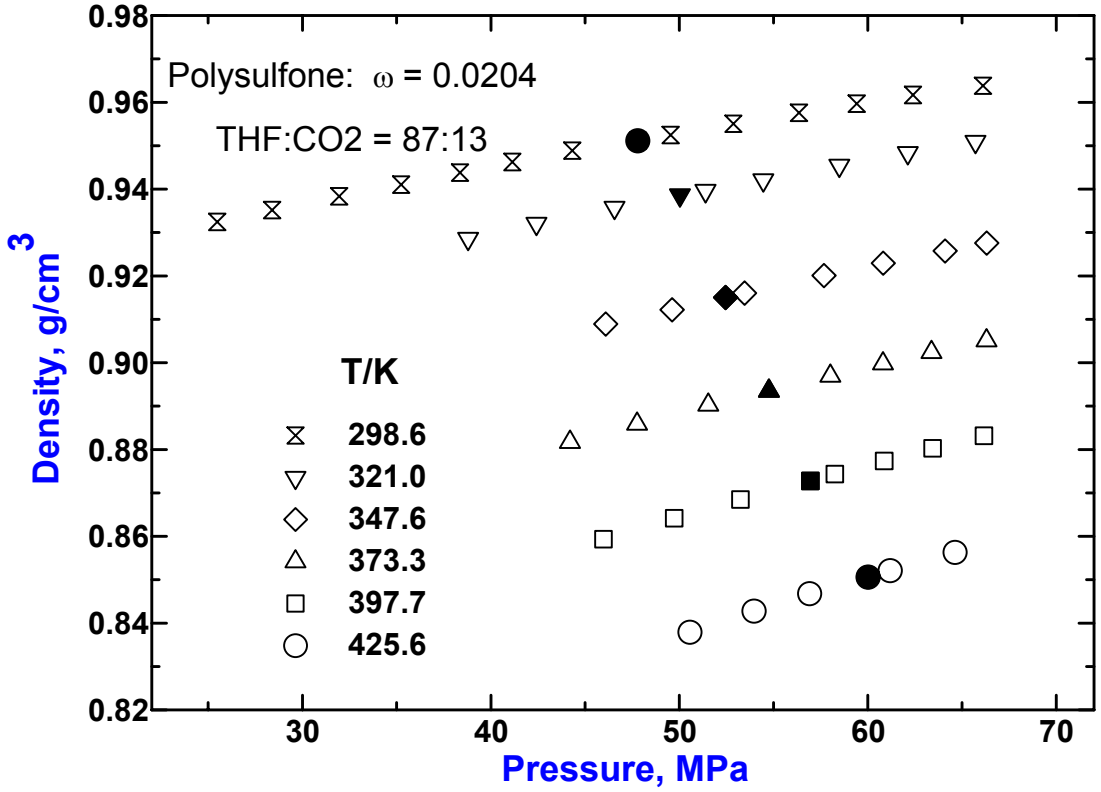

Figure B.4. Pressure dependence of density for 2.04 wt % polysulfone solution in the THF and CO_2 solvent mixture (THF:CO_2 = 87:13) at 298.6, 321.0, 347.6, 373.3, 397.7, and 425.6 K. Filled data points are the densities at the phase separation points.

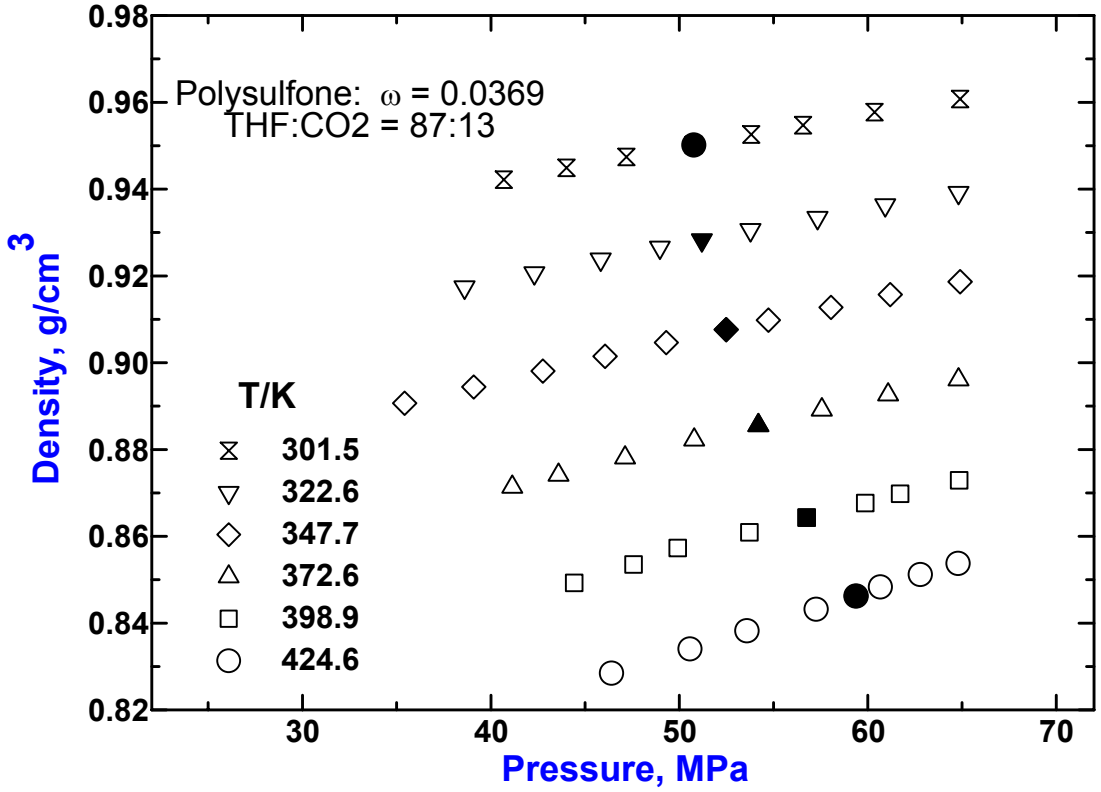

Figure B.5. Pressure dependence of density for 3.69 wt % polysulfone solution in the THF and CO_2 solvent mixture (THF:CO_2 = 87:13) at 301.5, 322.6, 347.7, 372.6, 398.9, and 424.6 K. Filled data points are the densities at the phase separation points.

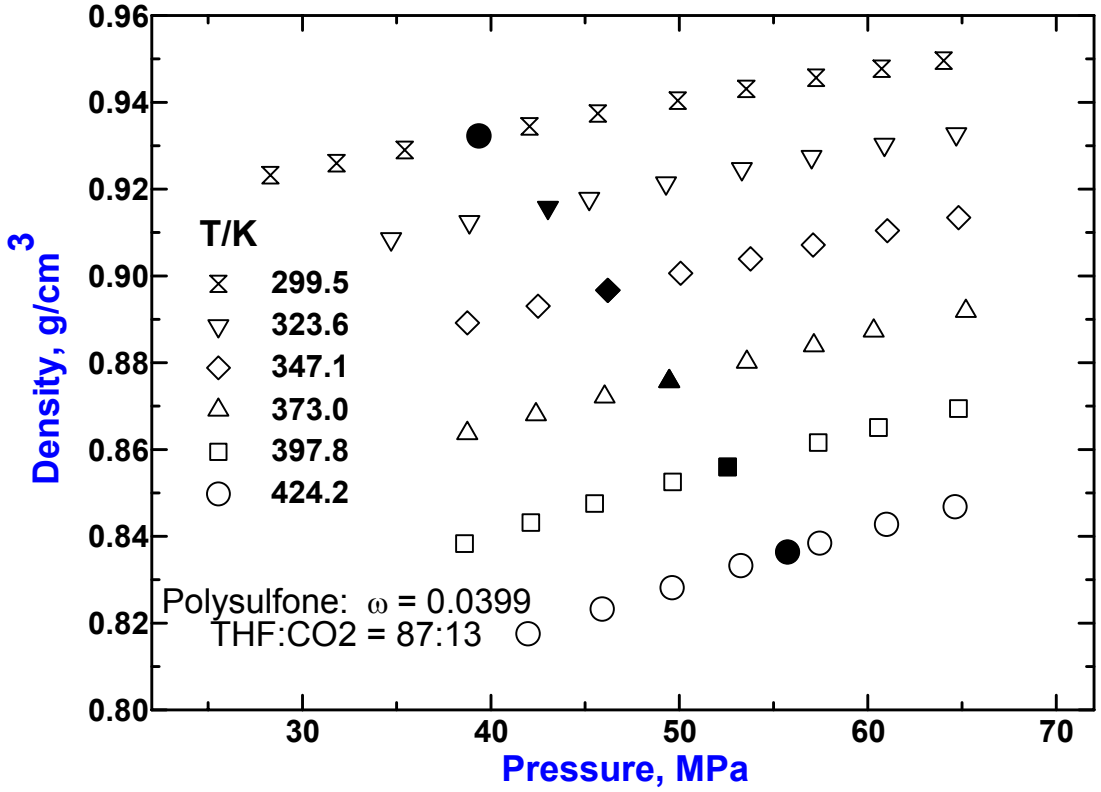

Figure B.6. Pressure dependence of density for 3.99 wt % polysulfone solution in the THF and CO_2 solvent mixture (THF:CO_2 = 87:13) at 299.5, 323.6, 347.1, 373.0, 397.8, and 424.2 K. Filled data points are the densities at the phase separation points.

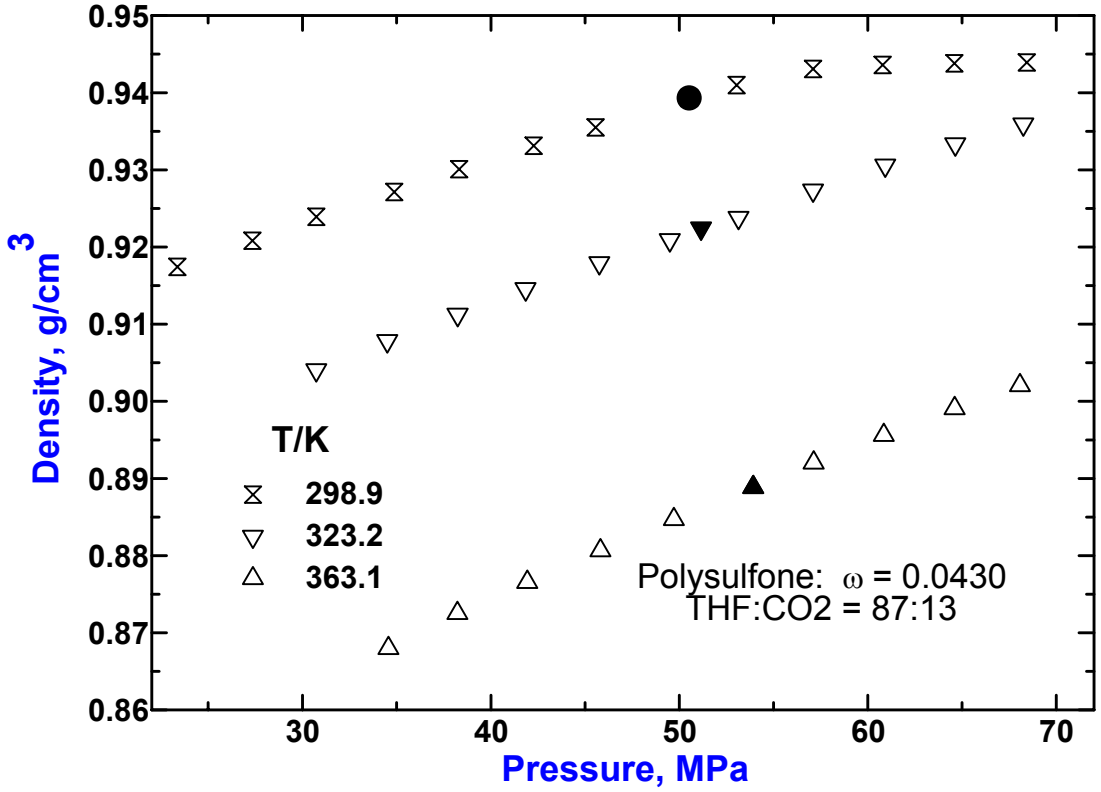

Figure B.7. Pressure dependence of density for 4.30 wt % polysulfone solution in the THF and CO_2 solvent mixture (THF:CO_2 = 87:13) at 298.9, 323.2 and 363.1 K. Filled data points are the densities at the phase separation points.

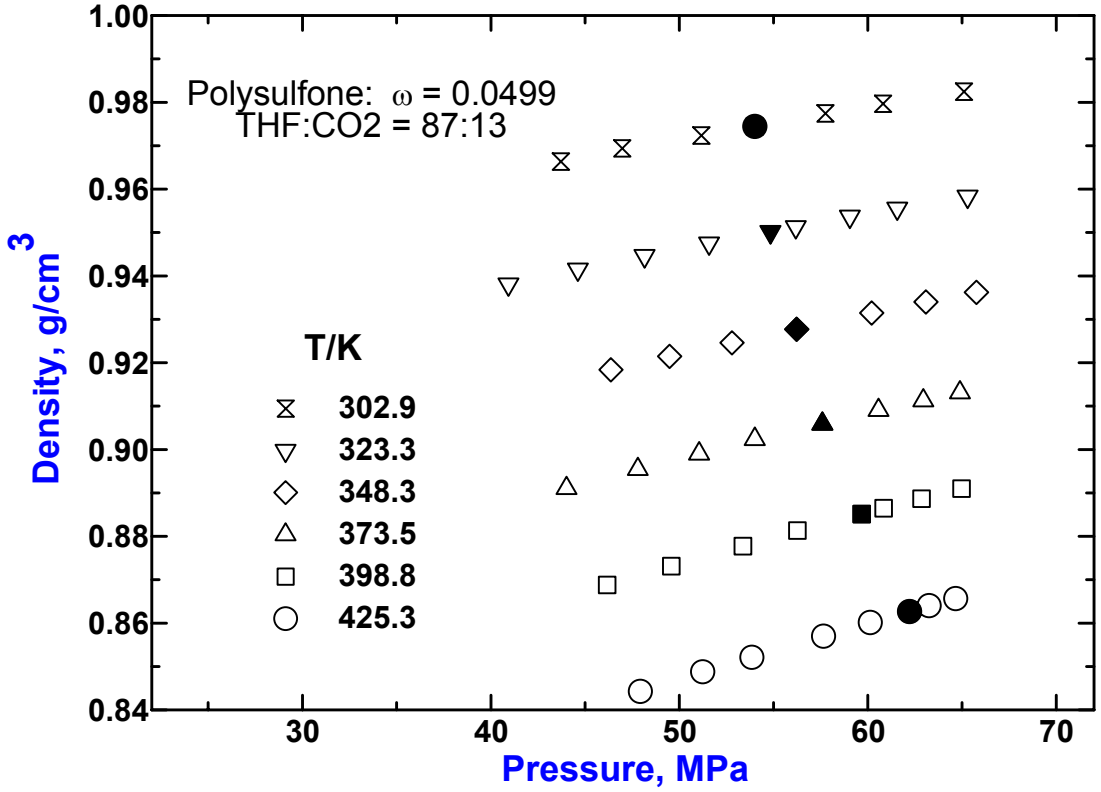

Figure B.8. Pressure dependence of density for 4.99 wt % polysulfone solution in the THF and CO_2 solvent mixture (THF:CO_2 = 87:13) at 302.9, 323.3, 348.3, 373.5, 398.8, and 425.3 K. Filled data points are the densities at the phase separation points.

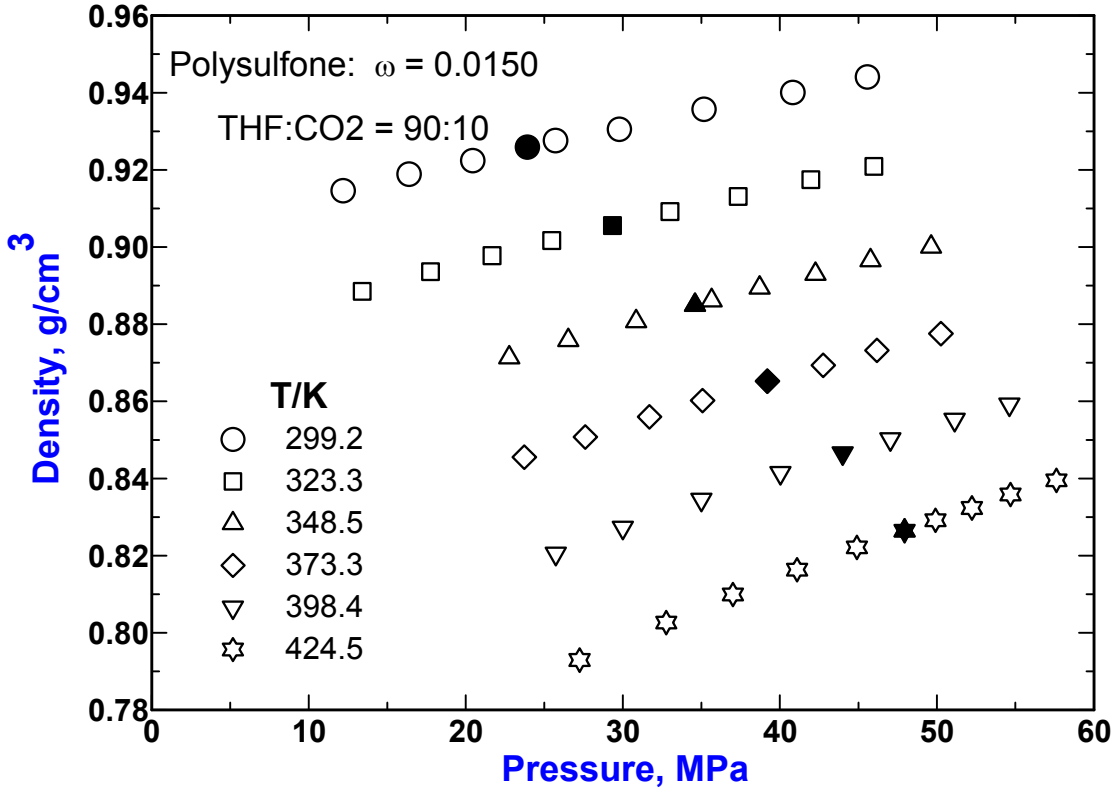

Figure B.9. Pressure dependence of density for 1.50 wt % polysulfone solution in the THF and CO_2 solvent mixture (THF:CO_2 = 90:10) at 299.2, 323.3, 348.5, 373.3, 398.4, and 424.5 K. Filled data points are the densities at the phase separation points.

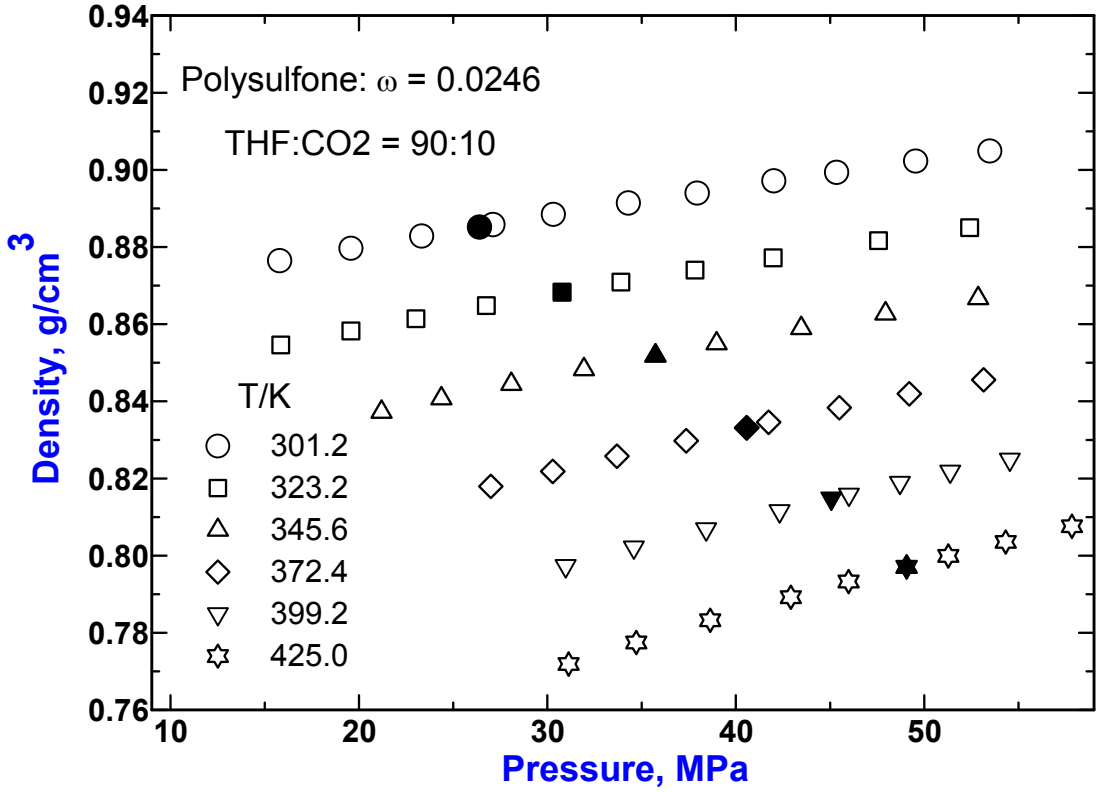

Figure B.10. Pressure dependence of density for 2.46 wt % polysulfone solution in the THF and CO_2 solvent mixture (THF:CO_2 = 90:10) at 301.2, 323.2, 345.6, 372.4, 399.2, and 425.0 K. Filled data points are the densities at the phase separation points.

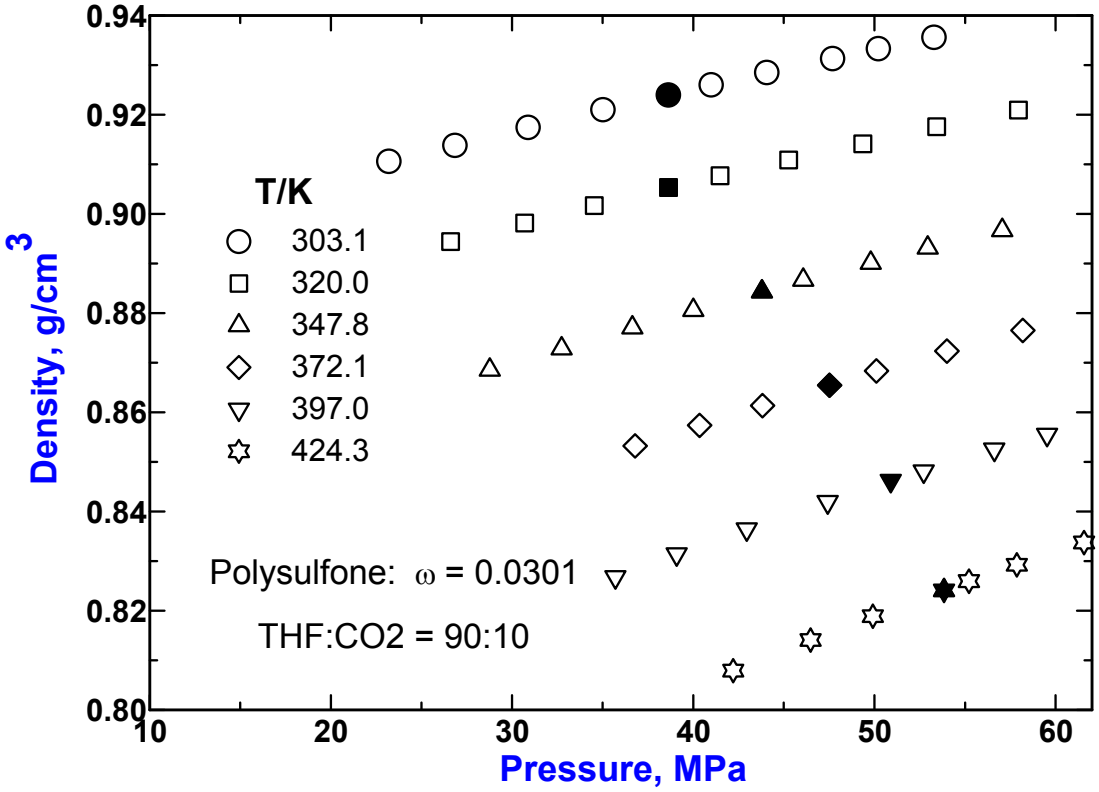

Figure B.11. Pressure dependence of density for 3.01 wt % polysulfone solution in the THF and CO_2 solvent mixture (THF:CO_2 = 90:10) at 303.1, 320.0, 347.8, 372.1, 397.0, and 424.3 K. Filled data points are the densities at the phase separation points.

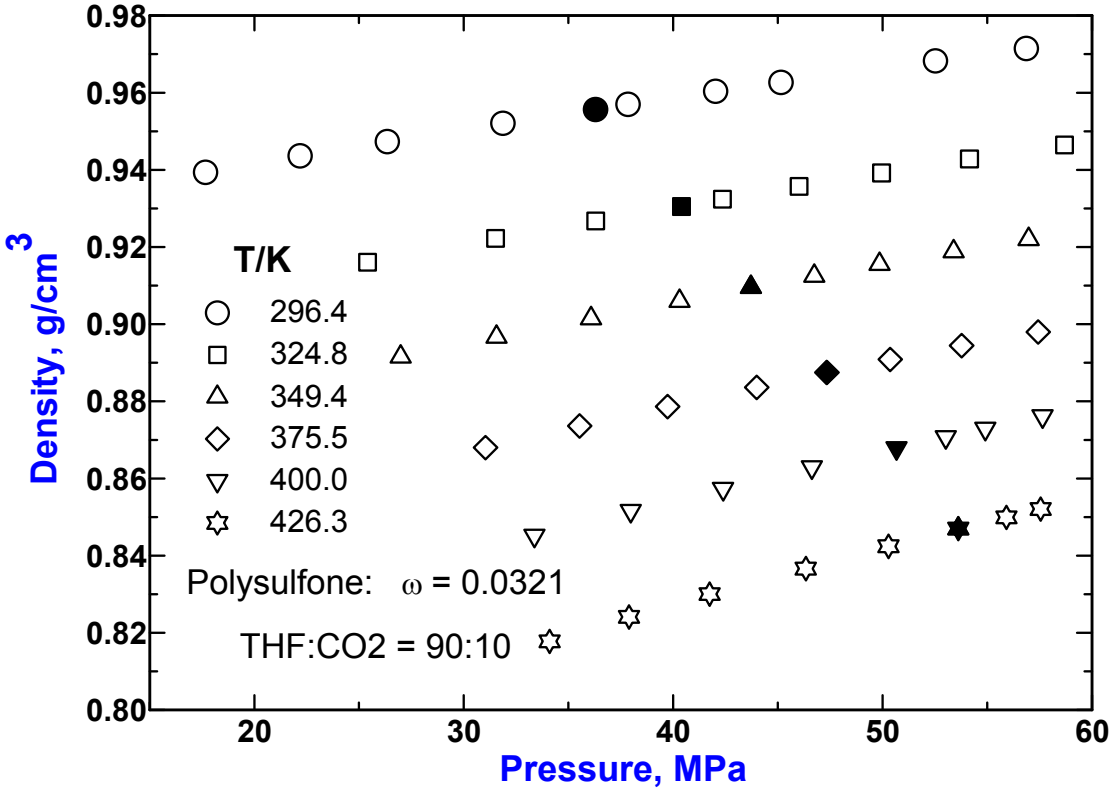

Figure B.12. Pressure dependence of density for 3.21 wt % polysulfone solution in the THF and CO_2 solvent mixture (THF:CO_2 = 90:10) at 296.4, 324.8, 349.4, 375.5, 400.0, and 426.3 K. Filled data points are the densities at the phase separation points.

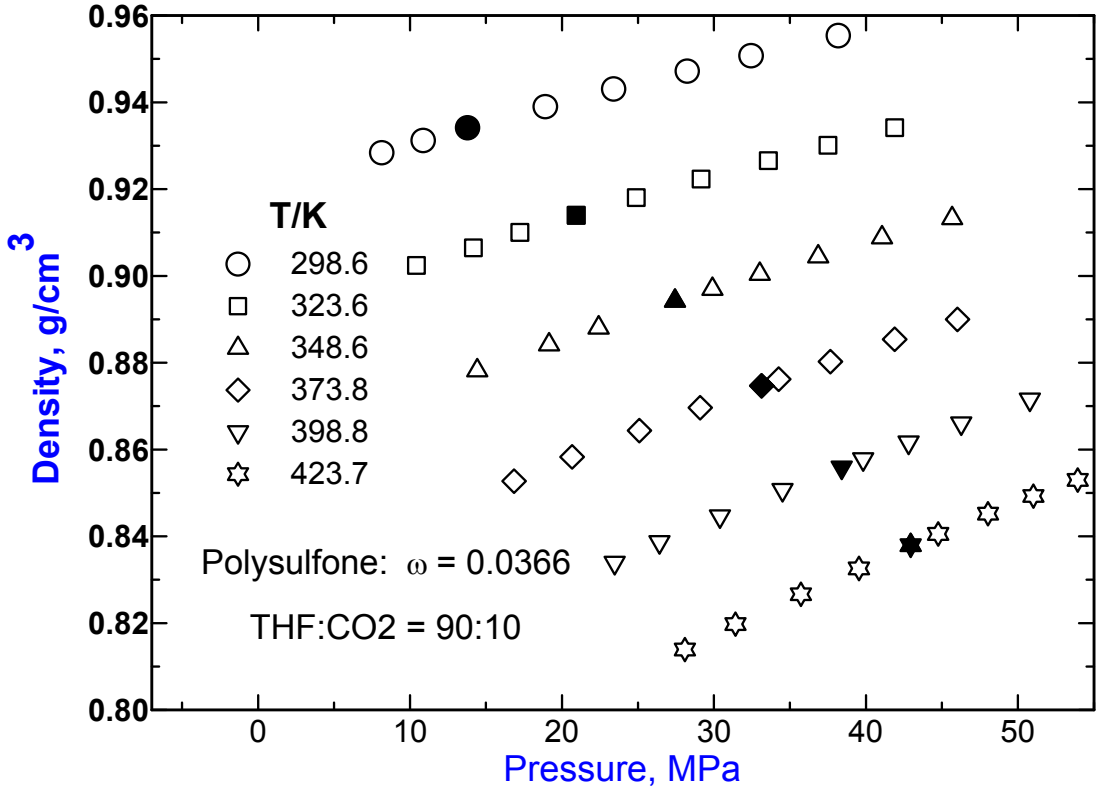

Figure B.13. Pressure dependence of density for 3.66 wt % polysulfone solution in the THF and CO_2 solvent mixture (THF:CO_2 = 90:10) at 298.6, 323.8, 348.6, 373.8, 398.8, and 423.7 K. Filled data points are the densities at the phase separation points.

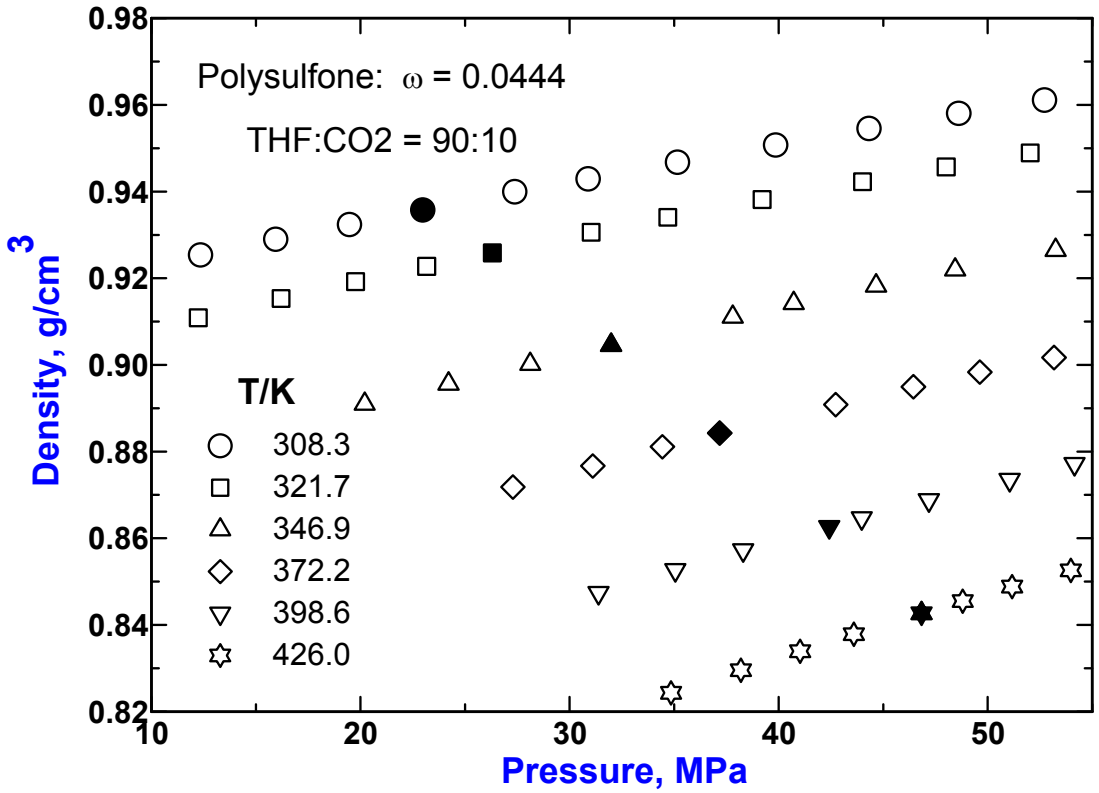

Figure B.14. Pressure dependence of density for 4.44 wt % polysulfone solution in the THF and CO_2 solvent mixture (THF:CO_2 = 90:10) at 308.3, 321.7, 346.9, 372.2, 398.6, and 426.0 K. Filled data points are the densities at the phase separation points.

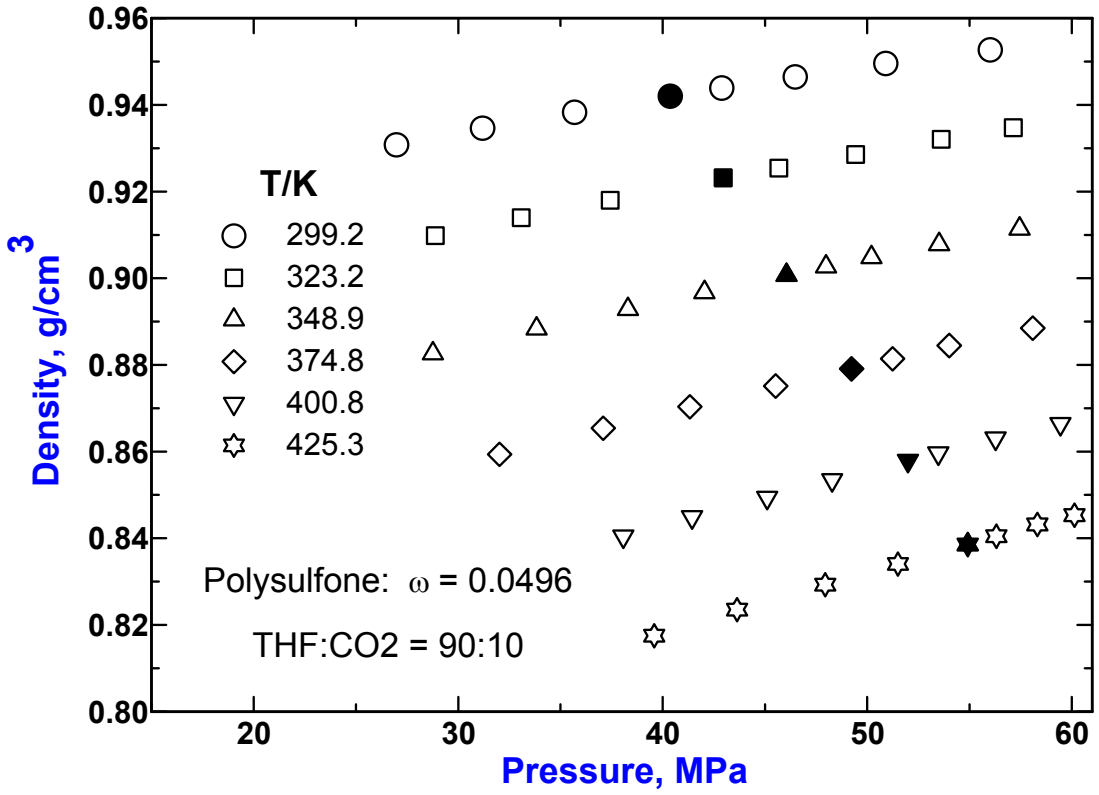

Figure B.15. Pressure dependence of density for 4.96 wt % polysulfone solution in the THF and CO_2 solvent mixture (THF:CO_2 = 90:10) at 299.2, 323.2, 348.9, 374.8, 400.8, and 425.3 K. Filled data points are the densities at the phase separation points.

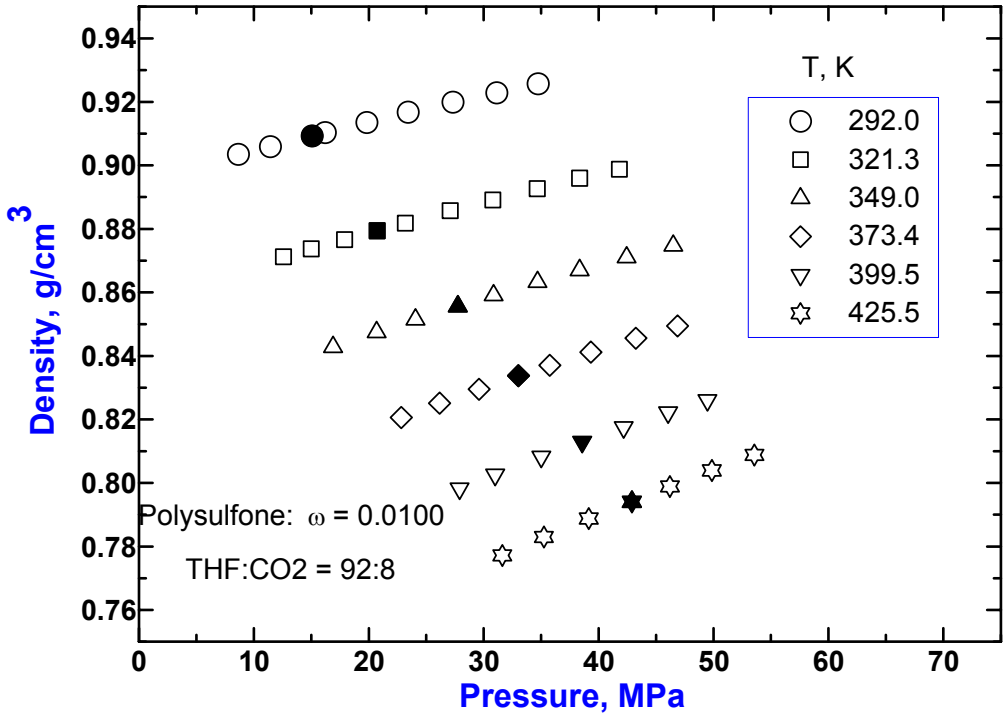

Figure B.16. Pressure dependence of density for 1.00 wt % polysulfone solution in the THF and CO_2 solvent mixture (THF:CO_2 = 92:8) at 299.0, 321.3, 349.0, 373.4, 399.5, and 425.5 K. Filled data points are the densities at the phase separation points.

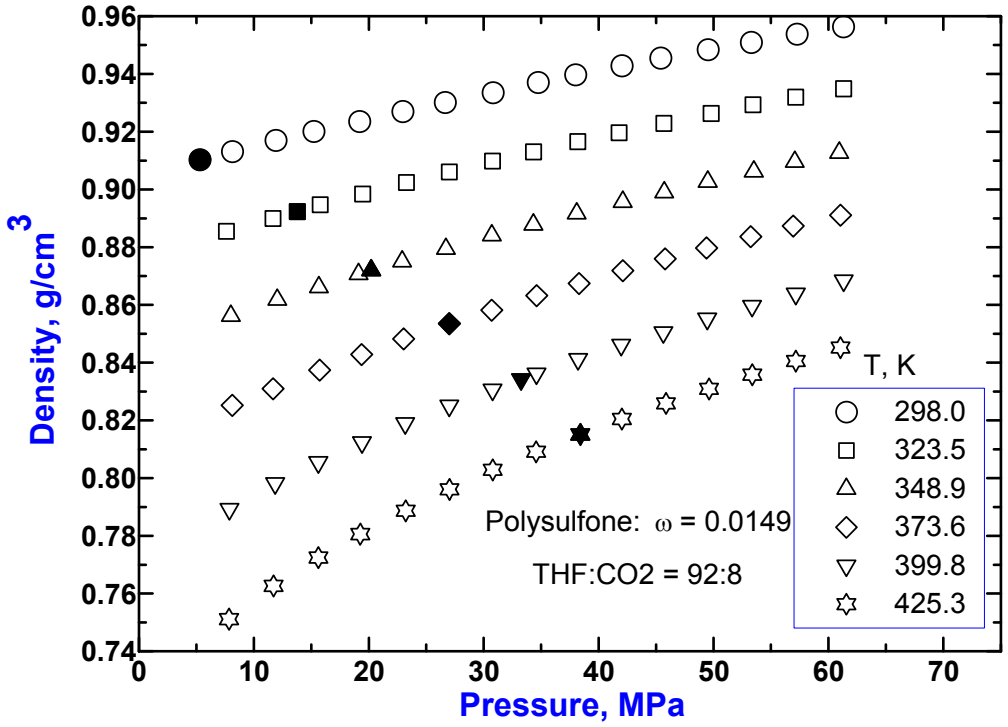

Figure B.17. Pressure dependence of density for 1.49 wt % polysulfone solution in the THF and CO_2 solvent mixture (THF:CO_2 = 92:8) at 298.0, 323.5, 348.9, 373.6, 399.8, and 425.3 K. Filled data points are the densities at the phase separation points.

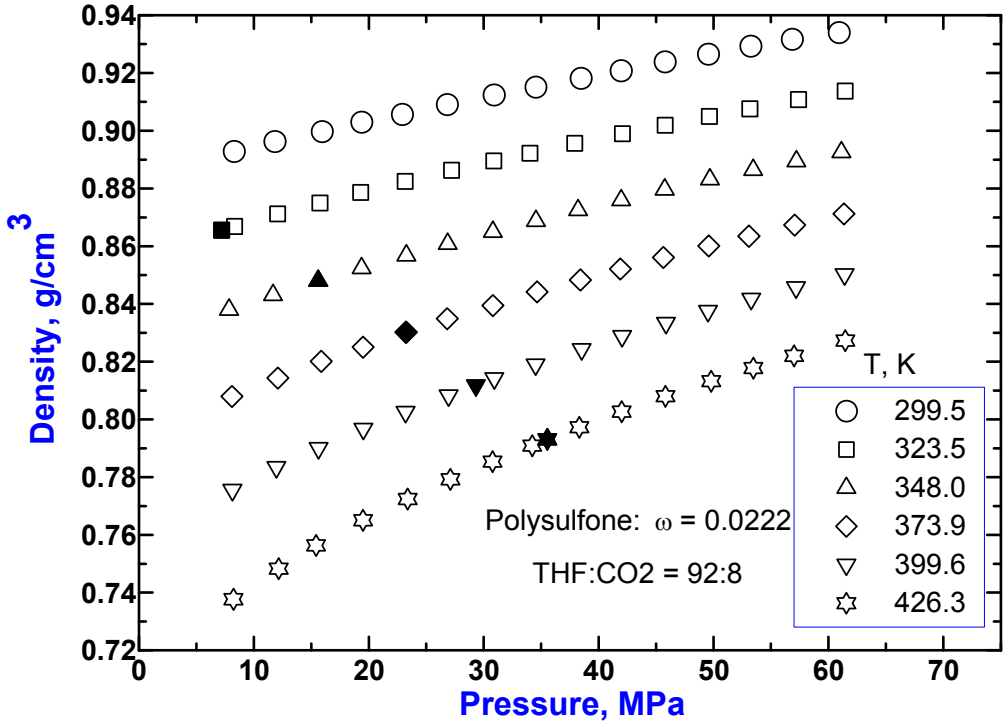

Figure B.18. Pressure dependence of density for 2.22 wt % polysulfone solution in the THF and CO_2 solvent mixture (THF:CO_2 = 92:8) at 299.5, 323.5, 348.0, 373.9, 399.6, and 426.3 K. Filled data points are the densities at the phase separation points.

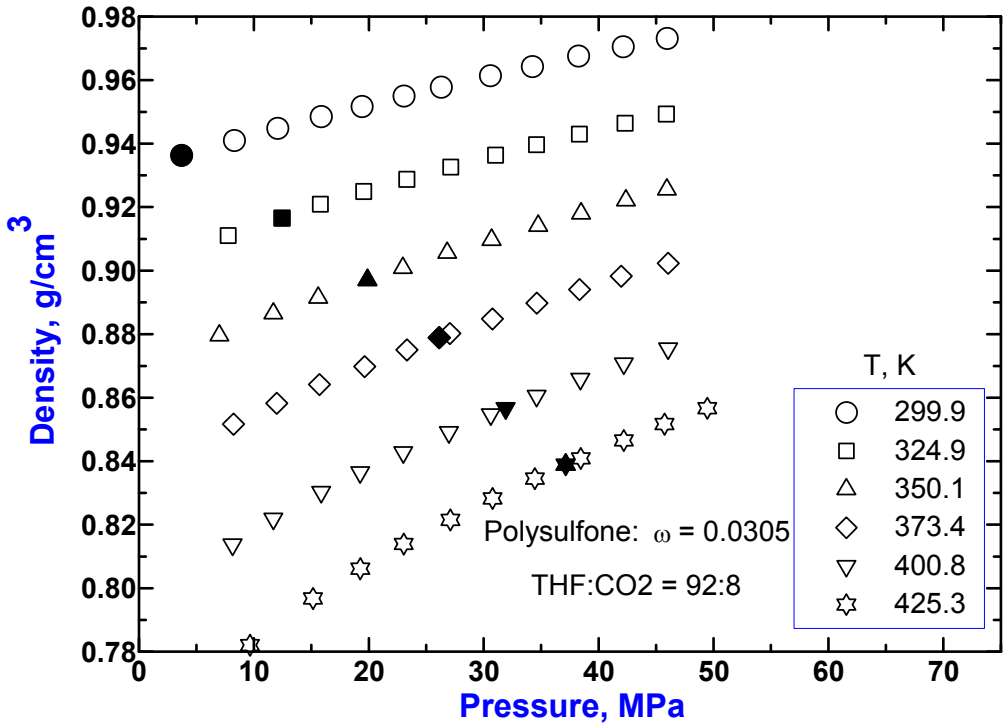

Figure B.19. Pressure dependence of density for 3.05 wt % polysulfone solution in the THF and CO_2 solvent mixture (THF:CO_2 = 92:8) at 299.9, 324.9, 350.1, 373.4, 400.8, and 425.3 K. Filled data points are the densities at the phase separation points.

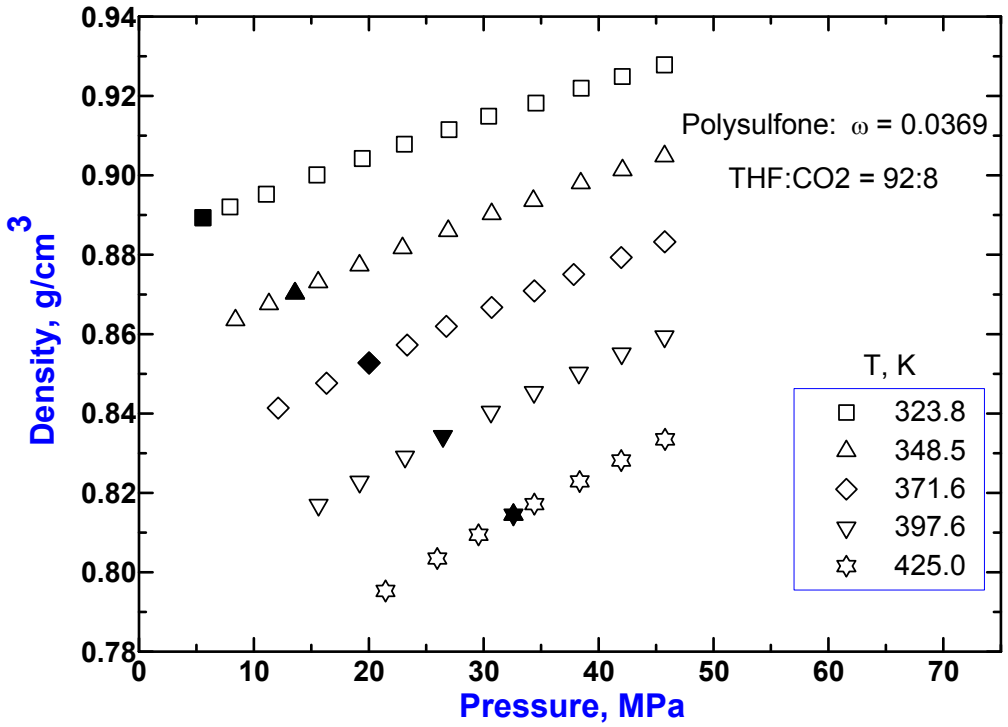

Figure B.20. Pressure dependence of density for 3.69 wt % polysulfone solution in the THF and CO_2 solvent mixture (THF:CO_2 = 92:8) at 323.8, 348.5, 371.6, 397.6, and 425.0 K. Filled data points are the densities at the phase separation points.

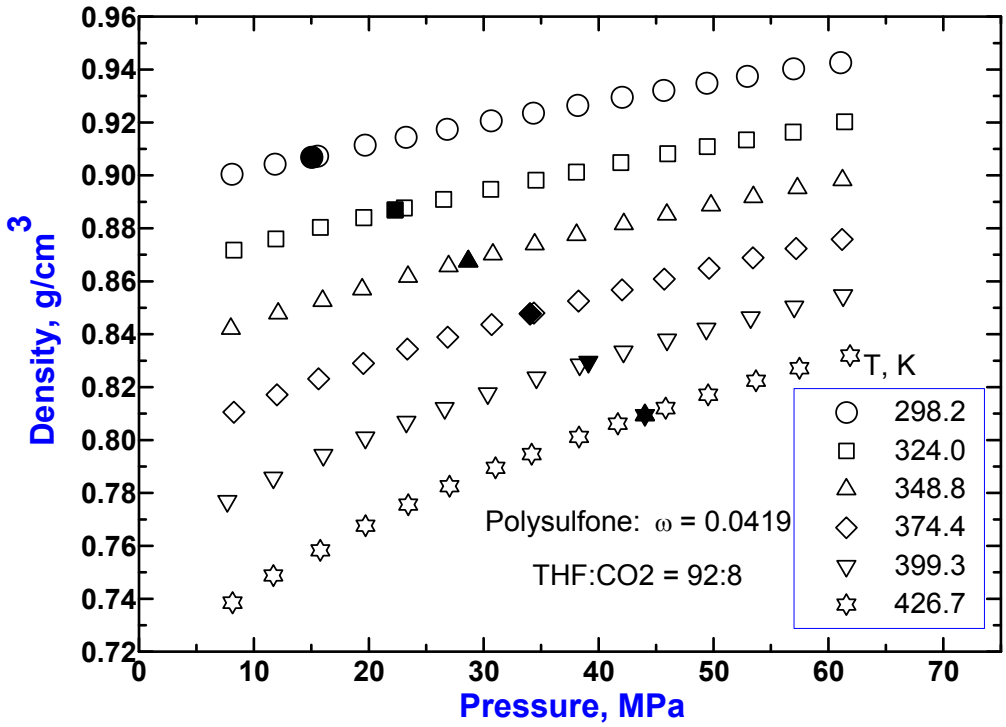

Figure B.21. Pressure dependence of density for 4.19 wt % polysulfone solution in the THF and CO_2 solvent mixture (THF:CO_2 = 92:8) at 298.2, 324.0, 348.8, 374.4, 399.3, and 426.7 K. Filled data points are the densities at the phase separation points.

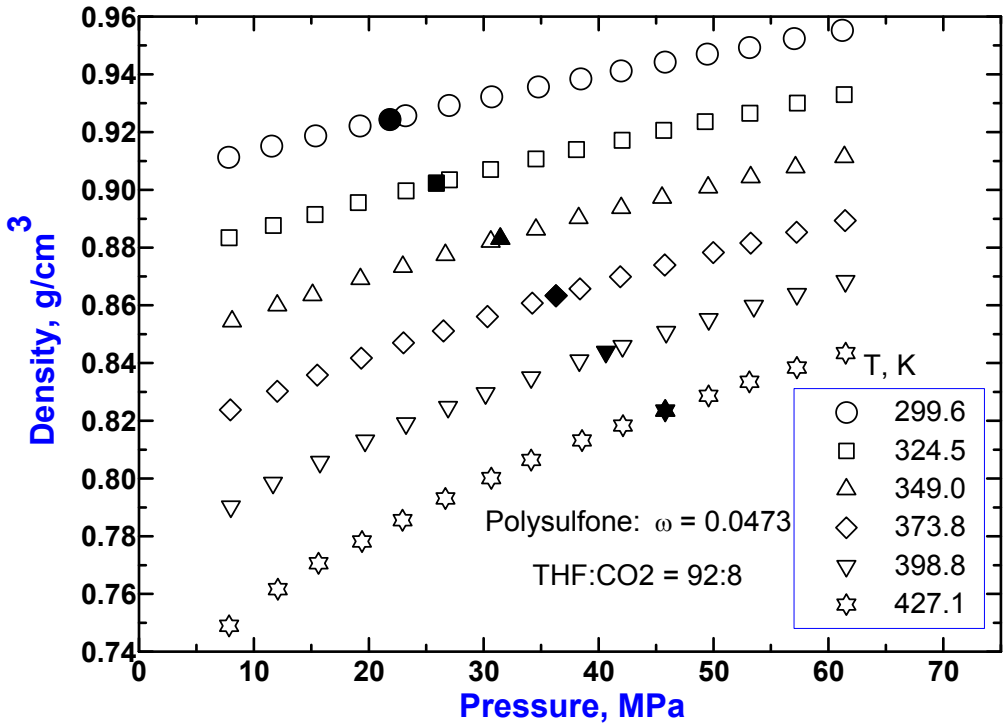

Figure B.22. Pressure dependence of density for 4.73 wt % polysulfone solution in the THF and CO_2 solvent mixture (THF:CO_2 = 92:8) at 299.6, 324.5, 349.0, 373.8, 398.8, and 427.1 K. Filled data points are the densities at the phase separation points.

Appendix C

Scattering Profiles for Polysulfone Solutions in THF + CO_2

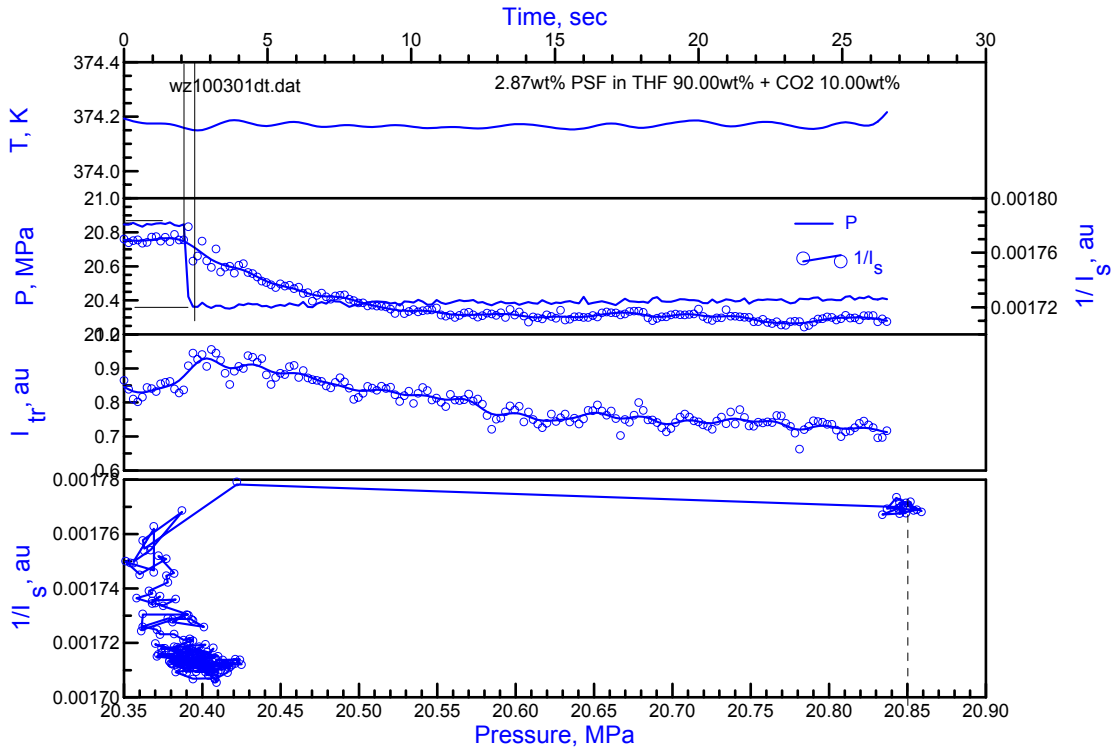

Figure C.1. Variation of temperature (T), Pressure (P), transmitted light intensity (I_{tr}), and inverse averaged scattered light intensity (1/Is) with time during a fast pressure quench in 2.87 wt % solution of PSF in a mixture of THF (90 wt %) + CO_2 (10 wt %).

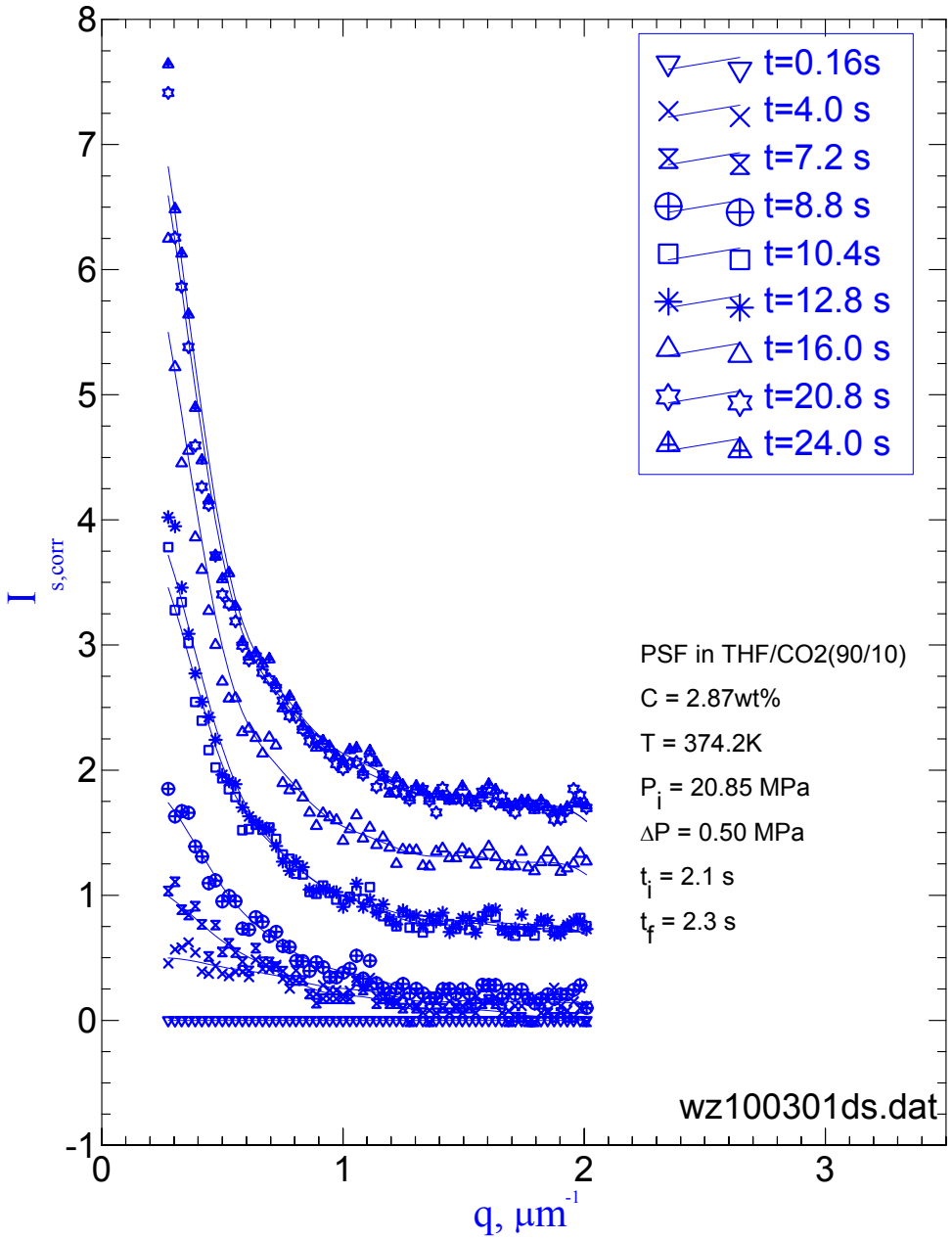

Figure C.2. Time evolution of the scattered light intensities as a function of the wave number q after a pressure quench ΔP = 0.50 MPa in 2.87 wt % solution of PSF in a mixture of THF (90 wt %) + CO_2 (10 wt %) at 374.0 K. The total observation time is 26 seconds. t_i: the time when the pressure quench starts; t_f: the time when the pressure quench ends.

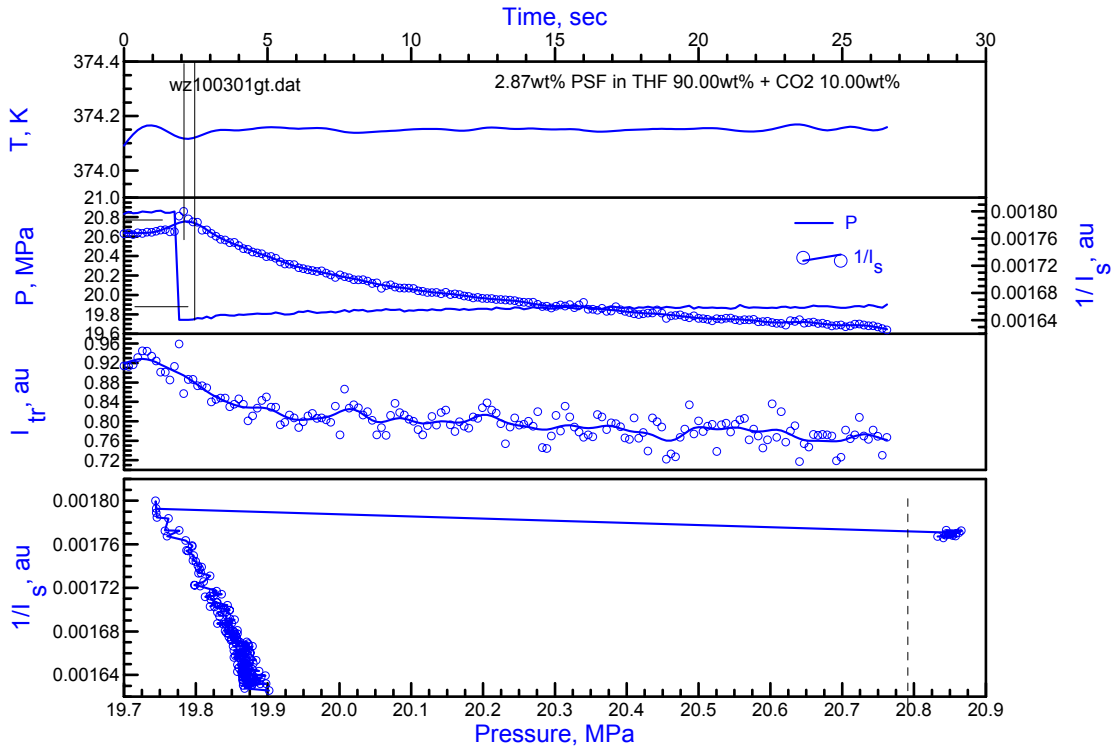

Figure C.3. Variation of temperature (T), Pressure (P), transmitted light intensity (I_{tr}), and inverse averaged scattered light intensity (1/Is) with time during a fast pressure quench in 2.87 wt % solution of PSF in a mixture of THF (90 wt %) + CO_2 (10 wt %).

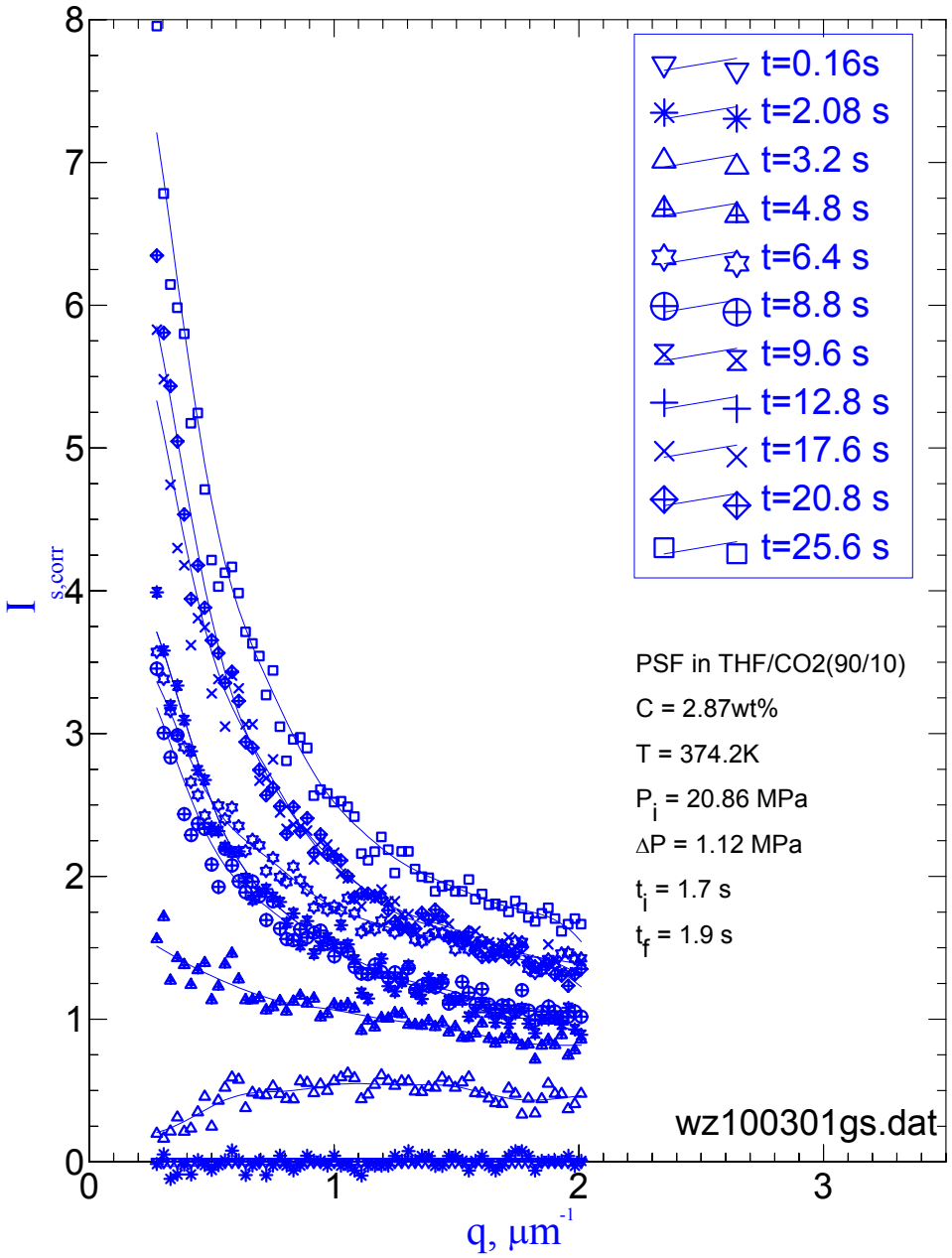

Figure C.4. Time evolution of the scattered light intensities as a function of the wave number q after a pressure quench ΔP = 1.12 MPa in 2.87 wt % solution of PSF in a mixture of THF (90 wt %) + CO_2 (10 wt %) at 374.0 K. The total observation time is 26 seconds. t_i: the time when the pressure quench starts; t_f: the time when the pressure quench ends.

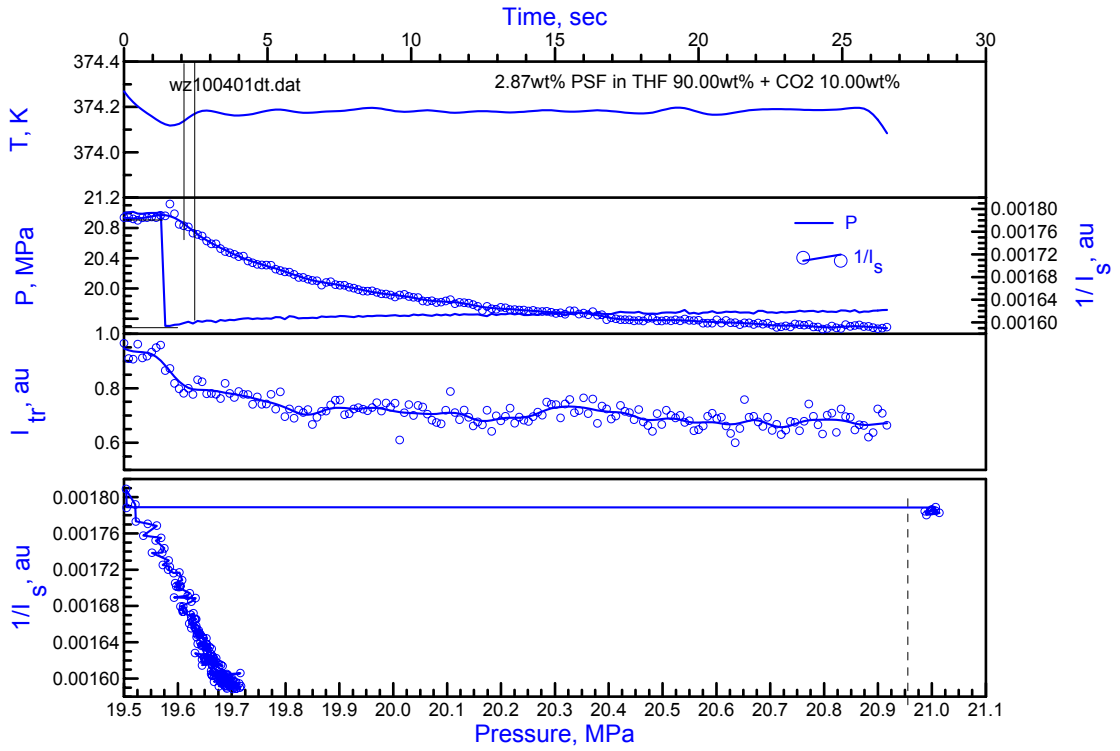

Figure C.5. Variation of temperature (T), Pressure (P), transmitted light intensity (I_{tr}), and inverse averaged scattered light intensity (1/Is) with time during a fast pressure quench in 2.87 wt % solution of PSF in a mixture of THF (90 wt %) + CO_2 (10 wt %).

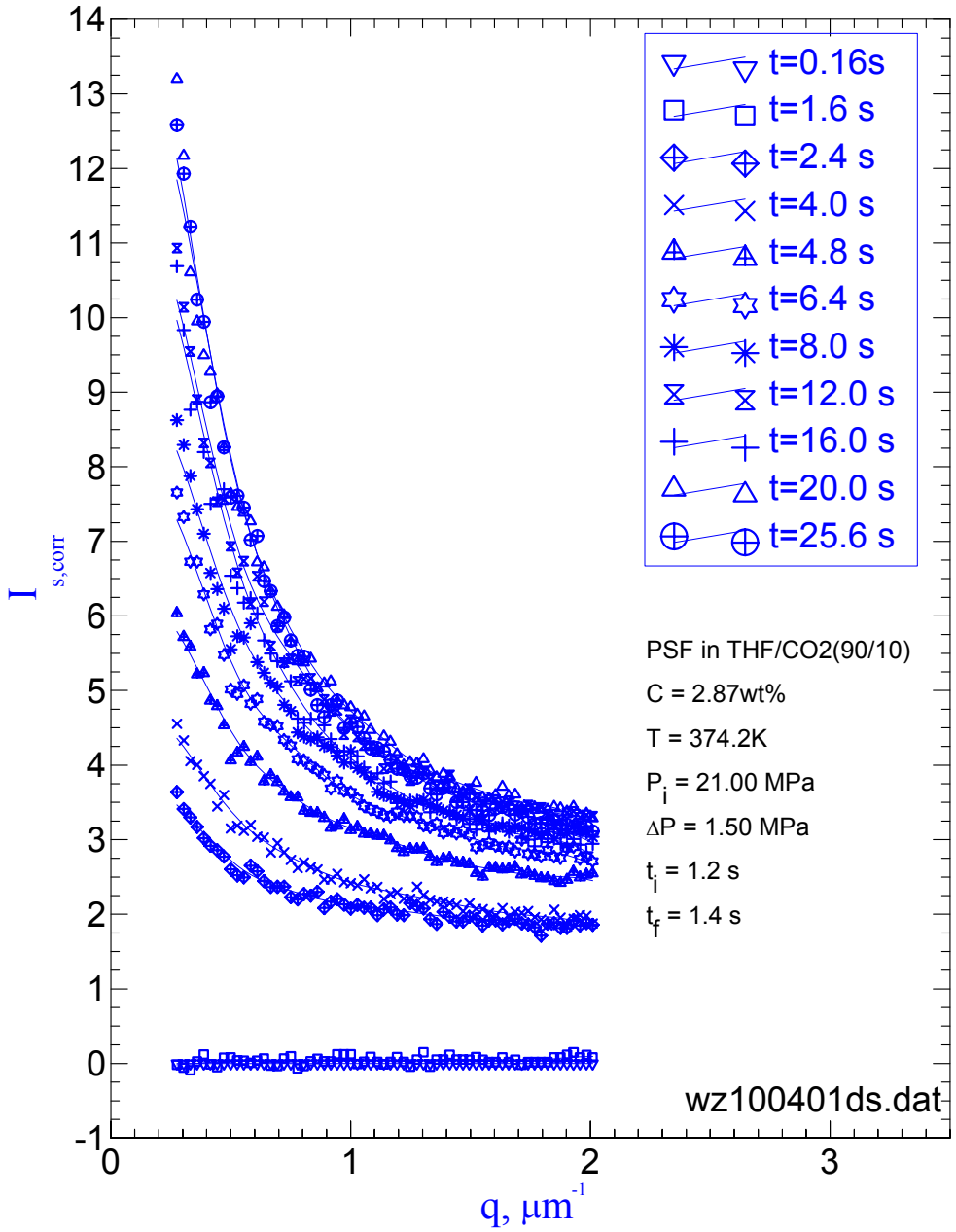

Figure C.6. Time evolution of the scattered light intensities as a function of the wave number q after a pressure quench ΔP = 1.50 MPa in 2.87 wt % solution of PSF in a mixture of THF (90 wt %) + CO_2 (10 wt %) at 374.0 K. The total observation time is 26 seconds. t_i: the time when the pressure quench starts; t_f: the time when the pressure quench ends.

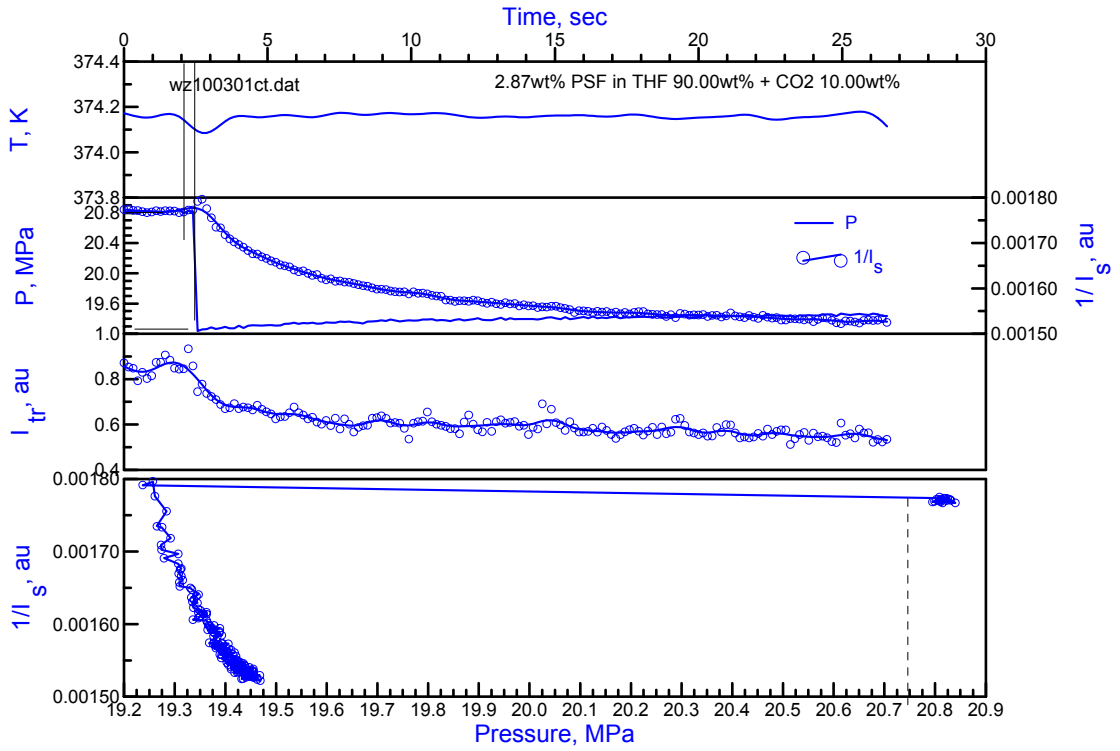

Figure C.7. Variation of temperature (T), Pressure (P), transmitted light intensity (I_{tr}), and inverse averaged scattered light intensity (1/Is) with time during a fast pressure quench in 2.87 wt % solution of PSF in a mixture of THF (90 wt %) + CO_2 (10 wt %).

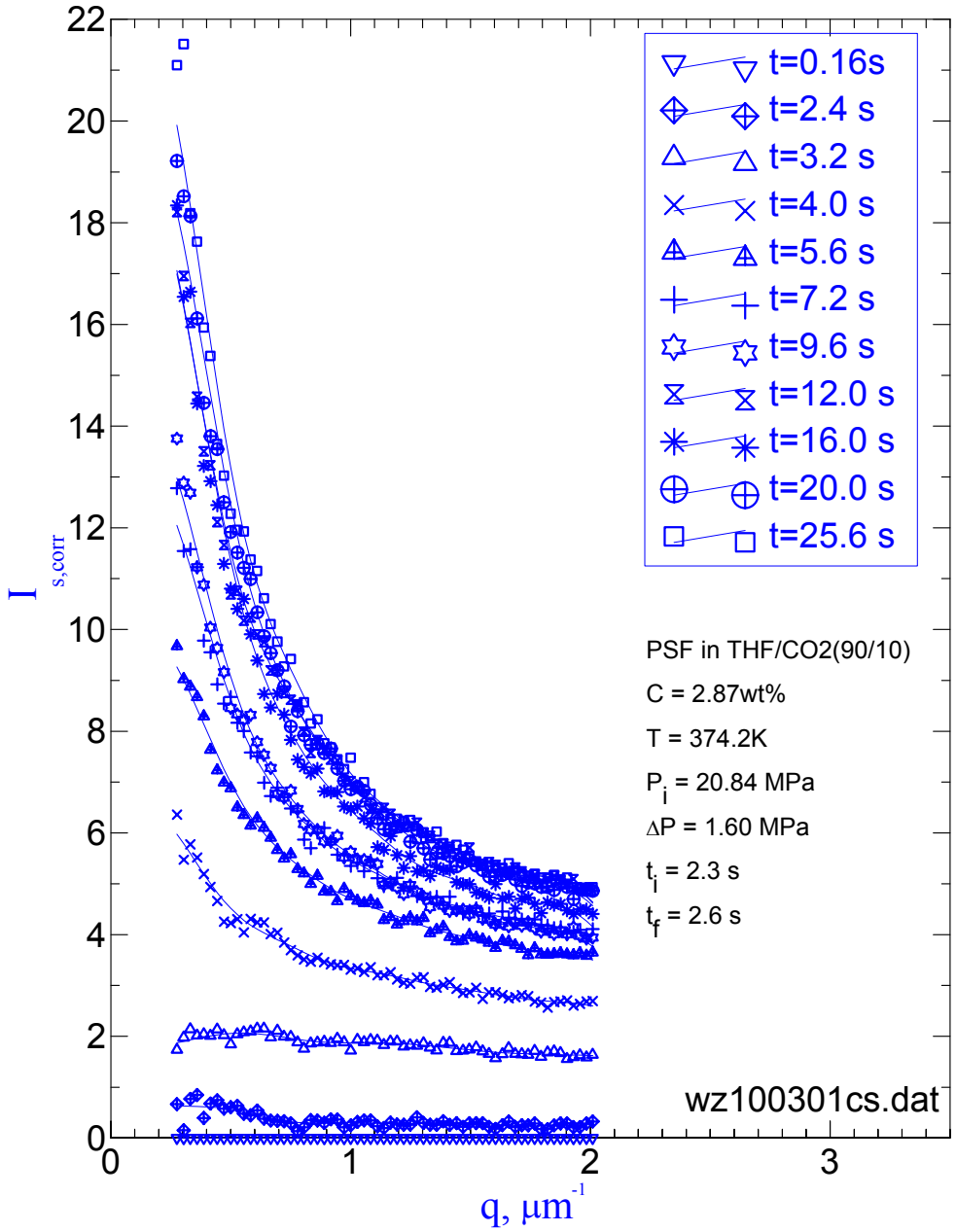

Figure C.8. Time evolution of the scattered light intensities as a function of the wave number q after a pressure quench ΔP = 1.60 MPa in 2.87 wt % solution of PSF in a mixture of THF (90 wt %) + CO_2 (10 wt %) at 374.0 K. The total observation time is 26 seconds. t_i: the time when the pressure quench starts; t_f: the time when the pressure quench ends.

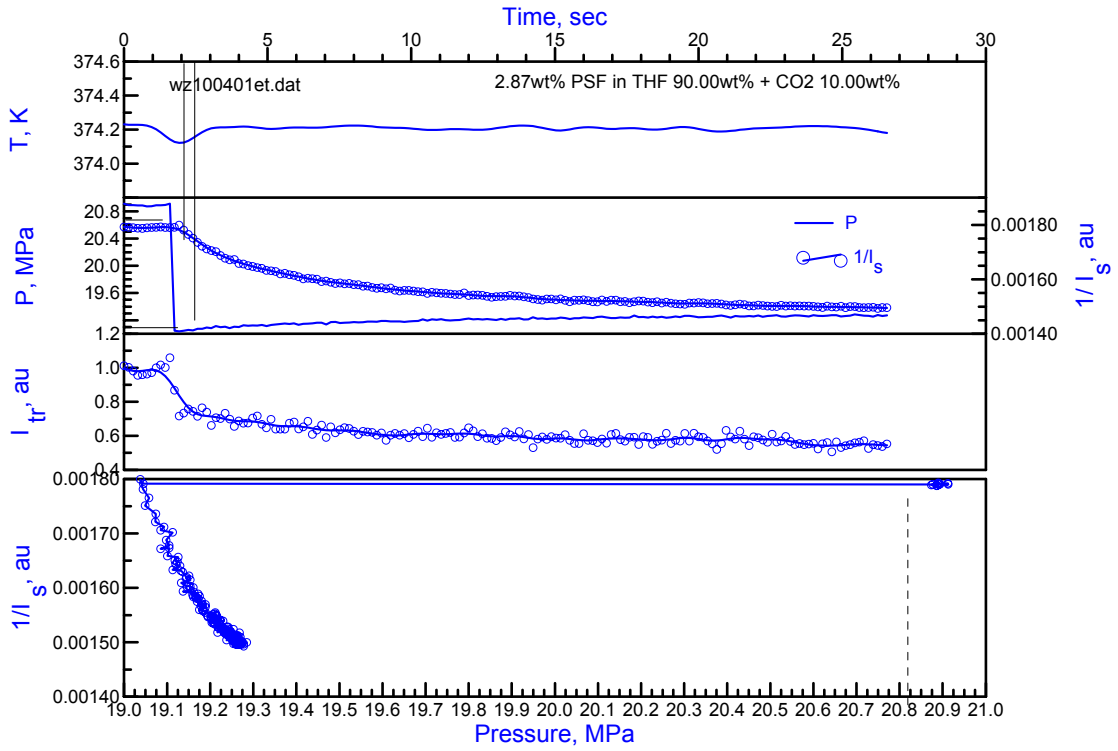

Figure C.9. Variation of temperature (T), Pressure (P), transmitted light intensity (I_{tr}), and inverse averaged scattered light intensity (1/Is) with time during a fast pressure quench in 2.87 wt % solution of PSF in a mixture of THF (90 wt %) + CO_2 (10 wt %).

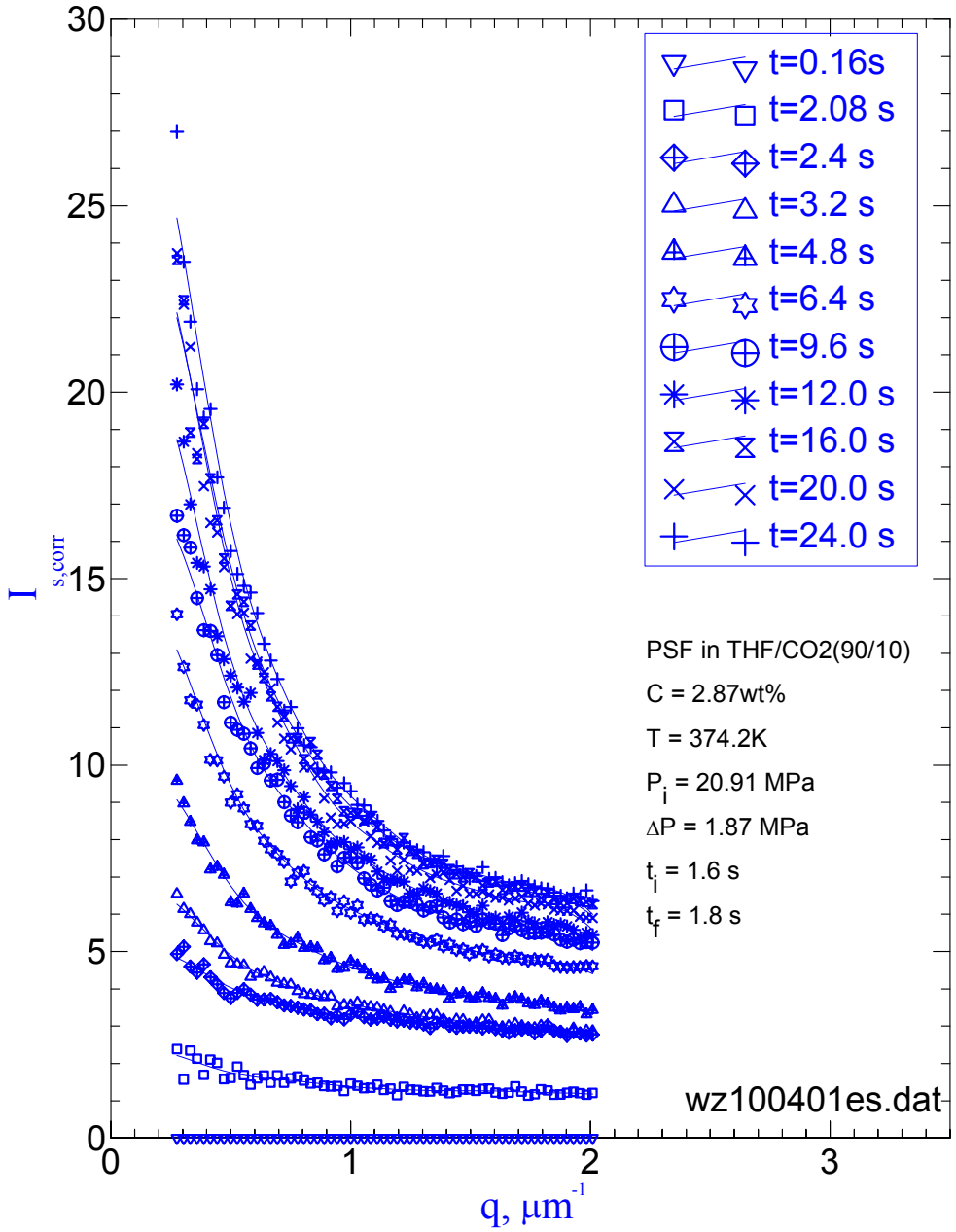

Figure C.10. Time evolution of the scattered light intensities as a function of the wave number q after a pressure quench ΔP = 1.87 MPa in 2.87 wt % solution of PSF in a mixture of THF (90 wt %) + CO_2 (10 wt %) at 374.0 K. The total observation time is 26 seconds. t_i: the time when the pressure quench starts; t_f: the time when the pressure quench ends.

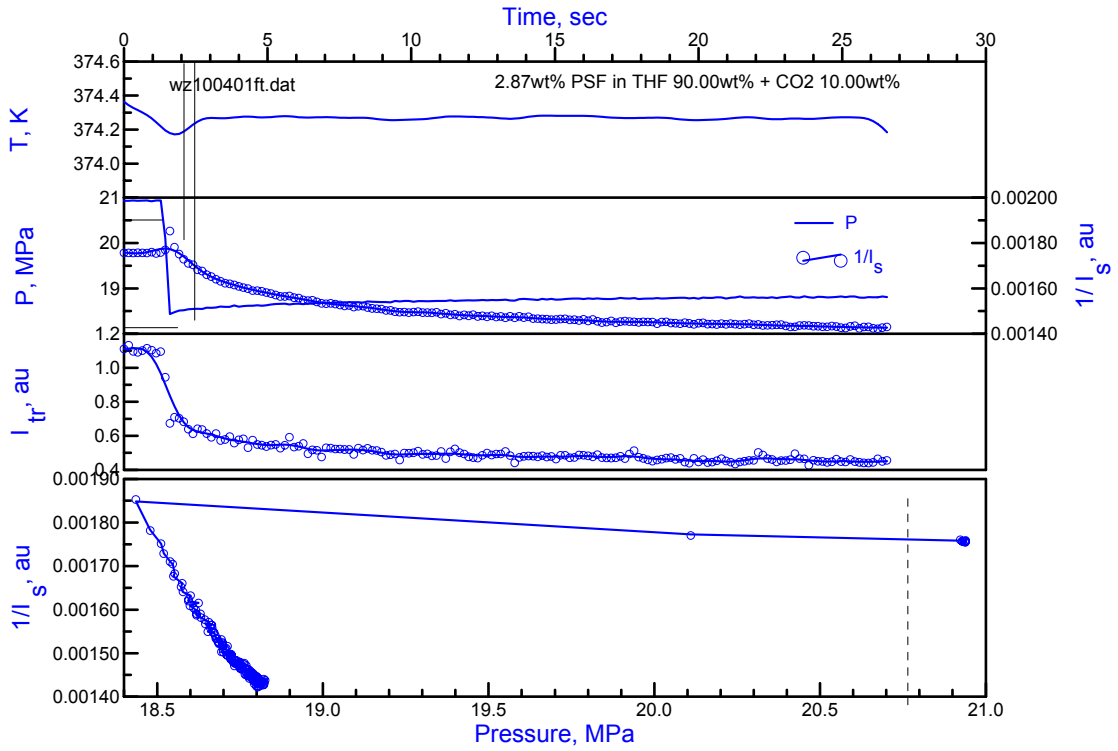

Figure C.11. Variation of temperature (T), Pressure (P), transmitted light intensity (I_{tr}), and inverse averaged scattered light intensity (1/Is) with time during a fast pressure quench in 2.87 wt % solution of PSF in a mixture of THF (90 wt %) + CO_2 (10 wt %).

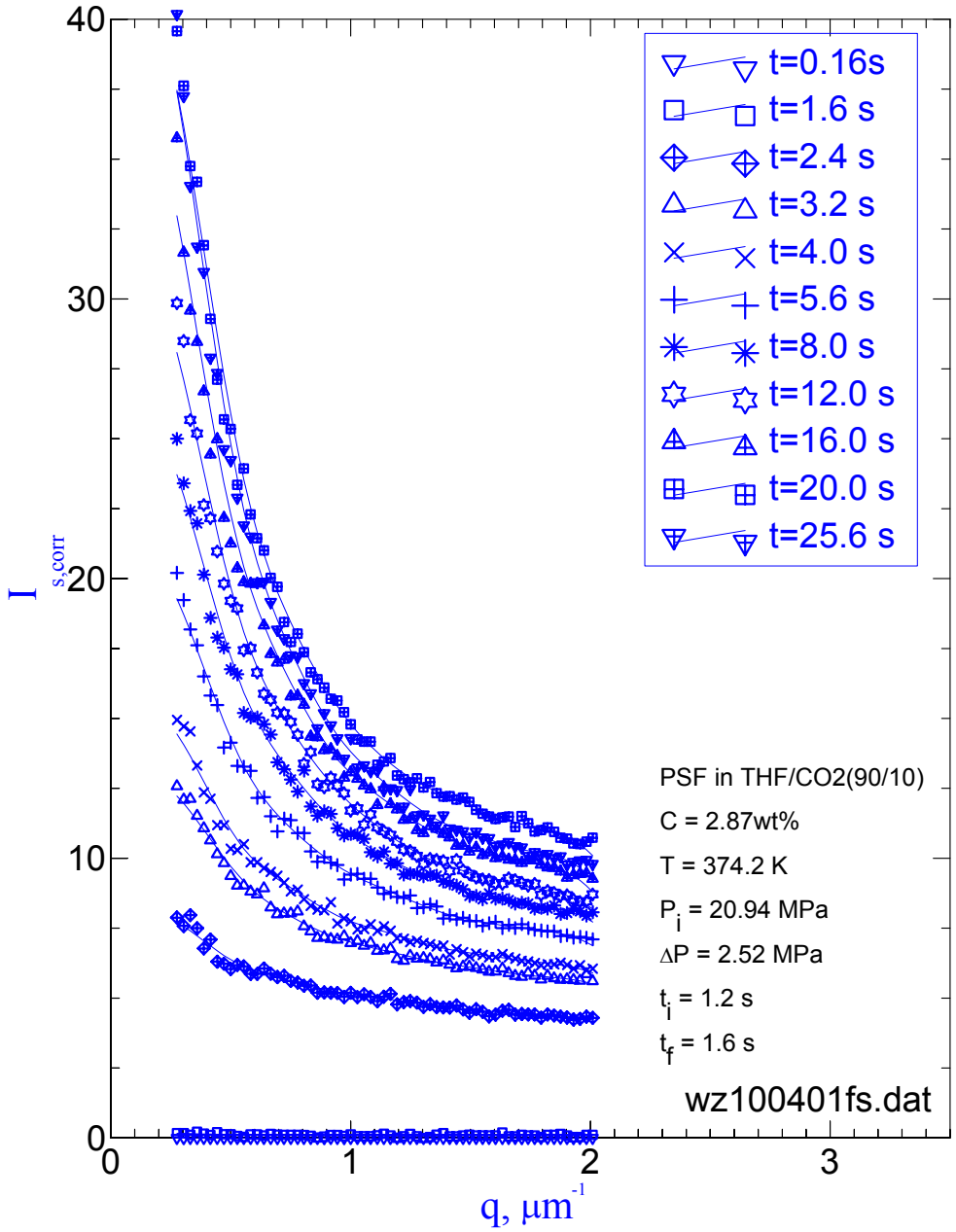

Figure C.12. Time evolution of the scattered light intensities as a function of the wave number q after a pressure quench $\Delta P = 2.52$ MPa in 2.87 wt % solution of PSF in a mixture of THF (90 wt %) + CO_2 (10 wt %) at 374.0 K. The total observation time is 26 seconds. t_i: the time when the pressure quench starts; t_f: the time when the pressure quench ends.

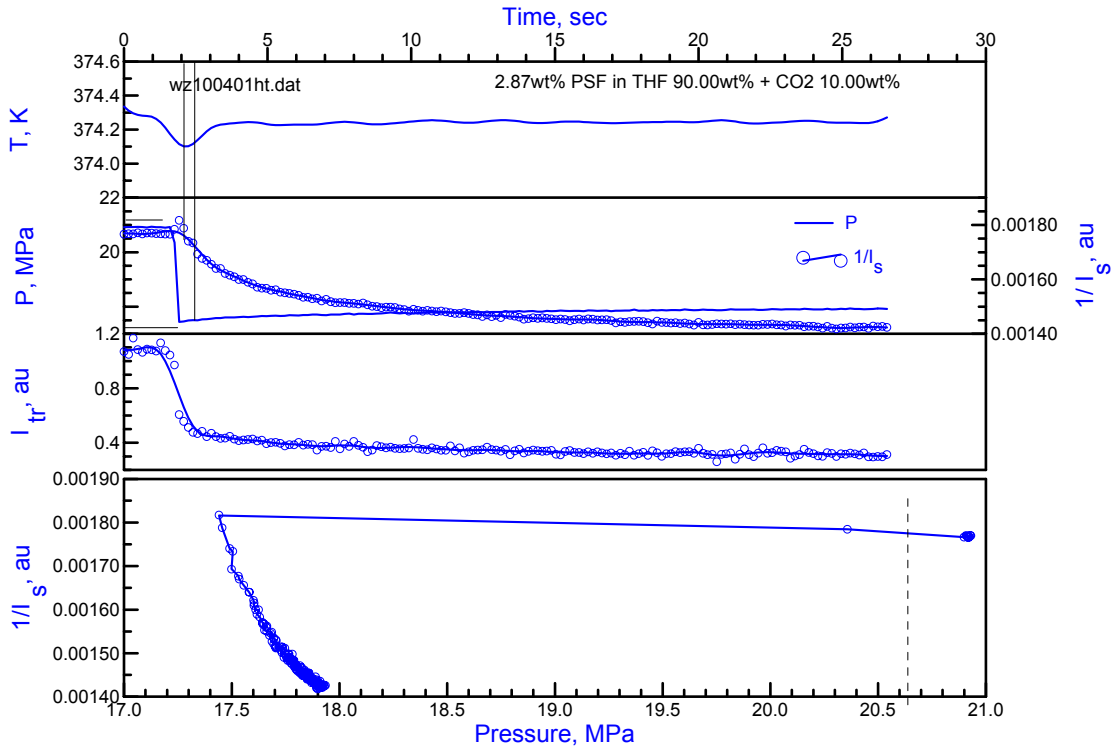

Figure C.13. Variation of temperature (T), Pressure (P), transmitted light intensity (I_{tr}), and inverse averaged scattered light intensity (1/Is) with time during a fast pressure quench in 2.87 wt % solution of PSF in a mixture of THF (90 wt %) + CO_2 (10 wt %).

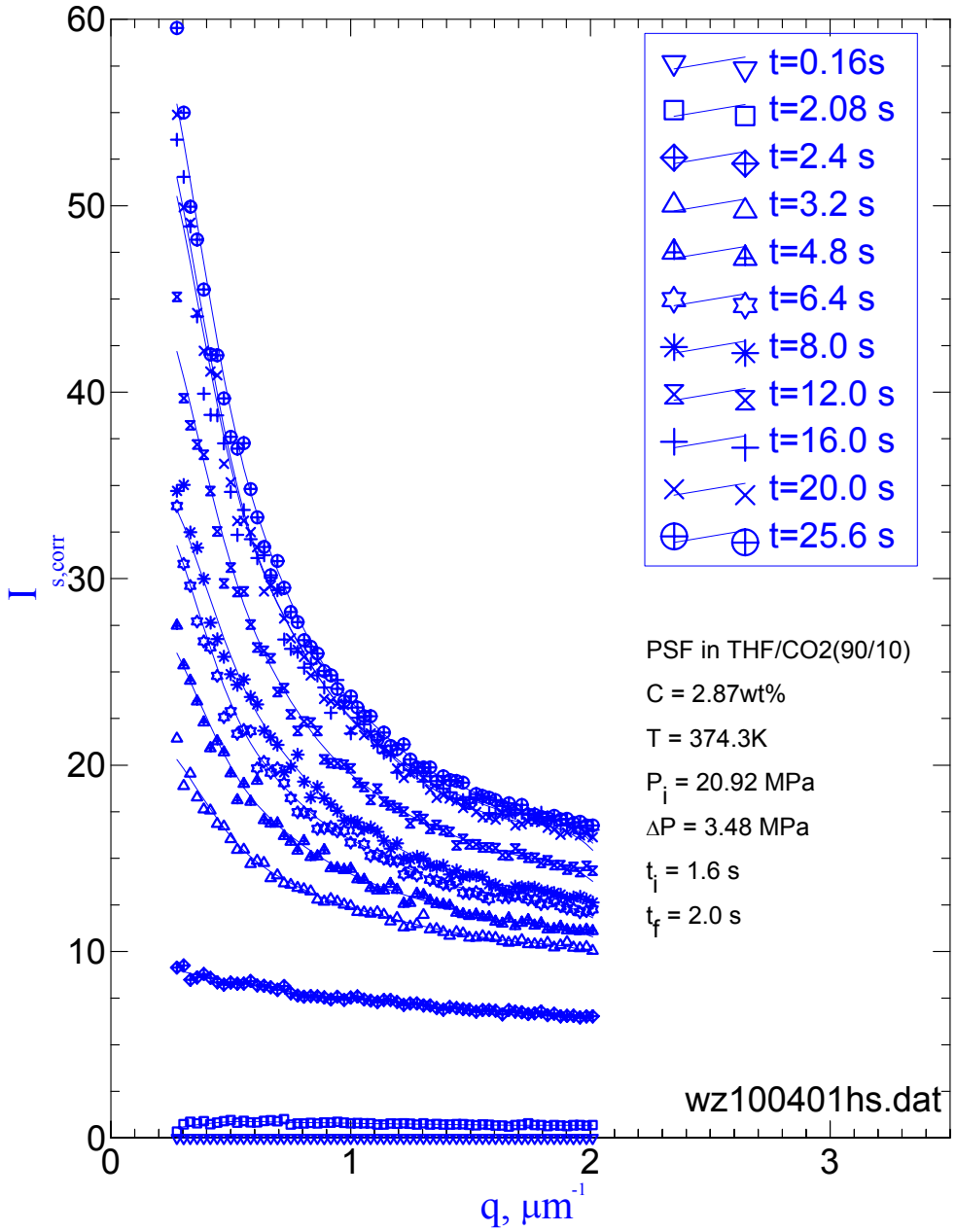

Figure C.14. Time evolution of the scattered light intensities as a function of the wave number q after a pressure quench $\Delta P = 3.48$ MPa in 2.87 wt % solution of PSF in a mixture of THF (90 wt %) + CO_2 (10 wt %) at 374.0 K. The total observation time is 26 seconds. t_i: the time when the pressure quench starts; t_f: the time when the pressure quench ends.

Vita

The author, Wei Zhang, was born in Shandong Province, China on February 5, 1975. He went to Tianjin Unviersity after graduation from Anqiu First High School. He was enrolled in the Polymer Chemical Engineering Department to study his favorite major, polymer science and engineering. He earned his Bachelor's degree in June 1996. After that, he attended The Institute of Chemical Metallurgy (which is now Institute of Process Engineering), The Chinese Academy of Sciences. In July 1999, he was awarded a Master of Science degree for his three years work on the polymer blend database.

In the fall of 1999, Wei enrolled at Chemical Engineering Department at University of Maine as a graduate student of Professor Erdogan Kiran. Shortly, in January 2000, he transferred to Virginia Polytechnic Institute and State University with Professor Kiran's group to continue his Ph.D. study. Here, his research interest is on the thermodynamics and phase separation kinetics of polymer solutions in supercritical fluids at high pressures. Besides being a research assistant, Wei also worked as a teaching assistant for several undergraduate courses with Prof. David Cox, Prof. Ravi Saraf and Prof. Erdogan Kiran, and as an instructor for one summer session of Unit Operation Laboratory under Dr. Steve York and Dr. Yasar Demirel.